# Effective Interactions between Colloidal Particles in Critical Solvents

Von der Fakultät Mathematik und Physik der Universität Stuttgart
zur Erlangung der Würde eines Doktors der Naturwissenschaften
(Dr. rer. nat.) genehmigte Abhandlung

Vorgelegt von

## Marcel Maxime Labbé-Laurent

aus Waiblingen

| | |
|---|---|
| Hauptberichter: | **Prof. Dr. Siegfried Dietrich** |
| Mitberichter: | **Prof. Dr. Udo Seifert** |

Tag der mündlichen Prüfung: **20. Februar 2018**

Max-Planck-Institut für Intelligente Systeme &
Institut für Theoretische Physik IV, Universität Stuttgart

2018

# Erklärung

Hiermit erkläre ich, dass ich, abgesehen von den ausdrücklich bezeichneten Hilfsmitteln, die Dissertation selbständig verfasst habe.

Stuttgart, den 21. November 2017

Marcel Labbé-Laurent

# Contents

# Chapter 1

# Introduction

*Effective interactions between colloidal particles in critical solvents...* The scientific background evoked by this title may be clear to the expert reader; at the same time, the concepts may also be just simple enough to be understandable for the scientific interested layman. A short introduction of the general ideas and the historical context is therefore provided.

A *critical solvent* is not necessarily a particular solvent. For example, the "best known" liquid, water[1], exhibits a critical point at 374 °C and 22064 MPa = 221 bar [1]. By varying the temperature $T$ or the pressure $p$ of a sample of water, its state can change from solid (ice) to liquid (water) to gas (vapor). Along a so-called coexistence line in terms of $p$ and $T$, water is found to coexist at the same time as vapor and liquid. If one crosses this line, a transition from the liquid to the gas state (or vice versa) occurs; the change from one state to the other is actually characterized by the jump in density $\rho$ between the high density of the liquid and the low density gaseous phase. This is called a first-order phase transition. Note that the coexistence line ends at the critical point. Beyond this critical point, the substance no longer exhibits qualitatively different phases. Instead, in this so-called fluid phase, the density changes continuously. Thus, the critical point separates two regimes: one with only a single phase, and another with two coexisting phases. Finally, there is a special path: By changing $p$ and $T$ along the coexistence, at first two phases coexist, but upon closing in on the critical point, their densities approach each other and crossing the critical point, the two phases continuously merge into a single fluid. This is a second-order or continuous phase transition.

Surprisingly, this holds also for different types of liquids: A binary liquid mixture is a mixture of two components (typically of water and an oil), with a miscibility gap (explained below). In this case, the phases are characterized by their composition $c$, instead of the density $\rho$ for a gas-liquid transition. Considering the phase diagram of the mixture in terms of mixing composition $c$ and temperature $T$, there is a regime in which

---

[1] Clearly, this accounts only for the amount of everyday contact and disregards the scientific complexity of water.

the two constituent liquids are not miscible and demix into two phases, e.g., one finds a water-rich and an oil-rich phase separated by an interface. This miscibility gap may end in one or two critical points. Thus, there are two types of critical points: A lower critical point for which the demixing occurs above the critical temperature and the one phase region exists below, as well as an upper critical point for which, conversely, the two phase separation occurs below the critical temperature. A number of binary mixtures exhibit a closed-loop miscibility gap, i.e., the upper critical point is above the lower critical point with respect to the temperature. Interesting phenomena can be observed at temperatures close to the critical points. Note that at a critical point, phase transitions are always second order and continuous.

The critical opalescence has been described as a clouding effect occurring in experiments on liquefying carbon dioxide by T. Andrews in 1869 [2] close to the critical temperature. It was then qualitatively explained by M. v. Smoluchowski [3] as evidence in favor of the kinetic gas theory, by associating it with scattering at density fluctuations in the liquid in reminiscence of the Rayleigh scattering of light at particles in the atmosphere, which was then quantitatively confirmed by Einstein [4]. As the difference in density or concentration between the two phases vanishes towards the critical point, the fluctuations in density increase. The range over which the density is correlated is given by the bulk correlation length $\xi$, which is typically microscopically small in liquids, but becomes macroscopically large around the critical point. Specifically, the correlation length $\xi$ attains the same order of magnitude as the wave length of visible light, leading to scattering of the light at the fluctuations and, overall, to the turbidity of the liquid.

Even more surprisingly, the basic principles of critical phase transitions apply not only to liquids, but also to completely different physical systems such as ferromagnets and superconductors. For example, in a ferromagnetic material (i.e., an ordinary magnet) the atomistic magnetic dipoles are aligned, so that overall there is a non-zero magnetization. In a paramagnetic material, the magnetic dipoles are unordered so that overall no net magnetization results. The presence of an external magnetic field induces an alignment of these magnetic dipoles, so that the material becomes temporarily “magnetic”. However, the magnetization is lost again once the external field vanishes. For an uniaxial ferromagnet, the magnetic dipoles can only align along one axis. For a range of temperatures, there are two possible ground states, either all dipoles are aligned upwards, or all are aligned downwards. Above a critical temperature, the Curie temperature $T_c$, the magnetization vanishes and the material becomes paramagnetic. The two ordered ground states may coexist at the same time in different regions within the material which are known as *Weiss domains*. This description is analogous to the previous liquid phase transition and the correspondence translates also to the mathematical relations, e.g., the density is now replaced by the total magnetization $m$. The total magnetization behaves as $m \sim |T - T_c|^\beta$ as a function of temperature $T > T_c$ close to the critical temperature $T_c$, with a so-called critical exponent $\beta > 0$, whereas $m = 0$ for $T < T_c$. The exact same relation holds for the composition difference $\phi = c - c_c$ in a binary mixture, with $c_c$ being the composition at the critical point, and for the difference $\rho_l - \rho_g$ between the density $\rho_l$ of the liquid and the density $\rho_g$ of the gas in a gas-liquid phase transition. Remarkably, the exponent $\beta$ even has the same numerical value in these cases. As such, $\beta$ is one of the so-called universal critical exponents, and the associated quantity is denoted as the order parameter of the system.

It turns out that critical phenomena can be classified into only a small number of universality classes that exhibit the same critical exponents. Since very different systems such as fluids, liquid mixtures or uniaxial ferromagnets, which have nothing in common microscopically, behave similarly, this suggests that only some collective, macroscopic properties are relevant for the critical phenomena. Historically, this motivated the search for phenomenological models, pioneered by Landau [5], to describe such phase transitions. Remember that the crossover from microscopic to macroscopic size is a feature of the bulk correlation length $\xi$. As a consequence, the universal behavior can be described in terms of scaling functions depending only on scaling variables which are ratios of the relevant macroscopic length scales of the system and of the correlation length $\xi$.[2]

Continuing with the explanation of the title, *colloidal particles* are not uniquely defined. The term traces back to T. Graham [6] who distinguished the diffusion of certain dispersions as gelatine-like and called them *colloids* (from Greek *κόλλα* meaning glue) in contrast to the crystallization behavior of other solutions. Generally, today [7] one considers as a colloidal suspension those solutions with a subdivision into microscopic solvent components (molecules) and particles or droplets with a mesoscopic size of nanometers to ten micrometers [$(10^{-9} - 10^{-5})$ m] [8–10]. This is similar to the definition of sand, which is not one specific mineral, but any granular material with particle sizes two orders of magnitude below and up to a few millimeters [9]. While "colloid" originally referred to the dispersion in total, in modern usage it is usually meant as a short form of *colloidal particle*, i.e., it denotes the immersed particles of the colloidal dispersion. Aerosol, emulsion, foam, and suspension are, among others, names for the different combinations of gaseous or liquid solvent medium and gaseous, liquid or solid solute components [10]. The solvent medium itself can be of complex molecular structure and may even contain multiple components, surfactants, ions or other particles smaller than the colloidal regime. This thesis focuses on *colloidal particles in critical solvents*, for which universality holds, so that no particular solvent needs to be specified. However, in view of experimental measurements, binary liquid mixtures represent the most convenient realizations.

---

[2] It is a wonder to behold that nature is offering this universal behavior, allowing for simple, yet general and powerful theories. On the other hand, the universal behavior follows unambiguously from the mathematical descriptions, so that one may conclude that nature had no other choice. This thesis cannot provide anything to the philosophical question which came first, however it owes everything to the fact that such beautiful relations exist.

With such broad definitions, it is clear that countless direct and *effective interactions* may affect the *colloidal particles* depending on the solvent; also several interactions can be present at the same time. Direct interactions are those directly between the colloids themselves. A colloid will also interact with the solvent, typically via a microscopic interaction. The response of the solvent may then also affect a second colloid, giving rise to an indirect or *effective interaction* between the colloids. However, this distinction is often not very productive since the same fundamental force can lead to both types of interaction: The Coulomb interaction between charged colloids is a direct interaction in vacuum, but in a solvent electric double layers of solvent ions *effectively* screen the interaction. Another prominent example of colloidal interactions is the van der Waals interaction between the atoms of the colloids, which, together with the aforementioned screened electrostatic interaction, is combined into the Derjaguin-Landau-Verwey-Overbeek (DLVO) potential [11]. Additionally, when intermediate solute particles are present, entropic depletion forces occur [12]. Within this thesis, particular interest is set on the critical Casimir forces appearing for temperatures in the vicinity of the critical point of the solvent. The name refers to the quantum-mechanical Casimir effect predicted in 1948 by Hendrik B. G. Casimir [13]. He surmised that two perfectly conducting metal plates in vacuum experience an attractive force as the space between them is still filled with vacuum fluctuations. These fluctuations are however bounded by the metal plates, so that only specific modes fit inside. On the outside, there is no restriction on the spectrum of the modes, leading to a pressure against the plates. The strength of this Casimir force is so small that it took nearly half a century to reach the necessary experimental precision in order to measure the Casimir force [14].

In analogy, it was realized by M. E. Fisher and P.-G. de Gennes [15] that the confinement of a critical solvent will result analogously in a thermodynamic *critical Casimir force* between the surfaces due to the confinement of the critical solvent fluctuations. However, there are a number of unique features compared to the quantum-mechanical Casimir effect. The critical Casimir effect can both be attractive as well as repulsive, depending on the chemical properties of the surfaces. In the case of a binary liquid mixture, the surfaces have an adsorption preference for one of the components in the solvent, e.g., they are either hydrophilic or hydrophobic. Furthermore, the distance-dependence of the critical Casimir forces changes upon approaching the critical point. Whereas it decays exponentially with distance away from the critical point, at criticality it turns into a power law and becomes long-ranged. Additionally, the critical Casimir force inherits the property of universality from the critical solvent, thus it can be expressed in terms of scaling functions. Whereas most other interactions cannot be controlled in the experiment after preparation of the particles, the strength of the critical Casimir interaction can be fine-tuned by minute temperature changes.

The first experimental evidence for critical Casimir forces was provided only indirectly by studying the thickness of thin wetting films in classical binary liquid mixtures [16, 17] near demixing, as well as in mixtures of $^3$He / $^4$He [18, 19] and liquid $^4$He close to their normal-superfluid transition [20, 21]. Corresponding Monte Carlo simulations for the film geometry [22–27] are in very good quantitative agreement with the experiments. The first direct measurement of the critical Casimir effect [28] was performed by monitoring optically the thermal motion of a single spherical colloid, immersed in a binary liquid mixture of water and 2,6-lutidine close to demixing and near a chemically homogeneous substrate. The experimental results are in excellent agreement with corresponding theoretical predictions [28–30], which make use of the Derjaguin approximation (DA) [31] with Monte Carlo (MC) simulation results for the film geometry as input. A full MC simulation for the sphere-wall geometry has been performed only recently [32]. Other theoretical studies rely on field-theoretical methods [33–37].

If two colloids of similar surface chemistry are brought close to one another, a liquid bridge between the two colloids can form [38]. This bridging transition is another distinct phenomenon resulting also from confinement and can be thought of as being analogous to capillary condensation, in which the vapor condensates at a pressure below the saturation vapor pressure (see, e.g., Refs. [39, 40]). In recent years, studies have been carried out which have examined the bridging transition for spherical particles by using local field theory [41, 42], density functional theory (DFT) [43–45], and Monte Carlo simulations [46, 47]. Similarly, a gas-bridge has been observed for solvophobic block-shaped particles using DFT [48].

Attractive forces between the *colloidal particles* can lead to aggregation. With a view on applications, undirected and irreversible aggregation is usually not a favorable result. Early experiments showed a reversible aggregation occurring around the lower critical point of binary liquid mixtures [49–51], though theoretical interpretation remained inconclusive [52], see also Refs. [53, 54] for reviews.

Recent research interest has risen in “designing” colloidal particles for *self-assembly*, i.e., the reversible and directed aggregation into specific structures, which may have vast applications. In a sense, if colloidal particles are the analogue of sand, the ultimate goal is to build colloidal sandcastles by self-assembly of the particles. For this reason, strong experimental and theoretical interests emerged in patchy colloidal particles with chemically heterogeneous surface properties and in Janus particles with “two faces” — a topic which has been popularized by the Nobel prize lecture of de Gennes [55]. These particles have the potential to be building blocks for directed self-assembly of new materials, such as the Kagome open-lattice structure [56–58]. Topical reviews concerning both experimental and theoretical aspects of patchy particles are provided in Refs. [59] and [60]. From an experimental point of view, the fabrication of such particles poses a research challenge in itself [61–63], followed by the experimental observation of their (self-)assembly behavior [56, 64, 65].

In principle, any anisotropic surface structure gives rise to an orientation dependent behavior caused by surface mediated interactions, e.g., due to surface charges [66, 67] or critical fluctuations. In this sense, the critical Casimir effect is a viable candidate to achieve controlled self-assembly, as demonstrated experimentally by the trapping of homogeneous colloids adjacent to chemically patterned substrates [68, 69], in very good agreement with corresponding theoretical predictions [69, 70].

The study of Janus particles exposed to the critical Casimir effect represents a rather new research issue, encompassing a few promising experimental investigations [71,72]. The critical Casimir effect provides a controllable effective interaction which can be directed by both attraction and repulsion between the patches of the particles, depending on the design and surface treatment of the particles. The surfaces can also be modified in order to change boundary conditions for the order parameter of the underlying continuous phase transition of the solvent, e.g., by producing a surface with only weak adsorption preference for one of the two species forming the binary liquid solvent [73].

With the purpose to discuss in detail the *effective interactions between colloidal particles in critical solvents*, the thesis is organized as follows: In chapter 2, this broad introduction is refined by providing in short form the necessary theoretical relations. It is divided into universal theoretical models, and those additional descriptions necessary to comprehend experimental results. The following chapters present results which in part have been worked out in consultation with other scientists (named in the publication list below) and which have been published. Based on this context, the first person plural *we* is used for the author. In chapter 3, the critical Casimir forces, torques and effective potentials of a cylindrical Janus particle are calculated in the presence of a substrate. The results are directly relevant for chapter 4 concerning the pair interaction between Janus spheres. After this view on critical Casimir interactions, another effective interaction is discussed in chapter 5 by considering the bridging transition occurring between colloidal particles and comparing it in strength with the critical Casimir interaction. Finally in chapter 6, the theory is put to test by analyzing an experimental realization. The limits of the comparison are documented as well as where good agreement with the theoretical critical Casimir interaction is achieved. The work is summarized in chapter 7, and a possible outlook to further research is given. For reference, Appendices A and B lay out explicitly the Derjaguin approximation and derive the scaling function of the force and the potential for two homogeneous cylinders and for two Janus spheres, respectively. For the interested reader not versed in the mathematical models that have formed the fundamental understanding of phase transitions, brief discussions are offered in Appendix C. However, the latter are not necessary in order to derive the main results of this thesis.

Parts of this thesis have already been published:

- As Ref. [74]: M. Labbé-Laurent, M. Tröndle, L. Harnau, and S. Dietrich,
  *Alignment of cylindrical colloids near chemically patterned substrates induced by critical Casimir torques*,
  Soft Matter **10**, 2270 (2014)

- As Ref. [75]: M. Labbé-Laurent and S. Dietrich,
  *Critical Casimir interactions between Janus particles*,
  Soft Matter **12**, 6621 (2016)

- As Ref. [76]: S. G. Stuij, M. Labbé-Laurent, T. E. Kodger, A. Maciolek, and P. Schall,
  *Critical Casimir interactions between colloids around the critical point of binary solvents*,
  Soft Matter **13**, 5233 (2017)

- As Ref. [77]: M. Labbé-Laurent, A. D. Law, and S. Dietrich,
  *Liquid bridging of cylindrical colloids in near-critical solvents*,
  J. Chem. Phys **147**, 104701 (2017)

# Chapter 2

# Theoretical and Experimental background

## 2.1 Theory

### 2.1.1 Scaling laws in the bulk

In the case of a gas-liquid phase transition, the density difference between the phases $(\rho_l - \rho_g) \sim |T - T_c|^\beta$ vanishes at $T_c$. At coexistence, the pressure of the gas and the pressure of the liquid phase are the same. We may express this using the equation of state $p(\rho)$ as the condition $p(\rho_g) = p(\rho_l)$. Away from the critical point, this can only hold true if the pressure curve has an inflection point in-between the two densities $\rho_g$ and $\rho_l$, i.e., there is a point at which $\frac{\partial^2 p}{\partial \rho^2} = 0$. The critical point is obtained from [78]

$$\left.\frac{\partial p}{\partial \rho}\right|_T = \left.\frac{\partial^2 p}{\partial \rho^2}\right|_T = 0. \tag{2.1}$$

The isothermal compressibility is defined as $\kappa_T = \frac{1}{\rho} \left.\frac{\partial \rho}{\partial p}\right|_T$ [78], which in consequence means $\kappa_T \to \infty$ at the critical point. This has the physical meaning that any small change in pressure will lead to a large change in density, so that any small, local perturbation gives rise to large density fluctuations – which become visible in the form of critical opalescence. The isothermal compressibility also adheres to a power law $\kappa_T \sim |T - T_c|^{-\gamma}$, with the critical exponent $\gamma$. These power laws derive from the thermodynamic potential of the system. (In fact, the original classification of phase transition as first, second and higher order was numbered according to which consecutive derivative of the thermodynamic potential is discontinuous [79].) Thus, by definition the free energy $\mathcal{F}$ cannot be analytic (i.e., infinitely differentiable), but must contain a non-analytic part, i.e., it can be separated into a regular, analytic part $\mathcal{F}_{\text{reg}}$ and a singular part $\mathcal{F}_{\text{sing}}$. Only the singular part determines the critical exponents.

In order to bear out these relations, it was postulated by B. Widom [80] that the free energy density $f = \mathcal{F}_{\text{sing}}/V$ of the singular part takes a homogeneous form, that is

$$f(b^{p_1}\omega_1, b^{p_2}\omega_2, \ldots) = b^d\, f(\omega_1, \omega_2, \ldots), \tag{2.2}$$

where $\omega_i$ are not yet specified dimensionless variables (called scaling fields) and $p_i$ are the associated scaling dimensions. This holds also for the specific choice $b = \omega_1^{-1/p_1}$, such that $b^{p_1}\omega_1 = 1$, and

$$f(\omega_1, \omega_2, \ldots) = \omega_1^{d/p_1}\, f\left(1, \frac{\omega_2}{\omega_1^{p_2/p_1}}, \ldots\right). \tag{2.3}$$

In the notation of the Ising model, $\omega_1 = t = (T - T_c)/T_c$ and $\omega_2 = h$ are the only relevant fields, so that the Widom scaling hypothesis is given by [79–81]

$$f(t, h) = t^{d/p_1}\, f\left(1, \frac{h}{t^{\Delta}}\right) \tag{2.4}$$

with $\Delta = p_2/p_1$. Thus, the free energy is restricted to a functional form that can be rendered using a scaling function of a single dimensionless parameter.

The consequences of the homogeneous form are quite profound, as it establishes relations between the exponents of all thermodynamic quantities derived from the free energy:

1. Magnetization: $m = -\frac{\partial f}{\partial h} \overset{(2.2)}{\Rightarrow} b^{p_2}\, m(b^{p_1}t, b^{p_2}h) = b^d\, m(t, h)$.
   For an uniaxial ferromagnet, the magnetization represents the so-called order parameter (OP). The same role is fulfilled by the difference in density $(\rho_l - \rho_g)$ for the gas-liquid phase transition and by the concentration difference $(c - c_c)$ for the demixing phase transition.

   - The magnetization is non-vanishing only for $t < 0$, so that the choice $b = (-t)^{-1/p_1}$ is a real number. For zero bulk-field $h = 0$, we obtain

     $$m(t, 0) = (-t)^{-(p_2-d)/p_1} m(-1, 0). \tag{2.5}$$

     If this is compared with the expected power law $m(t) \propto (-t)^{\beta}$ (see Table 2.1), and taken as the definition of the critical exponent $\beta$, we obtain $\beta = (d - p_2)/p_1$.
   - On the critical isotherm $t = 0$, we may set $b = h^{-1/p_2}$, yielding

     $$m(0, h) = h^{(d-p_2)/p_1} m(0, 1). \tag{2.6}$$

     One expects the power law $m(h) \propto h^{1/\delta}$, from which we find $1/\delta = (d - p_2)/p_1$.

   We can additionally identify the exponent $\Delta$ in Eq. (2.4) as $\Delta = p_2/p_1 = \beta\delta$.

| Exponent | Quantity | Scaling | d=3 [82] | d=4 [81] |
|---|---|---|---|---|
| $\alpha$ | specific heat | $c_h \sim \lvert t\rvert^{-\alpha}$ | 0.11 | 0 |
| $\beta$ | magnetization (ferromagnet)<br>density diff. (gas-liquid)<br>concentration diff. (demixing) | $m \sim \lvert t\rvert^{\beta}$<br>$(\rho_l - \rho_g) \sim \lvert t\rvert^{\beta}$<br>$(c - c_c) \sim \lvert t\rvert^{\beta}$ | 0.326 | 1/2 |
| $\gamma$ | susceptibility<br>isothermal compressibility | $\chi \sim \lvert t\rvert^{-\gamma}$<br>$\kappa_T \sim \lvert t\rvert^{\gamma}$ | 1.237 | 1 |
| $\delta$ | equation of state | $m \sim h^{1/\delta}$<br>$(\rho_l - \rho_g) \sim \lvert\Delta p\rvert^{1/\delta}$ | 4.789 | 3 |
| $\eta$ | pair correlation function | $C(r) \sim r^{-(d-2+\eta)}$ | 0.0364 | 0 |
| $\nu$ | correlation length | $\xi \sim \lvert t\rvert^{-\nu}$ | 0.6301 | 1/2 |

Table 2.1: Overview of the critical exponents for the Ising universality class. Values in $d = 3$ are based on Monte-Carlo simulations listed in Ref. [82] and analytic results for $d = 4$ correspond to mean field or Landau theory [81]. The quantities depend on the fields $t = (T - T_c)/T_c$ and $h$. The critical exponent $\beta$ is associated with the order parameter (OP) of the specific system.

2. Susceptibility: $\chi_T = \frac{\partial m}{\partial h} = -\frac{\partial^2 f}{\partial h^2} \overset{(2.2)}{\Rightarrow} b^{p_2}\,\chi_T(b^{p_1}t, b^{p_2}h) = b^d\,\chi_T(t,h)$.
   As before, we set $b = t^{-1/p_1}$. For vanishing bulk-field $h = 0$, one finds

   $$\chi_T(t,0) = t^{-(2p_2-d)/p_1}\chi_T(1,0). \tag{2.7}$$

   Defining the critical exponent $\gamma$ via the power law $\chi_T \propto t^{-\gamma}$ leads to $\gamma = (2p_2 - d)/p_1$.

3. The specific heat $C_h = \frac{\partial U}{\partial T}\big|_h$ can also be derived from the free energy $f = (U - T\,S)/V$ via $\frac{\partial(\beta f)}{\partial \beta} = U/V$, so that

   $$C_h = -VT\frac{\partial^2 f}{\partial T^2} = -\frac{VT}{T_c}\frac{\partial^2 f}{\partial t^2} \overset{(2.2)}{\Rightarrow} b^{2p_1}\,C_h(b^{p_1}t, b^{p_2}h) = b^d\,C_h(t,h). \tag{2.8}$$

   As expected, a scaling law follows by setting $b = (-t)^{-1/p_1}$

   $$C_h(t,h) = t^{-(2p_1-d)/p_1}C_h(1,0) \propto t^{-\alpha}, \tag{2.9}$$

   with the critical exponent $\alpha = 2 - d/p_1$.

Making use of these scaling relations, the free energy is commonly expressed as

$$f(t,h) = t^{2-\alpha}\,g\left(\frac{h}{t^{\Delta}}\right) \tag{2.10}$$

with $\Delta = \beta\delta$ and an universal scaling function $g(x) = f(1,x)$. Evidently, the critical exponents are not independent, but are related by so-called scaling relations. For a system with two relevant scaling variables, only two are independent and the remaining ones follow from [79, 81, 83]

$$\gamma/\beta = \delta - 1 \quad \text{Widom's identity,} \qquad (2-\eta)\nu = \gamma \quad \text{Fisher's identity,} \tag{2.11}$$

$$\alpha + 2\beta + \gamma = 2 \quad \text{Rushbrooke's identity,} \qquad 2 - \alpha = d\nu \quad \text{Josephson's identity,} \tag{2.12}$$

$$\alpha + \beta(\delta + 1) = 2 \quad \text{Griffiths' identity,} \tag{2.13}$$

The Josephson's identity is notable in that it is a hyperscaling relation containing the dimension $d$ of the system. It is valid only for $d \leq d_u$ below the upper critical dimension $d_u$. Above the upper critical dimension, the Ising model crosses over into the mean field theory (presented below), which does not adhere to Josephson's identity. The critical exponents and their values for the Ising universality class are listed in Table 2.1.

Close to the critical point of a fluid, thermal fluctuation become correlated over macroscopic distances and are, to a large extent, independent of microscopic details. Upon approaching the critical demixing point $T_c$ of a binary liquid mixture at its critical concentration, the bulk correlation length diverges as $\xi(t) \sim |t|^{-\nu}$, with the critical exponent $\nu \simeq 0.63$ in $d = 3$ and $\nu = 1/2$ in $d = 4$ (see Table 2.1).

Generally, the correlation length $\xi$ is a function of both $t$ and $h = 0$. By dimensional arguments, close to the critical point the singular contribution to the free energy density must scale with the correlation length as $f(t, h) \sim \xi^{-d}$. Thus, based on the scaling hypothesis Eq. (2.10), the bulk correlation length $\xi$ depends on both scaling fields $t$ and $h$, and close to the bulk critical point can be written in the scaling form

$$\xi(t, h) = \xi_t\, \Xi_\pm \left( |\Sigma| = \frac{\xi_t}{\xi_h} \right), \tag{2.14}$$

where $\xi_t(t) = \xi_{t,\pm}^{(0)} |t|^{-\nu}$ and $\xi_h(h) = \xi_h^{(0)} |h|^{-\nu/(\beta\delta)}$ are the solvent correlation lengths as functions of the individual fields, and the universal bulk scaling function $\Xi_\pm$ satisfies $\Xi_\pm(|\Sigma| \to \infty) = 1$ and $\Xi_\pm(|\Sigma| \to 0) = |\Sigma|^{-1}$. The sign of $t$ is chosen such that $t > 0$ corresponds to the homogeneous, mixed state, whereas $t < 0$ corresponds to the two phase region. Many experiments are performed advantageously in binary liquid mixtures with a lower critical point [28, 29, 68, 69, 71, 72, 84]; in this case one has $t = (T_c - T)/T_c$. The functional form of $\Xi_\pm(|\Sigma|)$ depends on the sign $\pm$ of $t$, but not on the sign of the bulk scaling variable $\Sigma$. Similarly, the amplitudes $\xi_{t,\pm}^{(0)}$ reflect the sign of $t$ and are non-universal, but their ratio $R_\xi = \xi_{t,+}^{(0)}/\xi_{t,-}^{(0)} = 1.96$ in $d = 3$ [82] and $R_\xi = \sqrt{2}$ in $d = 4$ [85] is universal. The amplitude $\xi_h^{(0)}$ is also non-universal; $\nu$, $\beta$, and $\delta$ are standard bulk critical exponents, see Table 2.1. The scaling variable $\Sigma$ is further related to the OP $\phi$, which is the direct experimental control parameter in the case of binary liquid mixtures (for which $\phi = c - c_c$). This is expressed by the equation of state, which close to the critical point takes the scaling form [82]

$$h = \mathcal{D}\,\mathrm{sign}(\phi)\,|\phi|^{\delta}\,\mathrm{F}_{\pm}\left(\mathrm{sign}(t)\,|t\mathcal{B}/\phi|^{1/\beta}\right), \tag{2.15}$$

where $\mathrm{F}_{\pm}(|X| = |t\mathcal{B}/\phi|^{1/\beta})$ is a universal scaling function and ± refers to the sign of $t$. $\mathcal{D}$ and $\mathcal{B}$ are non-universal amplitudes that depend on the definition of the order parameter $\phi$. For example, $\mathcal{B}$ is defined via the near-critical behavior of the OP on the coexistence curve:

$$\phi_{\mathrm{b}}(t \to 0^{-}, h = 0) = \mathcal{B}\,|t|^{\beta}\,. \tag{2.16}$$

$\mathcal{D}$, $\mathcal{B}$, and the correlation length amplitudes $\xi^{(0)}_{t,\pm}$ and $\xi^{(0)}_{h}$ are related to each other by universal amplitude ratios such that only two of them are independent [36,82]. To linear order in $X$, the universal scaling function $\mathrm{F}_{\pm}(|X|)$ has the form $\mathrm{F}_{\pm}(|X|) = 1 \pm |X|$, capturing the crossover between the critical behavior at $t = 0$ and $h = 0$ [82]. In terms of the scaling variables $\Sigma$ and $X$, the equation of state takes the scaling form

$$\mathrm{sign}(\Sigma)\,|\Sigma|^{\beta\delta/\nu} = (R_{\chi}\delta/Q_2)^{\delta/(\delta-1)}(Q^{+}_{\xi}/Q^{c}_{\xi})^{\beta\delta/\nu}\,\mathrm{sign}(X)\,|X|^{-\beta\delta}\,F_{\pm}(|X|), \tag{2.17}$$

where $R_{\chi}$, $Q_2$, $Q^{+}_{\xi}$, and $Q^{c}_{\xi}$ are universal amplitude ratios [82].

### 2.1.2 Finite size scaling

In a confined system, e.g., in the film geometry bounded by two walls $a$ and $b$ of area $A$ with distance $D$ between them, the singular contribution to free energy close to criticality is supplemented by additional terms in the form

$$\lim_{A\to\infty}\frac{\mathcal{F}_{\mathrm{sing}}(t,h;h_a,h_b;D)}{A} = Df(t,h) + f_s(t,h;h_a) + f_s(t,h;h_b) + \delta f(t,h;h_a;h_b;D), \tag{2.18}$$

where $f(t,h)$ is the bulk, per volume contribution from the enclosed volume $V = A\,D$, $f_s(t,h;h_{a,b})$ are two individual surface contributions from each wall, and $\delta f(t,h;h_a;h_b;D)$ is a true finite-size contribution. Generically, in binary liquid mixtures, surfaces have a preference for one of the components of the mixture. Such an adsorption preference belongs to the normal surface universality class and is captured by a surface field $h_{a,b}$, which is the analogue to the bulk field $h$. The strong adsorption limit $h_{a,b} \to \pm\infty$ is typically denoted in short form by a $(+)$ and $(-)$ notation representing the sign of the surface field and indicating which component is preferred. For brevity, we omit the discussion of a surface enhancement $c$ relevant in other surface universality classes.

This allows to define a solvent-mediated force $F$ between two walls from the *excess* part of the free energy via

$$F = -\frac{\partial \mathcal{F}^{ex}}{\partial D} = -\frac{\partial(\mathcal{F} - Vf)}{\partial D}, \tag{2.19}$$

where $f$ is the bulk free energy density of the solvent and $\mathcal{F}$ is the total free energy of the solvent. Remember that $\mathcal{F}$ contains both singular and regular contributions. The critical Casimir force $F^{(\mathrm{Cas})}$ is the singular contribution to $F$, which emerges upon approaching the bulk critical point of the solvent. The associated critical Casimir potential is found from

$$V^{(\mathrm{Cas})}(D, \ldots) \equiv \int_D^\infty \mathrm{d}z\, F^{(\mathrm{Cas})}(z, \ldots). \tag{2.20}$$

According to finite size scaling theory, in the vicinity of its bulk critical point, not only the bulk and surface free energy contribution exhibit a scaling form, but also the finite-size contribution $\delta f$, which can be written in terms of a universal scaling function that depends only on the shape of the sample and on coarse features of the system, summarized by universality classes.

With respect to the experiment analyzed in chapter 6 (see also Ref. [76]), and similar studies [28, 29, 68, 69, 71, 72, 84], the relevant scaling fields of the near-critical solvent are $t = (T_c - T)/T_c$ (for a lower lower-critical point) and the bulk ordering field, $h$, conjugate to the order parameter $\phi$. The bulk field $h$ is proportional to the deviation of the chemical potential difference $\Delta\mu = \mu_a - \mu_b$ of the two species $a$ and $b$ from its critical value, i.e. $h \sim \Delta\mu - \Delta\mu_c$. Each point in the solvent phase space is uniquely defined by $t$ and $h$. (Note that the use of the scaling fields of the Ising model is not exact due to the lack of symmetry between coexisting fluid phases; the actual scaling fields are linear combinations of $t$ and $h$, which we neglect here). For the demixing phase transition of a binary liquid mixture, the OP $\phi$ is proportional to the deviation of the composition $c_a$ of species $a$ from its value $c_{a,c}$ at the critical point, i.e. $\phi = c_a - c_{a,c}$. The composition $c_a = \varrho_a/(\varrho_a + \varrho_b)$ is defined by the number densities $\varrho_\alpha$, $\alpha \in \{a, b\}$ of the molecules of species $a$ and $b$, respectively. Generally one may leave out the explicit $a$ dependence as this choice is arbitrary and write $\phi = c - c_c$. The OP can be controlled experimentally by changing the mass or the volume fraction of one of the components of the mixture. The conjugate bulk field $h$ cannot be changed directly, but is also controlled via $\phi$ according to Eq. (2.15). Note that zero bulk field $h = 0$ corresponds to $\phi = 0$, i.e., the composition $c$ is at its critical value $c_c$.

Accordingly, the critical Casimir force is described by an universal scaling function uniquely determined by the bulk universality class [82] (here: Ising), the surface universality class [86, 87] (here: normal transition with symmetry-breaking boundary conditions (+) and (−)), the spatial dimensional (here: $d = 3$ and $d = 4$ in mean field theory), and the geometry of the confinement [81, 88, 89] (here: cylinders, spheres, and planar walls).

In the case of the *film* geometry with two flat, parallel, homogeneous, strongly adsorbing and macroscopically large walls at distance $D$, renormalization group theory predicts the following form for the critical Casimir force $F_{(a,b)}$ per area of the wall at zero bulk field $h = 0$ [90]:

$$\frac{F_{(a,b)}(D,T)}{A} = k_B T \, \frac{1}{D^d} \, k_{(a,b)}(\Theta = \mathrm{sign}(t)\, D/\xi_{\pm}), \tag{2.21}$$

where the subscript $(a, b)$ indicates the pair of boundary conditions (BC) $(a) = (\pm)$ and $(b) = (\pm)$ characterizing the two walls. In the absence of a bulk ordering field and for infinitely strong surface fields, the scaling function $k_{(a,b)}$ depends only on a single scaling variable, which is given by the sign of the reduced temperature $t$ and the film thickness $D$ in units of the bulk correlation length $\xi_{\pm}$ (with $\pm$ taken for $t \gtrless 0$; for simplicity, the index $t$ is omitted for $h = 0$ so that $\xi_t(t) \equiv \xi_{\pm}$ and $\xi^{(0)}_{t,\pm} \equiv \xi^{\pm}_0$). Note that the scaling variable $\Theta = \mathrm{sign}(t)\, D/\xi_{\pm}$ contains distinct denominators $\xi^{\pm}_0$ for $t \gtrless 0$. We emphasize that Eq. (2.21) describes the behavior of the *singular* contribution to the effective force acting on the confining walls, in addition to any background forces.

At the critical point $T = T_c$, $\xi_{\pm}$ diverges and the scaling function of the force $k_{(a,b)}$ between two walls reduces to an universal number referred to as the critical Casimir amplitude (see Ref. [81]; the notation differs slightly)

$$k_{(a,b)}(D/\xi_{\pm} = 0) = \Delta_{(a,b)}, \tag{2.22}$$

which leads to an algebraic decay $\sim D^{-d}$ of the critical Casimir force as a function of the film thickness. In contrast, away from criticality the critical Casimir force decays exponentially as a function of $D/\xi_{\pm}$. For the symmetry-breaking BCs $(-,-)$ or $(+,-)$ valid for binary liquid mixtures and for $t > 0$, the critical Casimir force is expected to decay as (see Refs. [29, 70, 91])

$$k_{(+,\pm)}(l/\xi_{+} \gg 1) = \mathcal{A}_{\pm} \left(\frac{D}{\xi_{+}}\right)^{d} \exp(-D/\xi_{+}), \tag{2.23}$$

where $\mathcal{A}_{\pm}$ are universal amplitudes [29]. Note that the force is the same for equal BCs and we define the shorthand $k_{\|} := k_{(+,+)} = k_{(-,-)}$ for the scaling function between two identical, parallel walls.

Consequently, the critical Casimir potential between identical spherical particles a surface-to-surface distance $D = r - 2R$ apart and at off-critical concentrations is given by a scaling function that depends on three scaling variables, which can be written as [92]

$$V^{(\mathrm{Cas})}(D, \ldots) = k_B T \, \frac{R}{D} \, \Phi^{(ss)}_{(+,+)} \left(\Theta = sgn(t)\frac{D}{\xi_t}, \Delta = \frac{D}{R}, \Sigma = sgn(th)\frac{\xi_t}{\xi_h}\right), \tag{2.24}$$

where $\xi_t(t \gtrless 0) = \xi^{(0)}_{t,\pm}|t|^{-\nu}$ and $\xi_h = \xi^{(0)}_h |h|^{-\nu/(\beta\delta)}$ are the solvent correlation lengths governing the exponential decay of the solvent bulk two-point OP correlation function along the specific paths $t \to 0^{\pm}$ for $h = 0$, and $h \to 0$ for $t = 0$, respectively, and ± refers to the sign of $t$. The thermodynamic paths of fixed solvent composition are particularly experimentally relevant. Thus we take the convention to write the scaling function $\Phi$ of the critical Casimir potential as a function of the scaling variables $\Theta$, $\Delta$, $\Sigma$ rather than $\Theta$, $\Delta$, $\Lambda = \mathrm{s}gn(h)\, D/\xi_h$ used in Ref. [93]. The specific geometries studied in the following chapters give rise to additional parameters and $\Phi$ is decorated with corresponding symbols.

The scaling function of the potential between spherical colloids can in principle be calculated using different techniques: numerically within mean field theory (MFT), Monte-Carlo simulations (MC) and semi-analytically using Derjaguin approximation (DA). The computation time of the mean field minimization (explained in more detail below), as well as Monte-Carlo simulations, scales with the size of the simulation volume and quickly becomes prohibitively long for spherical particles. So far, only the sphere-plate geometry has been calculated using MC simulations [32]. In contrast, the critical Casimir force for the film geometry can be readily determined by using mean field theory within the framework of Landau-Ginzburg theory [91]. Some results beyond mean field theory are also available, e.g., from MC simulations [22–24, 94–96] or within the extended de Gennes-Fisher local functional method [93, 97, 98].

For this reason, we calculate the scaling function of the critical Casimir potential for spherical particles using a combination of these methods: The Derjaguin approximation is used to relate the scaling function of the potential between spherical particle to the scaling function of the force in the film geometry [29, 31, 35] via

$$\Phi^{(ss,d=3)}_{(+,+)}(\Theta, \Delta \to 0, \Sigma) = \pi \int_1^{\infty} \mathrm{d}x (x^{-2} - x^{-3}) k_{\|}^{(d=3)}(x\,\Theta, \Sigma). \tag{2.25}$$

The scaling function of the force $k_{\|}^{(d=3)}$ as a function of the composition-dependent scaling variable $\Sigma$ is calculated using the "dimensional" approximation introduced in Ref. [92]. Within that approximation, the scaling function $k_{\|}^{(d=3)}(\Theta, \Sigma)$ is constructed such that for $h \to 0$ it reduces exactly to $k_{\|}^{(d=3)}(\Theta, \Sigma = 0)$ and for fixed values of $\Theta$ its functional form is the one obtained from mean field theory ($d = 4$):

$$k_{\|}^{(d=3)}(\Theta, \Sigma) = \frac{k_{\|}^{(d=4)}(\Theta, \Sigma)}{k_{\|}^{(d=4)}(\Theta, \Sigma = 0)} k_{\|}^{(d=3)}(\Theta, \Sigma = 0). \tag{2.26}$$

We take $k_{\|}^{(d=3)}(\Theta, \Sigma = 0)$ from MC simulation data [23, 24] and assume that within the mean field expressions $k_{\|}^{(d=4)}(\Theta, \Sigma)$, the scaling variables involve the critical bulk exponents in spatial dimension $d = 3$. Thus the approximation concerns only the shape of the scaling function itself, which typically depends on the spatial dimension only mildly. The function $k_{\|}^{(d=4)}(\Theta, \Sigma)$ is calculated within mean field theory.

### 2.1.3 Mean field theory

Within MFT, the bulk and surface critical phenomena belonging to the Ising universality class are described by the standard Landau-Ginzburg-Wilson fixed point Hamiltonian [86, 87]

$$\mathcal{H}[\phi(\mathbf{r})] = \int_V \mathrm{d}^d\mathbf{r} \left(\frac{1}{2}\left(\nabla\phi(\mathbf{r})\right)^2 + \frac{\tau}{2}\left(\phi(\mathbf{r})\right)^2 + \frac{u}{4!}\left(\phi(\mathbf{r})\right)^4 - h\,\phi(\mathbf{r})\right) + \int_{\partial V} \mathrm{d}^{(d-1)}\mathbf{s} \left(\frac{c}{2}\left(\phi(\mathbf{s})\right)^2 - h_s\phi(\mathbf{s})\right), \quad (2.27)$$

which is a functional of the order parameter (OP) profile $\phi(\mathbf{r})$ of the fluid such as the difference between the local concentration of one of the two species and its critical value in a binary liquid mixture. The Hamiltonian consists of a volume term representing a $d$-dimensional liquid-filled volume $V$ and a term describing the confining surface $\partial V$ of this volume, e.g., provided by the surfaces of colloids immersed in the binary mixture, with $\phi(\mathbf{r})|_{\partial V} = \phi(\mathbf{s})$ evaluated at the boundary $\partial V$. Within MFT, the parameter $\tau$ is proportional to the reduced temperature $t$ as $\tau = t/(\xi_0^+)^2$ [81], while the coupling constant $u > 0$ ensures the stability of $\mathcal{H}[\phi(\mathbf{r})]$ for $t < 0$ in the demixed phase; $u$ is dimensionless in $d = 4$. The bulk field $h$ is proportional to the deviation of the chemical potential difference $\Delta\mu = \mu_A - \mu_B$ of the two species A and B from its critical value, i.e., $h = \Delta\mu - \Delta\mu_c$. Except for chapter 6, which concerns off-critical concentrations, we focus on being at the solvent phase coexistence or in the single phase region of the solvent at the critical concentration, so that $h = 0$. The surface enhancement $c$ and the symmetry breaking surface field $h_s$ determine the BC. Within the normal surface universality class $c = 0$ and the two fixed point values are $h_s = \pm\infty$, which is the generic one for liquids and expresses the preference of a colloid surface for one of the two species of the binary liquid mixture. This leads to a divergence of $\phi \to \pm\infty$ at the surface of the colloids corresponding to what is denoted as the $(+)$ and $(-)$ BC [87]. Concerning the numerical implementation, the divergence is realized by obtaining values of the OP close to the surface by use of a short distance expansion [99, 100] and setting these as Dirichlet boundary conditions for the minimization. Within MFT, only the order parameter configuration with the largest statistical weight $\exp\left(-\mathcal{H}[\phi(\mathbf{r})]\right)$ is considered and fluctuations of the order parameter are neglected, which corresponds to a saddle-point approximation. Within this approximation the free energy follows from $\delta\mathcal{H}[\phi]/\delta\phi|_{\phi=\langle\phi\rangle} = 0$. The MFT order parameter profile defined as $m = \langle\phi\rangle/\mathcal{B}$ minimizes the Hamiltonian $\mathcal{H}$, where $\mathcal{B} = \sqrt{6/u}/\xi_0^+$ within MFT is the non-universal amplitude of the bulk order parameter at coexistence $\phi_b = \mathcal{B}\,|t|^\beta$, with $\beta = 1/2$ in $d = 4$ and $\beta \simeq 0.33$ in $d = 3$. MFT captures correctly the critical behavior above the upper critical dimension $d_c = 4$, with logarithmic corrections in $d = 4$. In the context of renormalization group theory, the MFT results represent also the leading order contribution within an expansion in terms of $\epsilon = 4 - d$. There are only two independent non-universal bulk amplitudes [86,87], such as $\mathcal{B}$ and $\xi_0^+$.

For a film confined by two planar walls, the MFT scaling functions of the critical Casimir force have been determined analytically [91] and, inter alia, the critical Casimir amplitudes for symmetry breaking BC have been found as $\Delta_{(+,+)} = \Delta_{(-,-)} = -\Delta_{(+,-)}/4 = -24[K(1/\sqrt{2})]^4\, u^{-1} = -283.61\, u^{-1}$ where $K$ is the complete elliptic integral of the first kind.

For the geometries studied here within MFT, the Hamiltonian $\mathcal{H}[\phi]$ has been minimized numerically using a three-dimensional finite element method [101] in order to obtain the order parameter profiles. The system is assumed to be translationally invariant along an extra dimension in $d = 4$. The critical Casimir forces are determined directly from the order parameter profile using the stress-tensor method [36,91,102].

### 2.1.4 Derjaguin approximation

The Derjaguin approximation (DA) is a common technique to extend theoretically results for planar geometry, which can be derived directly, to curved objects, which are more common in practice. This approximation builds on the additivity of forces. Accordingly, a curved surface is sliced into infinitesimally small surface elements and the total force is calculated by summing up the individual planar wall-wall contributions $k_{(a,b)}$ from the surface elements vis-à-vis, with $(a)$ and $(b)$ indicating the BC at the two surfaces. In the case of a spherical object, its surface is divided into thin rings of radius $\rho$ [29,35], whereas the surface of cylindrical objects is decomposed into parallel pairs of infinitesimally narrow stripes at lateral positions $\pm\rho$ [74,103]. For both types of objects, the distance of each element from a planar wall is given by $D(\rho) = D + R(1 - \sqrt{1 - \rho^2/R^2})$, where $D$ is the closest distance between the particle surface with radius $R$ and the planar wall. Since the DA holds only in the limit of large particle radii $R$, i.e., $\Delta = D/R \to 0$, it is often [29,35,103] used in conjunction with the further "parabolic distance approximation" $D(\rho) \approx D(1 + \rho^2/(2RD))$. For comparison, the surface-to-surface distance $D(\rho) = D + 2R(1 - \sqrt{1 - \rho^2/R^2})$ either between two spheres or between two cylinders increases twice as fast with $\rho$; correspondingly, within the "parabolic distance approximation" one has in these two cases $D(\rho) \approx D(1 + \rho^2/(RD))$. As a basic example, the DA for two cylindrical particles is explicitly shown in Appendix A.

For Janus particles, the basic DA approach remains the same. However, for them the force contribution switches spatially between $k_{(+,+)} = k_{(-,-)}$ and $k_{(+,-)} = k_{(-,+)}$ due to the variation of the BC across the surface(s). Assuming again additivity and neglecting edge effects, the summation over these force contributions can be performed after appropriately subdividing the surface and grouping the surface elements according to the various pairs of BC. For the quite involved case of two Janus spheres the procedure is outlined in Appendix B.

The DA for these geometries is based on the scaling function of the force for the film geometry. For $d = 4$ this is adopted directly from our independent MFT calculations for two parallel walls. In $d = 3$ the scaling function of the force for the film geometry has been obtained from MC simulations [23, 24, 27, 94, 104]. Here, we rely on the numerical estimate referred to as "approximation (i)" in Figs. 9 and 10 of Ref. [24]. The systematic uncertainty of the overall amplitude of these scaling functions can, in the worst case, reach up to 10%–20% [24], which also affects our predictions. However, the impact on the scaling functions *normalized* by the critical amplitude $\Delta_{(+,+)}$ is greatly reduced and only on the relative level of at most 5% [103].

It has been shown that the DA is most reliable for $t \geq 0$ [32, 74], whereas for $(+,-)$ BC and $t < 0$ clear deviations from the DA occur, which can be explained in terms of the formation of an interface surrounding the particles [74].

## 2.2 Experimental non-universal contributions

### 2.2.1 Correlation length

The effective self-diffusion coefficient of the binary mixture is related to the size of the correlated regions $\xi$ via a relation analogous to Stokes-Einstein relation for Brownian particles, but depending intricately on additional microscopic details. Notably, close to the critical point, the diffusion coefficient decomposes into a critical and a background contribution [105],

$$D = D_{\mathrm{c}} + D_{\mathrm{bg}}, \tag{2.28}$$

similar to the viscosity that likewise separates into a critical and background part,

$$\eta = \eta_{\mathrm{bg}} + \eta_{\mathrm{c}}. \tag{2.29}$$

Bhattacharjee et. al. [106] have worked out a crossover function $H$ that relates $\eta$ to $\eta_{\mathrm{bg}}$,

$$\frac{\eta}{\eta_{\mathrm{bg}}} = \exp(z\, H(Q_0\, \xi, q_D/q_c)), \tag{2.30}$$

where $z = 0.065$ is a critical exponent (prediction from mode-coupling theory in good agreement with experiments), $Q_0$ a system-dependent wave number and $q_D/q_c$ is the ratio of two wave numbers; $q_D/q_c \to \infty$ corresponds to the case of a dominant background contribution whereas $q_D/q_c \to 0$ to the case of vanishing background. The dependence of the crossover function $H$ in Eq. (2.30) is obtained using the relation

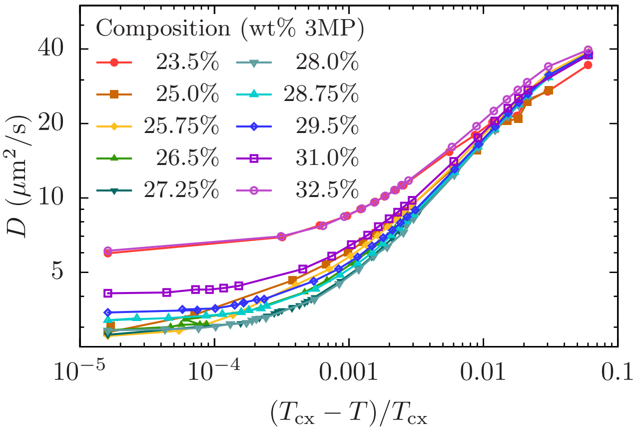

Figure 2.1: Effective self-diffusion coefficients for a binary mixture of 3-methylpyridine (3MP) and heavy water ($D_2O$) at different compositions, as a function of the normalized temperature distance from the phase-coexistence temperature $T_{cx}$. Original data of Ref. [76] acquired through dynamic light scattering of solvent fluctuations. The normalized second-order autocorrelation functions of the measured intensity exhibit a decay time $\tau$, which is related to the self-diffusion coefficient via $D = q^2\tau$, with $q$ being the diffraction vector given in Ref. [76].

$Q_0^{-1} = (1/2)\, e^{4/3} \left(q_c^{-1} + q_D^{-1}\right)$ [106–108], from which the substitutions

$$q_D\,\xi \mapsto \frac{1}{2}\, e^{4/3}\, Q_0\, \xi \left(1 + \frac{q_D}{q_C}\right), \tag{2.31}$$

$$q_C\,\xi \mapsto \frac{1}{2}\, e^{4/3}\, Q_0\, \xi \left(1 + \left(\frac{q_D}{q_C}\right)^{-1}\right) \tag{2.32}$$

in terms of $Q_0\,\xi$ and $q_D/q_C$ follow. We assume that around the critical point the crossover function $H$ depends on the thermodynamic state only via $\xi$ in the first variable, i.e. the ratio $q_D/q_c =$ const. is independent of $\phi$ and $T$. For $q_D/q_c \ll 1$, which holds for the present experimental system, the crossover function $H$ depends only weakly on $q_D/q_c$.

Using Eqs. (2.29) and (2.30) one can derive the expressions for the diffusion coefficient. The critical part is given by [105, 108, 109]

$$D_{\rm c} = \frac{\mathcal{R}\, k_B T}{6\pi\, \eta\, \xi}\, K(q\,\xi)\, \left(1 + b^2 (q\,\xi)^2\right)^{z/2}, \tag{2.33}$$

where $\eta$ is the full viscosity, and $\mathcal{R} \approx 1.05$ is a universal dynamic amplitude ratio [107, 108], $K(x) = 3/(4x^2)[1 + x^2 + (x^3 - x^{-1}) \arctan x]$ is the Kawasaki function [110], and Ref. [108] suggests the value $b = 0.55$ for the correction to scaling. The background contribution to the diffusion coefficient is given by [105, 108, 109]

$$D_{\rm bg} = \frac{k_B T}{16\, \eta_{\rm bg}\, \xi}\, \frac{1 + (q\,\xi)^2}{q_c\, \xi}. \tag{2.34}$$

From this it is possible to rewrite the complete expression for the diffusion coefficient

$$
\begin{aligned}
D(\xi, \phi, T; Q_0, q_D/q_C) = \frac{k_B T}{6\pi\, \eta_{\mathrm{bg}}(\phi, T)\, \xi} \Big[ \mathcal{R}\, & \frac{K(q\,\xi)\,(1 + b^2(q\,\xi)^2)^{z/2}}{\exp(z\, H(Q_0\, \xi, q_D/q_c))} \\
& + \frac{1 + (q\,\xi)^2}{\frac{8}{6\pi}\, e^{4/3}\, Q_0\, \xi\, (1 + (q_D/q_C)^{-1})} \Big], \qquad (2.35)
\end{aligned}
$$

as a function of $\xi$, $\phi$ and $T$, depending also on the known, universal constants $\mathcal{R}$ and $z$ and the a priori not known non-universal quantities $\eta_{\mathrm{bg}}$, $Q_0$ and the ratio $q_D/q_c$. $\eta_{\mathrm{bg}}$ can be determined as function of $T$ and $\phi$ by extrapolating off-critical measurements to the critical region, as in Ref. [111].

We are thus left with a relation with three unknowns: $\xi$, $Q_0$ and $q_D/q_c$, which we solve via numerical root finding, by determining iteratively the correlation length $\xi$ that yields the same diffusion coefficient as experimentally determined; see Fig. 2.1 for data taken from Ref. [76] and used in chapter 6. For the details of the specific implementation, see Appendix 6.A.

### 2.2.2 From strong to weak adsorption preferences

The scaling form of the critical Casimir potential in Eq. (2.24) is valid for strongly adsorbing particles in the limit $h_s = \pm\infty$, whereas for weakly adsorbing particles, the scaling function of the potential depends also on the surface field $h_s$. (Specifically, Eq. (2.10) is extended such that the surface free energy $f_s(t, h; h_s) = t^{2-\alpha}\, g_s\left(h|t|^{-\Delta}, h_s|t|^{-\Delta_s}\right)$ depends on a scaling variable $h_s|t|^{-\Delta_s}$ where $\Delta_s$ is a surface counterpart to the gap critical exponent $\Delta$ [87]. Typically, the value of the surface field cannot be quantified in the experiment; for simplicity, we will make no distinction between $h_s$ and the scaling variable.)

Theoretical and MC simulation results for the film geometry indicate [73, 112–114] that though the amplitude of the critical Casimir force decreases, the shape of the scaling function $k_\parallel$ does not vary significantly with $h_s$. Hence, within mean field theory and in $d = 4$ the dependence on $h_s$ at the critical concentration ($\Sigma = 0$) can be reduced to a re-mapping [73]

$$
k_\parallel^{(d=4)}(\Theta, \Sigma; h_s) = s^d\, k_\parallel^{(d=4)}(s^{-1}\Theta, \Sigma) \qquad (2.36)
$$

with a rescaling parameter $s = s(h_s)$.[1] To the best of our knowledge, it has not been studied yet whether such a rescaling holds in $d = 3$ and for off-critical concentrations, though we expect a similar result but with a parameter $s(h_s, h)$ that depends also on the bulk ordering field $h$.

---

[1] Note that Ref. [73] uses the notation $r$ for the rescaling variable (instead of $s$), with $r_{sd}$ for the short distance approximation, and $y = \left(\frac{D}{\xi_t}\right)^{1/\nu}$ for the argument of the scaling function, which is mapped via $y \to r^{-1/\nu} y$. In our notation $\Theta = \frac{D}{\xi_t}$, the mapping reads $\Theta \to s^{-1}\Theta$

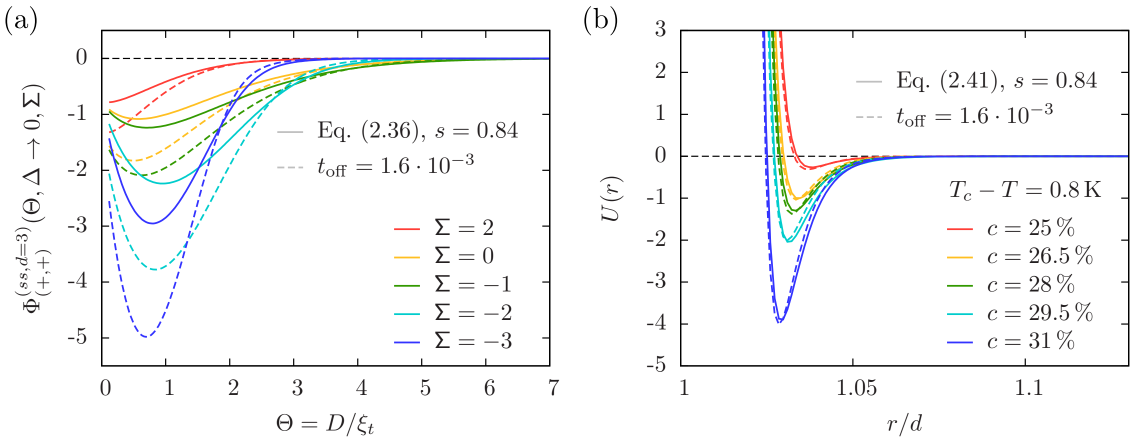

Figure 2.2: (a) Scaling function $\Phi^{(ss,d=3)}_{(+,+)}$ of the critical Casimir potential as obtained by rescaling according to Eq. (2.36) with $s = 0.84$ (solid lines) for several values of $\Sigma$. Rescaling mimics the case of particles with weak surface fields (note that it is exact only for $\Sigma = 0$ in $d = 4$). The same effect can be achieved by using the temperature offset $t_{\mathrm{off}} = 0.14$ (dashed lines) – at least for the exponentially decaying tails of the scaling function. (b) The two rescaling methods with the same values, but shown for the pair potential Eq. (2.41). The scaling variable $\Sigma$ has been replaced by the composition $c$ (see section 2.2.3).

We show the scaling function $\Phi^{(ss,d=3)}_{(+,+)}$ for the scaling parameter $s = 0.84$ and $(+,+)$ BCs in Fig. 2.2(a) (solid lines). The experimentally accessible range of the scaling function is usually limited to its exponential tail [28, 84, 115]. In this range, we found that one may mimic the rescaling using an effective temperature offset $t_{\mathrm{off}}$ that shifts the relative temperature according to

$$t' = \frac{T_{\mathrm{c}} - T_{\mathrm{exp}} + \Delta T_{\mathrm{off}}}{T_{\mathrm{c}}} = t + t_{\mathrm{off}}, \tag{2.37}$$

combining effects of a weak surface field and any small remaining temperature uncertainties: While the rescaling (solid lines) and the temperature offset (dashed lines) have different functional form close the critical point $\Theta = 0$, they give the same exponential decay for $\Theta \gg 1$. We show the resulting pair potentials in Fig. 2.2(b), where we have added the electrostatic repulsion present in the charge-stabilized colloidal system, see next section. Within the range of $\Theta$ explored in the experiment, the two approaches are indiscernible. We will employ $t_{\mathrm{off}}$ as a fitting parameter; any finite value of $t_{\mathrm{off}}$ should be understood as indicating the presence of weak surface fields that corresponds to a rescaling of the scaling function of the CCP. This rescaling is expected to depend on the bulk field $h$, and therefore on the composition of the solvent.

### 2.2.3 Effective pair potentials

Besides the critical Casimir forces, there are other interactions between the colloidal particles, including van der Waals attraction and hard-core as well as screened electrostatic repulsion of the charge-stabilized particles. Because of the large length-scale ratio between the colloidal particles and the solvent molecules, one can ignore the discrete nature of the solvent and use a simplified pair potential model as a background interaction potential. This background potential represents the regular part of the free energy, which depends on the system and microscopic details. For the comparison with experiments in chapter 6, the repulsive contribution is modeled based on the widely used Yukawa potential of particles charge-stabilized against flocculation [9, 116, 117]:

$$\frac{V_{\mathrm{rep}}^{(\mathrm{el})}(D)}{k_B T} = U_{\mathrm{rep}}^{(\mathrm{el})}(D) = U_0 \frac{\exp(-\kappa D)}{\kappa(D+2R)}, \qquad D = r - 2R > 0. \tag{2.38}$$

where the Debye screening length $\kappa^{-1} = \sqrt{\epsilon k_B T/(e^2 \sum_i \rho_i)}$ (see, e.g. Ref. [118]), with $e$ the elementary charge, $\epsilon$ the permittivity of the solvent relative to vacuum, and $\rho_i$ the number density of ions, sets the range of the repulsion. A simplified, purely exponential form of the repulsive pair potential,

$$V_{\mathrm{rep}}^{(\mathrm{el})}(D)/(k_B T) = U_{\mathrm{rep}}^{(\mathrm{el})}(D) = A \exp(-\kappa D), \tag{2.39}$$

is often used for suspensions in which $\kappa^{-1} \ll R$ for distances $2R > D > R + \kappa^{-1}$, for which all curvature effects associated with the spherical geometry of the colloidal particles effectively drop out [11, 119]. The corresponding condition $\kappa^{-1} \ll R$ is practically satisfied for the experimentally relevant systems for which the Debye length is of the order of 10 nm and the colloidal size of the order of 1 $\mu$m. The amplitude $A$ is given by [9]

$$A = U_0/(2\kappa R) = 2\pi(\epsilon\epsilon_0)^{-1}\Upsilon^2\kappa^{-2}R/(k_B T), \tag{2.40}$$

where $\epsilon_0$ is the permittivity of the vacuum, and $\Upsilon$ is the surface charge density of the colloidal particles.

The amplitude of the van der Waals dispersion forces is given by the Hamaker constant, which depends on the dielectric properties of the materials involved in the experiment under consideration [118]. In index-matched colloidal suspensions, this amplitude is strongly reduced and the contribution will not be considered in chapter 6.

Our pair potential model for colloidal particles interacting in near-critical solvents due to screened electrostatic and critical Casimir forces hence corresponds to the sum of

Eqs. (2.38) and (2.24):

$$U(r) = \begin{cases} \infty, & D < 0 \\ U_{\text{rep}}^{(\text{el})}(D) + \dfrac{R}{D}\,\Phi_{(+,+)}^{(ss,d=3)}(\Theta, \Delta \to 0, \Sigma), & D > 0. \end{cases} \tag{2.41}$$

Using this effective pair potential, we can calculate the second virial coefficient $B_2$, which for dilute suspensions is a useful measure of the strength of the attraction and may be a useful measure for predicting of the onset of colloid aggregation. For radially symmetric spherical particles [78], $B_2$ is calculated from the pair potential using

$$B_2 = 2\pi \int_0^\infty \mathrm{d}r\, r^2 \left[1 - \exp(-U(r))\right]. \tag{2.42}$$

$B_2$ occurs in the expansion of pressure $p$ in terms of the number density $\rho$ of the colloid $p(\rho)/(k_B T \rho) = 1 + B_2\rho + \ldots$ as a leading correction to the ideal gas pressure. It has been shown that an extended law of corresponding states can be applied to colloidal suspensions with short-ranged interactions [120, 121], meaning that different systems exhibit approximately the same thermodynamic behavior if they have the same value for the reduced second virial coefficient $B_2^* = B_2/B_2^{(hs)}$, independent from details of the pair interaction. Here, $B_2^{(hs)} = 2\pi d^3/3$ is the second virial coefficient of a *h*ard-*s*phere reference system with diameter $d$. For systems with a soft-core repulsion and an attractive contribution, as is the case here, the reference system is commonly chosen to be a hard-core interaction with an effective diameter $d_{\text{eff}} > 2R$ in order to incorporate effectively the soft-core repulsion. The separation of the pair potential into a repulsive and attractive part is not unique. We follow the Weeks, Chandler, and Andersen [122] (WCA) separation into an attraction

$$U_a(r) = \begin{cases} U_{min}, & r \le r_{min} \\ U(r), & r > r_{min}, \end{cases} \tag{2.43}$$

where $U_{min} = U(r_{min})$ is the minimum of the pair potential, and a repulsion

$$U_r(r) = \begin{cases} U(r) - U_{min}, & r \le r_{min} \\ 0, & r > r_{min}. \end{cases} \tag{2.44}$$

The effective diameter is given by the repulsive contribution via [78]

$$d_{\text{eff}} = \int_0^\infty \mathrm{d}r\, \left[1 - \exp(-U_r(r))\right]. \tag{2.45}$$

Only a few attractive model interactions allow to calculate $B_2$ analytically. For the sticky hard-sphere model [123] of vanishing interaction range and strength given by the inverse stickiness parameter $\tau$, one finds $B_2^* = 1 - 1/(4\tau)$. A gas-liquid phase transition is found for values of $\tau$ smaller than a critical value, leading to $B_2^* < B_{2,c}^* = -1.212$ [124]. Though critical Casimir interactions are long-ranged (algebraically decaying with distance) right at the critical point, in the experimentally studied regime near the critical point, the interaction is short-ranged (exponentially decaying with distance). We can thus evaluate the "stickiness" of the particles by comparison of the experimental results for $B_2^*$ with the sticky hard-sphere model in the form of $B_{2,c}^*$.

# Chapter 3

# Critical Casimir interaction between a cylindrical colloid and a substrate

The analysis in this chapter follows Fig. 3.1 by first stating from literate the case of a homogeneous cylindrical particle above a substrate with a chemical step, then by introducing a Janus particle of type A (formally defined below) above a homogeneous substrate before considering a type A Janus particle above a substrate step, which will later connect to the case of two Janus particles. For type B, we first revisit the case of a homogeneous cylinder above a substrate with a chemical step and calculate the torque acting on the particle. This configuration can then be used as a building block to construct the situation of a type B Janus particle above a striped substrate.

We briefly clarify the ambiguous definition of a (hyper-)cylinder in higher dimensions ($d \geq 4$). In the present context, a cylinder in $d = 4$ is a geometrical object with radius R and two lengths $L$ and $L_4$, defined by the volume $x^2 + y^2 \leq R^2$, $0 \leq z \leq L$ and $0 \leq w \leq L_4$, where $w$ is the coordinate in the extra dimension and $L_4$ is the length in that direction[1]. We will use the $(d-2)$ dimensional length $\mathcal{L}$ in order to denote $\mathcal{L} = L$ in $d = 3$ and $\mathcal{L} = L \times L_4$ in $d = 4$.

The Janus character due to the BCs at the surface of a cylinder can be realized in two distinct ways in $d = 3$ [see Fig. 3.1] and in three ways in $d = 4$. The two possibilities in $d = 3$ are evident with the chemical step, separating two domains of BCs, either running along the length of the cylinder, cutting it into two half-cylinders [type A, see Fig. 3.1(b)], or perpendicular to the length of the cylinder, cutting it in two cylinders of half the length [type B, see Fig. 3.1(d)]. We will demonstrate that the latter case can be constructed within DA by a straightforward combination of two cylinders (see also Ref. [74]). The third case, occurring for a cylinder in $d = 4$, has the step in the BCs in

---

[1] Another definition of the volume of a hypercylinder would be $x^2 + y^2 + z^2 \leq R^2$, $0 \leq w \leq L_4$, which we dismiss for formal reasons: The projection of this object onto three dimensions renders a sphere instead of a cylinder. Thus this object does not fulfill the expectation for a basic extension of a cylinder from three to four dimensions.

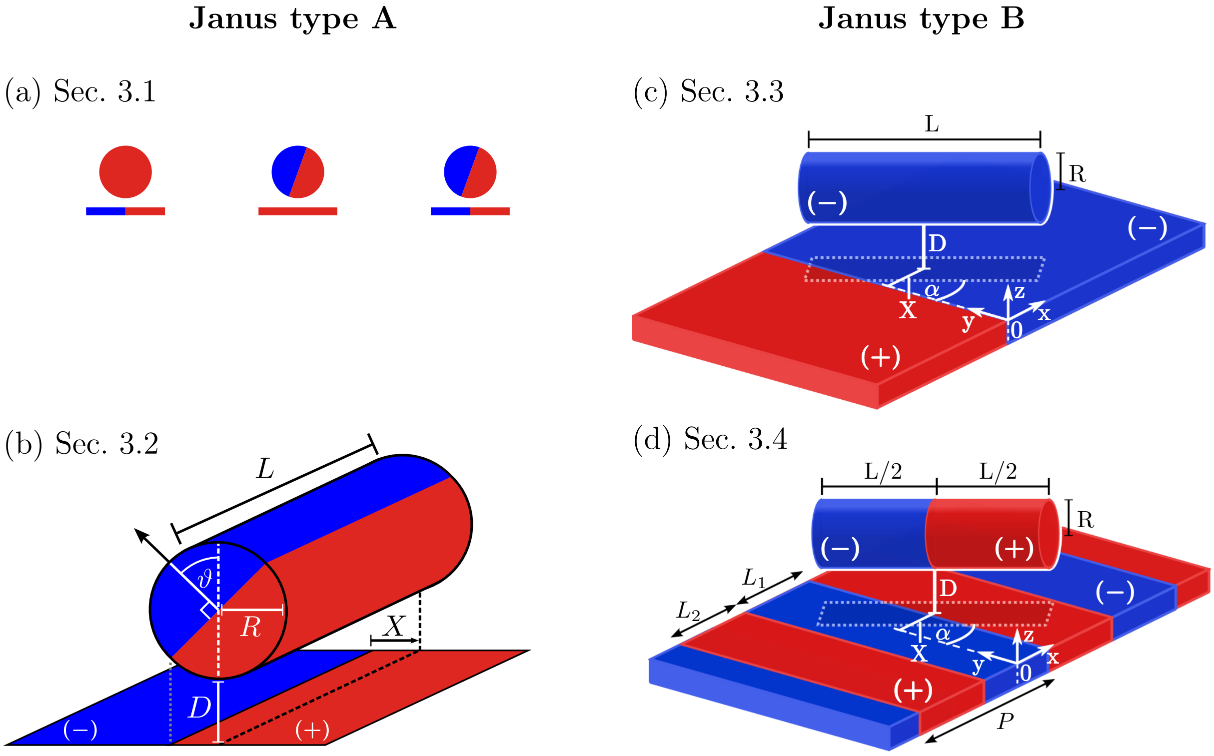

**Janus type A** **Janus type B**

(a) Sec. 3.1

(b) Sec. 3.2

(c) Sec. 3.3

(d) Sec. 3.4

Figure 3.1: Illustration of the geometries and the boundary conditions (BCs) considered in this chapter, divided by the two different realizations (denoted as type A and B) of a cylindrical Janus particle in $d = 3$: (a) Sideview sketches of all types of configurations considered working towards Janus type A in Sec. 3.1: chemically homogeneous cylinder vs. substrate with a chemical step — Type A Janus cylinder vs. homogeneous substrate — Type A Janus cylinder vs. substrate with a chemical step (same as in (b)). (b) Sec. 3.2: Janus cylinder of type A with the chemical step along the cylinder axis, shown in proximity and parallel to a planar substrate. The orientation of the Janus cylinder is given by the angle $\vartheta$ between the normal of the equatorial plane of the Janus cylinder and the substrate normal. The substrate features a chemical step parallel to the cylinder at which the adsorption preference of the substrate changes discontinuously along the lateral direction $x$ from $(-)$ BC at $x < 0$ to $(+)$ BC at $x \geq 0$. (c) Towards the second variant in Sec. 3.3: cylinder of radius $R$ and length $L$ at a surface-to-surface distance $D$ to a chemical step with the cylinder axis being rotated by an angle $\alpha \in [0, \pi/2]$ with respect to the chemical step at $x = 0$. (d) Sec. 3.4: Janus cylinder of type B with the chemical step perpendicular to the axis of the cylinder, close to a periodically striped substrate. The Janus cylinder exhibits opposing $(+)$ and $(-)$ BCs at its two halves, and the substrate consists of stripes of width $L_1$ with $(-)$ BC neighboring stripes of width $L_2$ with $(+)$ BC such that the periodicity is $P = L_1 + L_2$. Moreover, the cylinder is rotated by an angle $\alpha$ with respect to the chemical steps of the stripes. The vertical projection of the cylinder onto the substrate surface forms a $2R \times L$ rectangle (dashed lines). In all cases with at least one chemical step on the substrate, the center of the colloid is located at $x = X$ with respect to the step and $z = D + R$, while the y coordinate is irrelevant.

the extra dimension, rendering two equal sized hypercylinders with different BCs. This is of limited practical use regarding the comparison with results in $d = 3$. We therefore restrict our description to the "natural" choices in $d = 3$, denoted as types A and B.

## 3.1 Janus cylinder (type A) above a homogeneous substrate

### 3.1.1 Implications of the DA

In order to set the stage, we recall from previous works the case of a chemically homogeneous cylinder close to a substrate with a chemical step (see Fig. 3.1(a)). The lateral position of the cylinder axis relative to a chemical step in parallel on the substrate is denoted by $X$ (compare Fig. 3.1(b)). Moreover, we always consider the cylinder to be parallel to the substrate (and to the step). The critical Casimir force $F_{\bullet|}^{(cs)}(X, D, R, T)$ between a *homogeneous* *c*ylindrical particle of length $L$ and radius $R$, and a *s*ubstrate with a step, at a lateral position $X$, has the scaling form (see Eq. (D1) in Appendix D of Ref. [103])

$$F_{\bullet|}^{(cs)}(X, D, R, T) = k_B T \, \frac{\mathcal{L}}{R^{d-1}} \, \frac{K_{\bullet|}^{(cs)}(\Xi, \Delta, \Theta)}{\Delta^{d-1/2}}, \tag{3.1}$$

with the dimensionless scaling variables $\Xi = X/\sqrt{RD}$, $\Delta = D/R$, and $\Theta = \pm D/\xi_{\pm}(T)$ (with $\operatorname{sign}(\Theta) = \operatorname{sign}(t)$) in $d$ dimensions. The scaling function $K_{\bullet|}^{(cs)}(\Xi, \Delta, \Theta)$ of the force $F_{\bullet|}^{(cs)}$ can be decomposed as [103]

$$K_{\bullet|}^{(cs)}(\Xi, \Delta, \Theta) = \begin{cases} K_{(+,+)}^{(cs)}(\Delta, \Theta) - \Delta K_{\bullet|}^{(cs)}(|\Xi|, \Delta, \Theta) & \text{for } \Xi > 0, \\ K_{(+,-)}^{(cs)}(\Delta, \Theta) + \Delta K_{\bullet|}^{(cs)}(|\Xi|, \Delta, \Theta) & \text{for } \Xi \leq 0, \end{cases} \tag{3.2}$$

where (see Eq. (D3) in Ref. [103])

$$K_{(+,\pm)}^{(cs)}(\Delta \to 0, \Theta) = \sqrt{2} \int_1^{\infty} \mathrm{d}\alpha \, \frac{k_{(+,\pm)}(\alpha\Theta)}{\alpha^d \sqrt{\alpha - 1}} \tag{3.3}$$

is the scaling function of the force within DA for a homogeneous *c*ylindrical particle (+ or −) close to a homogeneous *s*ubstrate (+ or −), and thus does not depend on $\Xi$. (Note that $K_{(+,\pm)}^{(cs)}$ is $\sqrt{2}$ larger than the scaling function of the force between two homogeneous cylinders derived within DA in Appendix A, see Eq. (A.2).) The scaling function $k_{(+,\pm)}$ for the slab geometry serves as an input, which is obtained either from MFT calculations for the film geometry in $d = 4$ or from an interpolation of MC data provided in Ref. [24] for $d = 3$. The choice of signs in Eq. (3.2) reflects $\Xi \gtrless 0$, chosen such that the direction of positive $X$ points to the side of the step with the same BC as the colloid (see Fig. 3.1) which is (+) in the present notation.

The excess scaling function $\Delta K_{\bullet|}^{(cs)}$ involving the step position $X$ is given within DA by (see Eq. (D6) in Ref. [103])

$$\Delta K^{(cs)}_{\bullet|}(|\Xi|, \Delta \to 0, \Theta) = \frac{1}{\sqrt{2}} \int_{1+\Xi^2/2}^{\infty} \mathrm{d}\alpha \, \frac{\Delta k(\alpha\Theta)}{\alpha^d \sqrt{\alpha - 1}}, \tag{3.4}$$

where $\Delta k = k_{(+,+)} - k_{(+,-)} < 0$ is the difference between the slab scaling functions for distinct BCs, which is negative for all temperatures $\Theta$. Note that $\Delta K^{(cs)}_{\bullet|}$ depends only on the absolute value of the scaled distance $\Xi$, because the inverted position is equivalent to a switch of the BCs of the step, which is covered by Eq. (3.2).

As a function of the scaled temperature $\Theta$, in Fig. 3.2(a) we compare the scaling function of the force $K^{(cs)}_{\bullet|}$ obtained within DA for $d = 4$ via Eqs. (3.2)–(3.4) (dashed curves) with the corresponding full MFT results (solid lines) determined by numerical minimization of the Ginzburg-Landau-Wilson Hamiltonian given in Eq. (2.27) for this particular geometry and BCs. As expected from Ref. [103], in Fig. 3.2(a) the DA scaling function approximates the full MFT results well for the geometry of a *homogeneous* cylinder above a *s*ubstrate step, shown for various scaled step positions $\Xi$ on both sides of the step.

In accordance with the second sketch in Fig. 3.1(a), we now go beyond the previous works and consider a Janus *c*ylinder, but placed above a homogeneous *s*ubstrate. The corresponding critical Casimir force $F^{(cs)}_{\text{◒}|}(\vartheta, \Delta, \Theta)$ depends on the orientation angle $\vartheta$ (Fig. 3.1(b)) of the Janus cylinder. The scaling form remains the same as in the previous case, i.e.,

$$F^{(cs)}_{\text{◒}|}(\vartheta, D, R, T) = k_B T \, \frac{\mathcal{L}}{R^{d-1}} \, \frac{K^{(cs)}_{\text{◒}|}(\vartheta, \Delta, \Theta)}{\Delta^{d-1/2}}. \tag{3.5}$$

Comparing in Fig. 3.1(a) the sketch for the case of a homogeneous cylinder near a stepped substrate with the case of a Janus cylinder above a homogeneous substrate, one realizes that for a suitable orientation $\vartheta$ of the Janus cylinder the same pairings of BC between the substrate and the particle enter the DA. Projecting the equatorial plane of a Janus cylinder onto a homogeneous substrate yields a distance $X = X_J = R\cos\vartheta$ between the (left) edge of the projection and the projection of the cylinder axis (Fig. 3.1(b)). Conversely, the projection of the axis of a homogeneous cylinder onto a substrate with a chemical step renders a distance $X$ between them (Fig. 3.1(b)). Choosing $X = X_J = R\cos\vartheta$, within DA the sums of the surface elements vis-à-vis for these two configurations are the same and thus yield the same force. In terms of the present scaling function the relation $X = X_J$ translates into $\cos\vartheta = \Xi\sqrt{\Delta}$. This implies that within DA the scaling function $K^{(cs)}_{\text{◒}|}$ of the force between a Janus cylinder and a homogeneous substrate follows from Eqs. (3.2–3.4) upon substituting $X = R\cos\vartheta$ therein. Figure 3.2(b) shows for a Janus cylinder next to a homogeneous wall as function of the scaled temperature $\Theta$ the full MFT results (solid lines) for various orientations $\vartheta$ (chosen independently from Fig. 3.2(a)). The corresponding DA scaling functions are shown as dashed lines. In Fig. 3.2(b), for the same distance $\Delta = 1/5$, the DA scaling functions appear to deviate

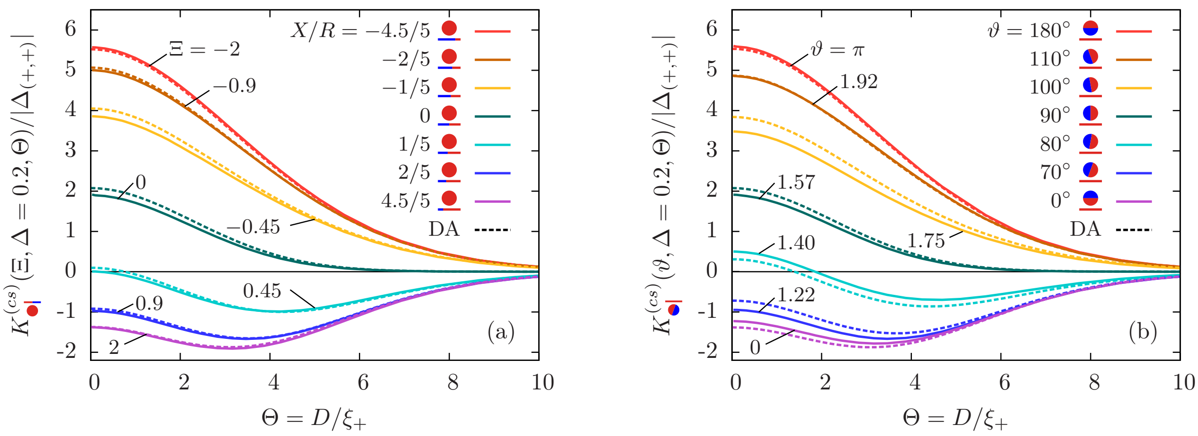

Figure 3.2: (a) Scaling function $K^{(cs)}_{\bullet|}$ of the force between a homogeneous cylindrical particle above a substrate with a chemical step at various scaled lateral positions $\Xi$. (b) Scaling function of the force $K^{(cs)}_{\bullet|}$ between a Janus cylinder and a homogeneous substrate for various orientations $\vartheta$. The full MFT results are shown as solid lines, whereas the corresponding DA scaling functions are shown as dashed lines. The DA yields a qualitatively adequate approximation for the MFT scaling functions, with varying quantitative deviations in (a) and (b).

slightly more from the corresponding full MFT results than those in Fig. 3.2(a).

In order to asses quantitatively the difference between DA and full MFT, it is more suitable to compare the corresponding scaling functions $K^{(cs)}_{\bullet|}$ and $K^{(cs)}_{\bullet|}$ of the force for fixed scaled temperature $\Theta$ as function of the scaling variable $\Xi = X/\sqrt{RD}$, which either corresponds to the lateral position $X$ of the axis of a homogeneous cylinder relative to a chemical step on the substrate, or to the orientation $\cos\vartheta = \Xi\sqrt{\Delta}$ of a Janus cylinder above a homogeneous substrate. Accordingly, for the two scaled temperatures $\Theta = 1$ and $\Theta = 5.65$ in Fig. 3.3 we show the full MFT scaling function $K^{(cs)}_{\bullet|}(\Xi, \Delta, \Theta)$ of the force for the homogeneous cylinder-step geometry [Eq. (3.1)] as solid lines and the full MFT scaling function $K^{(cs)}_{\bullet|}(\vartheta, \Delta, \Theta)$ of a Janus cylinder next to a homogeneous substrate [Eq. (3.5)] as dashed lines. In the spirit of the aforementioned equivalence within DA, the orientation angle $\vartheta$ of the Janus cylinder is related to the distance $X$ between the projected axis of a homogeneous cylinder and the chemical step at the wall via the DA relation $\Xi = \Delta^{-1/2}\cos\vartheta$. For $\Delta = 1$ in Fig. 3.3(a), there is a visible difference between the two scaling functions. However, for $\Delta = 1/5$ in Fig. 3.3(b), which is closer to the DA limit $\Delta \ll 1$, the difference is considerably smaller. For comparison, in gray the scaling function of the force within DA is shown, which approximates both MFT scaling functions for $\Delta \ll 1$.

Thus it appears that the MFT results of both geometries approach each other in the limit of $\Delta \to 0$. This raises the question whether the relation between the two configurations, as implied by DA, reflects a more general foundation beyond DA.

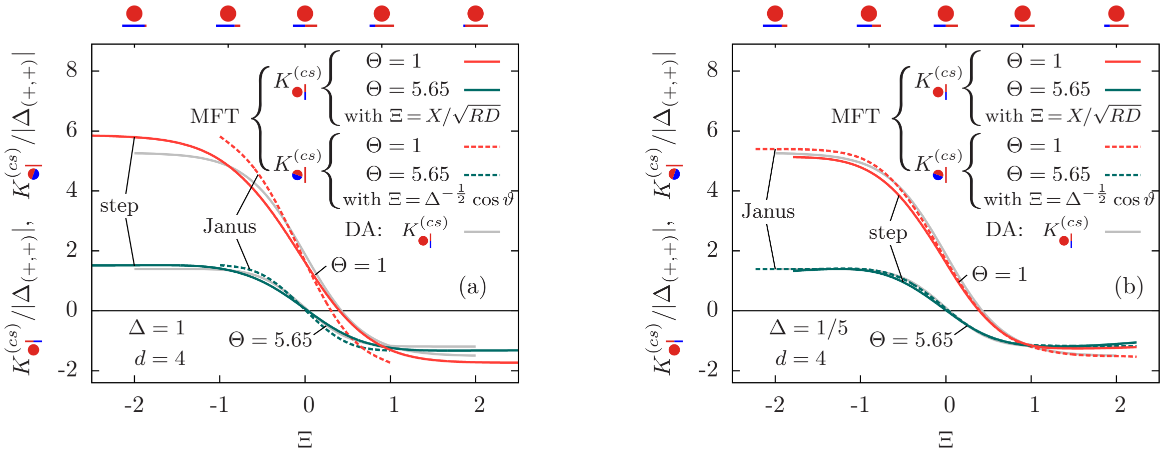

Figure 3.3: Comparison of the scaling functions of the force $K^{(cs)}_{\bullet|}$ between a homogeneous cylinder above a chemical step on the substrate (solid lines) and $K^{(cs)}_{◐|}$ for a Janus cylinder above a homogeneous substrate (dashed lines). The DA (valid for $\Delta \ll 1$) implies the same scaling function in both cases (gray lines), provided the tilt angle $\vartheta$ of the Janus cylinder (see Fig. 3.1(b)) is related to the scaled step position on the substrate as $\Xi = \Delta^{-1/2}\cos\vartheta$. The full mean field results for $K^{(cs)}_{\bullet|}$ (step) and $K^{(cs)}_{◐|}$ (Janus) are shown for $\Delta = 1$ in (a) and $\Delta = 1/5$ in (b), each for the two scaled temperatures $\Theta = 1$ (red) and $\Theta = 5.65$ (green). From (a) it can be seen that within full MFT the correspondence between the case of a homogeneous cylinder above a chemical step on the substrate and a Janus particle above a homogeneous substrate does not hold in general. It holds roughly for $\Theta = 5.65$ and further away from $T_c$, but not close to $T_c$ (such as for $\Theta = 1$). However, for $\Delta = 1/5$ in (b), i.e., close to the DA limit of $\Delta \ll 1$, the correspondence of the two scaling functions within DA carries over to the MFT results. As a guide to the eye, visualizations of the geometry corresponding to certain values of $\Xi$ are provided at the top of the panels.

### 3.1.2 Comparison of forces in terms of order parameter profiles

Contrary to the DA, the MFT minimization technique renders equilibrium order parameter profiles for each scaled temperature $\Theta$. Nonetheless, the DA implies a certain structure of the order parameter profile, even though in general it is ignorant concerning the profile.

The reduced MFT order parameter profiles $m(\mathbf{r})$ for a homogeneous cylinder above a chemical step are depicted in Fig. 3.4(a) for $\Theta = 1$ and in Fig. 3.4(b) for $\Theta = 5.65$. In this example, the geometric parameters have been chosen such that $D = R$, i.e., $\Delta = 1$; the colloid with $(+)$ BC is positioned at $X = -0.9\,R$ on the left side of the step with opposite $(-)$ BC there, and the cylinder axis is normal to the cut plane of the order parameter profiles, which are invariant along the cylinder axis. The profiles are taken for $\Theta > 0$ at the critical concentration, i.e., in the mixed phase, in which the order parameter differs from zero primarily only near the surfaces. Due to the opposing BCs on the colloid and on the left half of the substrate surface, the profile must cross zero (green line), although this does not indicate the formation of an actual interface. The gray line represents the zero crossing (at the same temperature) of the profile between a homogeneous particle and a

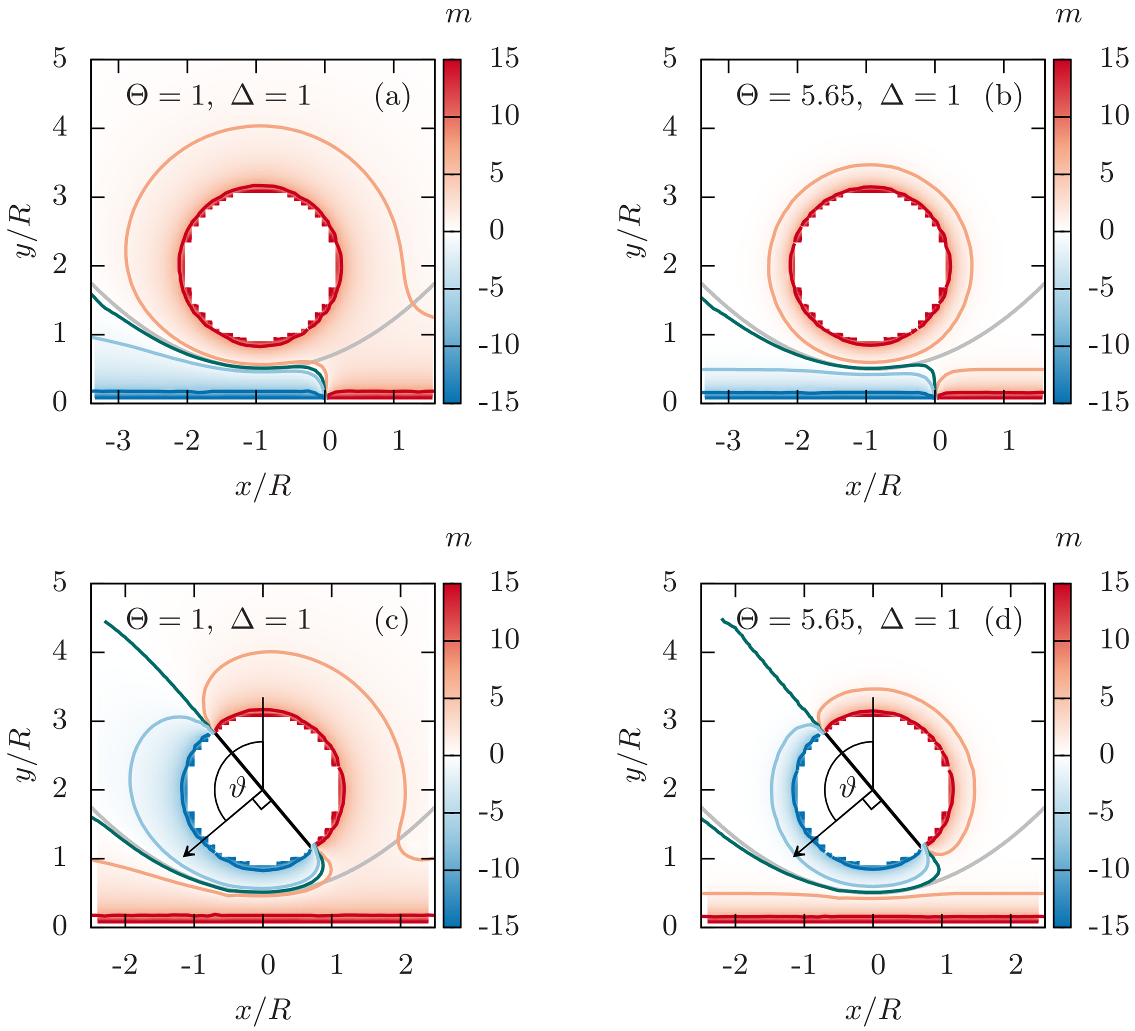

Figure 3.4: Reduced order parameter profiles $m$ as obtained from MFT in $d = 4$ and in units of the amplitude $\mathcal{B}$ of the bulk order parameter $\phi_b = \mathcal{B}\,|t|^{1/2}$. The values of the order parameter are color coded, with red for positive values and blue for negative values, following the convention for the BCs in Fig. 3.1. For $\Theta = 1$ (a) depicts a homogeneous cylinder with (+) BC at $X = -0.9\,R$ above a substrate with a chemical step between (+) BC for $x > 0$ and ($-$) BC for $x < 0$. Panel (b) features the same geometry at $\Theta = 5.65$, i.e., further away from $T_c$. For comparison, in (c) a Janus cylinder above a homogeneous substrate with (+) BC is shown for $\Theta = 1$ and in (d) for $\Theta = 5.65$. The orientation of the Janus cylinder is taken as $\vartheta = 130°$, so that $\cos\vartheta = -0.64$. We have included certain isolines of the profile as a guide to the eye. The green line represents the zero crossing of the profiles, which has a special significance discussed in the main text. The gray curve indicates the zero crossing expected (at the same temperate) for the profile in the case that both the particle and the substrate are homogeneous, but with opposite BC.

homogeneous substrate, but with opposing BCs. In the case of a chemical step on the substrate, the DA implicitly assumes that the order parameter profile follows that for a homogeneous substrate up to the lateral position $x = 0$ of the step (Figs. 3.4(a) and (b)). Generally, Figs. 3.4(a) and (b) show that the actual zero crossing (green) follows closely the homogeneous case (gray), as assumed by the DA, up to a certain lateral position.

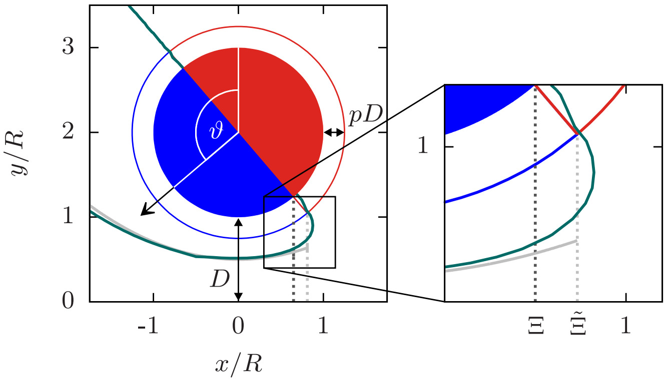

Figure 3.5: A generic sketch depicting the essential features of a Janus cylinder at distance $D$ above a homogeneous substrate, tilted by an angle $\vartheta$, akin to Figs. 3.4(c) and (d). An example for the actual zero crossing line of the order parameter profile, as found within full MFT, is shown in green. The zero crossing implied by the DA is shown in gray (solid light gray line, light and dark gray vertical dotted lines). In DA, the zero crossing is taken into account up to the scaled position $\Xi = \Delta^{-1/2}\cos\vartheta$ of the step in BC of the Janus particle, projected onto the substrate along the normal of the substrate (dark gray dotted line). The improved DA relation $\tilde{\Xi}(\vartheta)$ in Eq. (3.6) follows the same principle, but applied to a fictitious particle of increased radius $R+pD$, with the rescaling parameter $p$, resulting in the solid light gray zero crossing line and the light gray vertical dotted line. The inset provides a magnified view of the relevant features.

However, the point of deviation between the green and the gray lines occurs at a lateral position which is to the left of the step position, because the actual zero crossing line (green) smoothly bends towards the step. The curvature of this bending depends on the temperature and broadens upon increasing the correlation length (i.e., decreasing $\Theta$).

In Fig. 3.4(c) [(d)], the configuration of a Janus cylinder above a homogeneous substrate is shown in comparison to (a) [(b)], for the scaled temperature $\Theta = 1$ [$\Theta = 5.65$]. The orientation $\vartheta$ of the Janus cylinder has been chosen such that the configuration (a) [(b)] and the configuration (c) [(d)] yield forces within MFT which are approximately equal to each other. For both scaled temperatures, this was found to be the case for $\vartheta \approx 130°$, which deviates significantly from the DA relation $\vartheta = \cos^{-1}(X/R) = 154°$ for $X/R = -0.9$. Such a deviation is expected to occur away from the DA limit of $\Delta \ll 1$ [compare Figs. 3.3(a) and (b)]. For the Janus particles, we find that the zero crossing of the profiles (green line) again follows the one for a homogeneous colloid (gray line), but now bending towards the Janus equator on the particle. A systematic analysis reveals that one always finds equal values of the force in MFT for the step on the surface and for the Janus particle whenever the bending and the extension of the zero crossing line are closely mirroring each other in the two geometries. The reason for the equality of these forces within MFT goes right back to Eq. (2.27). The Hamiltonian depends on the gradient of the order parameter profile, which relates to the bending of the zero line, but only via its square, which is independent of the direction of the bending. In Figs. 3.4(c) and (d) there is also an upper green zero crossing line, which is absent in (a) and (b). This line contributes only little to the force because it is relatively straight and because in that region the order parameter is small.

Based on the knowledge of the full MFT order parameter profiles, we construct a phenomenological relation beyond the DA relation of $\Xi = \Delta^{-1/2} \cos\vartheta$, which seeks to incorporate the bending of the zero crossing line. The base of this idea follows from Ref. [74], where a similar principle was used successfully in order to reconcile DA with MFT results.

In Fig. 3.5, we sketch the essential features of a Janus cylinder of radius $R$, close to a homogeneous wall at distance $D$; the actual zero crossing line of the order parameter profile is shown in green (which is taken from Fig. 3.4(c), but here serves to represent a generic case), and the zero crossing implied by DA is shown as a solid light gray line. The dotted, vertical dark gray line indicates the original DA relation, which cuts off the solid gray zero crossing line (of the homogeneous system with opposing BC at the colloid and substrate surface) at the projected position of the Janus equator. The visual agreement of the zero crossing lines can be improved by considering the DA for a fictitious scaled colloid (the blue and red semi-rings), with an effective radius of $\tilde{R} = R + pD$ and an effective surface-to-surface distance $\tilde{D} = (1-p)D$, so that the zero crossing line follows the solid light gray line. This yields an improved scaled position (dotted, vertical light gray line)

$$\tilde{\Xi}(\vartheta) = \tilde{\Delta}^{-1/2} \cos(\vartheta) = \sqrt{\frac{1}{1-p}} \cdot \sqrt{\frac{1}{\Delta} + p}\, \cos(\vartheta), \tag{3.6}$$

where $p$ is a free parameter which describes the rescaling of the particle size.

Independently, we have calculated the scaling functions of the force within full MFT as function of the position $X$ of a homogeneous cylinder relative to a stepped substrate and for the orientation $\vartheta$ for the Janus cylinder, at fixed scaled temperatures $\Theta$ and distances $\Delta$. Via linear interpolation within the two MFT scaling functions, we have extracted those values of $X$ and $\vartheta$ for which both scaling functions of the force render the same value, which in turn renders a relation between the numeric values of $\vartheta$ and $X$. The proposed model $\tilde{\Xi}(\vartheta)$ in Eq. (3.6) can be checked against this discrete set $\{\Xi, \vartheta\}$. We note that the projected, scaled step position $\tilde{\Xi}$ is proportional to $\tilde{\Delta}^{-1/2} > \Delta^{-1/2}$ for $p > 0$, i.e., for the same orientation $\vartheta$, the scaled step position $\tilde{\Xi}$ is larger than $\Xi$. However, for values of $\Xi \gg 1$, the scaling function of the force saturates (see Fig. 3.3) and relating $\Xi$ and $\vartheta$ numerically via the force within MFT becomes rather error-prone. This discredits fitting assumptions beyond linear order. However, the relation in Eq. (3.6), linearized around $\vartheta \approx \frac{\pi}{2}$ by using $\cos(\vartheta) \approx \frac{\pi}{2} - \vartheta$, results in a reasonable fit for $p \approx 1/4$. Within fitting errors, the fit parameter $p$ does not depend noticeably on the scaled temperature $\Theta$ and the scaling variable $\Delta$. The value of the rescaling parameter $p = 1/4$ is in line with the presentation in Fig. 3.5, as it places the surface of the fictitious colloid halfway between

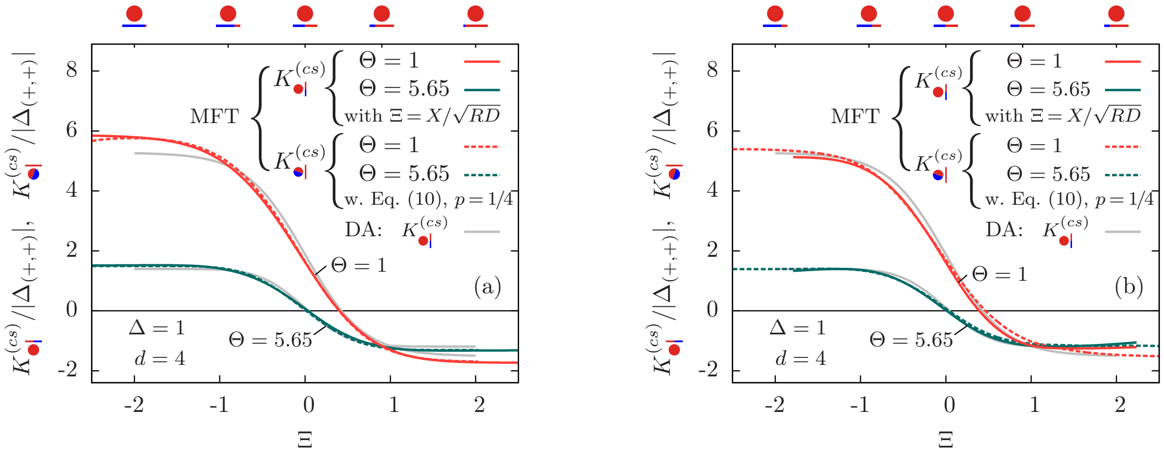

Figure 3.6: Same as Fig. 3.3 but replacing Ξ by $\tilde{\Xi} = \tilde{\Delta}^{-1/2}\cos\vartheta$ (Eq. (3.6) with $p = 1/4$) for $K^{(cs)}_{\bullet|}$. In this case, the correspondence between the scaling functions of the two configurations ●| and ●| holds within full MFT, for values of $\Delta$ outside the DA limit $\Delta \ll 1$.

the physical particle and the zero crossing line.

For comparison, Fig. 3.6 demonstrates the improved performance of the phenomenological relation $\tilde{\Xi} = \tilde{\Delta}^{-1/2}\cos\vartheta$ in Eq. (3.6) with $p = 1/4$ compared with that of the approach used in Fig. 3.3, even for $\Delta = 1$.

As a final remark, we emphasize that, in the above approach, within DA we counted the force to be normal to the substrate. An approach alternative to the DA considers the forces to be normal to the surface of the particle [125], which, however, leads to the same formal expressions for the critical Casimir forces. The improved DA relation in Eq. (3.6) can be interpreted as a partial consideration of forces directed normal to the particle surface, with $p$ being a weighting factor for the two force directions (see Fig. 3.5).

## 3.2 Janus cylinder (type A) above a chemical step

Here we analyze fully the case depicted in Fig. 3.1(b) of a single cylindrical Janus particle floating above a chemical step on the substrate. The cylindrical particle is taken to be oriented horizontally and all chemical steps are parallel to each other. Within DA, the configuration of a Janus particle above a step relates to the case of two walls each endowed with a chemical step, shifted with respect to each other [126], but accounting for distinct distance relations between the surface elements appearing in DA. Since the presence of two chemical steps can have a profound effect on the order parameter profile, one has to check whether this spoils the usefulness of the relation introduced in Eq. (3.6).

Within DA and for special configurations, the scaling function of the force $K^{(cs)}_{\bullet|}(\vartheta, \Xi, \Delta \ll 1, \Theta)$ between a chemical step on the substrate and a Janus particle with orientation $\vartheta$ and its center shifted by $\Xi = X/\sqrt{RD}$ from the substrate step, attains certain limiting expressions. For an upright orientation $\vartheta = 0$ it has the same value as the scaling function $K^{(cs)}_{\bullet|}(\Xi, \Delta \ll 1, \Theta)$ of the force between a homogeneous cylinder and a stepped substrate. If the Janus cylinder is positioned far away from the step, i.e., $\Xi \gg 1$, $K^{(cs)}_{\ominus|}$ reduces to the scaling function of a Janus cylinder above a homogeneous substrate, so that $K^{(cs)}_{\ominus|}(\vartheta, \Xi \to \infty, \Delta \ll 1, \Theta) = K^{(cs)}_{\ominus|}(\vartheta, \Delta \ll 1, \Theta) = K^{(cs)}_{\bullet|}(\Xi(\vartheta), \Delta \ll 1, \Theta)$ (where $\Xi(\vartheta) = \Delta^{-1/2}\cos\vartheta$ or is given by Eq. (3.6); analogously for $\Xi \to -\infty$).

Thus, similar to $K^{(cs)}_{\bullet|}$ in Eqs. (3.2) and (3.3), the scaling function $K^{(cs)}_{\ominus|}$ can be decomposed as $K^{(cs)}_{\ominus|}(\vartheta, \Xi, \Delta, \Theta) = K^{(cs)}_{(+,\pm)} \mp \Delta K^{(cs)}_{\ominus|}(\vartheta, |\Xi|, \Delta, \Theta)$, where $K^{(cs)}_{(+,\pm)}$ again refers to the scaling function of the force between a homogeneous cylinder and a homogeneous substrate (the rules when to use the upper and lower signs depend on $\vartheta$ and $\Xi$; see below):

$$K^{(cs)}_{(+,\pm)}(\Delta \ll 1, \Theta) = \sqrt{2}\int_1^{1+\Delta^{-1}/2} \mathrm{d}\alpha\, \frac{k_{(+,\pm)}(\alpha\Theta)}{\alpha^d\sqrt{\alpha - 1}}. \tag{3.7}$$

However, here the rhs of Eq. (3.7) carries a finite upper limit of integration, i.e., without explicitly setting $\Delta \to 0$. But the expression is still valid only in the DA limit $\Delta \ll 1$. The dependence on nonzero values of $\Delta$ ensures consistency with the scaling function of the excess force $\Delta K^{(cs)}_{\ominus|}(\vartheta, |\Xi|, \Delta \ll 1, \Theta)$. The latter depends on the position of the Janus cylinder relative to the substrate step (again only via the scaled absolute value $|\Xi|$ of the distance) and on the orientation $\vartheta \in [-\pi, \pi)$. The sign of the position $\Xi$ and the sign of the orientation $\vartheta$ can be chosen according to different conventions. Here, the coordinates are chosen such that $\vartheta > 0$ rotates the normal of the equatorial plane of the Janus particle towards that side of the substrate which has the same BC, i.e., here, the rotation is counter-clockwise towards the side $\Xi < 0$ (see Fig. 3.1(b)). We note that the force is invariant under reflection at the plane normal to the substrate and containing the cylinder axis ($\vartheta \to -\vartheta$, $\Xi \to -\Xi$ and exchange of BC on the substrate), i.e., $K^{(cs)}_{\ominus|} = K^{(cs)}_{\ominus|}$. Utilizing this symmetry, the decomposition reads

$$K^{(cs)}_{\ominus|}(\vartheta, \Xi, \Delta, \Theta) = \begin{cases} K^{(cs)}_{(+,+)}(\Delta, \Theta) - \Delta K^{(cs)}_{\ominus|}(\vartheta, |\Xi|, \Delta, \Theta) & \text{for } \Xi(\vartheta)\,\Xi > 0, \\ K^{(cs)}_{(+,-)}(\Delta, \Theta) + \Delta K^{(cs)}_{\ominus|}(-\vartheta, |\Xi|, \Delta, \Theta) & \text{for } \Xi(\vartheta)\,\Xi \le 0. \end{cases} \tag{3.8}$$

(Note that, as indicated, in Eq. (3.8), only in the first factor of the conditions, $\Xi$ is replaced by $\Xi(\vartheta) = \Delta^{-1/2}\cos\vartheta$ or, alternatively, by Eq. (3.6).) The condition $\Xi(\vartheta)\,\Xi \gtrless 0$ considers in which direction the Janus cylinder is tilting (e.g., $\Xi(\vartheta) \propto \cos\vartheta > 0 \Rightarrow$ upwards) and over which side of the step it levitates (via $\Xi$). Additionally, the equivalences $k_{(+,+)} = k_{(-,-)}$ and $k_{(+,-)} = k_{(-,+)}$ of the interaction between homogeneous, planar, and parallel walls lead to an invariance of the scaling function $K^{(cs)}_{\ominus|}$ upon inverting the normal of the particle, i.e., $\vartheta \to \vartheta \pm \pi$ (such that $\vartheta \in [-\pi, \pi)$) and exchanging the BC of the substrate step (but without changing the position $\Xi$), so that $K^{(cs)}_{\ominus|} = K^{(cs)}_{\ominus|}$.

The excess scaling function $\Delta K^{(cs)}_{\bullet|}$ is obtained from the careful DA summation of the corresponding surface elements:

$$\Delta K^{(cs)}_{\bullet|}(\vartheta, \Xi, \Delta \ll 1, \Theta) = \left\{ \begin{array}{ll} +1, & \text{if } |\Xi(\vartheta)| < |\Xi| \text{ or } \vartheta < 0, \\ -1, & \qquad\qquad\quad \text{otherwise} \end{array} \right\}$$
$$\times \left( \frac{1}{\sqrt{2}} \int_{1+\Xi(\vartheta)^2/2}^{1+\Delta^{-1}/2} \mathrm{d}\alpha \, \frac{\Delta k(\alpha\Theta)}{\alpha^d \sqrt{\alpha - 1}} - \frac{\operatorname{sign}(\vartheta)}{\sqrt{2}} \int_{1+\Xi^2/2}^{1+\Delta^{-1}/2} \mathrm{d}\alpha \, \frac{\Delta k(\alpha\Theta)}{\alpha^d \sqrt{\alpha - 1}} \right), \quad (3.9)$$

which has the structure of the difference between two expressions, resembling the scaling function corresponding to the chemical step on the substrate as in Eq. (3.4). The intricate prefactor effectively exchanges $\Xi(\vartheta) \leftrightarrow \Xi$ if $|\Xi(\vartheta)| \geq |\Xi|$, which affects the sign only if $\vartheta \geq 0$. Note that $\Delta K^{(cs)}_{\bullet|}$ depends on $\vartheta$ only via the sign and via $|\Xi(\vartheta)| \propto |\cos\vartheta|$. One can verify that both the symmetry operations of reflection ($\vartheta \to -\vartheta$) as well as inversion ($\vartheta \to \vartheta \pm \pi$ such that $\vartheta \in [-\pi, \pi)$) yield the same result for the excess scaling function, i.e., that $\Delta K^{(cs)}_{\bullet|}(-\vartheta, \dots) = \Delta K^{(cs)}_{\bullet|}(\vartheta \pm \pi, \dots)$. Note that neither reflecting the position $\Xi \to -\Xi$ nor exchanging the BC affects $\Delta K^{(cs)}_{\bullet|}$, but only $K^{(cs)}_{\bullet|}$.

In Fig. 3.7, we compare the DA with the full MFT results for the scaling function $K^{(cs)}_{\bullet|}$ for two separations $\Delta = 1$ in (a) and $\Delta = 1/5$ in (b), with the step on the substrate fixed at $\Xi = 0$ (red sets of squares and lines). Within DA, this represents a peculiar configuration in that the orientations $\vartheta = \pm\pi/2$ of the Janus particle correspond to configurations in which both the step on the particle and the one on the substrate share a common vertical plane (see the sketches below the horizontal axis). At $\vartheta = -\pi/2$, due to opposing BC between all DA surface elements, the force (red lines) is repulsive ($> 0$). For $\Delta = 1$, around $\vartheta = -\pi/2$ the DA result slightly overestimates the MFT result. Similarly, the special orientation at $\vartheta = \pi/2$ leads to an attractive force ($< 0$); here, however, and for $\Delta = 1$, DA clearly underestimates the MFT results. The cusplike shape of the scaling function around the maximum and minimum is an artifact of the DA; MFT renders a smooth and broader curve. In general, the MFT results are slightly more attractive and less repulsive than predicted by DA. Nonetheless, for $\Delta \ll 1$ [Fig. 3.7(b)] DA and MFT agree rather well, even at $\vartheta = \pm\pi/2$. This is reassuring because for these orientations the shortcomings of the DA are particularly pronounced. As implied by the DA and in view of its reliability, the overall shape of the scaling function $K^{(cs)}_{\bullet|}(\vartheta, \Xi = 0, \Delta \to 0, \Theta)$, within MFT and as a function of $\vartheta$, is consistent with the dependence of the scaling function of the force between two patterned, planar substrates on a lateral shift (see Ref. [126]).

We point out that the DA curves shown in Fig. 3.7 are based on the improved relation given by Eq. (3.6). For the original DA relation $\Xi(\vartheta) = \Delta^{-1/2}\cos\vartheta$, the agreement between DA and MFT turns out to be poorer in Fig. 3.7(a), i.e., for $\Delta = 1$, but remains comparable to the good agreement evident in Fig. 3.7(b), i.e., for $\Delta = 1/5$ (see also Fig. 3.3). We find that the explicit dependence on $\Delta$ introduced by Eqs. (3.6) and (3.7)

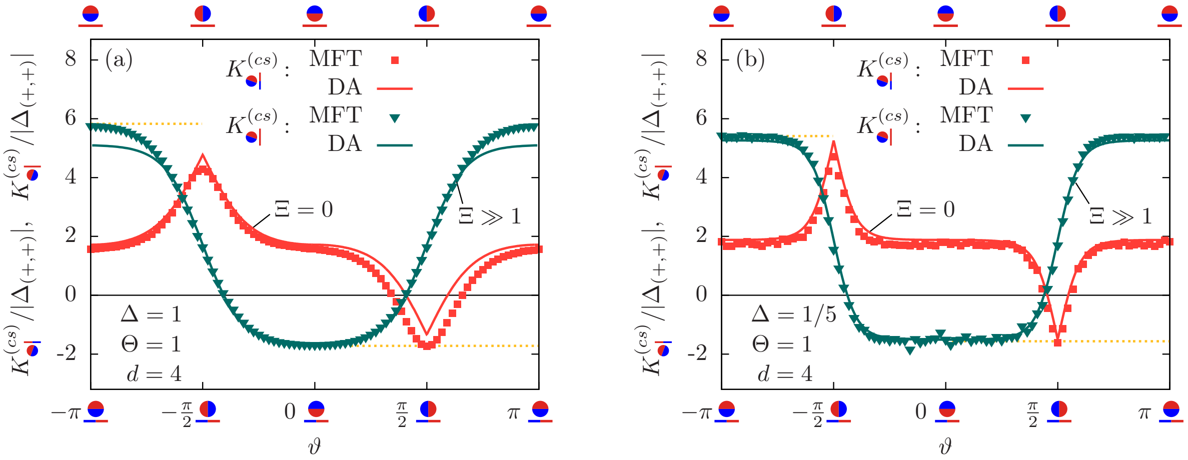

Figure 3.7: (a) Scaling function $K^{(cs)}_{◐|}$ of the force between a Janus cylinder and a step on the substrate (in red), as a function of the particle orientation $\vartheta$ for $\Xi = 0$. The solid lines represent the results within DA, whereas the squares correspond to numerical MFT results for a separation $\Delta = D/R = 1$. The green lines and triangles represent the scaling function $K^{(cs)}_{◐|}$ of the force which corresponds to the case of a homogeneous substrate, or equally, to the case of a step that is far away from the particle, i.e., $|\Xi| \gg 1$ [see Eq. (3.2)]. (b) The same, but for $\Delta = 1/5$. Both in (a) and (b), the MFT values of the scaling functions $K^{(cs)}_{(+,+)}$ and $K^{(cs)}_{(+,-)}$ [Eq. (3.7)] for the fully attractive ($< 0$) and repulsive ($> 0$) cases, respectively, of a homogeneous cylinder and substrate are indicated by dotted golden lines. At the top of the panels, we indicate configurations with the Janus cylinder above a homogeneous substrate corresponding to certain points of the green curve for $\Xi \gg 1$. Similarly, at the bottom of the panels, configurations are shown with the Janus particle directly above the step corresponding to the red curve, i.e., $\Xi = 0$.

does not improve the agreement between DA and MFT for the strongly attractive or repulsive configurations: in Fig. 3.7(a) see the difference between the green line and the green symbols as well as the dotted golden lines which refer to MFT results for $K^{(cs)}_{(+,+)} < 0$ and $K^{(cs)}_{(+,-)} > 0$. However, the dependence on $\Delta$ of the MFT scaling functions for the case of a homogeneous cylinder and substrate has a different cause [74]. Within DA, a dependence on $\Delta$ has been introduced via the DA relation $\Xi(\vartheta) = \Delta^{-1/2}\cos\vartheta$ or via Eq. (3.6) along with the dependence on $\vartheta$. Thus, the good agreement between the slopes of the DA and MFT scaling functions shown in Fig. 3.7 as a function of $\vartheta$ for different $\Delta$ indicates the consistency of these relations beyond the DA limit.

From these findings we conclude that the DA, although for $\Delta \gtrsim 1$ it deviates quantitatively from the MFT results in $d = 4$, exhibits no basic flaws. In fact, studying the implication of the use of the DA in this section has revealed that the parameters $\Xi$ and $\vartheta$, associated with the positions of the chemical steps on the substrate and on the Janus cylinder, are related according to $\Xi(\vartheta) = \Delta^{-1/2}\cos\vartheta$. The modified scaling variable $\tilde{\Xi}(\vartheta)$ (Eq. (3.6)) improves quantitatively the agreement with the full MFT results. We consider these properties as a justification for the continued study of critical Casimir interactions based on the DA, even in the case of Janus particles.

## 3.3 Critical Casimir torque on a homogeneous cylinder

As outlined, we once more visit the case of a homogeneous cylindrical particle close to a substrate with a chemical step. The critical Casimir potential can be obtained from the force $F^{(cs)}_{\bullet|}$ (Eq. (3.1)), via $V^{(cs)}_{\bullet|}(D,\ldots) \equiv \int_D^\infty \mathrm{d}z\, F^{(cs)}_{\bullet|}(z,\ldots)$. With now considering additionally a dependence on the angle $\alpha$ as shown in Fig. 3.1(c), the critical Casimir potential can be written in the scaling form

$$V^{(cs)}_{\bullet|}(X,\alpha,D,R,L,T) = k_B T\, \frac{\mathcal{L} R^{1/2}}{D^{d-3/2}}\, \Phi^{(cs)}_{\bullet|}(\Xi,\alpha,\Theta,\Delta,\mathscr{L}) \tag{3.10}$$

with the scaling variables $\Xi = X/\sqrt{RD}$ and $\mathscr{L} = L/\sqrt{RD}$. The scaling function of the potential for the step geometry

$$\begin{aligned}\Phi^{(cs)}_{\bullet|}(\Xi,\alpha,\Theta,\Delta,\mathscr{L}) = {} & \frac{\Phi^{(cs)}_{(a_<,b)}(\Theta,\Delta) + \Phi^{(cs)}_{(a_>,b)}(\Theta,\Delta)}{2} \\ & + \frac{\Phi^{(cs)}_{(a_<,b)}(\Theta,\Delta) - \Phi^{(cs)}_{(a_>,b)}(\Theta,\Delta)}{2}\, \omega_{(a_<|a_>,b)}(\Xi,\alpha,\Theta,\Delta,\mathscr{L}),\end{aligned} \tag{3.11}$$

is conveniently written using a relative scaling function $\omega_{(a_<|a_>,b)}$ of the chemical step between the scaling functions of the laterally homogeneous substrates

$$\Phi^{(cs)}_{(a,b)}(\Theta,\Delta\to 0) = \int_1^\infty \mathrm{d}z\, \frac{K^{(cs)}_{(+,\pm)}(\Delta\to 0, z\Theta)}{z^{d-1/2}} = 2\sqrt{2}\int_1^\infty \mathrm{d}\nu\, \sqrt{\nu-1}\,\nu^{-d}\, k_{(a,b)}(\Theta\nu), \tag{3.12}$$

which are attained for $X \to \pm\infty$. (Note that, following from the scaling function $K^{(cs)}_{(+,\pm)}$ of the force in Eq. (3.3), $\Phi^{(cs)}_{(a,b)}$ for a cylindrical particle above a substrate is larger by a factor $\sqrt{2}$ than the scaling function of the potential $\Phi^{(cc)}_{(a,b)}$ between two homogeneous cylinders in Eq. (A.7).) Thus, $\omega_{(a_<|a_>,b)}$ crosses over from $+1$ at $\Xi \to -\infty$ to $-1$ at $\Xi \to +\infty$. The full result for the relative scaling function $\omega_{(a_<|a_>,b)}$ was derived previously in Refs. [74] and [127].

Since the critical Casimir potential depends on the angle $\alpha$ between the axis of the cylinder and the chemical step, a critical Casimir torque $\tau^{(cs)}_{\bullet|}$ acting on the particle arises. The torque is a vector in the direction of the substrate normal with $\tau^{(cs)}_{\bullet|} = \frac{d}{d\alpha} V^{(cs)}_{\bullet|}$ as the only nonzero component. The orientation of the particle being parallel to the chemical step corresponds to $\alpha = 0°$, while an orthogonal orientation corresponds to $\alpha = 90°$, so that a positive torque $\tau^{(cs)}_{\bullet|}$, i.e., an increase of $V^{(cs)}_{\bullet|}$ upon an increase of $\alpha$, leads to a preferred parallel alignment and negative torques to the preference of the perpendicular orientation.

Based on Eq. (3.10), the critical Casimir torque acting on the cylindrical particle can be written in the following scaling form:

$$\tau^{(cs)}_{\bullet|}(X, \alpha, D, R, L, T) = k_B T \, \frac{\mathcal{L} R^{1/2}}{D^{d-3/2}} \, M_s(\Xi, \alpha, \Theta, \Delta, \mathscr{L}), \tag{3.13}$$

where the scaling function $M_s$ follows from Eq. (3.11) to be

$$M_s(\Xi, \alpha, \Theta, \Delta, \mathscr{L}) = \frac{\Phi^{(cs)}_{(a_<,b)}(\Theta, \Delta) - \Phi^{(cs)}_{(a_>,b)}(\Theta, \Delta)}{2} \, \frac{d}{d\alpha} \omega_{(a_<|a_>,b)}(\Xi, \alpha, \Theta, \Delta, \mathscr{L}). \tag{3.14}$$

Now within this thesis, based on the expressions for $\omega_{(a_<|a_>,b)}$ in Refs. [74, 127], we have newly derived the alignment of a cylindrical colloid close to a chemical step as presented in the following. The dependence on the relative position $X/L = \Xi/\mathscr{L}$ is illustrated in Fig. 3.8 where we present the scaling function $M_s$ as obtained within the DA for $d = 3$ as a function of the rotation angle $\alpha$ with the temperature fixed at its critical value, i.e., $\Theta = 0$. The relative position $X/L = \Xi/\mathscr{L}$ is independent of the aspect ratio $L/R = \mathscr{L}\sqrt{\Delta}$ of the particle; therefore the shape of the particle affects the torque only through the scaling variable $\mathscr{L} = L/\sqrt{RD}$. For negative values of $\Xi$, the scaling function can be obtained via a point reflection, i.e., $M_s(\Xi < 0, \cdots) = -M_s(-\Xi, \cdots)$.

Our results show that for large aspect ratios $L/R$ (i.e., rod-like particles), for which $\mathscr{L} \gg 1$, the torque acting on the colloid is positive for $0 < X/L = \Xi/\mathscr{L} < 0.5$ and basically vanishes for $X/L = \Xi/\mathscr{L} > 0.5$ for all rotation angles $\alpha \in [0, \pi/2]$. As can be seen in Fig. 3.8(a) for a particle with $\mathscr{L} = 10$, the torque vanishes when the particle is orientated parallel ($\alpha = 0°$) or perpendicular ($\alpha = 90°$) relative to the chemical step on the substrate. For $X/L > 0$, the torque is positive and reaches a maximum value at an intermediate angle, so that the orientation with $\alpha = 0$ is stable against rotations of the particle, whereas the perpendicular orientation is unstable and thus the rod-like particles with $\mathscr{L} = 10$ prefer to orientate themselves parallel to the chemical step. For $X/L < 0$, due to its above mentioned antisymmetry, the torque is negative, so that in this case the orientation with $\alpha = 90°$ is stable against rotations of the particle, whereas the parallel orientation becomes unstable, in contrast to the case $X/L > 0$. As shown in Fig. 3.8(b), for smaller aspect ratios $L/R$ and $\mathscr{L} \simeq 4$ the torque changes sign upon varying the position $\Xi/\mathscr{L}$ of the colloid. The torque is positive if the particle is close to the step and the maximal strength of the torque first increases with the relative position $\Xi/\mathscr{L}$, but then decreases and finally the torque changes into the opposite direction. This sensitivity of the orientation with respect to the geometrical features is due to the comparable length scales of the particle length $L$ and the radius $R$. For disk-like particles with $\mathscr{L} \lesssim 2$ as shown in Fig. 3.8(c), we find that for $X/L > 0$ the torque is mostly negative for all orientations of the particle, so that in this case the perpendicular orientation is the preferred one, whereas for $X/L < 0$ the torque is positive and the parallel colloidal orientation is the preferred one. Our results obtained within the DA for $\mathscr{L} = 2$ indicate a change of sign

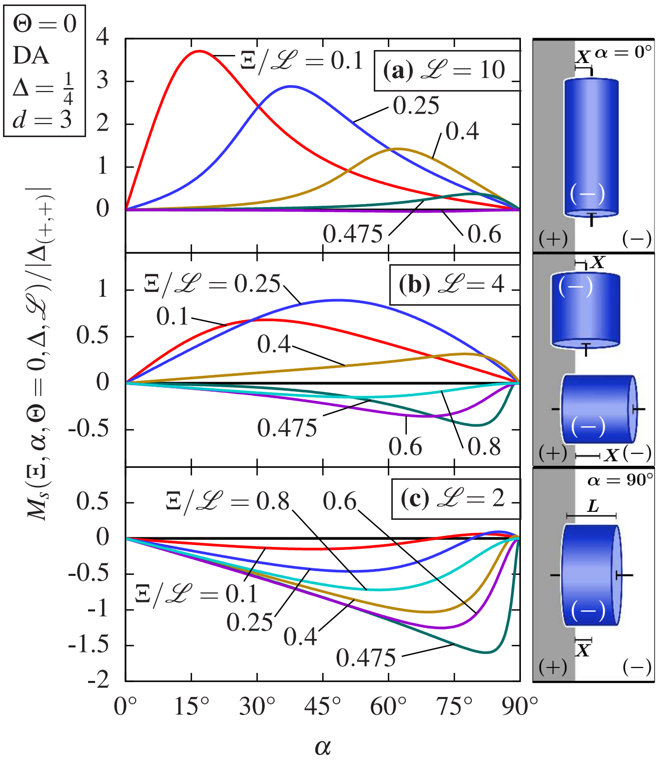

Figure 3.8: Scaling function $M_s(\Xi, \alpha, \Theta = 0, \Delta \to 0, \mathscr{L})$ for the torque in $d = 3$ spatial dimensions as obtained within the DA as a function of the orientation $\alpha$ of the colloid relative to a chemical step [Fig. 3.1(c)]. The suitably normalized scaling function is shown for three different aspect ratios of the cylindrical colloids, i.e., for $\mathscr{L} = L/\sqrt{RD} = 10$ in (a), for $\mathscr{L} = 4$ in (b), and for $\mathscr{L} = 2$ in (c) as well as for various lateral distances $\Xi/\mathscr{L} = X/L > 0$ from the chemical step. For negative values of $\Xi$, the scaling function can be obtained via a point reflection, i.e., $M_s(\Xi < 0, \cdots) = -M_s(-\Xi, \cdots)$. The solvent is considered to be at its bulk critical point $\Theta = 0$. For rod-like particles as in (a), we find for $0 < X/L = \Xi/\mathscr{L} < 0.5$ the torque to be always positive, which leads to a preferred alignment parallel to the chemical step, as sketched right next to the graph. On the other hand for disk-like particles, as for $\mathscr{L} = 2$ in (c), the torque is negative for positive values of $X/L$, so that the colloid self-aligns perpendicular to the chemical step, as indicated in the sketch next to the graph. For the intermediate case $\mathscr{L} = 4$ in (b) we find both negative and positive values of the critical Casimir torque for $X/L > 0$, depending on the lateral position of the colloid. (The sketches next to the graphs correspond to aspect ratios $L/R = \mathscr{L}\sqrt{\Delta}$ obtained for $\Delta = D/R = 0.25$.)

of the critical Casimir torque at angles $\alpha = \alpha_0 \gtrsim 70°$ for $0.1 < \Xi/\mathscr{L} < 0.5$. However, for larger values of $\alpha > \alpha_0$ the magnitude of the scaling function $M_s$ is very small compared with the Casimir amplitude $|\Delta_{(+,+)}|$.

In order to analyze the rotational orientation of the cylinder and its statistical characteristics with respect to thermal fluctuations in more detail, we investigate the planar

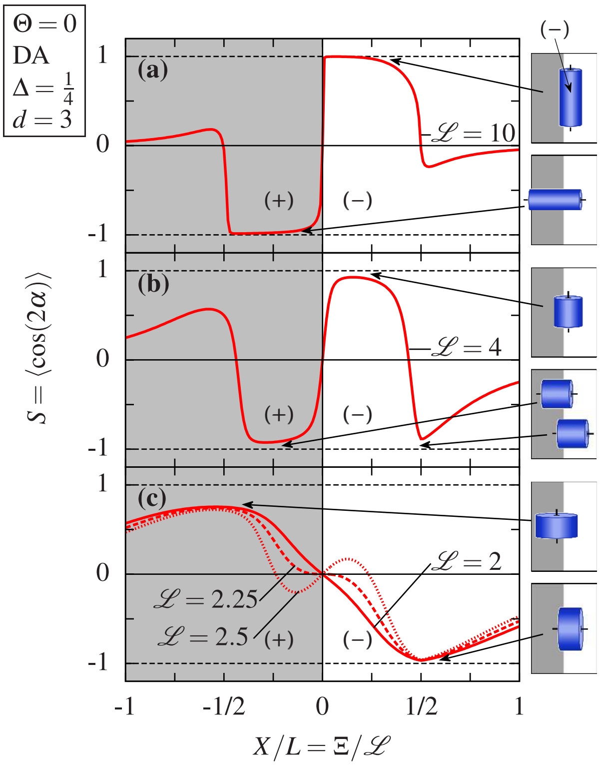

Figure 3.9: Planar nematic order parameter $S$ [Eq. (3.15)] for a cylindrical colloid close to a chemical step as obtained within the DA for $d = 3$ and $\Delta = D/R = 1/4$ as a function of the lateral particle position $X$ in units of its length $L$. The solvent is taken to be at its bulk critical point $\Theta = 0$. For rod-like particles with $\mathscr{L} = 10$ in (a), upon increasing $X$ the nematic order parameter $S$ changes abruptly from $S \simeq -1$ to $S \simeq +1$ at $\Xi = 0$, corresponding to a change from a preferred colloid orientation perpendicular to the step to an orientation parallel to the step. Both configurations are very stable against thermal fluctuations. At $|\Xi/\mathscr{L}| \simeq 0.5$ in (a) $S$ again changes sign but it attains only small values for $|\Xi/\mathscr{L}| > 0.5$, corresponding to a weak preference of the colloid orientation, and tends to a uniform angular distribution ($S = 0$) for $|\Xi/\mathscr{L}| \gtrsim 1$. For a shorter cylinder with $\mathscr{L} = 4$, in (b) the behavior for small values of $|\Xi/\mathscr{L}|$ is similar as in (a), but the alignment at $|\Xi/\mathscr{L}| \simeq 0.5$ becomes very pronounced; $S$ is close to $-1$ for $\Xi/\mathscr{L} = 0.5$ which corresponds to a strong orientational alignment of the cylinder perpendicular to the chemical step. For disk-like particles with $\mathscr{L} = 2$, $\mathscr{L} = 2.25$, and $\mathscr{L} = 2.5$ the behavior of $S$ is different. Upon lowering $\mathscr{L}$ the order parameter extrema close to $\Xi/\mathscr{L} = 0$ disappear and the angular distribution becomes almost uniform (i.e., $|S|$ is small). On the other hand the alignment at $|\Xi/\mathscr{L}| \simeq 0.5$ is pronounced, but with the opposite preference of the orientations as compared with the case $\mathscr{L} = 10$ and $|\Xi/\mathscr{L}| < 0.5$ in (a). The sketches next to the graphs, correspond to aspect ratios $L/R = \mathscr{L}\sqrt{\Delta} = \mathscr{L}/2$.

nematic order parameter $S$ defined as [128, 129]

$$S \equiv \langle\cos(2\alpha)\rangle = \frac{1}{N}\int\limits_0^{\pi/2} \mathrm{d}\alpha\,\cos(2\alpha)\exp\left(-\frac{V^{(cs)}(X,\alpha,D,R,L,T)}{k_B T}\right), \tag{3.15}$$

where the normalization constant is given by $N = \int_0^{\pi/2} \mathrm{d}\alpha \exp\left(-\beta V_{\bullet|}^{(cs)}(X, \alpha, D, R, L, T)\right)$. $S = 1$ corresponds to perfect alignment of the cylindrical colloid parallel to the chemical step ($\alpha = 0$), whereas $S = -1$ corresponds to perfect alignment perpendicular to the step ($\alpha = 90°$). Isotropic orientation is characterized by $S = 0$. In Fig. 3.9 the nematic order parameter $S$ as obtained within the DA for $\Xi = 0$ and $\Delta = 1/4$ is shown for the same values of $\mathscr{L}$ as in Fig. 3.8 as a function of the relative position $X/L = \Xi/\mathscr{L}$. As can be inferred from Fig. 3.9(a), a rod-like particle with $\mathscr{L} = 10$ exhibits a strong rotational alignment when its center is close to the chemical step. Whereas for $-0.5 \lesssim \Xi/\mathscr{L} < 0$ the cylinder is strongly aligned perpendicular to the step due to the critical Casimir torque, it abruptly changes orientation upon crossing the chemical step at $\Xi = 0$. For $0 < \Xi/\mathscr{L} \lesssim 0.5$ the cylinder is aligned parallel to the step, exploiting fully the attractive critical Casimir interaction between surfaces of same chemical preference. At $|\Xi/\mathscr{L}| \simeq 0.5$ the nematic order parameter $S$ again changes its sign. However, for $0.5 \lesssim |\Xi/\mathscr{L}| \lesssim 1$ the magnitude of $S$ is rather small and vanishes for $|\Xi/\mathscr{L}| \simeq 1$, corresponding to a uniform angular distribution.

For a reduced cylinder length $\mathscr{L} = 4$, the change of the sign of $S$ at $|\Xi/\mathscr{L}| \approx 0.5$ becomes much more pronounced [see Fig. 3.9(b)]. Whereas close to the chemical step at $\Xi = 0$ the behavior of the order parameter $S$ resembles the one for $\mathscr{L} = 10$ in Fig. 3.9(a) (but less abruptly), a strong orientational alignment of the cylinder perpendicular to the step ($S = -1$) develops at $\Xi/\mathscr{L} \simeq 0.5$. In addition for $\Xi/\mathscr{L} \lesssim -0.5$ the degree of orientational order is higher than the corresponding one of the rod-like particle with $\mathscr{L} = 10$ in Fig. 3.9(a). Thus, as a function of its lateral position a cylindrical particle of reduced length $\mathscr{L} = 4$ exhibits various changes of its preferred orientation parallel or perpendicular to the chemical step.

For even smaller values of $\mathscr{L}$, i.e., disk-like particles, the strong orientational alignment close to $\Xi/\mathscr{L} = 0$ disappears in that the nematic order parameter $S$ acquires a small amplitude, as can be inferred from Fig. 3.9(c). In addition, $S$ flips upon lowering $\mathscr{L}$, such that for $\mathscr{L} = 2$ the particles align with their axis parallel to the step for $\Xi < 0$ and perpendicular to it for $\Xi > 0$. Moreover, the change between these two orientations as function of $\Xi$ is much smoother as compared with the case of rod-like particles in Fig. 3.9(a). This is due to the relatively small strength of the critical Casimir torque for small values of $\Xi/\mathscr{L}$, as shown in Fig. 3.8(c). A change of sign of $M_s(\alpha)$ and the accompanying reversal of stability of the corresponding configurations signal the presence of competing minima in the free energy landscape. For Fig. 3.9(c) those are very shallow in units of $k_B T$ and therefore easily washed out by thermal fluctuations.

For a disk-like particle with a reduced length $\mathscr{L} = 2$ Fig. 3.10 illustrates the temperature dependence of the orientational order parameter profile $S(X/L)$ by comparing the system at bulk criticality $\Theta = 0$ [Fig. 3.10(a)] and off criticality $\Theta = 3$ [Fig. 3.10(b)]. As discussed above in Fig. 3.9(c), in Fig. 3.10(a) for $\Theta = 0$ the critical Casimir torque

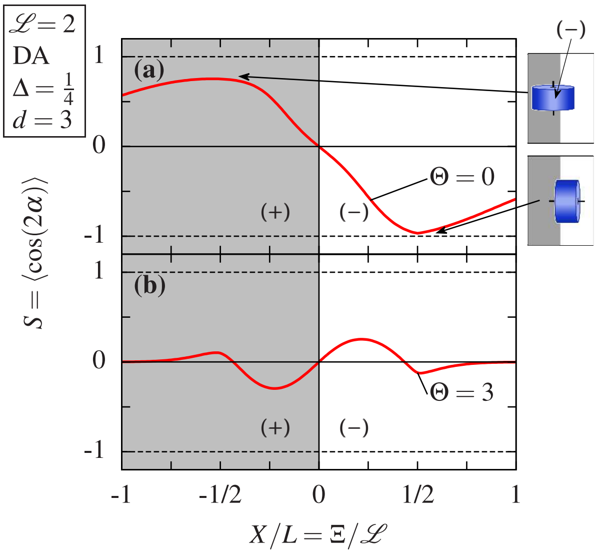

Figure 3.10: Planar nematic order parameter $S$ [Eq. (3.15)] for a cylindrical colloid close to a chemical step as obtained within the DA for $d = 3$, $\Delta = D/R = 1/4$, and $\mathscr{L} = 2$ as a function of the lateral particle position $X$ in units of its length $L$. For such a disk-like particle we find a preferred parallel [perpendicular] orientation of the particle axis relative to the chemical step for $\Xi/\mathscr{L} < 0$ [$\Xi/\mathscr{L} > 0$] at the bulk critical point ($\Theta = 0$) in (a) [same as in Fig. 3.9(c)]. On the other hand, for a high temperature corresponding to $\Theta = 3$ in (b), the nematic order parameter changes sign at $\Xi = 0$ and $|\Xi/\mathscr{L}| \approx 0.4$. Thus, for $|\Xi/\mathscr{L}| \lesssim 0.4$ the preferential orientation of the disk-like particle switches upon varying temperature.

leads to a preferential alignment of the cylinder axis parallel to the chemical step for $\Xi < 0$ and perpendicular to the step for $\Xi > 0$. However, for $\Theta = 3$ in Fig. 3.10(b) the nematic order parameter $S$ changes sign at $\Xi = 0$ and at $|\Xi/\mathscr{L}| \approx 0.4$. Thus, whenever the perpendicular [parallel] orientation is the preferred one at the bulk critical point for $|\Xi/\mathscr{L}| \lesssim 0.4$ as sketched in Fig. 3.10(a), the disk-like colloid prefers a parallel [perpendicular] orientation at higher temperatures as sketched in Fig. 3.10(b). Accordingly, the orientation of a disk-like colloid near a chemical step can be reversibly and continuously switched by minute temperature changes. We attribute this behavior to the fact that the ratio of the strengths of the critical Casimir forces in the film geometry for $(+,-)$ and $(-,-)$ BCs varies as function of $\Theta$. Whereas close to $T_c$ the critical Casimir force for $(+,-)$ BCs is much stronger than for $(-,-)$ BCs, both become comparable in strength for $\Theta \gg 1$. However, the maximal absolute value of the nematic order parameter $S$ for $\Theta = 3$ in Fig. 3.10(b) is rather small so that the degree of orientational order is low. Upon increasing $\Theta$ the nematic order parameter $S$ vanishes gradually and the angular distribution of the colloids becomes uniform.

We note that within the DA the range of the effective interaction of the colloid with the substrate along the direction normal to the cylinder axis tends to be overestimated due to the parabolic distance approximation $D(\rho) \approx D(1 + \rho^2/(2RD))$ (see Sec. 2.1.4).

However, this is less important far away from criticality because the scaling function of this potential decays exponentially with respect to the surface-to-surface distance between the particle and the substrate, and within DA contributions of surface elements at the ends of the cylinder become negligible. On the other hand, within DA we expect the torque to be underestimated in the regime of disk-like particles. However, it has been found in Ref. [74] that the ratio between the scaling functions the force $K^{(cs)}_{(+,-)}(\Theta = 0, \Delta, \mathscr{L})/K^{(cs)}_{(-,-)}(\Theta = 0, \Delta, \mathscr{L})$ for cylinders of finite length is maintained constant even for small values of $\mathscr{L} \sim 1$. Thus, we expect that these deficiencies of the DA do not affect the sign of the torque and the qualitative results for the particle orientation presented above for $\mathscr{L} \geq 2$, concerning the distinct behavior of rod-like and disk-like particles.

## 3.4 Janus cylinder (type B) close to a periodically striped substrate

Knowledge of the critical Casimir potential of a cylinder near a chemical step allows one, within DA, to describe more complex geometrical features of the chemical boundary conditions on the substrate and on the colloid. Here, we consider a pattern of chemical stripes, which are alternating *p*eriodically along the $x$ direction. The pattern consists of stripes of width $L_1$ with $(a_1)$ BC neighboring stripes of width $L_2$ with $(a_2)$ BC such that the periodicity is given by $P = L_1 + L_2$. The coordinate system is chosen such that $x = 0$ corresponds to the lateral center of a stripe with $(a_1)$ BC. Due to the assumed additivity of the forces underlying the DA, within this approximation the critical Casimir potential of a Janus particle as in Fig. 3.1(d) with its center located at a lateral position $x = X$ at a distance $D$ from such a patterned substrate can be constructed by considering two homogeneous cylinders of half the particle length $L/2$ and summing their scaling functions given in the preceding section. We consider this case as an example of certain experimentally relevant geometries, which are difficult to treat even within MFT.

The critical Casimir potential $V_p^{(cs)}$ acting on a Janus cylinder exhibits the following scaling form:

$$V_p^{(cs)}(L_1, P, X, \alpha, D, R, L, T) = k_B T \, \frac{\mathcal{L}\, R^{1/2}}{D^{d-3/2}} \, \Phi_p^{(cs)}(\Lambda, \Pi, \Xi, \alpha, \Theta, \Delta, \mathscr{L}), \tag{3.16}$$

where $\Lambda = L_1/\sqrt{RD}$ and $\Pi = P/\sqrt{RD}$ are, compared with the single chemical step, two additional scaling variables describing the stripe width and the periodicity, respectively, and $\Phi_p^{(cs)}$ is the corresponding universal scaling function.

Since the stripe pattern and the surface of the Janus particle are combinations of the $(+)$ and $(-)$ BCs it is convenient to follow Eq. (3.11) and introduce the normalized scaling

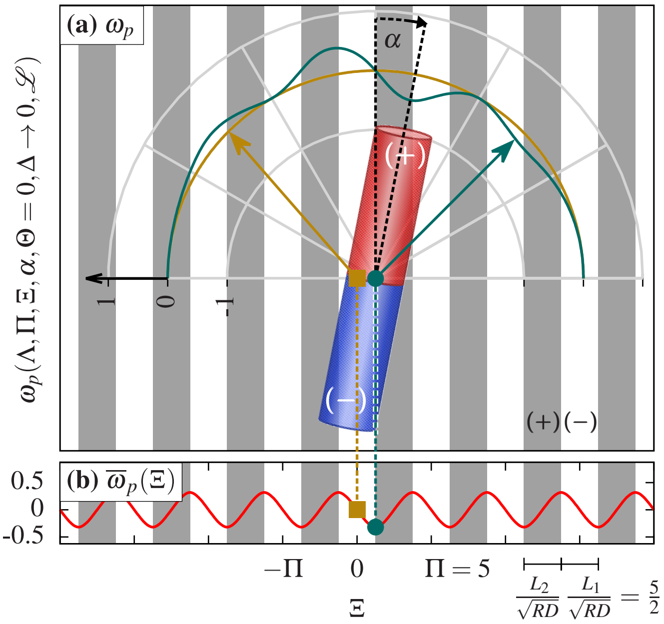

Figure 3.11: Scaling function of the critical Casimir potential $\omega_p(\Lambda, \Pi, \Xi, \alpha, \Theta = 0, \Delta \to 0, \mathscr{L})$ [Eq. 3.18] within DA for $d = 3$ and $\Theta = 0$ acting on a Janus cylinder with opposite $(+)$ and $(-)$ BCs (red and blue areas, respectively) and of reduced length $\mathscr{L} = L/\sqrt{RD} = 20$ near a chemically patterned substrate. The substrate is periodically patterned with $(a_1) = (-)$ BC on one kind of stripes (white areas) and $(a_2) = (+)$ BC on the other kind of stripes (shaded areas). Due to this choice of the BCs, the red (blue) part of the Janus cylinder is attracted by the shaded (white) stripes and repelled by the others. The geometry of the pattern is characterized by $\Pi = P/\sqrt{RD} = 5$ and $\Lambda = L_1/\sqrt{RD} = 5/2$, where $L_1 = L_2 = P/2 = L/8$ is the width of the stripes. The Janus cylinder, located at lateral position $X$ (so that $X = 0$ corresponds to the center of a stripe with $(-)$ BC), is rotated by an angle $\alpha \in [-\pi/2, \pi/2]$ relative to the translationally invariant direction of the stripes. The normalized scaling function $\omega_p \in [-1, 1]$ is shown in (a) as a function of $\alpha$ for the two colloid positions $X = 0$ ($\Xi = 0$, yellow curve) and $X = P/4$ ($\Xi = 5/4$, green curve and illustrated by the sketched cylinder). The greyish curves are semi-circles around the green dot. Accordingly, for each point on the green line one can infer the corresponding angle $\alpha$ by drawing the green arrow footed at $X \neq 0$. Consequently, the angles belonging to points on the yellow line can be read off from the yellow arrow which, however, is footed at $X = 0$. Thus green and yellow data points belonging to the same angle $\alpha$ are not radially connected. Since $\omega_p(X = 0) = 0$, as explained in the main text, the yellow line coincides with the semi-circle around the green dot corresponding to the zero of $\omega_p$. In (b) the angularly averaged value $\overline{\omega}_p(X)$ of $\omega_p$ for orientations $\alpha \in [0, \pi/2]$ is shown in red. For the other scaling variables fixed, $\overline{\omega}_p$ represents the critical Casimir potential as function of the lateral colloid position $X$, independent of the orientation of the colloid. This average exhibits extrema at the edges of the chemical stripes. The sketched Janus particle corresponds to the configuration of minimal energy both with respect to its orientation (see the green line) and its lateral position (see the red line).

function $\omega_p(\Lambda, \Pi, \Xi, \alpha, \Theta, \Delta, \mathscr{L}) \in [-1, 1]$ such that

$$\begin{aligned}\Phi_p^{(cs)}\Lambda, \Pi, \Xi, \alpha, \Theta, \Delta, \mathscr{L}) &= \frac{1}{2}\left(\Phi_{(+,-)}^{(cs)}(\Theta, \Delta) + \Phi_{(-,-)}^{(cs)}(\Theta, \Delta)\right) \\ &\quad + \frac{1}{2}\left(\Phi_{(+,-)}^{(cs)}(\Theta, \Delta) - \Phi_{(-,-)}^{(cs)}(\Theta, \Delta)\right)\omega_p(\Lambda, \Pi, \Xi, \alpha, \Theta, \Delta, \mathscr{L}). \qquad (3.17)\end{aligned}$$

Without loss of generality, here we limit the rotation angle $\alpha$ between the chemical steps of the stripes and the axis of the Janus cylinder to the range $\alpha \in [-\pi/2, \pi/2]$ (see Fig. 3.11). Moreover, we restrict ourselves to the symmetry-breaking BCs $(a_1) = (-)$ and $(a_2) = (+)$ on the substrate as well as on the two halves of the Janus cylinder. We note that, within DA, $\omega_p$ is independent of this particular choice of BCs.

Within the DA, the scaling functions for the critical Casimir force and the corresponding potential can be constructed via suitably adding and subtracting scaling functions for the step geometry, analogous to the case of a sphere as described in detail in Ref. [103]. For the sake of brevity, we focus on the normalized scaling function $\omega_p$ [Eq. (3.17)] of the critical Casimir potential:

$$\begin{aligned}\omega_p(\Lambda, \Pi, \Xi, \alpha, \Theta, \Delta \to 0, \mathscr{L}) = \sum_{n=-\infty}^{\infty} \Big\{ &\omega_{(+|-,-)}\left(\Xi - \tfrac{\mathscr{L}}{2}\sin(\alpha) + n\Pi + \tfrac{\Lambda}{2}, \alpha, \Theta, \Delta \to 0, \tfrac{\mathscr{L}}{2}\right) \\ &-\omega_{(+|-,-)}\left(\Xi + \tfrac{\mathscr{L}}{2}\sin(\alpha) + n\Pi + \tfrac{\Lambda}{2}, \alpha, \Theta, \Delta \to 0, \tfrac{\mathscr{L}}{2}\right) \\ &-\omega_{(+|-,-)}\left(\Xi - \tfrac{\mathscr{L}}{2}\sin(\alpha) + n\Pi - \tfrac{\Lambda}{2}, \alpha, \Theta, \Delta \to 0, \tfrac{\mathscr{L}}{2}\right) \\ &+\omega_{(+|-,-)}\left(\Xi + \tfrac{\mathscr{L}}{2}\sin(\alpha) + n\Pi - \tfrac{\Lambda}{2}, \alpha, \Theta, \Delta \to 0, \tfrac{\mathscr{L}}{2}\right) \Big\}.\end{aligned} \tag{3.18}$$

The sum over $\omega_{(+|-,-)}(\Xi, \alpha, \Theta, \Delta, \mathscr{L})$ (see Refs. [74, 127]) with appropriate combinations of the first scaling variable takes into account all stripes from $x = -\infty$ to $x = \infty$, and considers four contributions to the potential: the half of the Janus particle with $(-)$ BC interacting with stripes of $(+)$ and $(-)$ BCs, and the other half of the Janus cylinder with $(+)$ BC, which also interacts with stripes of $(+)$ and $(-)$ BCs; here we exploit the fact that the potentials for $(+,+)$ and $(-,-)$ BCs are the same.

The resulting scaling function of the potential $\omega_p$ as obtained within the DA $(\Delta \to 0)$ for $d = 3$ and $\Theta = 0$ is shown in Fig. 3.11 for a cylinder of reduced length $\mathscr{L} = 20$ and for a substrate pattern with $L_1 = L_2$ and $P = L/4$, so that $\Pi = 5$ and $\Lambda = 5/2$. According to our analysis above, for these parameters we expect the DA to provide a good estimate for the critical Casimir force.

Within the DA, for a Janus particle located opposite to the center of one stripe, i.e., at $X = 0$, the scaling function $\omega_p$ of the critical Casimir potential comprises terms $\omega_{(+|-,-)}\left(\pm\tilde{\Xi}_{1,2}, \alpha, \Theta, \Delta \to 0, \frac{\mathscr{L}}{2}\right)$, where $\tilde{\Xi}_1 = \frac{\mathscr{L}}{2}\sin(\alpha) + n\Pi + \frac{\Lambda}{2}$ and $\tilde{\Xi}_2 = \frac{\mathscr{L}}{2}\sin(\alpha) + n\Pi - \frac{\Lambda}{2}$. Since the scaling function $\omega_{(+|-,-)}$ is an odd function of $\tilde{\Xi}_{1,2}$ and $n \in \mathbb{Z}$, there are always two terms in the sum in Eq. (3.18) which cancel each other. Therefore, the scaling function $\omega_p$ vanishes for $\Xi = 0$ and thus the critical Casimir potential does not depend on the orientation of the particle as shown by the yellow curve in Fig. 3.11(a). Due to Eqs. (3.12) and (3.17), this corresponds to the potential [Eq. (3.16)] being the

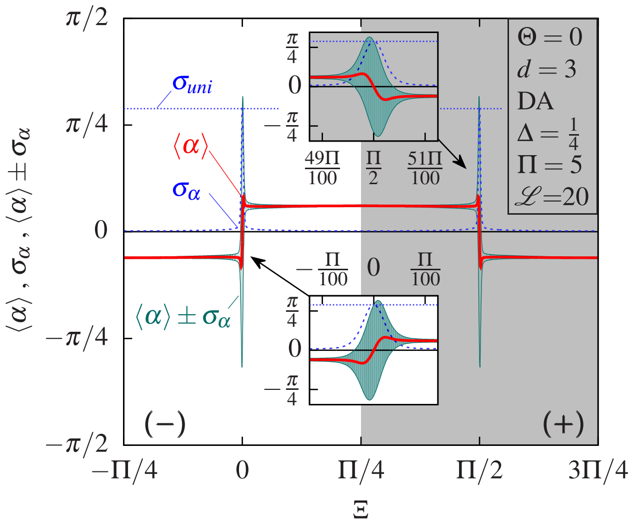

Figure 3.12: Expectation value $\langle\alpha\rangle$ (red curve) and the corresponding standard deviation $\sigma_\alpha$ (blue dashed curve) of the angular probability distribution function $p(\alpha) \propto \exp(-\Phi_p/(k_BT))$ of the same Janus cylinder and for the same parameters as in Fig. 3.11; there the cylinder is centered at $\Xi = \Pi/4$. The dotted blue line denotes the value of the standard deviation $\sigma_{uni}$ of the uniform distribution, up to which, in the present system, $\sigma_\alpha$ grows for specific scaled lateral positions close to $\Xi = m\Pi/2$ with $m \in \mathbb{Z}$. In the insets the green areas are limited by the full green curves $\langle\alpha\rangle \pm \sigma_\alpha$ and visually indicate the areas of the most probable rotation angles $\alpha$ close the lateral positions $\Xi = 0$ and $\Xi = \Pi/2$.

simple average of the potentials of homogeneous cylinders near homogeneous substrates:

$$V_p^{(cs)}(L_1, P, X = 0, \alpha, D, R, L, T) = \left[V_{(+,+)}^{(cs)}(D, R, T) + V_{(+,-)}^{(cs)}(D, R, T)\right]/2. \tag{3.19}$$

However, these positions of the colloid center directly above a stripe center are unstable against lateral shifts, which can be inferred from, e.g., the yellow square in Fig. 3.11(b), where we show the value $\overline{\omega}_p(\Xi)$ of the scaling function $\omega_p$ averaged over the tilt angles $\alpha \in [0, \pi/2]$ (red curve). Therefore $\overline{\omega}_p$ describes the orientationally averaged critical Casimir potential acting on the colloid as a function of its lateral position $X$. The critical Casimir potential becomes minimal for particle positions at the edges of the stripes, e.g., $X = L_1/2 = P/4$, and with an orientation $\alpha > 0$ of the Janus particle such that the overlap of the stripes and of the projected surfaces of the cylinder with equal BCs is maximal, as shown in Fig. 3.11 (a) by the green curve. As a function of $\alpha$ there are also secondary and higher order local minima of the potential, with their number increasing for more elongated particles or thinner stripes. From our analysis we find, depending on the particle length and the stripe periodicity, $\lceil L/(2P)\rceil$ minima, where $\lceil\ldots\rceil$ indicates the ceiling function.

Equation (3.19) is also obtained in the limit $\Pi = P/\sqrt{RD} \to 0$, so that for (infinitely) narrow stripes the angular dependence of the critical Casimir potential disappears. However, we note that for relatively narrow stripes one has to expect significant deviations from the DA due to the increasing interference of the effects of the chemical steps on the order parameter profile across the stripes. Within MFT in Ref. [103] the range of validity of the DA has been assessed for the case of a spherical colloid next to a periodically patterned substrate. Indeed, in Ref. [130] it has been found within a study based both on MC simulations and MFT for the film geometry, that very narrow stripes of alternating $(+)$ and $(-)$ BCs combine to an effective symmetry-preserving Dirichlet $(o)$ BC. Nonetheless, for the relatively large value $\Pi = 5$ as shown in Fig. 3.11, we expect the DA to be reliable.

The critical Casimir potential $V_p^{(cs)}$ provides the angular probability distribution function $p(\alpha) \propto \exp(-\beta V_p^{(cs)})$ characterizing the orientational fluctuations of the cylindrical colloid. Distinct from the case of a *homogeneous* cylinder near a *single* chemical step, for which we have found a preference for either the parallel or the perpendicular orientation, here we observe local minima of the potential (see the green curve in Fig. 3.11). In order to determine both the preferential particle orientation and the degree of orientational order we calculate the moments of the angular probability distribution function as functions of the reduced lateral position $\Pi$ of the center of the cylinder:

$$\langle \alpha^n \rangle = \frac{1}{N} \int\limits_{-\pi/2}^{\pi/2} \mathrm{d}\alpha \; \alpha^n \, e^{-\frac{V_p^{(cs)}}{k_B T}} , \tag{3.20}$$

where the normalization constant is given by $N = \int_{-\pi/2}^{\pi/2} \mathrm{d}\alpha \, \exp\left(-\beta V_p^{(cs)}\right)$. In the following, we employ the usual definitions of the expectation value of $\alpha$ as the first moment $\langle \alpha \rangle$ and the standard deviation of the angular distribution $\sigma_\alpha = \sqrt{\langle \alpha^2 \rangle - \langle \alpha \rangle^2}$. For comparison, the expectation value and the standard deviation of the uniform distribution in the interval $[-\pi/2, \pi/2]$ is $\langle \alpha \rangle_{uni} = 0$ and $\sigma_{uni} = \pi/(2\sqrt{3})$, respectively. These quantities are depicted in Fig. 3.12 for the same parameters and the same geometry as in Fig. 3.11, i.e., for a reduced length $\mathscr{L} = 20$ of the Janus particle and a periodicity $\Pi = 5$ of the stripes. The expectation value $\langle \alpha \rangle$ is shown in red. It is nearly constant for roughly 48% of the first period (i.e., 48% of the range $\Xi \in [-\Pi/4, 3\Pi/4]$) and attains a value $\langle \alpha \rangle \approx 0.191$ ($\langle \alpha \rangle \approx 11^\circ$) at $\Xi = \Pi/4$. This nicely agrees with the calculated location $\alpha = \alpha_0 = 0.192$ of the first minimum as a function of $\alpha$ of the critical Casimir potential at $\Xi = \Pi/4$ and for this particular set of parameters. For $\Xi > \Pi/2$ the resulting graph is the mirror image of that for $0 < \Xi < \Pi/2$. Only within a range of 2% of the interval of the period $\Xi \in [-\Pi/4, 3\Pi/4]$ the expectation value $\langle \alpha \rangle$ deviates noticeably from either $\alpha_0$ or $-\alpha_0$.

In Fig. 3.12 the standard deviation $\sigma_\alpha$ is plotted as a blue dashed line. It turns out to be remarkably small for a broad range of values of $\Xi$, indicating in that range a very narrow angular distribution around the expectation value. However, for positions close to the centers of the stripes, i.e., $\Xi = m\Pi/2$ with $m \in \mathbb{Z}$, the standard deviation increases, in the present system, up to the value of the uniform distribution $\sigma_{uni}$. Consequently, within this 2% range around the centers of the stripes the variation of the expectation value $\langle\alpha\rangle$ does not indicate a change of the orientation but rather a loss of alignment. As a more intuitive visualization, in Fig. 3.12 we also draw $\langle\alpha\rangle \pm \sigma_\alpha$ as full green curves, with the encompassed area shown in light green, indicating the range of the most probable rotation angles $\alpha$. This emphasizes that the Janus particle aligns itself very precisely at a certain angle relative to the pattern, which depends on the stripe width and periodicity, but quite insensitive to the lateral position. Only very close to the center of each stripe the orientation is uniformly distributed. But this is an unstable configuration, as illustrated in Fig. 3.11. When the particle is moved laterally over the pattern by external means, its orientation flips between only two preferred alignments $\pm\alpha_0$.

## 3.5 Conclusions

First, we have calculated the critical Casimir force acting on a single cylindrical Janus particle of type A in the presence of a homogeneous substrate (see Fig. 3.1) both by using the Derjaguin approximation (DA), and by applying mean field theory (MFT), which is valid in $d = 4$ spatial dimensions.

The DA implies a close relation between the critical Casimir forces for distinct geometries. Indeed, a comparison of DA with results from full MFT in $d = 4$ reveals that, in the limit $\Delta = D/R \to 0$ of the ratio of the distance $D$ and radius $R$, the DA holds equally both for the force between a Janus cylinder and a substrate and for the force between a homogeneous cylinder and a substrate with a chemical step (see Fig. 3.2). However, as shown in Fig. 3.3, the MFT scaling functions for the two geometries are distinct for nonzero $\Delta$. This caused us to address the question whether the relation between these two geometries has any merit beyond the limit $\Delta \to 0$ in which DA holds.

The DA makes implicit assumptions about the OP profile based on the one between a homogeneous particle and a homogeneous substrate with opposing BC and at the same temperature. We have have inspected the MFT order parameter profiles shown in Fig. 3.4 and found that the isoline $\phi(\mathbf{r}) = 0$ indeed follows closely the profile for homogeneous surfaces, however it smoothly bends towards the particle or the substrate, which is unaccounted for within DA. An improved model has been introduced by applying the DA for a fictional, scaled colloid in order to incorporate the bending of the isoline into DA by fiat (see Fig. 3.5). The improvement achieved using this relation is demonstrated in Fig. 3.6. Thus, the correspondence between these two configurations holds with some modification also within MFT

The correspondence of Janus particles and chemical steps on a substrate is also relevant for Section 3.2 which discusses the scaling function of the force between a Janus cylinder and a substrate with a chemical step. The MFT scaling function in Fig. 3.7 for a Janus cylinder and a step at a lateral position $X = 0$ is qualitatively similar to the dependence of the scaling function of the force between two patterned substrates on a lateral shift [126].

This configuration reveals a deficiency of DA: For an orthogonal orientation of the Janus particle, i.e., when the Janus equator faces the substrate at $\vartheta = \pm\pi/2$, within DA the scaling function of the force exhibits cusplike extrema of attraction or repulsion as a function of the particle orientation, whereas the MFT results are smooth. However, for $\Delta = 1/5$, i.e., close to the DA limit $\Delta \to 0$, the agreement between DA and full MFT is surprisingly good even for this pathological case (see Fig. 3.7(b)).

In Sec. 3.3, we have revisited the homogeneous cylindrical particle above a chemical step. The anisotropy shape induces a critical Casimir torque acting on the cylindrical particle. From our analysis we have found that this torque can align the colloid parallel or perpendicular to the chemical step, depending on the lateral distance from the step, the combination of BCs of the substrate and the colloid, as well as its aspect ratio (see Fig. 3.8). In order to analyze the degree of orientational order we have investigated the planar nematic order parameter $S$ [Figs. 3.9 and 3.10]. The alignment behavior changes in an intricate matter with length of the cylinder, from rod-like particles to disk-like particles.

We have then considered the type B cylindrical Janus particle. In Sec. 3.4 we have made use of the general expressions for the critical Casimir potential derived within DA in order to study the effective interaction between a cylindrical Janus particle and a chemically striped substrate. The effective potential $V_p^{(cs)}$ [Eq. (3.16)] of the colloid exhibits several maxima and minima depending on the position and the orientation of the particle [Fig. 3.11], so that its preferred axial alignment is rotated relative to the chemical stripes and shifted laterally with respect to the center of the stripes. We have characterized the degree of the orientational order using the standard deviation $\sigma_\alpha$ of the angular probability distribution function, which is surprisingly small except for colloid positions very close to the centers of the chemical stripes. A cylindrical Janus particle located at the center of a chemical stripe can rotate de facto freely; but this is an unstable configuration with respect to the lateral position. The most favorable configuration is achieved when the particle center is positioned at the edge of a stripe and aligned as depicted in Fig. 3.11. For this particle orientation, the degree of orientational order is very high and insensitive to small fluctuations of the particle position (see Fig. 3.12).

In summary, the present analysis shows that upon approaching the critical point of the solvent, elongated colloidal particles can be reversibly aligned in a designed way via minute temperature changes by suitably choosing the geometrical parameters of the setup. Our results provide a means to predict the alignment of homogeneous cylindrical colloids and Janus cylinders near chemically patterned substrates. Previously, it has been demonstrated experimentally that chemically homogeneous spherical colloidal particles can be reversibly trapped above a chemically patterned substrate via critical Casimir interactions in binary liquid mixtures [68–70, 103]. Using a similar setup, cylindrical colloidal particles with homogeneous and Janus surfaces properties may be trapped laterally as well as oriented in a designed way, which can be adjusted by the geometrical parameters of the substrate pattern and minute temperature changes.

# Chapter 4

# Critical Casimir interaction between Janus spheres

Reassured by the result that DA can be used reliably for describing the force acting on a single Janus particle near a substrate, in this chapter we determine the force and the effective potential between two Janus particles.

The case of two cylindrical Janus particles has already been derived before this thesis in earlier work, see Refs. [75, 131]. We only summarize the findings in the interest of the reader, as subsequent work builds upon these results, and we consider it more comprehensible to first introduce a geometry with reduced complexity. Some outlook to spherical Janus particles was already given in Ref. [131]. However, a conclusive analysis of the scaling functions of the force and pair potential between Janus spheres is now provided in this chapter. In view of the experimental interest in such Janus particles, in the following figures we depict the scaling function in $d = 3$. This is accomplished by taking the wall-wall scaling functions $k_{(a,b)}$, which are needed as input for the DA, from Ref. [24], i.e., from numerical simulations in $d = 3$.

## 4.1 Reminder: Janus cylinders

For reasons of simplicity, let us assume the long axes of the two cylinders to be parallel to each other, i.e., the positions and rotations of the cylinders are confined to a plane. This amounts to consider effectively discs in a two-dimensional system but with interactions corresponding to an embedding solvent in $d = 3$.

The scaling form of the critical Casimir force between such two Janus cylinders is given by

$$F^{(cc)}_{\text{◐◐}}(\vartheta_1, \vartheta_2, D, R, T) = k_B T \, \frac{\mathcal{L}}{R^{d-1}} \, \frac{K^{(cc)}_{\text{◐◐}}(\vartheta_1, \vartheta_2, \Delta, \Theta)}{\Delta^{d-1/2}}. \tag{4.1}$$

Within DA, the force $F^{(cc)}_{\text{◐◐}}$ between two Janus cylinders orientated top-to-bottom $[(\vartheta_1, \vartheta_2) =$

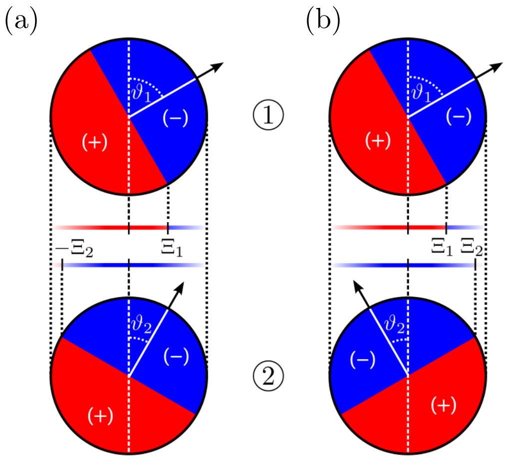

Figure 4.1: Sketch of the geometry for the Derjaguin approximation concerning the force between two Janus cylinders ① and ② for $\vartheta_2 > 0$ in (a) and $\vartheta_2 < 0$ in (b). The cylinder axes are supposed to extend out of the plane of view. The angles $\vartheta_1$ and $\vartheta_2$ of the orientation are relative to the axis connecting the centers of the two particles. All orientations can be mapped onto the principal domain $\vartheta_{1,2} \to \hat{\vartheta}_{1,2} \in [-\pi/2, \pi/2)$. The middle parts show the unrolled surfaces of the Janus cylinders opposing each other. The construction of the DA for two Janus cylinders is akin to the interaction between two structured substrates interacting [126, 132], considering, however, only that portion of the chemical structure which ranges from $-R$ to $+R$, i.e., from $-\Delta^{-1/2}$ to $+\Delta^{-1/2}$ in terms of the scaling variable, and using the appropriate local surface-to-surface distance. In its straightforward version, the DA projects the Janus equators to step positions at $\Xi_{1,2} \equiv \Xi(\vartheta_{1,2}) = \Delta^{-1/2}\cos(\vartheta_{1,2})$. Additionally, depending on $\operatorname{sign}(\vartheta_1\,\vartheta_2)$, either the left or the right edge of the equatorial plane enters into the projection, leading to opposite step positions $\pm\Xi_{1,2}$.

$(0,0)$ and $(\pm\pi,\pm\pi)$], bottom-to-bottom [$(0,\pm\pi)$], or top-to-top [$(\pm\pi,0)$], is identical to the force between two homogeneous cylinders $F^{(cc)}_{(a,b)}$ (see Eq. (A.2) in Appendix A), with $(a,b)$ as the BC of the sides facing each other (compare Fig. 4.1). The scaling function of the force between two Janus cylinders $K^{(cc)}_{◐◐}$ can be expressed relative to the scaling function $K^{(cc)}_{(+,\pm)}$ between two homogeneous cylinders as

$$K^{(cc)}_{◐◐}(\vartheta_1,\vartheta_2,D,R,T) = \begin{cases} K^{(cc)}_{(+,-)}(\Delta,\Theta) + \Delta K^{(cc)}_{\oslash\oslash}(\hat{\vartheta}_1,\hat{\vartheta}_2,\Delta,\Theta), & \text{for } \Xi(\vartheta_1)\,\Xi(\vartheta_2) > 0, \\ K^{(cc)}_{(+,+)}(\Delta,\Theta) - \Delta K^{(cc)}_{\oslash\oslash}(\hat{\vartheta}_1,\hat{\vartheta}_2,\Delta,\Theta), & \text{for } \Xi(\vartheta_1)\,\Xi(\vartheta_2) < 0 \end{cases} \tag{4.2}$$

with $\Xi(\vartheta_i) = \Delta^{-1/2}\cos\vartheta_i$ and where, without loss of generality, reduced angles $\hat{\vartheta}_{1,2} = \vartheta_{1,2} \mp \pi$ such that $\hat{\vartheta}_{1,2} \in [-\pi/2, \pi/2)$ are used. Note that a shift of $\pm\pi$ amounts to reflecting the normals $\mathbf{n}_1$ and $\mathbf{n}_2$ at the corresponding equatorial plane of particle ① and ②, respectively. The subscript of the excess scaling function $\Delta K^{(cc)}_{\oslash\oslash}(\hat{\vartheta}_1,\hat{\vartheta}_2,\Delta,\Theta)$ is not colored in order to emphasize that only the reduced angles enter. The subscript of the forces $K^{(cc)}_{\bullet\bullet} = K^{(cc)}_{(+,-)}$ and $K^{(cc)}_{\bullet\bullet} = K^{(cc)}_{(+,+)}$ between homogeneous particles have been colored in order to visualize the BC.

For homogeneous particles, the limit $\Delta \to 0$ , in which DA holds, can be carried out explicitly. However, in order for the separation in Eq. (4.2) to be consistent, both scaling functions $K^{(cc)}_{(+,\mp)}$ and $\Delta K^{(cc)}_{\oslash\oslash}$ need to retain their dependence on $\Delta$. Nonetheless, the scaling functions within DA are expected to hold only for small but nonzero $\Delta$; keeping the dependence on $\Delta$ is not necessarily a refinement (see Sec. 3.2).

The scaling function $\Delta K^{(cc)}_{\oslash\oslash}$ is constructed from the sum of surface elements as sketched in Fig. 4.1. This is similar to the case of two opposing structured substrates [126, 132], but with the appropriately varying distance between the surface elements. For simplicity, we use the DA projection $\Xi(\vartheta_{1,2}) = \Delta^{-1/2}\cos(\vartheta_{1,2})$, instead of the improved relation discussed in Sec. 3.2. The complete scaling function of the force is found to be given by

$$\Delta K^{(cc)}_{\oslash\oslash}(\vartheta_1, \vartheta_2, \Delta, \Theta) \;=\; \Delta k^{(cc)}(|\Xi(\vartheta_1)|, \Delta, \Theta) + \operatorname{sign}(\vartheta_1\,\vartheta_2)\,\Delta k^{(cc)}(|\Xi(\vartheta_2)|, \Delta, \Theta), \quad (4.3)$$

with a pseudo-step scaling function (compare Eq. (3.4))

$$\Delta k^{(cc)}(\Xi, \Delta, \Theta) = \frac{1}{2}\int_{1+\Xi^2}^{1+\Delta^{-1}} \mathrm{d}\alpha\, \frac{\Delta k(\alpha\Theta)}{\alpha^d\sqrt{\alpha-1}}. \quad (4.4)$$

We point out the similarity between Eqs. (3.9) and (4.3). However, in comparison, the sign-prefactor in Eq. (3.9) is superseded by the imposed restriction $|\cos\vartheta_1| \le |\cos\vartheta_2|$. Moreover, the factor $-\operatorname{sign}(\vartheta_1)$ is replaced by $\operatorname{sign}(\vartheta_1\,\vartheta_2)$; a configuration $\vartheta_1 > 0$ and $\vartheta_2 > 0$ results in a projected step-step configuration with opposite signs for the step positions $\Xi(\vartheta_1)$ and $\Xi(\vartheta_2)$ (see Fig. 4.1(a)), thus, compared to Eq. (3.9), changing the sign of the term. This concise representation of $\Delta K^{(cc)}_{\oslash\oslash}$ in terms of the sign function is possible only for the reduced domain $\hat{\vartheta}_{1,2} \in [-\pi/2, \pi/2)$.

## 4.2 Janus spheres

The effective interaction between parallel, cylindrical Janus particles was conveniently described by only two orientational degrees of freedom $\vartheta_1$ and $\vartheta_2$. While this constrained setup poses an additional experimental challenge, the behavior of spherical colloids can, instead, be studied straightforwardly. Therefore, in the following we determine the scaling function of the force and of the effective potential between two spherical Janus particles, without constraints on the orientation.

We consider a conventional sphere in $d = 3$, for which the Janus characteristics are unambiguous. In $d = 4$, we consider a three-dimensional sphere extended along an extra dimension with a length $L_4$, which is formally called a hyper-cylinder (rather than a hyper-sphere). This definition is distinct from the hyper-cylinder discussed before. In the context of spheres, $\mathcal{L}$ denotes $\mathcal{L} = 1$ in $d = 3$ and $\mathcal{L} = L_4$ in $d = 4$.

### 4.2.1 Scaling function of the force

The force between two Janus spheres depends, in principle, on their orientation vectors $\mathbf{n}_1$ and $\mathbf{n}_2$ and the vector $\mathbf{r}_{12}$ connecting their centers[1]. The force takes the scaling form

$$F^{(ss)}_{\text{◐◐}}(\mathbf{n}_1, \mathbf{n}_2, \mathbf{r}_{12}, R, T) = k_B T \, \frac{\mathcal{L}}{R^{d-2}} \, \frac{K^{(ss)}_{\text{◐◐}}(\mathbf{n}_1, \mathbf{n}_2, \hat{\mathbf{r}}_{12}, \Delta, \Theta)}{\Delta^{d-1}}, \tag{4.5}$$

where for the scaling function, the connecting vector $\mathbf{r}_{12} = (D + 2R)\,\hat{\mathbf{r}}_{12} = R(\Delta + 2)\hat{\mathbf{r}}_{12}$ is expressed in terms of the surface-to-surface distance $D$ along the direction $\hat{\mathbf{r}}_{12} = \mathbf{r}_{12}/|\mathbf{r}_{12}|$. Note that in the case of two spheres, at $T_c$ the force decays as $\Delta^{-(d-1)}$ with distance [29], compared to $\Delta^{-(d-1/2)}$ for the force between two cylinders (see Appendix A and Refs. [75, 77]). Within DA, the force $F^{(ss)}_{\text{◐◐}}$ between two Janus spheres with $\alpha = 0$, orientated top-to-bottom $[(\vartheta_1, \vartheta_2) = (0, 0)$ and $(\pm\pi, \pm\pi)]$, bottom-to-bottom $[(0, \pm\pi)]$, or top-to-top $[(\pm\pi, 0)]$, is identical to the force between two homogeneous spheres $F^{(ss)}_{(a,b)}$ with $(a, b)$ as the BC of the sides facing each other. Thus, we decompose the scaling function $K^{(ss)}_{\text{◐◐}}$ of the force into a part given by the scaling function $K^{(ss)}_{(+,\pm)}$ between two homogeneous spheres [29]

$$K^{(ss)}_{(+,\pm)}(\Delta, \Theta) = \pi \int_1^{1+\Delta^{-1}} \mathrm{d}\alpha \, \alpha^{-d} \, k_{(+,\pm)}\,(\alpha\Theta)\,, \tag{4.6}$$

and an excess scaling function $\Delta K^{(s)}_{\oslash\oslash}$:

$$K^{(ss)}_{\text{◐◐}}(\mathbf{n}_1, \mathbf{n}_2, \hat{\mathbf{r}}_{12}, \Delta, \Theta) = K^{(ss)}_{(+,+)}(\Delta, \Theta) - \Delta K^{(ss)}_{\oslash\oslash}(\mathbf{n}_1, \mathbf{n}_2, \hat{\mathbf{r}}_{12}, \Delta, \Theta). \tag{4.7}$$

This leaves one with the arbitrary choice of whether to relate $\Delta K^{(ss)}_{\oslash\oslash}$ to $K^{(ss)}_{(+,+)}(\Delta, \Theta)$ or $K^{(ss)}_{(+,-)}(\Delta, \Theta)$; we follow the definition in Eq. (4.7). Note that it is not necessary to express $\Delta K^{(ss)}_{\oslash\oslash}$ in terms of reduced angles, because as a spherical coordinate $\vartheta_{1,2} \in [0, \pi]$ is a reduced angle by definition. Again, the uncolored subscript emphasizes invariance with respect to the shift $\vartheta_i \to \vartheta_i \pm \pi$.

Determining completely the excess scaling function $\Delta K^{(ss)}_{\oslash\oslash}$ requires careful considerations of all possible orientations. It turns out that within DA, the force necessarily depends only on the relative coordinates, because the interaction is expressed via the overlap of surface elements projected along the connecting vector $\mathbf{r}_{12}$. This is worked out in detail in Appendix B, using spherical coordinates $\mathbf{n}_1 = (\phi_1, \vartheta_1)$ and $\mathbf{n}_2 = (\phi_2, \vartheta_2)$. Thus the interaction depends only on the polar angles $\vartheta_1$ and $\vartheta_2$, and the dependence on $\phi_1$ and $\phi_2$ reduces to one on the angle difference $\alpha = \phi_2 - \phi_1$ (see Fig. 4.2). For comparison,

---

[1] We only consider orientations of the Janus spheres in $d = 3$ and disregard the possible, but contrived case of orientations in $d = 4$ which would violate the invariance in the extra dimension.

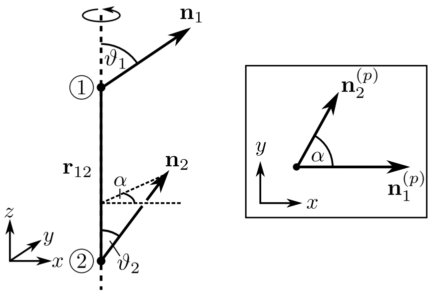

Figure 4.2: Generic sketch of the orientations of the Janus spheres ① and ② defining the azimuthal angle $\alpha = \phi_2 - \phi_1$, and the polar angles $\vartheta_1$ and $\vartheta_2$ of the relative coordinate system which has the z-axis aligned with the vector $\mathbf{r}_{12}$ and orientated such that $\phi_1 = 0$. Left: side view with a slight perspective in order to depict $\alpha$. Right: top view of the same configuration, with $\mathbf{n}_i^{(p)}$ the projection of $\mathbf{n}_i$ onto the xy plane. The DA considers pairs of surface elements projected along $\mathbf{r}_{12}$, thus effectively representing a top-down view. Rotating the frame of reference, so that $\phi_1 \neq 0$ but $\alpha = \phi_2 - \phi_1$ is kept constant, does not affect the interaction in that case.

we briefly consider the pair potential between two point dipoles of strength $\mu$:

$$V^{(\mathrm{dip})} = -\frac{\mu^2}{r_{12}^3}\,\left[3\left(\mathbf{n}_1 \cdot \hat{\mathbf{r}}_{12}\right)\left(\mathbf{n}_2 \cdot \hat{\mathbf{r}}_{12}\right) - \mathbf{n}_1 \cdot \mathbf{n}_2\right] \tag{4.8}$$

Written similarly in the relative coordinate system connecting the two dipoles, these render $\mathbf{n}_i \cdot \mathbf{r}_{12} = \cos\vartheta_i$ and $\mathbf{n}_1 \cdot \mathbf{n}_2 = \cos\vartheta_1 \cos\vartheta_2 + \sin\vartheta_1 \sin\vartheta_2 \cos(\phi_1 - \phi_2)$. Thus, concerning the dependence on the orientations, the critical Casimir interaction between two Janus spheres exhibits the same level of complexity as the dipole-dipole interaction.

Here, we provide the excess scaling function $\Delta K_{\oslash\oslash}^{(ss)}$ as a function of $\vartheta_1$, $\vartheta_2$, and the relative coordinate $\alpha$ (see Appendix B):

$$\begin{aligned}
\Delta K_{\oslash\oslash}^{(ss)}(\alpha, \vartheta_1, \vartheta_2, \Delta, \Theta) = {} & \pi\, H\left((\cos\vartheta_1)(\cos\vartheta_2)\right) \int_1^{1+\Delta^{-1} r_s^2} \mathrm{d}x\, x^{-d}\, \Delta k\,(x\vartheta) \\
& - \operatorname{sign}\left((\cos\vartheta_1)(\cos\vartheta_2)\right) \\
& \times \left[ \int_{1+\Delta^{-1}\cos^2\vartheta_1}^{1+\Delta^{-1} r_s^2} \mathrm{d}x\, \arccos\left( |\cot\vartheta_1| \sqrt{\frac{1}{\Delta(x-1)} - 1} \right) x^{-d}\, \Delta k\,(x\Theta) \right. \\
& \left. + c(\alpha, \vartheta_1, \vartheta_2) \int_{1+\Delta^{-1}\cos^2\vartheta_2}^{1+\Delta^{-1} r_s^2} \mathrm{d}x\, \arccos\left( |\cot\vartheta_2| \sqrt{\frac{1}{\Delta(x-1)} - 1} \right) x^{-d}\, \Delta k\,(x\Theta) \right] \\
& + \alpha \int_{1+\Delta^{-1} r_s^2}^{1+\Delta^{-1}} \mathrm{d}x\, x^{-d}\, \Delta k\,(x\Theta)\,.
\end{aligned} \tag{4.9}$$

Note that one has $\Delta k = k_{(+,+)} - k_{(+,-)} < 0$. The first term with the Heaviside step function $H\left((\cos\vartheta_1)(\cos\vartheta_2)\right)$ as a prefactor effectively switches between the limiting cases of top-to-bottom, bottom-to-bottom or top-to-top. Additionally, $\Delta K_{\oslash\oslash}^{(ss)}$ depends non-trivially on $\alpha, \vartheta_1$, and $\vartheta_2$, inter alia, via the dimensionless radius $r_s = R_s(\alpha, \vartheta_1, \vartheta_2)/R$ (see Eq. (B.8)) of a particular ring of surface elements occurring within DA in the subdivision of the surfaces. The projection of the equatorial steps of both Janus spheres onto a common plane, normal to the axis connecting the colloids, results in two half-ellipses corresponding to each configuration. The surface ring with radius $R_s$ intersects the projections of the equatorial steps of both Janus spheres in a single point. Thus, the scaled radius $r_s$ is defined as $r_s = \sqrt{x^2 + y^2}$, with the intersection point $(x, y)$ of the two ellipses determined by a particular solution of a system of two equations. For details, we refer to Appendix B.

Certain configurations of the two Janus particle give rise to forces which consist of force contributions of the same strength, but of opposite signs. All these cases can be subsumed by Eq. (4.9) via the common prefactor $\operatorname{sign}((\cos\vartheta_1)(\cos\vartheta_2))$ and via the sign picking function $c(\alpha, \vartheta_1, \vartheta_2)$ defined in Eq. (B.10).

The scaling function $K^{(ss)}_{\bullet\bullet}(\alpha, \vartheta_1, \vartheta_2, \Delta, \Theta)$ of the force (see Eqs. (4.7) and (4.9); also Appendix B) is shown in Fig. 4.3 for various configurations with $\alpha = 0$, i.e., $\phi_1 = \phi_2$. In accordance with Fig. 4.2, $\alpha = 0$ implies that the two orientation vectors $\mathbf{n}_1$ and $\mathbf{n}_2$ lie in the same plane, so that the corresponding equatorial planes are rotated with respect to each other ($\vartheta_1 \neq \vartheta_2$), but not tilted. On first sight, the scaling functions of the force for Janus spheres and for Janus cylinders appear to be qualitatively very similar (compare Ref. [75]). Quantitatively, the force between spheres appears to be stronger than the force between parallel cylinders. However, one has to take into account that the force between two Janus cylinders is proportional to their length. A fair comparison of the strengths of the forces requires to consider a cylinder length which is comparable with the size of the sphere, i.e., $L \approx 2R$. In this case the force between two parallel cylinders is stronger. Additionally, the scaling function for Janus spheres decays slightly faster as function of $\Theta$. Generally, the scaling function of the force between two Janus spheres is slightly more sensitive to small rotations of one particle than the one for cylinders.

### 4.2.2 Scaling function of the effective potential

As stated in Eq. (2.20), the effective potential between two Janus spheres of radius $R$ can be determined from the critical Casimir force in the relative coordinate system according to

$$V^{(ss)}_{\bullet\bullet}(\mathbf{n}_1, \mathbf{n}_2, \mathbf{r}_{12} = (D + 2R)\mathbf{e}_z, R, T) = \int_D^\infty \mathrm{d}z\, F^{(ss)}_{\bullet\bullet}(\mathbf{n}_1, \mathbf{n}_2, \mathbf{r}_{12} = (z + 2R)\mathbf{e}_z, R, T). \tag{4.10}$$

After inserting Eq. (4.5), this can be cast into the scaling form

$$V^{(ss)}_{\bullet\bullet}(\mathbf{n}_1, \mathbf{n}_2, \mathbf{r}_{12} = (D + 2R)\mathbf{e}_z, R, T) = k_B T\, \frac{\mathcal{L}}{R^{d-3}}\, \frac{\Phi^{(ss)}_{\bullet\bullet}(\alpha, \vartheta_1, \vartheta_2, \Delta, \Theta)}{\Delta^{d-2}}. \tag{4.11}$$

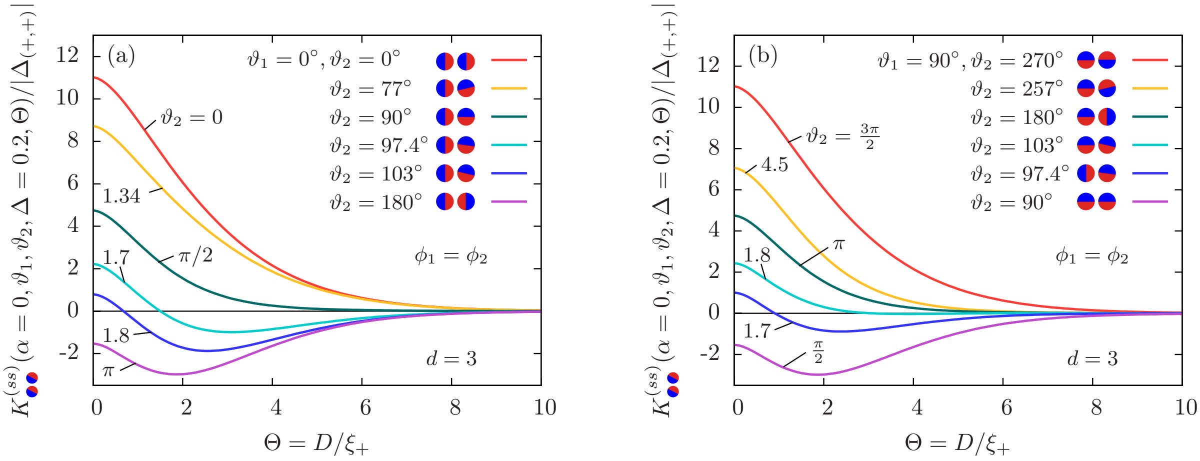

Figure 4.3: The normalized scaling function of the force $K^{(ss)}_{\bullet\bullet}$ between two Janus spheres within DA in $d = 3$, as a function of $\Theta = D/\xi_+$ for several orientations. (a) Configurations with $\vartheta_1 = 0$ for the orientation of the left particle ① for various orientation angles $\vartheta_2$ of the right particle ②, as visualized in the legend. (b) The case of $\vartheta_1 = \pi/2$ for various orientations $\vartheta_2$ of the second particle. In order to provide a simple initial view on the scaling function, the azimuthal angle $\alpha$ is set to $\alpha = 0$, i.e., $\phi_1 = \phi_2$, which restricts the orientation vectors $\mathbf{n}_1$ and $\mathbf{n}_2$ to lie in a common plane.

Following Eq. (4.7), the scaling function $\Phi^{(ss)}_{\bullet\bullet}$ of the potential is divided up into the two contributions

$$\Phi^{(ss)}_{\bullet\bullet}(\alpha, \vartheta_1, \vartheta_2, \Delta, \Theta) = \Phi^{(ss)}_{(+,+)}(\Delta, \Theta) - \Delta\Phi^{(ss)}_{\oslash\oslash}(\alpha, \vartheta_1, \vartheta_2, \Delta, \Theta), \tag{4.12}$$

where

$$\begin{aligned}\Phi^{(ss)}_{(+,\pm)}(\Delta, \Theta) =& \pi \int_1^\infty \mathrm{d}x\,(x-1)x^{-d}\,k_{(+,\pm)}(x\,\Theta)\\ &- \pi \int_{1+\Delta^{-1}}^\infty \mathrm{d}x\,(x - 1 - \Delta^{-1})\,x^{-d}\,k_{(+,\pm)}(x\,\Theta)\end{aligned} \tag{4.13}$$

is the scaling function of the potential between two homogeneous spheres, and $\Delta\Phi^{(ss)}_{\oslash\oslash}$ is the Janus-induced excess scaling function. In view of the known expression for $\Phi^{(ss)}_{(+,\pm)}(\Delta \to 0, \Theta)$ [29, 35], we again retain the explicit dependence on $\Delta$ in the scaling function of the homogeneous case for reasons of consistency with the orientation dependent excess scaling function in Eq. (4.12). The previous caveats regarding the dependence on $\Delta$ within DA apply here, too.

Upon inserting the scaling function $K^{(ss)}_{\bullet\bullet}$ of the force into Eqs. (4.10)-(4.13), the excess scaling function of the potential is given by (see Appendix B.2)

$$\begin{aligned}\Delta\Phi^{(ss)}_{\oslash\oslash}(\alpha,\vartheta_1,\vartheta_2,\Delta,\Theta) =&\pi\, H\left((\cos\vartheta_1)\,(\cos\vartheta_2)\right)\Delta u^{(ss)}(r_s^2,0,\Delta,\Theta)\\ &-\operatorname{sign}\left((\cos\vartheta_1)\,(\cos\vartheta_2)\right)\Big[\Delta v^{(ss)}(r_s^2,\vartheta_1,\Delta,\Theta)\\ &\qquad\qquad\qquad + c(\alpha,\vartheta_1,\vartheta_2)\Delta v^{(ss)}(r_s^2,\vartheta_2,\Delta,\Theta)\Big]\\ &+\alpha\,\Delta u^{(ss)}(1,r_s^2,\Delta,\Theta)\end{aligned} \tag{4.14}$$

with $c(\alpha,\vartheta_1,\vartheta_2)$ defined by Eq. (B.10) and where

$$\begin{aligned}\Delta u^{(ss)}(a,b,\Delta,\Theta) =& \int_{1+b/\Delta}^{\infty} \mathrm{d}y\,(y-1-b/\Delta)\,y^{-d}\Delta k(y\,\Theta)\\ &-\int_{1+a/\Delta}^{\infty}\mathrm{d}y\,(y-1-a/\Delta)\,y^{-d}\Delta k(y\,\Theta)\end{aligned} \tag{4.15}$$

and (see Eq. (B.8) concerning $r_s$)

$$\begin{aligned}\Delta v^{(ss)}(r_s^2,\vartheta,\Delta,\Theta) =&\Delta^{-1}\int_{1+\cos^2\vartheta/\Delta}^{1+r_s^2/\Delta}\mathrm{d}y\, g\big(\Delta(y-1),\vartheta\big)\,y^{-d}\,\Delta k\left(y\,\Theta\right)\\ &+\Delta^{-1}\int_{1+r_s^2/\Delta}^{\infty}\mathrm{d}y\, g(r_s^2,\vartheta)\,y^{-d}\,\Delta k\left(y\,\Theta\right)\end{aligned} \tag{4.16}$$

are excess scaling functions of Janus spheres (vaguely analogous to the chemical step-like scaling functions for Janus cylinders). The integrand of the latter scaling function $\Delta v^{(ss)}$ contains a geometry specific expression

$$\begin{aligned}g(u,\vartheta) &= \int_{\cos^2\vartheta}^{u}\mathrm{d}w\ \arccos\left(|\cot\vartheta|\sqrt{\frac{1}{w}-1}\right)\\ &= u\arccos\left(|\cot\vartheta|\sqrt{\frac{1}{u}-1}\right) - |\cos\vartheta|\arccos\left(|\csc\vartheta|\sqrt{1-u}\right),\ \ \cos^2\vartheta\le u.\end{aligned} \tag{4.17}$$

The free energy landscape of the scaling function $\Phi^{(ss)}_{\oslash\oslash}$ of the pair potential between two Janus spheres can be presented in a single plot only as a function of two variables, but not for the full set $\alpha,\vartheta_1,\vartheta_2$ of three variables. Accordingly, in Fig. 4.4 we choose to show the scaling function of the pair potential between Janus spheres for the two values $\alpha=0$ and $\alpha=\pi$. For $\alpha=0$, in the range $\vartheta_1>0$ the scaling function of the potential is qualitatively very similar to the one for cylinders (see Ref. [75] for a detailed comparison). On the other hand, for Janus spheres, the case of $\alpha=\pi$ in Fig. 4.4 is similar to the one of $\vartheta_1<0$ for Janus cylinders. Obviously, in spherical coordinates an orientation vector with $\alpha=\pi$ and $\vartheta_1\in[0,\pi]$ lies in the same plane as an orientation vector with $\alpha=0$, and can be mapped to a cylindrical angle $\vartheta_1\in[-\pi,0]$. The scaling function of

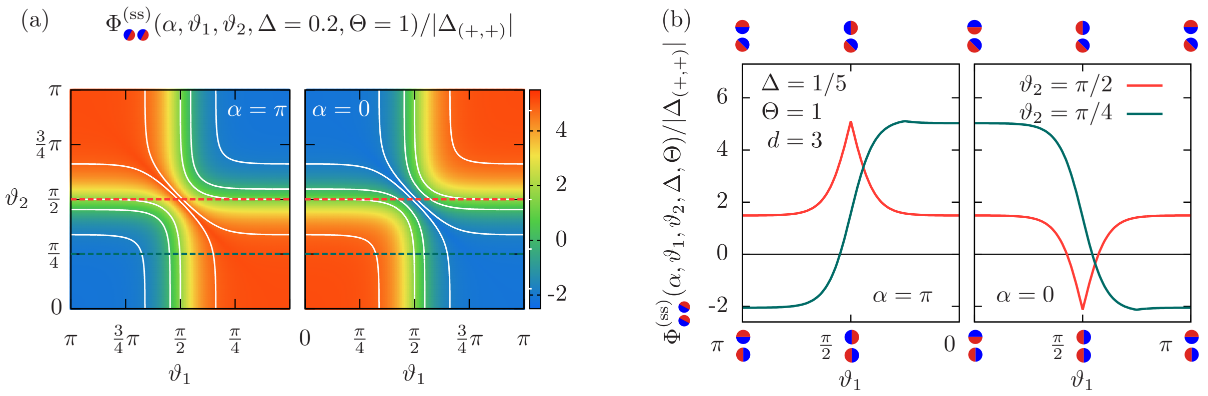

Figure 4.4: The scaling function $\Phi^{(ss)}$ of the effective pair potential between two Janus spheres in $d=3$ for $\alpha=\pi$ and $\alpha=0$ presented (a) as a free energy landscape in terms of $\vartheta_1$ and $\vartheta_2$ for a fixed scaled temperature $\Theta=1$, and (b) as a function of $\vartheta_1$ along the two paths $\vartheta_2=\pi/2$ (red dashed line) and $\vartheta_2=\pi/4$ (green dashed line). At the top of the panel, the geometric configurations indicate those which correspond to points of the green curve; configurations corresponding to the red curve are indicated at the bottom. Note that for $\alpha=\pi$ in (a) and (b) the horizontal axes are inverted in order to emphasize the geometric correspondence of $\alpha=\pi$ and $\vartheta_1>0$ in spherical coordinates to $\vartheta_1<0$ in cylindrical coordinates. An increase of $\alpha$ affects the potential only within a limited angular range around $\vartheta_1=\vartheta_2=\pi/2$, changing the potential in that range from being attractive ($\alpha=0$) to being repulsive ($\alpha=\pi$). This means that upon increasing $\alpha$ the potential gradually develops a potential barrier (see the red curve in (b)).

the pair potential between Janus spheres is also dominated by the attractive minima and the repulsive plateaus of interaction (Fig. 4.4(a)). The variation of the relative azimuthal angle $\alpha$ affects the potential only locally around $\vartheta_1=\vartheta_2=\pi/2$. Upon increasing $\alpha$, the potential energy smoothly changes from having the potential minima connected by a valley to having the plateaus bridged.

With the scaling function of the potential at our disposal, inter alia we are able to elucidate a certain experimental aspect. A general issue concerning experimental studies of colloidal aggregation consists of the influence of the unavoidable presence of a substrate. It can be used deliberately, e.g., for the gravity induced formation of a monolayer of homogeneous particles on the bottom wall of the sample. Experimentally, the particles can be prevented from sticking to the substrate by applying a surface treatment of the substrate such that it becomes repulsive at small distances between the particles and the wall. For Janus particles, the experimental situation can be more intricate. Typically, the interaction with the wall is biased towards favoring one side of the colloid over the other. If the attractive interaction with the wall dominates over the inter-particle interaction (or similarly, if the substrate is repulsive towards only one of the two sides of the Janus particle), a scenario can prevail according to which all Janus particles orientate with one and the same side towards the substrate.

Within this line of reasoning, let us suppose that the interaction with the substrate

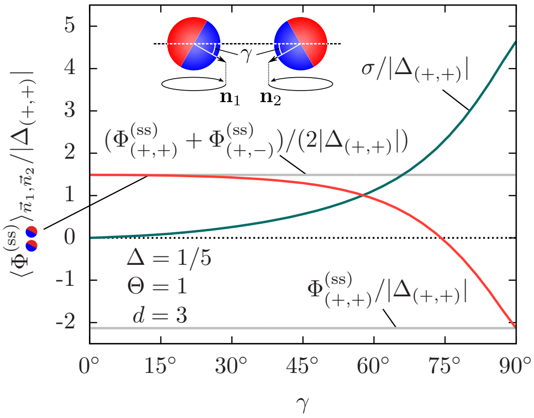

Figure 4.5: Angularly averaged and normalized scaling function $\Phi^{(ss)}_{\bullet\bullet}$ of the effective pair potential for two Janus particles, which are considered to be at equal height above a substrate (not depicted), but far enough so that the influence of the substrate is weaker than that of the pair interaction between the particles. The orientations $\mathbf{n}_1$ and $\mathbf{n}_2$ are tilted by a common angle $\gamma$ towards the substrate and out of the plane which contains both particles centers and is parallel to the substrate. However, the influence of the substrate is taken to be isotropic in the remaining lateral directions. This is supposed to mimic a typical experimental setup. Thus, we consider the average $\langle \Phi^{(ss)}_{\bullet\bullet} \rangle$ taken over $\mathbf{n}_1$ and $\mathbf{n}_2$ (see the main text), such that the tips of $\mathbf{n}_1$ and $\mathbf{n}_2$ form circles lying in a common plane parallel to the substrate surface (see the inset). The influence of the externally imposed tilt $\gamma$ on the effective pair potential is visualized by the dependence on $\gamma$ of the averaged scaling function $\langle \Phi^{(ss)}_{\bullet\bullet} \rangle$ (red curve) and its standard deviation $\sigma$ with respect to the scaling function for $\gamma = 0$ (green curve; see the main text). For $\gamma \to 0$ the average approaches the simple mean $(\Phi^{(ss)}_{(+,+)} + \Phi^{(ss)}_{(+,-)})/2$ of attraction and repulsion of homogeneous spheres (upper gray curve). For $\gamma = 90°$ the Janus equators are tilted such that they are parallel to the substrate and thus unaffected by rotations around the normal of the substrate, leading to an average $\Phi^{(ss)}_{(+,+)}$ (lower gray curve). All quantities are normalized by $|\Delta_{(+,+)}|$.

has been reduced substantially, but is still present, resulting in a small biased tilt of all Janus particles relative to the substrate normal. Depending on the setup, this tilt might be barely noticeable, but would still affect the experimental determination of the effective pair potential between the particles.

In Fig. 4.5, we show the scaling function of the effective potential between two Janus spheres, which are tilted by a common angle $\gamma$ relative to the axis connecting the centers of the two particles, due to the effects of a hypothetical substrate below the particles and parallel to the axis. Within this model, the horizontal components of the orientations $\mathbf{n}_1$ and $\mathbf{n}_2$ of the two Janus spheres are distributed isotropically in a plane parallel to the substrate; but the tilt $\gamma$ is fixed to a given value, corresponding to an equilibrium configuration of the Janus colloids relative to the substrate. Thus, the tips of $\mathbf{n}_1$ and $\mathbf{n}_2$ fluctuate on circles in a plane parallel to the substrate. Note that for $\gamma > 0$ a rotation of the whole configuration around the normal of the plane corresponds to a non-trivial trajectory in the three-dimensional space of the relative spherical coordinates $\alpha, \vartheta_1, \vartheta_2$, so that determining the average $\langle \Phi^{(ss)}_{\oslash\oslash} \rangle$ requires knowledge of the full scaling function of the potential. Due to problems associated with the multivalued nature of the transformation functions, we refrain from providing an explicit parametrization of the orientations $\mathbf{n}_1$ and $\mathbf{n}_2$ in terms of the new coordinates which would include $\gamma$. Instead, for a fixed value of the tilt angle $\gamma$, we evaluate the scaling function $\Phi^{(ss)}_{◐◐}$ numerically on a discretized set of $64 \times 64$ orientations $\mathbf{n}_1$ and $\mathbf{n}_2$, each of them describing a circular path on the unit sphere. The set is expressed in terms of Cartesian coordinates and then transformed into spherical coordinates determining $\alpha, \vartheta_1$, and $\vartheta_2$.[2] The average $\langle \Phi^{(ss)}_{◐◐}(\alpha, \vartheta_1, \vartheta_2) \rangle_{\mathbf{n}_1,\mathbf{n}_2}$ of the scaling function $\Phi^{(ss)}_{◐◐}$ of the effective potential, i.e., the arithmetic mean of the data set, is plotted as a function of the tilt angle $\gamma$, together with the standard deviation $\sigma = \sqrt{\left\langle \left( \Phi^{(ss)}_{◐◐} - \langle \Phi^{(ss)}_{◐◐} \rangle_{\gamma=0} \right)^2 \right\rangle}$ relative to the averaged scaling function for $\gamma = 0$. For $\gamma = 0$, the average is taken such that both $\mathbf{n}_1$ and $\mathbf{n}_2$ describe a great circle on each sphere. They can be parameterized unambiguously by the relative coordinates $\alpha = 0$, $0 \leq \vartheta_{1,2} \leq \pi$, and $\alpha = \pi$, $0 < \vartheta_{1,2} < \pi$ (i.e., both free energy landscapes shown in Fig. 4.4(a) enter into the mean value), resulting within DA in the average $\left( \Phi^{(ss)}_{(+,+)} + \Phi^{(ss)}_{(+,-)} \right)/2$ due to the symmetry of the potential.

The presence of a planar substrate effectively leads to a tilt $\gamma > 0$. In the extreme case of a strongly dominant substrate force, a tilt of $\gamma = 90°$ towards the substrate rotates the two Janus equators into a configuration in which both of them are parallel to the substrate surface. In this case, the rotation around the normal of the substrate does not affect the pair interaction, so that always equal boundary conditions face each other. Accordingly, within DA, the average is simply given by $\Phi^{(ss)}_{(+,+)}$. Figure 4.5 tells that even intermediate tilt angles $\gamma$ do not alter the effective interaction drastically. Up to $\gamma \approx 30°$ the mean value and the standard deviation remain rather constant and small, respectively. The deviations become significant only above $\gamma \approx 45°$, which can be expected to be an experimentally detectable tilt. For smaller angles $\gamma$, ignoring the tilt entirely turns out to be a safe approximation.

The weak influence of small tilt angles on the appearance of the effective pair potential is associated with the flat plateaus in the energy landscape of the scaling function of the potential (see, e.g., Fig. 4.4(a)). However, the proper average takes fully into account the trough- and ridge-like extrema occurring for orthogonal orientations (see, e.g., Fig. 4.4(b)). This shows that the critical Casimir interaction is not only rather insensitive to small tilts for specific configurations, but even for a statistical ensemble of orientations.

---

[2] Although the transformation $(x, y, z) \to (\alpha, \vartheta_1, \vartheta_2)$ also involves inverse trigonometric functions, which are multivalued within the principal domains $\alpha \in [0, 2\pi)$ and $\vartheta_i \in [0, \pi]$ the only points which give rise to ambiguities are the "north" and "south" pole at $\vartheta_i = 0$ and $\vartheta_i = \pi$, for which the value of $\alpha$ is completely arbitrary. However, for tilt angles $\gamma > 0$ these poles do not lie on the circular paths of $\mathbf{n}_1$ and $\mathbf{n}_2$ and therefore are avoidable by this transformation.

However, experimentally observed aggregation structures may be driven by additional effects not captured by the DA-based effective pair potential, such as the occurrence of order parameter bridges between the particles (see chapter 5 and Ref. [77]). Thus, the aggregation of Janus particles into a complex spatial structure should still be analyzed carefully by taking into account the relevance of substrate induced tilting beyond the DA.

## 4.3 Comparison with other model potentials

Here, we compare two well-known model interactions in their ability to render correctly the properties of the critical Casimir interaction between Janus spheres. The Kern-Frenkel model (KF) [133] for patchy particles has been used before to explain qualitatively the interaction between Janus particles (e.g., [57,134–138]), even under the critical Casimir effect [71]. However, note that in Ref. [71], the two sides of the particles are both hydrophilic, but to different degrees, in contrast to our description of a hydrophilic/hydrophobic chemical step on the particle, and thus lacking the strong repulsive forces present for our Janus particles. The KF model is well-studied and successful, yet rather simple and intuitive, so that it is imperative to study whether it is already well-suited to describe the full critical Casimir interaction. A large benefit of the KF model is that it provides unambiguous definitions for the range of the interaction, the interaction strength, and the patch-size. Note that the interaction range of the critical Casimir effect grows with increasing correlation length $\xi(t \to 0)$ as a function of the reduced temperature $t = (T - T_c)/T_c$ and diverges at $T_c$. Simultaneously, the amplitude of the interaction, given by a scaling function, increases non-monotonically towards $T \to T_c$. In the spirit of the 'law of corresponding states' [121,139], for comparison we will define the corresponding range and patch-size of the critical Casimir interaction in terms of the KF parameters such that both interaction yield the same second virial coefficient.

As illustrated in Appendix B, we may exchange the language of the problem, and decide to call the blue side 'north' and the red side 'south', without change to the physical interaction itself. Having this directionality, we can fully replace the information about the BC of the Janus particles with a vector from south to north. Thus, we may arbitrarily reformulate the critical Casimir interaction between Janus particles as one between hard spheres with some *special* dipole moment embedded. The pair potential between two dipoles decays as $\sim 1/r^3$ (see Eq. (4.8)), which is different from the decay $\sim 1/(r - 2R)$ of the critical Casimir interaction between spheres at $T = T_c$. Nonetheless, employing methods valid for the dipole-dipole interaction for the critical Casimir interaction may be more appropriate than a model that can only capture interactions of finite range such as the KF. Regarding the orientation dependence, the two model potentials are quite distinct, as sketched in Fig. 4.6, with the KF model being very sharp in contrast to the smooth dipole-dipole potential. The aim of the proposed model potentials is to reproduce the

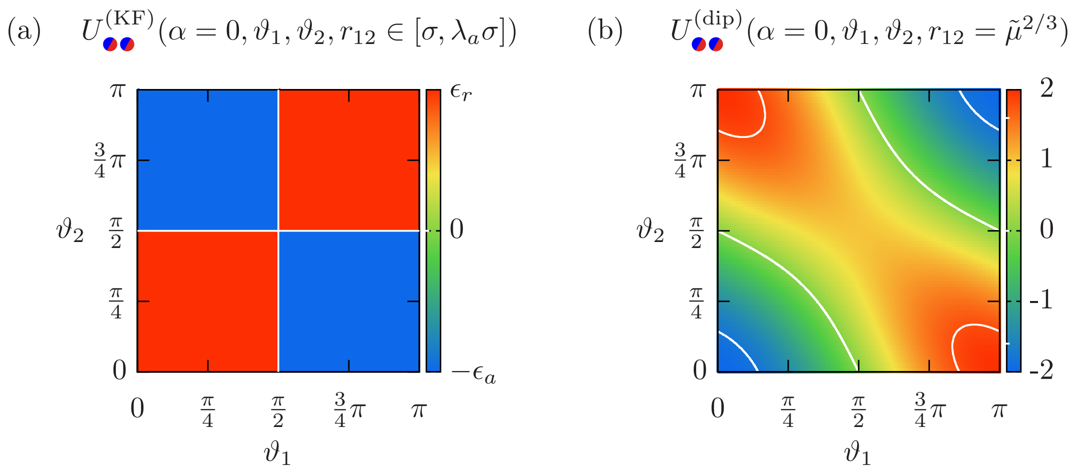
(a) $U^{(\mathrm{KF})}_{\bullet\bullet}(\alpha = 0, \vartheta_1, \vartheta_2, r_{12} \in [\sigma, \lambda_a \sigma])$ (b) $U^{(\mathrm{dip})}_{\bullet\bullet}(\alpha = 0, \vartheta_1, \vartheta_2, r_{12} = \tilde{\mu}^{2/3})$

Figure 4.6: Schematic pair potentials for (a) the *modified* Kern-Frenkel model with a half-opening angle at the maximum $\delta = 90°$, and (b) the dipole-dipole interaction (Eq. (4.8)) at fixed distance and temperature, plotted as an energy landscape for the orientations $\vartheta_1$ and $\vartheta_2$ analogously to Fig. 4.4.

angular dependence of the critical Casimir potential for fixed distance and temperature, i.e., the energy landscape shown in Fig. 4.4. Therefore, we will explore the distinctive features of the critical Casimir interaction between Janus spheres in terms of the Kern-Frenkel model as well as using methods established for the dipole-dipole interaction.

Generally, the dependence on the particle orientations is most conveniently expressed for all interaction types in the relative coordinate system where the $z$ axis points along the vector connecting the two particle centers, i.e., $\mathbf{r}_{12} = (D + 2R)\mathbf{e}_z$, where $D$ is the surface-to-surface distance and $R$ is the radius of the Janus spheres. The dependence on the orientations $\mathbf{n}_1 = (\phi_1, \vartheta_1)$ and $\mathbf{n}_2 = (\phi_2, \vartheta_2)$ relative to the connecting axis reduces to a dependence on the azimuthal angle $\alpha = \phi_2 - \phi_1$ and the polar angles $\vartheta_1$ and $\vartheta_2$. In this section, the alternatively scaled temperature $\Theta^* = R/\xi = \Theta/\Delta$ will be used in order to discuss the distance and temperature dependence of the critical Casimir potential separately, and we will only consider the case $d = 3$.

For a purposeful model that can be adopted to describe an experimental realization, we will make use of three variations of the effective pair potential (Eq. (2.41)):

$$U^{(\mathrm{Cas})}_{\bullet\bullet}(\mathbf{n}_1, \mathbf{n}_2, \mathbf{r}_{12}, R, T) = U^{(\mathrm{el})}_{\mathrm{rep}}(D) + \frac{R}{D}\,\Phi^{(ss)}_{\bullet\bullet}(\alpha, \vartheta_1, \vartheta_2, \Delta \to 0, \Theta^*\Delta), \tag{4.18}$$

$$U^{(\mathrm{Cas})}_{\mathrm{attr}}(D, R, T) = U^{(\mathrm{el})}_{\mathrm{rep}}(D) + \frac{R}{D}\,\Phi^{(ss)}_{(+,+)}(\Delta \to 0, \Theta^*\Delta), \tag{4.19}$$

$$U^{(\mathrm{Cas})}_{\mathrm{rep}}(D, R, T) = U^{(\mathrm{el})}_{\mathrm{rep}}(D) + \frac{R}{D}\,\Phi^{(ss)}_{(+,-)}(\Delta \to 0, \Theta^*\Delta). \tag{4.20}$$

### 4.3.1 Kern-Frenkel model

In order to capture the basic properties of the critical Casimir interaction between the considered Janus particles, we require a *modified* Kern-Frenkel model, such that

$$U^{(\mathrm{KF})}_{\text{◐◐}}(\mathbf{n}_1,\mathbf{n}_2,\mathbf{r}_{12}) = \begin{cases} U^{(\mathrm{KF})}_{\mathrm{attr}}(r_{12}) & \begin{array}{l}\text{if } \mathbf{n}_1\cdot\mathbf{r}_{12} > \cos\delta \ \wedge -\mathbf{n}_2\cdot\mathbf{r}_{12} > \cos\delta, \\ \text{or } \ -\mathbf{n}_1\cdot\mathbf{r}_{12} > \cos\delta \ \wedge \mathbf{n}_2\cdot\mathbf{r}_{12} > \cos\delta,\end{array} \\ U^{(\mathrm{KF})}_{\mathrm{rep}}(r_{12}) & \text{otherwise,} \end{cases} \tag{4.21}$$

where

$$U^{(\mathrm{KF})}_{\mathrm{attr}}(r_{12}) = \begin{cases} \infty & r_{12} \le \sigma, \\ -\epsilon_a & \sigma < r_{12} \le \lambda_a\sigma, \\ 0 & r_{12} > \lambda_a\sigma \end{cases} \tag{4.22}$$

is a square-well potential with range $\lambda_a$ and depth $\epsilon_a$; otherwise

$$U^{(\mathrm{KF})}_{\mathrm{rep}}(r_{12}) = \begin{cases} \infty & r_{12} \le \sigma, \\ \epsilon_r & \sigma < r_{12} \le \lambda_r\sigma, \\ 0 & r_{12} > \lambda_r\sigma \end{cases} \tag{4.23}$$

is a square-shoulder potential with range $\lambda_r$ and strength $\epsilon_r$. Note how this specifically models particles carrying two patches (A and B) at opposite sides with the same half-opening angle $\delta$, resulting in the energy landscape shown in Fig. 4.6(a). The patches are attractive to the same kind on another particle (A-A, B-B), but repulsive for the other type (A-B, B-A). This is in contrast to the conventional case for the KF model of a one-patch particle without repulsion, i.e., $U^{(\mathrm{KF})}_{\mathrm{rep}} = 0$ (see, e.g., Refs [57, 134–138]). For the attractive part $U^{(\mathrm{KF})}_{\mathrm{attr}}$, the depth of the square-well $\epsilon_a$ is chosen to be the same as the minimum $U_{min}$ of the critical Casimir potential between homogeneous spheres, see section 2.2.3. As will be shown below, it is usually sufficient to set the strength $\epsilon_r$ of the repulsion to some large value.

Within the KF model, the second virial coefficient (Eq. (2.42) with $U(r) \to U^{(\mathrm{el})}_{\mathrm{rep}} + U^{(\mathrm{KF})}_{\text{◐◐}}$) can be evaluated analytically, which carries over to our *modified* Kern-Frenkel. However, it is insightful to first consider only the purely attractive square-well interaction $U^{(\mathrm{KF})}_{\mathrm{attr}}$ with no dependence on the orientation. In this case, the second virial coefficient $B_2^{(\mathrm{attr})}$ is given by

$$\frac{B_2^{(\mathrm{attr})}}{B_2^{(\mathrm{hc})}} = 1 - (\lambda_a^3 - 1)(e^{\epsilon_a} - 1), \tag{4.24}$$

where $B_2^{(\mathrm{hc})} = \frac{2}{3}\pi\sigma_{\mathrm{eff}}^3$ is the second virial coefficient of the (effective) hard-core part due to the excluded volume.

Similarly, the purely repulsive square-shoulder interaction $U^{(\mathrm{KF})}_{\mathrm{rep}}$ would lead to a second

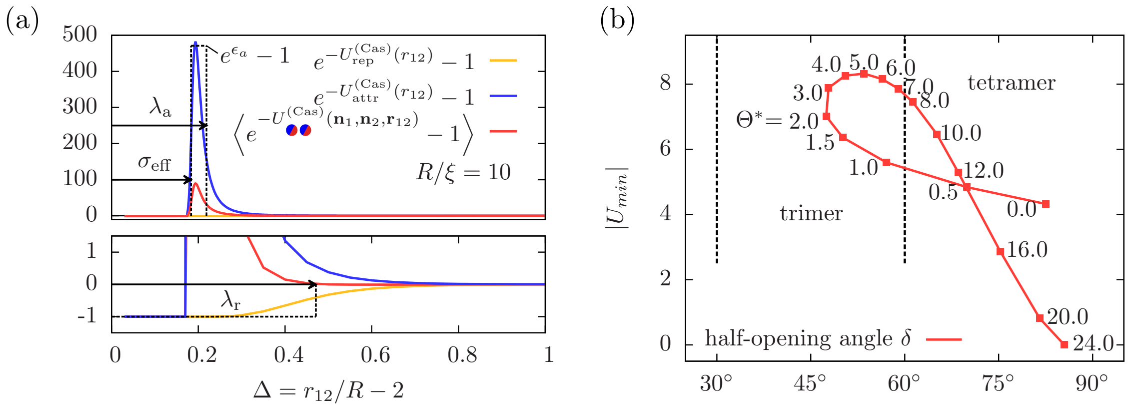

Figure 4.7: (a) Visualization of the parameters of the *modified* Kern-Frenkel model used to reproduce the critical Casimir potential between Janus spheres with an exemplary, short-ranged electrostatic repulsion. (b) Effective patch size of spherical Janus particles in the *modified* Kern-Frenkel model obtained for $A = 160$ and $\kappa R = 25$ along a thermodynamic path $\Theta^* \to 0$ approaching the critical point. With *tetramer* we indicate the region of the phase diagram in which the attractive patches are geometrically large enough to allow for a configuration with "bonds" to three neighboring particles. Similarly, in the *trimer* region, only two neighbor bonds fit inside the solid angle of the patch.

virial coefficient

$$\frac{B_2^{(\mathrm{rep})}}{B_2^{(\mathrm{hc})}} = 1-(\lambda_r^3-1)(e^{-\epsilon_r}-1) \approx \lambda_r^3 \quad \text{for } \epsilon_r \gg 1, \tag{4.25}$$
$$\text{i.e., } B_2^{(\mathrm{rep})} = \lambda_r^3\, B_2^{(\mathrm{hc})} = \frac{2}{3}\pi(\lambda_r\sigma_{\mathrm{eff}})^3.$$

Thus, for sufficiently large shoulder strength $\epsilon_r$, $B_2^{(\mathrm{rep})}$ amounts to an enlarged, effective excluded volume of diameter $\lambda_r\,\sigma_{\mathrm{eff}}$.

Clearly, the reduced second virial coefficient $B_2^* = B_2/B_2^{(\mathrm{hc})}$ of the full *modified* Kern-Frenkel model will contain a mixture of the contributions that amounted to $B_2^{(\mathrm{attr})}$ and $B_2^{(\mathrm{rep})}$. Based on the conditions in Eq. (4.21), this can be written using the coverage parameter $\chi = (1-\cos\delta)/2$ of the one-patch model, so that

$$B_2^* = 1-2\chi^2(\lambda_a^3-1)(e^{\epsilon_a}-1)+(1-2\chi^2)(\lambda_r^3-1). \tag{4.26}$$

Note that $2\chi^2$ is the fraction of attractive configurations, with the factor 2 because of the two attractive patch combinations A-A and B-B, and $1-2\chi^2$ is consequently the fraction of repulsive configurations.

These relation allow us to establish successively the parameters $\epsilon_a, \lambda_a, \lambda_r$ and $\chi$ of the *modified* Kern-Frenkel model corresponding to the critical Casimir interaction for a given temperature $\Theta^*$: $\epsilon_a$ is chosen to be the same as the potential minimum $U_{min}$ of effective potential in Eq. (4.19). The interaction range $l_a$ is then chosen such that $B_2^{(\mathrm{attr})}$ corresponds to the value calculated based on Eq. (2.42) for $U(r) \to U_{\mathrm{attr}}^{(\mathrm{Cas})}$. Similarly, the interaction range of the repulsion $l_r$ is chosen to yield for $B_2^{(\mathrm{rep})}$ the same value as Eq. (2.42) but with $U(r) \to U_{\mathrm{rep}}^{(\mathrm{Cas})}$. Lastly, $\chi$ can be fixed to yield the same reduced second virial coefficient $B_2^*$ using $U_{\bullet\bullet}^{(\mathrm{Cas})}$, with $\Phi_{\bullet\bullet}^{(ss)}$ from Eq. (4.11)). These parameters are visualized in Fig. 4.7(a) for an exemplary electrostatic repulsion.

As expected we find that the interaction ranges $\lambda_a$ and $\lambda_r$ increase with the correlation length. Although the behavior tends to break down close to $T_c$, where the actual interaction becomes long-ranged and cannot be captured anymore by a finite range model. It is worth pointing out again that close to $T_c$ the scaling function of the potential $\Phi_{+,+}^{(\mathrm{cc})}$ depends non-monotonically on the temperature $\Theta^*$. This leads to a non-monotonic relation between $\Theta^*$ and the potential depth $\epsilon_a$. Thus, in contrast to theoretical studies of the Kern-Frenkel model, where $\epsilon_a$ is treated as an effective temperature itself, in the context of the critical Casimir interaction $\epsilon_a$ does not fulfill the same role.

In Fig. 4.7(b) we plot the phase diagram of $|U_{min}| = \epsilon_a$ and the half-opening angle $\delta$ (via $\chi = (1 - \cos\delta)/2$) along a thermodynamic path with decreasing $\Theta^*$, which corresponds to a path of increasing $T$ towards a lower critical point $T_c$ in the experiment. The parameters of the electrostatic repulsion have been chosen as $A = 160$ and $\kappa R = 25$. The resulting path shows a non-trivial trend: far away from the critical point, the interaction strength $\epsilon_a$ is small, and the attractive patches have an effective patch size of $2\delta \lesssim 180°$, as expected from the Janus surface property. For a simple, qualitative argument, we consider states with a potential depth $\epsilon_a > 3\,k_BT$ as “bonded”, as it has been argued that this leads to colloidal aggregation [84]. Closer to the critical point, the effective patch size decreases. For purely geometrical reasons, a transition from a *tetramer* to a *trimer* state is expected to occur when the half-opening attains values below 60°, for which the particle can accommodate only two neighbor bonds.

The curve is continued for $\Theta^* < 2$ for the sake of completeness, showing *apparently* a re-entry into the tetramer phase. However, one cannot draw credible conclusions based on this. Below $\Theta^* < 2$, the critical Casimir interactions, both attraction and repulsion, become long-ranged in the practical sense that the numerical results starts to dependent on the (unavoidable) large distance cutoff value. Aside from the numerical problems, it is evident that a model with finite interaction range cannot truly capture the behavior close to $T_c$.

Experimentally, probing this phase transition must be done with extreme care; for example, considering Janus spheres of radius $R = 500\,\mathrm{nm}$ immersed in a binary mixture with $\xi_0 = 0.2\,\mathrm{nm}$ (the value for water and 2,6-lutidine), the effective temperature $\Theta^* = 5$, which is well within the *trimer* state, amounts to being as close as $16\,\mathrm{mK}$ from the critical point. For larger particles which are more convenient experimentally, the temperature range becomes even smaller. The thermodynamic path shown in Fig. 4.7(b) is severely shifted upon varying the parameters of the electrostatic repulsion. For increasing amplitude of the repulsion, as well as increasing the Debye length, the *tetramer* state appears to be more stable. This signals that the transition is indeed driven by the critical Casimir forces, but may be overshaded by a dominant close range repulsion. A full analysis of this dependence has not been performed within this thesis; the scope has been limited to establishing that the KF model is a valid simplification of the critical Casimir potential away from $T_c$ when the interaction is short-ranged.

### 4.3.2 Generalized dipole-dipole model

Interaction potentials of the form $V(\mathbf{n}_1, \mathbf{n}_2, \mathbf{r}_{12})/(k_B T) = U(\mathbf{n}_1, \mathbf{n}_2, \mathbf{r}_{12})$, which depend on three orientations (of the two particles and the connecting axis), can be expanded into a complete set of basis functions $\Psi_{l_1 l_2 l}$ given by the rotational invariants

$$\Psi_{l_1 l_2 l}(\mathbf{n}_1, \mathbf{n}_2, \mathbf{n}) = \sum_{m_1=-l_1}^{l_1} \sum_{m_2=-l_2}^{l_2} \sum_{m=-l}^{l} C(l_1 l_2 l, m_1 m_2 m)\, Y_{l_1}^{m_1}(\mathbf{n}_1) Y_{l_2}^{m_2}(\mathbf{n}_2) Y_l^{m*}(\mathbf{n}) \qquad (4.27)$$

where $C(l_1 l_2 l, m_1 m_2 m)$ denote the Clebsch-Gordan coefficients and $Y_l^m(\mathbf{n})$ the spherical harmonics.

In general, the expansion follows

$$U(\mathbf{n}_1, \mathbf{n}_2, \mathbf{r}_{12}) = \sum_{l_1 \geq 0} \sum_{l_2 \geq 0} \sum_{l=|l_1-l_2|}^{l_1+l_2} u_{l_1 l_2 l}\, \Psi_{l_1 l_2 l}, \qquad (4.28)$$

though some rotational invariants $\Psi_{l_1 l_2 l}$ vanish due to the selection rules of the Clebsch-Gordan coefficients. Inversely, the coefficients $u_{l_1 l_2 l}$ for a given potential $U(\mathbf{r}_{12}, \mathbf{n}_1, \mathbf{n}_2)$ are calculated from

$$u_{l_1 l_2 l}(r_{12}) = \frac{4\pi}{2l+1} \iint_{\Omega} \mathrm{d}\mathbf{n}_1 \iint_{\Omega} \mathrm{d}\mathbf{n}_2\, U(\mathbf{n}_1, \mathbf{n}_2, \mathbf{r}_{12} = r_{12}\mathbf{n}) \Psi^*_{l_1 l_2 l}(\mathbf{n}_1, \mathbf{n}_2, \mathbf{n}), \qquad (4.29)$$

where $\Psi^*_{l_1 l_2 l}$ denotes the complex conjugate of $\Psi_{l_1 l_2 l}$. Note the two solid angle integrals over all directions $\Omega$. The dipole-dipole pair potential (Eq. (4.8)), when expressed in rotational invariants, consist of only a single contribution

$$U^{(\mathrm{dip})}(\mathbf{n}_1, \mathbf{n}_2, r_{12}\mathbf{n}) = -\frac{8\pi^{3/2}}{\sqrt{15/2}} \frac{\tilde{\mu}^2}{r_{12}^3} \Psi_{112}(\mathbf{n}_1, \mathbf{n}_2, \mathbf{n}) = u_{112}(r_{12})\, \Psi_{112}(\mathbf{n}_1, \mathbf{n}_2, \mathbf{n}). \qquad (4.30)$$

Note that the electrostatic repulsion within the effective pair potential is independent of the orientation and will only contribute to the coefficient $u_{000}$ corresponding to $\Psi_{000}$. Thus, one can evaluate coefficients of higher order based on the critical Casimir potential alone. For the critical Casimir potential $U^{(ss)}_{\text{◐◐}} = V^{(ss)}_{\text{◐◐}}/(k_B T)$ between two Janus spheres, using the semi-analytical form in Eqs. (4.11ff.), the expansion coefficients in rotational invariants require numerical evaluation. Though in principle we have to deal with an infinite series of coefficients, we can conclude a certain structure based on symmetries of the interaction. While the attractive and repulsive contributions to the critical Casimir potential are of different absolute strength, this only enters the coefficient $u_{000}$ of $\Psi_{000}$ as an orientation independent shift. The higher order terms of $U^{(ss)}_{\bullet\bullet}$ must change sign with inversion of one particle orientation, that is,

$$\left[U^{(ss)}_{\bullet\bullet}(-\mathbf{n}_1, \mathbf{n}_2, r_{12}\mathbf{n}) - u_{000}\,\Psi_{000}\right] \overset{!}{=} (-1)\left[U^{(ss)}_{\bullet\bullet}(\mathbf{n}_1, \mathbf{n}_2, r_{12}\mathbf{n}) - u_{000}\,\Psi_{000}\right], \tag{4.31}$$

since this corresponds to the swap of the two BCs on particle 1. From the definition of the rotational invariants in Eq. (4.27) and the properties of the spherical harmonics, it follows that the rotational invariants are symmetric or anti-symmetric under this operation depending on $l_1$, i.e.,

$$\Psi_{l_1 l_2 l}(-\mathbf{n}_1, \mathbf{n}_2, \mathbf{n}) = (-1)^{l_1}\Psi_{l_1 l_2 l}(-\mathbf{n}_1, \mathbf{n}_2, \mathbf{n}). \tag{4.32}$$

As the same holds true for $l_2$, $U^{(ss)}_{\bullet\bullet}$ can consist only of terms with $l_1$ odd and $l_2$ odd, except for $l_1 = l_2 = 0$.[3]

Higher order terms represent additional anisotropic contributions. The terms of lowest order allowed by the Clebsch-Gordan coefficients are $\Psi_{000}, \Psi_{110}$ and $\Psi_{112}$. The coefficients for the terms $\Psi_{22x}$ vanish by the inversion argument. For symmetry conditions under exchange $\mathbf{n}_1 \leftrightarrow \mathbf{n}_2$ of the two particles, the next higher order terms with indices $(l_1, l_2, l) = (1, 3, 2)$ and $(3, 1, 2)$ are not independent and share the same coefficient, which can be expressed in a combined basis function $\Psi_{\overline{132}} = (\Psi_{132} + \Psi_{312})/2$. The same holds true for $(1, 3, 4)$ and $(3, 1, 4)$. The next allowed terms with symmetric indices are $(l_1, l_2, l) = (3, 3, 0), (3, 3, 2), (3, 3, 4), (3, 3, 6)$.

The coefficients for the critical Casimir potential in $d = 3$ follow from Eq. (4.29) together with Eq. (4.11); they may be factorized analogously to the scaling form such that $u_{l_1 l_2 l} = \Delta^{-1}\,\tilde{u}_{l_1 l_2 l}$. The first few coefficients $\tilde{u}_{l_1 l_2 l}$, calculated numerically, are shown in Fig. 4.8. Note that the coefficients adopt the dependence on $\Delta$ and $\Theta^*$ from the scaling function, whereas the orientation dependence is encoded by the rotation invariants. In Fig. 4.8(a), we show the absolute contributions of the expansion terms as a function of the scaled temperature $\Theta^* = R/\xi$ at a fixed distance $\Delta = 1/2$, together with the rotational invariant basis functions $\Psi_{l_1 l_2 l}(\phi_1{=}0, \vartheta_1{=}0, \phi_2{=}0, \vartheta_2{=}0, \phi{=}0, \vartheta{=}0, r_{12}{=}(5/2)R)$, i.e., for the case that both particles are orientated along the $z$ axis as well as the vector connecting the particle centers. This highlights that the zeroth coefficient amounts to the mean value of the scaling functions $\left(\Phi^{(ss)}_{(+,-)} - \Phi^{(ss)}_{(+,+)}\right)/2$, since the average $\langle\Psi_{l_1 l_2 l}\rangle_{\mathbf{n}_1,\mathbf{n}_2} = 0$ vanishes for $l_1, l_2 > 0$. As the given orientation of Janus particles is repulsive, the remaining

---

[3] Note that this symmetry does not apply to the Mayer function $f_M(\mathbf{n}_1, \mathbf{n}_2, r_{12}\mathbf{n}) = \exp(-U^{(\mathrm{Cas})}_{\bullet\bullet}(\mathbf{n}_1, \mathbf{n}_2, r_{12}\mathbf{n})) - 1$ (Eq. (4.18)), which enters the second virial coefficient $B_2$.

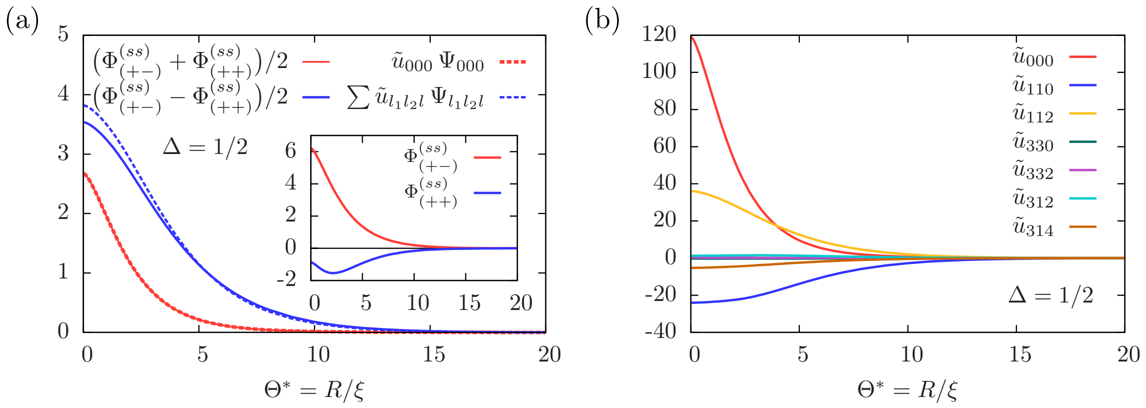

Figure 4.8: (a) Absolute contributions of the coefficients and rotational invariant basis functions $\Psi_{l_1 l_2 l}(\phi_1{=}0, \vartheta_1{=}0, \phi_2{=}0, \vartheta_2{=}0, \phi{=}0, \vartheta{=}0, r_{12}{=}(5/2)R)$, representing the case of both particles being positioned and orientated in-line along the $z$ axis, as function of $\Theta^* = R/\xi = \Theta/\Delta$ at fixed distance $\Delta$. In this case, the complete expansion is expected to yield the repulsive homogeneous scaling function $\Phi^{(ss)}_{(+,-)}$ (see red curve in the inset). The zeroth order (red dashed curve in main panel) reproduces the average of the $(+,+)$ and $(+,-)$ scaling functions (red solid curve), while the sum of the higher order terms (blue dashed curve; calculated up to $(3,1,4)$) approximates the remainder (blue solid curve in the main panel). (b) Numerically calculated values for the lowest order coefficients $\tilde{u}_{l_1 l_2 l}$ of the scaling function of the potential between Janus spheres as function of $\Theta^*$ up to the order $(l_1, l_2, l) = (3,1,4)$ at fixed distance $\Delta = 1/2$.

expansion terms must amount to $\left(\Phi^{(ss)}_{(+,-)} + \Phi^{(ss)}_{(+,+)}\right)/2$. Indeed, in sum the terms up to $(3,1,4)$ produce a good approximation of the scaling functions. The scaling function $\Phi^{(ss)}_{(+,\pm)}$ themselves are shown in the inset as a reminder. The actual values of the lowest order coefficients are similarly shown in Fig. 4.8. Note how the curves are reminiscent of the scaling functions, but appear to be always monotonic.

As a simple model, we formulate a generalized dipole-dipole interaction with only the lowest order expansion coefficients $u_{000}$, $u_{110}$ and $u_{112}$

$$U^{(\mathrm{gdd})}(\mathbf{n}_1, \mathbf{n}_2, \mathbf{r}_{12} = r_{12}\,\mathbf{n},) = u_{000}(r_{12})\,\Psi_{000}(\mathbf{n}_1, \mathbf{n}_2, \mathbf{n}) + u_{110}(r_{12})\,\Psi_{110}(\mathbf{n}_1, \mathbf{n}_2, \mathbf{n}) + u_{112}(r_{12})\,\Psi_{112}(\mathbf{n}_1, \mathbf{n}_2, \mathbf{n}) \quad (4.33)$$

which is a generalization of the dipole-dipole potential and a first-order approximation of the critical Casimir interaction. The treatment of the critical Casimir interaction in terms of a generalized dipole-dipole model allows to consider some aspects that are not covered by the Kern-Frenkel model. For example, two Janus colloids side by side ($\vartheta_1 = \vartheta_2 = \pi/2$), such that their equators are in line, are affected by strongly attractive critical Casimir forces (see the dip in Fig. 4.4(a) and (b)). For the closely related situation of a Janus colloid above a substrate with a chemical step (see Fig. 3.7), it has been verified that such a configuration is a potential minimum using both DA and MFT in $d = 4$, however, the sharp kink is smoothed out in the MFT results. Within the *modified* Kern-Frenkel model, these states are considered to be repulsive by definition, as the attractive patches have a coverage $\chi \in [0,1/2]$, so that attractive configurations are in the minority. (An alternative model that assumes the repulsive contribution to be in the minority fails to reproduce the full second virial coefficient $B_2^*$ of the critical Casimir interaction between Janus particles.)

Note that specific configurations may stabilize highly ordered phases and thus affect the phase behavior of Janus colloids. A phase with polar order, in which all Janus colloids are aligned along one axis, could be stabilized by the critical Casimir interaction along the equators, despite repulsive contributions along the orientation axes. In this picture, repulsive and attractive configurations are interchanged in comparison with the dipole-dipole interaction. We now evaluate analytically the energetic stability of a phase with polar order for the generalized dipole-dipole model.

Within the generalized model, the dipole-dipole interaction is described by coefficients $u_{000} = 0$, $u_{110} = 0$ and $u_{112} = -(8\pi^{3/2}/\sqrt{15/2})(\mu^2/r_{12}^3) < 0$, whereas we find from numerical evaluation for the critical Casimir interaction $u_{000} > 0$, $u_{110} < 0$ and $u_{112} > 0 \; \forall \; \Theta^* \geq 0$. As the coefficients carry different signs for the two interactions, it is insightful to consider the second virial coefficient in order to find fundamental implications of the signs for the lowest-order coefficients. To that end, we follow the procedure in Refs. [140, 141].

Analogously to the potential, the Mayer function $f_M = e^{-U} - 1$ can be expanded in rotational invariants

$$f_M(\mathbf{n}_1, \mathbf{n}_2, r_{12}\mathbf{n}) = \sum_{\Lambda} f_\Lambda(r_{12}) \Psi_\Lambda(\mathbf{n}_1, \mathbf{n}_2, \mathbf{n}) \tag{4.34}$$

with the distance-dependent coefficients $f_\Lambda(r_{12})$, using the shorthand notation $\Lambda = \{l_1, l_2, l\}$.

Assuming that the number density $\rho(\mathbf{r}, \mathbf{n})$ can be factorized as $\rho(\mathbf{r}, \mathbf{n}) = \rho(\mathbf{r})\alpha(\mathbf{r}, \mathbf{n})$ into a spatial dependent term $\rho(\mathbf{r})$ and a normalized orientation dependent term $\alpha(\mathbf{r}, \mathbf{n})$ (i.e., the probability to find any angle is $\int \mathrm{d}\mathbf{n}\, \alpha(\mathbf{r}, n) = 1$, irrespective of $\mathbf{r}$), it follows that the second virial coefficient is given by

$$\begin{aligned} B_2[\alpha(\mathbf{n})] = {} & B_2^{(\mathrm{hc})} \\ & - \frac{1}{2V} \int_V \mathrm{d}\mathbf{r}_1 \int\limits_{V \setminus V_\sigma} \mathrm{d}\mathbf{r}_2 \iint_\Omega \mathrm{d}\mathbf{n}_1 \iint_\Omega \mathrm{d}\mathbf{n}_2\, \alpha(\mathbf{r}_1, \mathbf{n}_1)\alpha(\mathbf{r}_2, \mathbf{n}_2)\, f_M(\mathbf{n}_1, \mathbf{n}_2, \mathbf{r}_2 - \mathbf{r}_1) \end{aligned} \tag{4.35}$$

where the integral over the position $\mathbf{r}_2$ of the second particle leaves out the volume $V_\sigma = \{\mathbf{r}_2 \in \mathbb{R}^d \,|\, |\mathbf{r}_2 - \mathbf{r_1}| < \sigma\}$ excluded by the first particle and already encoded in $B_2^{(\mathrm{hc})}$. It is handy to concomitantly expand the orientation distribution function using Legendre polynomials, so that

$$\alpha(\mathbf{r}_i, \mathbf{n}_i) = \sum_{l_i}^{\infty} \alpha_{l_i}(\mathbf{r}_i)\, P_{l_i}(\cos\vartheta_i). \tag{4.36}$$

Inserting both Eqs. (4.34) and (4.36) into $B_2$ in Eq. (4.35) yields

$$\begin{aligned} B_2 = B_2^{(\mathrm{hc})} - \frac{1}{2V} \int_V \mathrm{d}\mathbf{r}_1 \int_{\sigma}^{\infty} \mathrm{d}r_{12}\, r_{12}^2 \iint_\Omega \mathrm{d}\mathbf{n} \sum_{l_1 l_2 \Lambda} \alpha_{l_1}(\mathbf{r}_1)\alpha_{l_2}(\mathbf{r}_1 + r_{12}\mathbf{n}) f_\Lambda(r_{12}) \\ \times \iint_\Omega \mathrm{d}\mathbf{n}_1 \iint_\Omega \mathrm{d}\mathbf{n}_2\, P_{l_1}(\cos\vartheta_1) P_{l_2}(\cos\vartheta_2) \Psi_\Lambda(\mathbf{n}_1, \mathbf{n}_2, \mathbf{n}). \end{aligned} \tag{4.37}$$

The latter integrals can be evaluated by expressing the Legendre polynomials $P_l(\cos\vartheta)$ in terms of $Y_l^0(\vartheta, 0)$ and applying the orthogonality relation of the spherical harmonics. This results in

$$\begin{aligned} B_2 = -\frac{1}{2V} \int_V \mathrm{d}\mathbf{r}_1 \int_{\sigma}^{\infty} \mathrm{d}r_{12}\, r_{12}^2 \iint_\Omega \mathrm{d}\mathbf{n} \sum_{l_1 l_2 l} \frac{4\pi\, C(l_1 l_2 l, 000)}{\sqrt{(2l_1+1)(2l_2+1)}} \\ \times \alpha_{l_1}(\mathbf{r}_1)\alpha_{l_2}(\mathbf{r}_1 + r_{12}\mathbf{n}) f_{l_1 l_2 l}(r_{12})\, Y_l^0(\mathbf{n}). \end{aligned} \tag{4.38}$$

For the lowest order terms, evaluating the Clebsch-Gordan coefficients $C(l_1 l_2 l, 000)$ and $Y_l^0(\mathbf{n})$ yields

$$\begin{aligned} B_2 = &\overbrace{B_2^{(\mathrm{hc})} - \frac{1}{2}\int_\sigma^\infty \mathrm{d}r_{12}\, r_{12}^2\, (4\pi)^{3/2}\, \alpha_0^2\, f_{000}(r_{12})}^{B_2^{(iso)}} \\ &+ \frac{1}{2V} \int_V \mathrm{d}\mathbf{r}_1 \int_{\sigma}^{\infty} \mathrm{d}r_{12}\, r_{12}^2 \iint_\Omega \mathrm{d}\mathbf{n}\, \frac{4\pi}{3} \frac{1}{\sqrt{3}} \alpha_1(\mathbf{r}_1)\alpha_1(\mathbf{r}_1 + r_{12}\mathbf{n})\, f_{110}(r_{12}) \\ &- \frac{1}{2V} \int_V \mathrm{d}\mathbf{r}_1 \int_{\sigma}^{\infty} \mathrm{d}r_{12}\, r_{12}^2 \iint_\Omega \mathrm{d}\mathbf{n}\, \frac{4\pi}{3} \sqrt{\frac{2}{3}} \alpha_1(\mathbf{r}_1)\alpha_1(\mathbf{r}_1 + r_{12}\mathbf{n})\, f_{112}(r_{12}) \\ &\qquad \times \sqrt{\frac{5}{16\pi}} \left(3\cos^2\vartheta - 1\right). \end{aligned} \tag{4.39}$$

The first two terms are the only ones not vanishing for isotropic phases, for which $\alpha_0 = 1/(4\pi)$ is the only non-vanishing coefficient, so that we refer to them as $B_2^{(iso)}$. All following higher order terms determine the stability of an anisotropic phase with respect to the isotropic phase.

The coefficients $f_{000}$, $f_{110}$ and $f_{112}$ have been calculated numerical using the critical Casimir potential directly. Additionally, it is possible to obtain analytical expressions relating the coefficients of the Mayer function to the coefficients $u_{000}$ to $u_{112}$ of the generalized dipole-dipole interaction. For brevity, the full derivation is omitted, but follows analogously to Ref. [140] by including the terms of the generalized dipole-dipole interaction.

In an anisotropic but homogeneous phase, $\alpha_l$ are a scalar coefficients, and in Eq. (4.39) the third term with $f_{112}$ vanishes, while the second term attains the form $\sim \alpha_1^2 f_{110}(r_{12})$. The polarization of a phase is determined by $\mathbf{p} \propto \int \mathrm{d}\mathbf{n}\, \alpha(\mathbf{n})\, \mathbf{n} = \frac{4\pi}{3}\alpha_1$, and thus proportional to $\alpha_1$. For the dipole-dipole potential with $u_{000} = 0$, $u_{110} = 0$ and $u_{112} < 0$, one obtains $f_{110} \leq 0$ and $f_{112} \geq 0$. Due to the sign of $f_{110}$, for a polar phase with $\alpha_1 \neq 0$, this reduces the second virial coefficient such that

$$\Rightarrow B_2 - B_2^{(iso)} \leq 0. \tag{4.40}$$

Thus, the polar phase minimizes the free energy compared to the isotropic phase in the case of a dipole-dipole interaction. This is a necessary, but not a sufficient condition. However, the stability of a ferroelectric phase in a system with a dipolar phase is known [141, 142], and in line with this argument.

In contrast, for the critical Casimir potential with $u_{000} > 0$, $u_{110} < 0$ and $u_{112} > 0 \;\forall\; \Theta^* \geq 0$, one finds $f_{110} \geq 0$ and $f_{112} \leq 0$. The resulting signs of the expansion coefficients of the Mayer function lead to the opposite behavior for the free energy, i.e., according to Eq. (4.39),

$$\Rightarrow B_2 - B_2^{(iso)} \geq 0. \tag{4.41}$$

For the critical Casimir potential, any phase with a polarization, i.e., $\alpha_1 \neq 0$, has a higher free energy than the isotropic phase, making it thermodynamically unstable.

As a follow-up step, one may consider spatially ordered phases for which the coefficients $\alpha_l$ of the orientation distribution function are $\alpha_l \neq 0$ for $l > 1$. However, structured phases such as observed in Ref. [71] are likely described by a series of coefficients that cannot be truncated at low orders. Nonetheless, we hope for this basic formalism to provide a foundation for more extensive numerical computations and simulations of the phase behavior, for example by applying density functional theory using a number of pre-computed coefficients for the critical Casimir potential.

## 4.4 Conclusions

In this chapter, we have discussed the scaling function of the force between two Janus spheres in a relative coordinate system as a function of three spherical coordinates $\alpha = \phi_2 - \phi_1$, $\vartheta_1$, and $\vartheta_2$ (Fig. 4.2). The details of the derivation, accounting for all possible orientations, are provided in Appendix B. The result for the scaling function of the force is shown in Fig. 4.3. We find that the force between two Janus spheres can be attractive or repulsive, depending on their orientations. The strongest attraction is found in the case of the two Janus spheres facing each other with the same face, whereas the strongest repulsion occurs when they are orientated in line. The force is rather insensitive against tilts out of these two configurations. Based on the scaling function of the force we have also determined the scaling function of the effective pair potential between two Janus spheres. Since it is a function of three spherical coordinates, one cannot visualize, within a single plot, the full dependencies of the potential. In Fig. 4.4, we present it as an energy landscape in terms of the particle orientations $\vartheta_1$ and $\vartheta_2$ for the two cases $\alpha = 0$ and $\alpha = \pi$. There are two shallow and stable minima in the potential energy, which are connected by a narrow trough representing counter-rotating orientations of the Janus particles. The large plateaus of repulsive orientational states corresponding to opposing BC yield a checkerboard landscape pattern. For $0 < \alpha < \pi$ the scaling function of the effective potential varies primarily only around orientations $\vartheta_i = \pi/2$ for the two particles $i = \{1, 2\}$ (Fig. 4.4). However, the pronounced plateau structure is largely unaffected by changes of $\alpha$.

We have used the scaling function of the effective potential in order to address the special experimental situation in which the particle positions and orientations are confined to a plane parallel to the planar surface of a substrate, however such that the substrate does not alter the pair interaction among the particles. Using the full pair interaction potential, we have analyzed how the effective influence of the substrate, incorporated as an externally imposed common tilt $\gamma$ of all Janus particles, changes the effective pair interaction among the Janus particles. The deviations turn out to be small for tilts $\gamma \lesssim 30°$ and still acceptable for $\gamma \lesssim 45°$ (Fig. 4.5). Under this condition, concerning the interaction among the particles the substrate induced interaction can be discarded.

Thus our findings are to a certain extent compatible with the on-off “bond-like” interaction underlying the popular Kern-Frenkel model [133]. However, the critical Casimir potential carries both attractive and repulsive contributions. Since the repulsion is stronger than the attraction, less than half of all configurations are actually attractive (see Fig. 4.4), despite the overall Janus character. The effective pair potential can be used to characterize the thermodynamic properties of suspensions of Janus particles with a critical solvent via integrals of the effective potential over both orientations and the radial distance. However, in practical terms the numerical integration over all orientations and the distance between the particles results in problematically long runtimes. In order to make progress, we have laid out the foundation for expanding the critical Casimir pair potential in terms of the Kern-Frenkel (KF) model and a generalized dipole-dipole interaction in Sec. 4.3 (compare Fig. 4.6 with Fig. 4.4). The Kern-Frenkel model provides clear model parameters for the interaction strength, interaction range and the effective patch size (see Fig. 4.7). The long-ranged behavior and non-monotonic strength of the critical Casimir potential cannot be straightforwardly captured by the KF model. As a more aptly alternative, we have introduced the expansion of the critical Casimir potential in terms of rotational invariants, leading to a generalized dipole-dipole interaction. Analytic comparison with the dipolar interaction reveals opposite behavior in the second virial coefficient, which can be traced to the different signs of the coefficients (see Fig. 4.8). This scheme can be suitably extended for numerical evaluation (e.g., density functional theory) or (Monte-Carlo) simulations.

# Chapter 5

# Beyond Casimir: Liquid bridging between colloids

In the preceding chapters, we have focused on the critical Casimir force as the singular contribution to the force close to the critical point. However, the contribution of liquid bridges to the force had already been pointed out in the first reports of the direct measurement of critical Casimir forces [28,29]. In this chapter, we study in detail the interplay between the two forces as obtained from MFT by minimizing Eq. (2.27). We focus on the case of the solvent being at solvent phase coexistence, so that $h = 0$. In order to stabilize selectively the bulk $\beta$-phase, we consider the limit $h \to 0^-$, so that the coexistence line is approached from that side which is slightly poor in the A component. In order to minimize Eq. (2.27) numerically, we use an effectively two-dimensional adaptive finite element method [101] which uses quadratic interpolation in order to obtain a smooth order parameter profile [143]. We have performed the minimization iteratively (i.e., by recycling the finite element mesh of the previous solution in order find the next one) as a function of the reduced temperature $t$ and we have compared these results with non-iterative ones in order to check for any hysteresis effects. We emphasize that although we have varied the reduced temperature $t$ stepwise, the results correspond to a set of equilibrium order parameter profiles. In an experimental setting, they would be obtained at best by very slowly heating or cooling the sample and waiting for equilibration. Therefore these results represent a sequence of static behaviors and are not dynamic in any sense. The iteration can be implemented all the same by stepwise changes of the distance $D$. However, we expect a quasi-static experimental realization of this protocol to be much more difficult.

We have inferred the force acting on the colloids from the numerically determined order parameter profiles, by first calculating the effective interaction potential and then taking the derivative with respect to the separation $D$. The stress tensor method is not viable for the present case because the interfaces forming near the colloids exhibit large order parameter gradients which are prone to significant numerical errors.

As illustrated in Fig. 5.1, we consider two cylindrical colloidal particles of equal radius

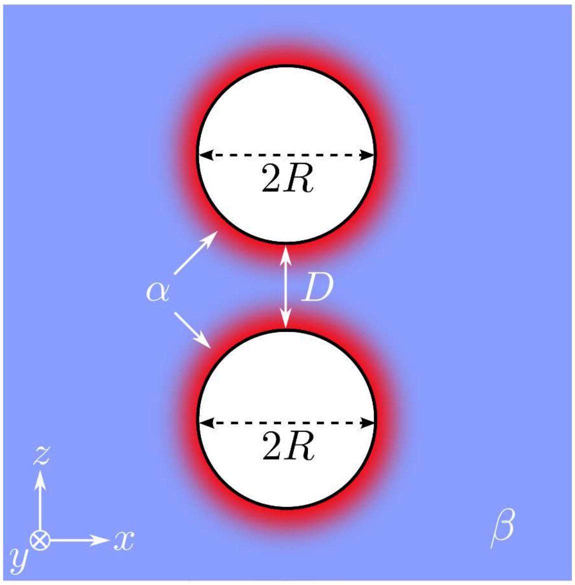

Figure 5.1: Cross-section of the system under study. It consists of two cylindrical colloids of radius $R$ with a preference for the adsorption of the $\alpha$ (A-rich, colored in red) phase, surrounded by the $\beta$ (B-rich, colored in blue) phase. In the bulk the phases $\alpha$ and $\beta$ coexist. The system is fixed at the critical composition and at reduced temperatures $t = (T - T_c)/T_c < 0$. The surface-to-surface separation is denoted as $D$. The colloids are aligned parallel to each other. Thus we investigate the effective interaction between the two colloids for different separations, i.e., we study the dependence of the interaction on $z$ for temperatures below the critical point ($t < 0$). The colloids are taken to be small enough so that gravitational effects are negligible.

$R$ which are translationally invariant along the $y$ direction. At a given temperature in the two-phase $\alpha$-$\beta$ coexistence region of the solvent, the colloids are fixed to be parallel and only their surface-to-surface separation $D$ is allowed to vary. We assume that the cylindrical colloids strongly prefer the $\alpha$ phase. Thus the global minimum of the free energy has them surrounded by a macroscopic $\alpha$ phase, in coexistence with a colloid-free $\beta$ phase. However, there is a broad and stable local minimum in which the colloids are trapped in the $\beta$ phase, sufficiently far away from the $\alpha$-$\beta$ interface, so that the interface is located outside our numerical calculation box (e.g., according to Ref. [143] the effective potential of a single colloid changes notably only close to the interface, and remains constant if the colloid is placed deeply within either phase). We note that in Refs. [45] and [48] analogous situations have been studied for cylindrical particles and block-shaped particles in a solvent close to gas-liquid coexistence, respectively. Our assumption of strong adsorption on the surface of the colloids corresponds to the case of complete wetting or drying, i.e., a contact angle of zero or 180°, respectively. Note that the notions of a liquid-bridge and a gas-bridge are the natural ones in the context of a solvent exhibiting a gas-liquid phase transition; both cases are consistently described by the contact angle between the particle surface and the liquid. While arbitrary, we choose to associate the preference for the $\alpha$-phase with zero contact angle and wetting by the liquid. In the case of a binary liquid mixture, one may find an $\alpha$-like (rich in component A) or a $\beta$-like bridge (rich in B), depending on the adsorption preference of the colloids, which is visualized by the contact angle. Occasionally, we shall call the $\alpha$-bridge a "liquid"-bridge as a means to invoke the broader context.

## 5.1 A framework for finite-size scaling

First, we extend our notation of finite-size scaling to incorporate interfacial contributions and define modified scaling functions. Close to the critical point, $|t| \ll 1$, and *at* the critical composition of the binary liquid mixture, the free energy $\Omega$ of the system (the symbol $\Omega$ is used in order to avoid confusion with the force $F$) can be decomposed into a singular contribution and a non-singular background term [81] $\Omega = \Omega_{\text{sing}} + \Omega_{\text{nonsing}}$. Within the critical regime, $\Omega_{\text{sing}}$ is expected to exhibit finite size scaling. We provide a framework discussing this finite size scaling for the effective potential and for the force between two colloidal particles using the definitions illustrated by Fig. 5.1. The singular contribution to the total free energy is the sum of three separate, identifiable contributions (compare with Eq. 2.18):

$$\Omega_{\text{sing}} = \Omega_b + 2\ \Omega_{s,c}^{(\beta)} + \Omega_i, \tag{5.1}$$

where $\Omega_b$ is the *b*ulk free energy, $\Omega_{s,c}^{(\beta)}$ is the *s*urface free energy of each *c*olloid in the $\beta$ phase, and $\Omega_i$ is the effective *i*nteraction, which includes the critical Casimir interaction. The critical behavior of the bulk and surface contributions of the total free energy is well-known and exhibits scaling. Note that in Eq. (5.1) there are no additional contributions from the side edges of the sample. We adopt periodic boundary conditions along the axes of the cylinders and the sample is taken to be large enough so that the bulk values corresponding to the $\beta$ phase are attained in the other two directions.

The bulk free energy $\Omega_b$ is proportional to the volume $V_\beta$ filled by the liquid phase $\beta$ of the binary liquid mixture. Therefore the bulk free energy takes the following form:

$$\Omega_b = k_B T\, \frac{V_\beta}{\xi_+^d}\, \frac{a_b^-}{\alpha(1-\alpha)(2-\alpha)}, \tag{5.2}$$

where $a_b^-$ is a universal number. Its value depends on whether $V_\beta$ is expressed in units of $\xi_+^d$ or $\xi_-^d$ (see Sec. IV in Ref. [144] as well as Ref. [145] and note that $a_b^-$ here equals $-\left(R_\xi\right)^d a_b^-$ with $a_b^-$ as introduced in Eq. (4.11) in Ref. [144]) and $\alpha$ is the universal critical exponent of the bulk specific heat capacity. (Here and in the following we omit those correction terms of the free energy which are generated by additive renormalization [144].) The total volume filled by the liquid phase $\beta$ is given by the total volume of the system minus the volume of the two cylindrical colloids of radius $R$:

$$V_\beta = \mathcal{L} \times \left(L_x L_z - 2\,\pi R^2\right), \tag{5.3}$$

where $L_{x,z}$ are the extensions of the $\beta$ phase along the $x$ and $z$ direction (see Fig. 5.1) and $\mathcal{L}$ is the extension of the system along the invariant directions, i.e., $\mathcal{L}(d=3) = L_y$ and $\mathcal{L}(d=4) = L_y\,L_4$.

From inserting both $\xi_+ = R_\xi\,\xi_0^-\,|t|^{-\nu}$ and Eq. (5.3) into Eq. (5.2), one finds that the bulk free energy scales as

$$\frac{\Omega_b}{k_B T} = \frac{L_x L_z - 2\,\pi R^2}{(\xi_0^-)^d}\,\mathcal{L}\,\frac{a_b^-}{\alpha(1-\alpha)(2-\alpha)}\,R_\xi^{-d}\,|t|^{d\nu}, \tag{5.4}$$

which provides the first term in Eq. (5.1).
The surface free energy $\Omega_{s,c}^{(\beta)}$ of a single colloid in the bulk $\beta$ phase is given by [143]

$$\Omega_{s,c}^{(\beta)} = k_B T\,\frac{A_c}{\xi_+^{d-1}}\,\vartheta_\beta(R/\xi_-), \tag{5.5}$$

where $A_c = \mathcal{L}\times 2\pi R$ is the surface area of one cylindrical colloid and $\vartheta_\beta$ is a universal scaling function. The above expression can be rewritten in order to illustrate the temperature dependence of the surface free energy of the colloid:

$$\frac{\Omega_{s,c}^{(\beta)}}{k_B T} = \frac{2\pi R}{(\xi_0^-)^{d-1}}\,\mathcal{L}\,\vartheta_\beta\left(\frac{R}{\xi_0^-\,R_\xi}\,|t|^\nu\right)\,R_\xi^{-(d-1)}\,|t|^{(d-1)\nu}. \tag{5.6}$$

Combining Eqs. (5.4) and (5.6) yields the total singular free energy of the system:

$$\begin{aligned}\frac{\Omega_{\text{sing}}}{k_B T} = {} & \frac{L_x L_z - 2\,\pi R^2}{(\xi_0^-)^d}\,\mathcal{L}\,\frac{a_b^-}{\alpha(1-\alpha)(2-\alpha)} R_\xi^{-d}\,|t|^{d\nu} \\ & + 2\times\frac{2\pi R}{(\xi_0^-)^{d-1}}\,\mathcal{L}\,\vartheta_\beta\left(\frac{R}{\xi_0^-\,R_\xi}\,|t|^\nu\right)\,R_\xi^{-(d-1)}\,|t|^{(d-1)\nu} \\ & + \Omega_i/k_B T.\end{aligned} \tag{5.7}$$

The last part, $\Omega_i$, is the contribution to the free energy which originates from the finite separation between the colloidal particles and thus represents the effective interaction between them. According to finite size scaling, this effective potential can be written in scaling form as [36]

$$\frac{\Omega_i}{k_B T} = \frac{\mathcal{L}}{R^{d-2}}\,G\left(\Delta = \frac{D}{R}, \Theta_- = \frac{R}{\xi_-}\right), \tag{5.8}$$

where $D$ is the surface-to-surface distance between the colloidal particles, $R$ is the radius of a single colloid (see Fig. 5.1), and $\xi_-$ is the correlation length (for $T$ below $T_c$). Note that the choice of the scaling form and of the scaling variables is not unique. In this chapter, we have opted for the choice $\Delta = D/R$ and $\Theta_- = R/\xi_-$ because it allows one to discuss separately the distance and the temperature dependence, and with a view on experiments, the radius $R$ can be considered as being fixed. The scaling form given by Eq. (5.8) holds generally for any geometric object in $d$ dimensions which has a characteristic size $R$ in 2 directions but is invariant in $d-2$ directions. At the critical point the distance dependence of the corresponding scaling function $G(\Delta, \Theta_- = 0)$ for the effective interaction follows the power law $\sim \Delta^{-(d-3/2)}$ which is borne out by the scaling form (see Appendix A)

$$\frac{\Omega_i}{k_B T} = \frac{\mathcal{L}}{R^{d-2}} \frac{\Phi^{(cc)}_{(+,+)}(\Delta, \Theta = \Theta_- \Delta)}{\Delta^{d-3/2}}. \tag{5.9}$$

The cylinder-specific scaling function $\Phi^{(cc)}_{(+,+)}$ has the property $\Phi^{(cc)}_{(+,+)}(\Delta, \Theta = 0) = \mathit{const.}$, i.e., it does not contain the aforementioned divergence for $\Delta \to 0$. In this chapter, it will turn out to be beneficial to use the scaling form given by Eq. (5.8) which keeps the whole distance dependence within the scaling function. The relation $G(\Delta, \Theta_-) = \Delta^{-(d-3/2)}\, \Phi^{(cc)}_{(+,+)}(\Delta, \Theta_- \Delta)$ from Eqs. (5.8) and (5.9) still allows the comparison with other presentations in this thesis and in the literature.

Due to the dependence of $\Omega_i$ on the separation $D$ between the colloids, an effective critical Casimir force $F_{sing}$ emerges, which acts on the particles along the $z$-direction (see Fig. 5.1):

$$\begin{aligned} F_{\text{sing}} = -\frac{\partial \Omega_i}{\partial D} &= -k_B T \, \frac{\mathcal{L}}{R^{d-1}} \, \frac{\partial}{\partial \Delta} G\left(\Delta, \Theta_-\right), \\ &= k_B T \, \frac{\mathcal{L}}{R^{d-1}} \, \mathcal{K}\left(\Delta, \Theta_-\right) \end{aligned} \tag{5.10}$$

with the scaling function $\mathcal{K}(\Delta, \Theta_-) = \Delta^{-(d-1/2)} K^{(cc)}_{(+,+)}$ found in Appendix A. In the following, the scaling function $\mathcal{K}$ of the force will be investigated as a function of temperature. In order to make progress in determining the effective potential and thus the force acting between the colloidal particles, we resort to mean field theory as described in Sec. 2.1.3 in order to be able to describe explicitly the order parameter distribution around the colloids.

## 5.2 Two particle order parameter profiles

We start our study by presenting the distribution of the order parameter $\phi$ for the binary solvent in the presence of two cylindrical, parallel colloidal particles. The explicit spatial variations of $\phi$ are calculated within MFT, see Sec. 2.1.3, and discussed along the lines presented in Sec. 5.1. Beyond such explicit (and thus approximate) calculations, for the present system under study, the theory of finite size scaling states that below but close to the critical point the order parameter exhibits the scaling form [36]

$$\phi(\mathbf{r},t) = \mathcal{B}\,|t|^{\beta}\,P_{\pm}\left(\frac{x}{\xi_{\pm}},\frac{z}{\xi_{\pm}};\Delta{=}\frac{D}{R},\Theta_{\pm}{=}\frac{R}{\xi_{\pm}}{=}\frac{R}{\xi_0^{\pm}}|t|^{\nu}\right), \tag{5.11}$$

where $\mathcal{B}$ is the non-universal amplitude of the bulk order parameter with $\beta \simeq 0.33$ in $d = 3$ and $\beta = 1/2$ in $d = 4$ as one of the standard bulk critical exponents. $D$ denotes the surface-to-surface distance between the two colloids of equal radius $R$ and $(x, z)$ are the coordinates of a point in the surrounding liquid. For the given geometry, we conveniently choose the coordinate system such that the $y$-axis is aligned with the axes of the parallel cylinders, so that $\phi$ is independent of that translationally invariant direction. The $z$-axis connects the centers of the two colloids (see Fig. 5.1) and the origin $(0, 0)$ is located at the center of the “bottom” particle (assuming the reader is holding the page upright). We remark that for $T \geq T_c$ the order parameter vanishes far away from the colloids and exhibits critical adsorption as described by the scaling function $P_+(x/\xi_+, z/\xi_+; \Delta, \Theta_+)$ [99]. At $T = T_c$, in Eq. (5.11) both scaling functions $P_{\pm}$ render the same, unique order parameter distribution.

In this study, we focus on the phase-separated region $T < T_c$. The boundary conditions are chosen such that the surfaces of the colloids strongly prefer the $\alpha$ phase, whereas far from the colloids the coexisting $\beta$ phase prevails. In Fig. 5.2, $P_-(x/\xi_-, z/\xi_-; \Delta, \Theta_-)$ is shown for the rescaled temperature $\Theta_- = 16.1$ at the rescaled surface-to-surface distance $\Delta = 2.35$. Two distinct profiles can be found, one in which the two particles are connected by an A-rich liquid bridge in Fig. 5.2(a), and one where each colloid is covered by a wetting-like layer of the $\alpha$ phase, the thickness of which is finite due to the curvature of the colloid surfaces [146]. At the given rescaled distance $\Delta = 2.35$, the two configuration have the same free energy. However, the bridged state (a) is more stable for smaller separations or upon approaching the critical point. In reverse, the separated state prevails for larger separations and further away from $T_c$. The two profiles in Fig. 5.2 have been obtained along two thermodynamic paths, moving away from $T_c$ in (a) and approaching $T_c$ in (b).

Quantitatively, in the $\alpha$ phase one has $\phi_\alpha = \mathcal{B}|t|^{\beta}$ (with $\mathcal{B} > 0$), so that $\phi_\beta = -\mathcal{B}|t|^{\beta}$. Accordingly, far from the colloids $P_-$ reduces to the value $-1$ (see Eq. (5.11)). In the presence of a liquid bridge (Fig. 5.2(a)), a sharp $\alpha$-$\beta$ interface is formed around both colloidal particles, the position of which can be described by the implicit equation $P_- = 0$. Within that bridge, the scaling function $P_-$ attains the bulk value of the $\alpha$ phase, $P_- = 1$. The liquid bridge exposes partially the preferred $\alpha$ phase to the colloids, thus reducing the surface free energy. The total free energy is counterbalanced by the additional interfacial energy required in order to maintain the bridge. Figure 5.2(b) shows that, at the transition distance between the bridged and separated state, the two separate wetting layers around the particles are de facto circularly symmetric, indicating that at this temperature the particles do not strongly interact with each other, in a way which is visibly distorting the

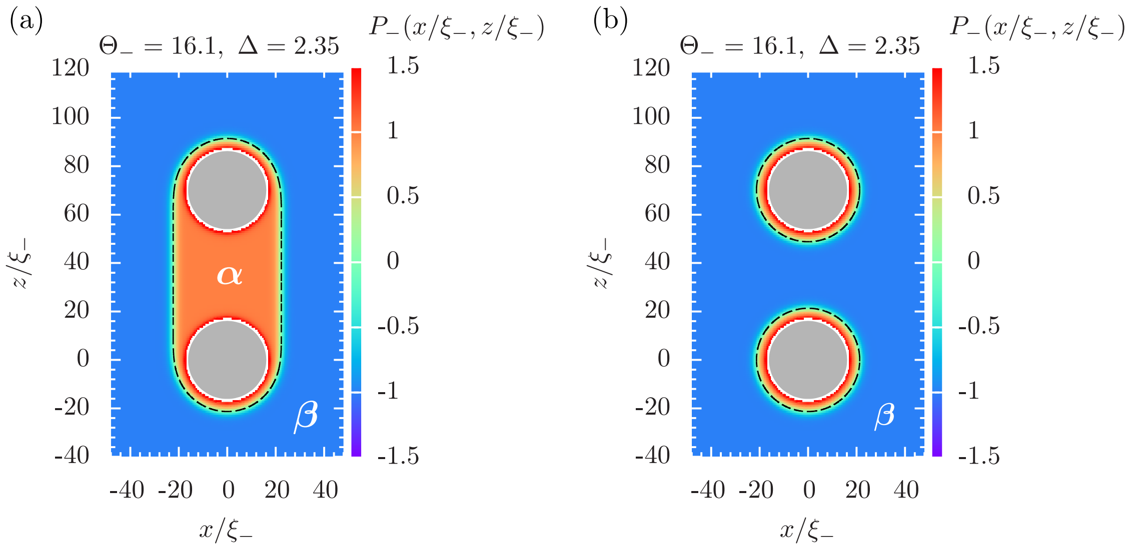

Figure 5.2: Scaling function $P_-(x/\xi_-, z/\xi_-)$ describing the order parameter profile around two colloids for $\Theta = R/\xi_- = 16.1$ at the rescaled distance $\Delta = D/R = 2.35$ corresponding to the first-order transition between the (a) bridged and (b) separated configuration. The surfaces of the gray colloids prefer the $\alpha$ phase ($P_- > 0$, red color) whereas far from the colloids the $\beta$ phase prevails ($P_- = -1$, blue color). Within the numerical procedure, the actual OP profile is not resolved inside a shell of radii R and $1.05\,R$ (white ring) due to the divergence of $P_- \to \infty$ at the surface of the colloids. Instead, in this shell the analytic expression for the asymptotic behavior of the profile [99] is used. The black dashed iso-lines correspond to $P_- = 0$. Within the liquid bridge in (a), the scaling function $P_-(x/\xi_-, z/\xi_-)$ follows mostly the bulk value of the $\alpha$ phase, i.e., $P_- = 1$ (see the rather uniform orange color).

A-rich fluid encasing each of the two colloids.

Note that the straight, flat shape of the bridge is not an artificial feature of the method, but a particular feature of the cylindrical geometry itself. In order to provide a short rationale, one has to realize that the cylinders extend out of the figure plane and thus the interface stretches along the $y$-direction by a length $L_y$. Any bending of the straight interface into the gap between the cylinders, such that the interface would wrap more closely around them, increases the arc length $s = \int \mathrm{d}s(z)$ and the surface area $A_c = L_y\, s \geq L_y\, l$ compared to the straight bridge of length $l$. In contrast, for spherical colloids, a bridge forms with a thinner neck between the particles, which bends inwards [38, 43–45, 47, 49, 147–154]. Considering a very sharp interface, the liquid bridge connecting the two spheres is a *solid of revolution*, e.g., a cylinder with radius $R_c$ for a straight bridge or a “body” with varying radius $r(z)$. According to Guldin’s theorem, the surface area of a *solid of revolution* with length $l$ is given by $A_s = 2\pi\, l\, \bar{r}$, where $\bar{r} = (1/l) \int_{z=0}^{l} r(z)\, \mathrm{d}s(z)$ is the radial distance of the centroid of the profile $r(z)$. Evidently, a tapering of the radial profile decreases the radial distance of the centroid and thus the surface area $A_s = 2\pi\, l\, \bar{r} \leq 2\pi\, l\, R_c$ decreases compared to that of the straight bridge. Thus the surface free energy contribution, which is proportional to the surface area of the

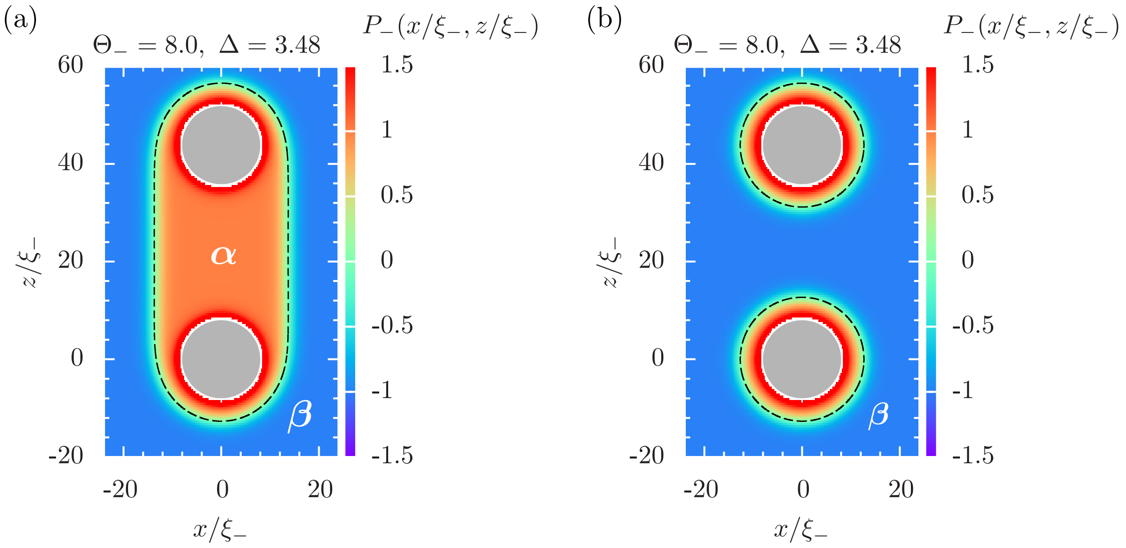

Figure 5.3: The same as Fig. 5.2 but for $\Theta_- = 8.0$ at the transition distance $\Delta = 3.48$, with the bridged configuration in (a) and the separated one in (b). Note that upon approaching $T_c$, i.e., for $\Theta_- \to 0$ the correlation length $\xi_-$ increases, resulting in a smaller scale of the plot. Still, in units of $\xi_-$, the halos around the particles are larger than in Fig. 5.2 and the transition distance has increased noticeably. For even smaller values of $\Theta_-$, the transition distance exceeds the plot range and requires also larger numerical calculation boxes.

interface, is minimized by profiles which are very different for two cylinders and for two spheres. Although cylindrical colloids are more difficult to realize experimentally, large elongated colloids can be fabricated and their physical properties can be studied (see, e.g., Refs. [155–158]). Within the present theoretical study, it turns out that they provide a particularly clear model system which allows one to identify the main effects associated with bridge formation.

We now consider the case in which the system is closer to the critical point $T_c$. Upon decreasing the rescaled temperature of the system to $\Theta_- = 8.0$ (see Fig. 5.3), the transition distance increases to $\Delta = 3.48$ along with the increasingly long-ranged correlations. The halos around the two colloids extend farther out, and the interfacial region, both of the bridge and around the cylinders, is more smeared out. Moving even closer to $T_c$, i.e., $\Theta_- \to 0$, these trends become even more pronounced: the transition distance then exceeds the plot range and the interface between the $\alpha$- and $\beta$-rich phases becomes smeared out over a range comparable to the size of the colloids; accordingly the bridge becomes less clearly visible.

## 5.3 Distance dependence of the scaling function for the effective potential

We now turn our attention to the effective potential between the two colloidal particles, in the bridged and the ruptured state. As already mentioned in Sec. 5.1, the singular part of the effective potential takes the form given by Eqs. (5.7) and (5.8). This form of the scaling function $G$ is suitable for studying the dependence on the distance $D$ of the effective potential $\Omega_i$ acting between the colloidal particles. The MFT results for the bridged states, obtained by using numerical minimization as described in Sec. 2.1.3, are shown in Fig. 5.4.

In Fig. 5.4(a), for the rescaled temperatures $\Theta_- = 12.25$, 6.00, and 0.45, we show the scaling function $G$ as a function of $\Delta$, normalized by the critical Casimir amplitude $k_{(+,+)}(0) = \Delta_{(+,+)} = -283.61\,u^{-1}$ (i.e., the amplitude of the critical Casimir force between two equal, symmetry breaking, parallel plates at the critical temperature — see Ref. [91] for further details) so that the results are independent of the dimensionless, unspecified coupling parameter $u$. The data corresponding to the system furthest from the critical point, i.e., for $\Theta_- = 12.25$, clearly reflect three stages of the evolution of the liquid bridge.

(i) For large separations $\Delta \gg 1$, one finds $G > 0$ for the bridged state. Since the surface free energy $2\,\Omega_{s,c}^{(\beta)}$ of two separate colloids is not included in $\Omega_i/(k_BT) = \left(\mathcal{L}/R^{(d-2)}\right) G$, a vanishing value $G = 0$ corresponds to the free energy of the completely separated state. Thus for $\Delta \gg 1$ the bridged state is only metastable compared to the separated state. In order to further illustrate this metastability, for $\Theta_- = 12.25$ we have followed the separated state along the reverse thermodynamic path beyond the transition distance at which the two free energy branches intersect. The resulting free energy of the separated state is very small and varies only very weakly. Upon lowering $D$ this state adheres to very small values of $G$ until it suddenly jumps onto the lower free energy branch of the stable, bridged state (see the vertical dashed line). Note that the bridged and separated states have actually been obtained along two thermodynamic paths, moving away from $T_c$ and approaching $T_c$, respectively, which renders the metastability upon varying the distance $D$ between the colloids, provided scaling holds.

(ii) For intermediate rescaled distances $0.5 < \Delta < 2.5$, the scaling function $G$ increases linearly upon increasing $\Delta$. This is a clear signature of the effective potential being dominated by the surface free energy contribution of the $\alpha$-$\beta$ interface, which encloses the bridge, because the surface area increases linearly upon stretching the interface. (The concomitant increase of the bridge volume does not generate a free energy cost because the two bulk phases $\alpha$ and $\beta$ are in thermal equilibrium.) In fact, the slope $\partial G/\partial\Delta = -\mathcal{K}$ of the scaling function matches exactly the interfacial tension contribution $\mathcal{K}_\sigma$ to the scaling function $\mathcal{K}$ of the force (see Eq. (5.10)).

In order to verify this, we start by identifying within MFT the interfacial contribution

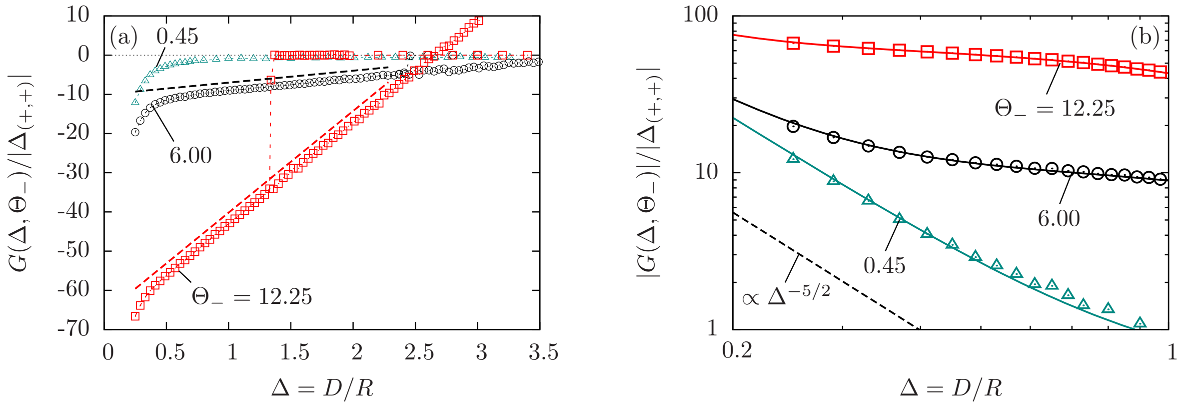

Figure 5.4: Normalized scaling function $G$ (Eq. (5.8)) of the effective potential between two cylindrical parallel colloids. In (a) $G$ is plotted as a function of $\Delta$ for three rescaled temperatures $\Theta_-$. The data points are numerical MFT results. The red data points, which form a line with a significant slope, correspond to the free energy branch of the bridged state. The red data points close to zero correspond to the weak interaction of the separated configuration. The bridged state prevails upon increasing $D$ from small values whereas the separated state prevails upon decreasing $D$ from large values. The thin vertical dashed line at $\Delta \simeq 1.27$ serves as a guide for the eye indicating the corresponding hysteretic behavior. (Its pendant, dropping off to zero from the positive part of the red line, is located at $\Delta > 3$ which has not been reached numerically and thus is not shown.) For $\Theta_- = 6.00$ and $\Theta_- = 0.45$ for reasons of clarity only the data for the bridged state are shown. Note that here the surface free energy $2\,\Omega_{s,c}^{(\beta)}$ is subtracted from the definition of $G$ (see Eqs. (5.1) and (5.8)), so that $G = 0$ corresponds to the free energy of the state of two completely separate colloids. The transition distance $D_t/R$ is determined by $G = 0$ so that $D_t(\Theta_- = 12.25)/R \simeq 2.7$. Upon increasing $D$, the bridged state may extend beyond the transition point given by the position of the intersection of the two branches. On the other hand, the separated state may exist as a metastable state for the two colloids pushed together closer than the transition distance. The intermediate region is dominated by the cost of stretching the interface enclosing the bridge which leads to the linear increase of $G$; the slopes match perfectly with the surface tension contribution to the force (see Eq. (5.14) and the thick dashed lines). See the main text for an in-depth discussion of this functional behavior. (b) The same data as in (a) but here $|G|$ is shown on double-logarithmic scales for separations $\Delta \leqslant 1$. The open symbols represent full, numerical data, and the solid colored lines are the Derjaguin approximations thereof. There is a tendency of the MFT results and of the Derjaguin approximation to more closely follow, on these scales, a straight line for $\Theta_- \to 0$, i.e., $T \to T_c$. This indicates the power law $G(\Delta \to 0) \propto \Delta^{-(d-3/2)}$ (see Eqs. (5.8) and (5.9)), i.e., $\propto \Delta^{-5/2}$ for $d = 4$ (black dashed line). For further discussions see the main text.

to the force for a rigid interface. Increasing the separation between the cylinders by an infinitesimal amount $\mathrm{d}D$ increases the interface area by $\mathrm{d}A = 2\,\mathcal{L}\,\mathrm{d}D$, which corresponds to adding two rectangular stripes of area $\propto \mathrm{d}D$ each. In accordance with Eq. (5.10) the interfacial tension is

$$\sigma = \frac{\mathrm{d}\Omega_i}{\mathrm{d}A} = \frac{1}{2\mathcal{L}}\frac{\mathrm{d}\Omega_i}{\mathrm{d}D} = -\frac{1}{2}\,\frac{k_B T}{R^{d-1}}\,\mathcal{K}. \tag{5.12}$$

Near $T_c$ the interfacial tension scales as $\sigma = \sigma_0\,|t|^{(d-1)\nu}$ where $\sigma_0$ is a non-universal amplitude [159]. The interfacial tension can be written in terms of quantities introduced in Sec. 5.1:

$$\frac{\sigma}{k_B T} = R_\sigma \left(\xi_0^+\right)^{-(d-1)} |t|^{\mu}, \tag{5.13}$$

where $R_\sigma = 4\sqrt{2}\,u^{-1} = 4\sqrt{2}\,|\Delta_{(+,+)}|/283.61$ and $\mu = (d-1)\nu = 3/2$ for $d = 4$ [143]. Therefore, the interfacial tension contribution to $\mathcal{K}$ can be written as

$$-\mathcal{K}_\sigma = \frac{2R_\sigma}{R_\xi^{d-1}} \left(\frac{R}{\xi_-}\right)^{d-1} = \frac{R_\sigma}{\sqrt{2}} (\Theta_-)^3 = \frac{|\Delta_{(+,+)}|}{70.9} (\Theta_-)^3, \tag{5.14}$$

in terms of the scaling variable $\Theta_-$ and using $R_\xi = \sqrt{2}$ in $d = 4$. In Fig. 5.4(a) the linear relation $(-\mathcal{K}_\sigma)\Delta$ is indicated by thick dashed lines for each rescaled temperature $\Theta_-$. The slopes agree perfectly with the numerical results, considering especially that $\mathcal{K}_\sigma/\Delta_{(+,+)}$ depends only on $\Theta_-$ and the a priori fixed amplitude $(70.9)^{-1}$. This confirms that the interface tension is the dominant contribution to the scaling function $G$ of the potential for intermediate separations $\Delta$.

(iii) At very close separations ($\Delta \leq 0.5$), there is a strongly attractive force $\propto \frac{\partial G}{\partial \Delta}$ which is stronger than the one required to stretch, upon increasing $\Delta$, the area of the $\alpha$-$\beta$ interface enclosing the bridge. The enhancement of the effective potential is found to be driven by the critical Casimir effect. Since the deviations become significant only for $\Delta = D/R \to 0$, corresponding to the limit of large colloids, due to their small curvature the surfaces resemble two planar parallel walls. One expects that in this limit the effective potential for two colloids can be expressed in terms of the critical Casimir forces in the film geometry. This approach can be implemented by using the so-called Derjaguin approximation (see, e.g., Refs. [69, 70, 74]). For two cylinders with the same adsorption preference immersed in a near-critical solvent, the effective potential is given by (see Eq. (5.8))

$$\frac{\Omega_i}{k_B T} = \frac{\mathcal{L}}{R^{d-2}} G(\Delta, \Theta_-), \tag{5.15}$$

where

$$G(\Delta, \Theta_-) = \Delta^{-(d-3/2)}\, \Phi^{(cc)}_{(+,+)}(\Delta, \Theta = \Theta_- \Delta), \tag{5.16}$$

and within DA the scaling function of the potential is found to be

$$\begin{aligned}\Phi^{(cc)}_{(+,+)}(\Delta, \Theta) = 2 \int_1^\infty & \mathrm{d}\eta\, \sqrt{\eta - 1}\, \eta^{-d}\, k_{(+,+)}(\eta\,\Theta) \\ & - 2 \int_{1+\Delta^{-1}}^\infty \mathrm{d}\eta \left(\sqrt{\eta-1} - \Delta^{-1/2}\right) \eta^{-d}\, k_{(+,+)}(\eta\,\Theta),\end{aligned} \tag{5.17}$$

where $k_{(+,+)}$ is the scaling function of the CCF between two planar walls with equal

(+) boundary condition [103]. The full details of the Derjaguin approximation for two cylinders are presented in Appendix A. In Fig. 5.4(b) we plot the effective potential for small interparticle separations and compare it with the Derjaguin approximation for two cylinders (note the double-logarithmic scales of the axes which facilitate to resolve the observed behavior). The agreement between the numerical data (open symbols) and the analytical prediction obtained via the Derjaguin approximation (solid lines) is very good for all three rescaled temperatures studied in the range $\Delta < 1$. The emergence of long-ranged correlations upon approaching $T_c$, i.e., $\Theta \to 0$ gives rise to the intuitive expectation that the Derjaguin approximation is valid even for $\Delta \lesssim 1$. Indeed, this behavior becomes more pronounced for the rescaled temperature $\Theta_- = 0.45$, i.e., closer to $T_c$. Here, the agreement is very good, even for larger values of $\Delta$. The power-law behavior $\propto \Delta^{-(d-3/2)}$ of the effective potential emerges clearly, as predicted by the DA. This observation is also in agreement with the down-shift of the critical point which occurs for finite size systems undergoing capillary condensation: [160] For symmetry breaking boundary conditions at the surfaces, the film critical point is shifted both in temperature (towards *lower* $T_c(D) < T_c(\infty) = T_{c,\text{bulk}}$) and composition of the solvent such that for small separations between the colloids, i.e., for $\Delta \lesssim 0.5$, CCF are present even for temperatures which can be considered as being not close to the *bulk* critical point of the solvent. For larger $\Delta$, this behavior crosses over to the regime linear in $\Delta$ within which the free energy cost of stretching the interface of the bridge dominates the effective potential.

Considering again Fig. 5.4(a), for the intermediate rescaled temperature, $\Theta_- = 6.00$, the trends in behavior are qualitatively very similar to those in the previous case $\Theta_- = 12.25$. The major difference is that close to $T_c$ the strength of the effective interaction, which is the magnitude of the scaling function $G(\Delta \to 0)$, is reduced. For the temperature closest to the critical point, i.e., $\Theta_- = 0.45$, there is a very gradual increase of the effective potential upon increasing $\Delta$. Therefore, upon approaching the critical point $\Theta_- = 0$, the distinction between the three regimes discussed above becomes blurred.

In sum, we have found that for cylindrical, parallel colloidal particles connected by a liquid bridge the effective interaction potential exhibits three distinct regimes concerning its dependence on the surface-to-surface distance. There is a power-law behavior at small distances caused by slab-like CCF, which crosses over to a linear regime reflecting the stretching of the interfacial area of the bridge, followed by a rupturing of the liquid bridge connecting the colloids. Upon approaching $T_c$, these regimes become less distinct. The clear distinguishability of these three regimes is a virtue of the cylindrical geometry. As discussed briefly, in the case of two spheres a stable bridge forms which has a thinner neck between the colloids. In this latter case stretching the associated interface does not result in a linear increase of the surface free energy and thus the scaling function $G$ of the effective potential is not a linear function of the separation $\Delta$. This more complicated dependence may mask the critical Casimir contribution. Furthermore, MFT

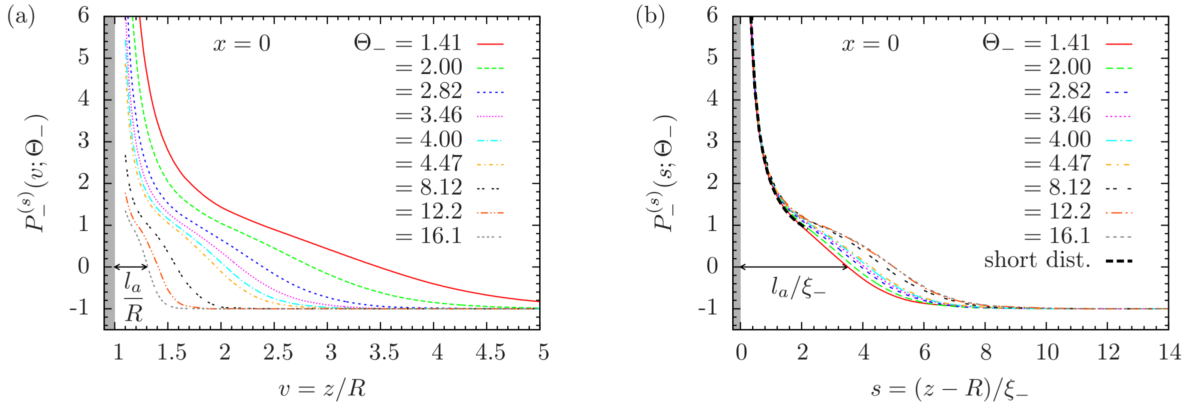

Figure 5.5: (a) The MFT scaling function $P_-^{(s)}(v = z/R; \Theta_- = R/\xi_-)$ (Eq. (5.19)) of the order parameter at the outside of a *single* colloid as function of the distance $z$ along $x = 0$ in units of the particle radius $R$, for various rescaled temperatures $\Theta_- = R/\xi_-$. The colloidal particle is indicated by the gray region $v = z/R < 1$. Each color and line style represents an order parameter profile for a given rescaled temperature $\Theta_-$. At $z = R + l_a$, the scaling function crosses $P_-^{(s)}(s = l_a; \Theta_-) = 0$ so that $l_a$ is the adsorption layer thickness. (b) Same as (a), but in terms of the scaling variable $s$, i.e., $(z - R)$ scaled in units of the correlation length $\xi_-$. Close to the surface of the particle, in the regime of strong adsorption, i.e., $s < 1$, the scaling functions $P_-^{(s)}(s; \Theta_-)$ for different rescaled temperatures $\Theta_-$ collapse onto the short distance approximation given in Eq. (5.20), the leading order of which depends on $s$ only (black dashed curve). On the other hand, around the emerging $\alpha$-$\beta$ interface, i.e., $z \approx R + l_a$, this is not the case. This shows that $P_-^{(s)}$ is a scaling function depending indeed on *two* independent scaling variables.

does not capture fluctuation effects. The first-order transition between the bridged and the separated state is expected to be smeared out due to finite-size induced fluctuations [161–163], to the effect that the adsorbed volume around and between the colloids changes sharply but continuously over a small range of $\Delta$, instead of doing so abruptly. We shall address this point in more detail in Sec. 5.6 after the discussion of the mean field results for the bridging transition.

## 5.4 Single particle order parameter profiles

From the previous view of the order parameter profiles and the scaling function $G$ of the effective potential, it is evident that for each rescaled temperature $\Theta_-$ there is one critical separation $D_t$ for which the free energy of the bridged and the separated state are equal, implying a first-order bridging transition. Thus, a complete description of the bridging transition cannot be an inherent property of the coupled *two*-particle state only, but must also take into account the state of two separated *single*-colloids.

Before discussing in detail the first-order bridging transition, we first consider the feature of the “halos” which grow around the separated colloids upon approaching $T_c$. As seen in Figs. 5.2(b) and 5.3(b), for $D \gtrsim D_t$ the order parameter distribution around each colloid is visually unaffected by the presence of the other colloid. In the absence of colloids and surfaces and in the phase separated regime $t < 0$ in which the two phases coexist, the mean field bulk values of the order parameter are given by $\langle\phi\rangle_{\alpha,\beta} = \pm\mathcal{B}\,|t|^{1/2}$, or in terms of the scaling function, by $P_- = \pm 1$. Generally, the superposition of two *single*-particle order parameter profiles $\phi_s$ provides a reliable estimate of the *two*-particle order parameter profile only for two distant colloidal particles:

$$\phi(\mathbf{r},t) \approx [(\phi_s(\mathbf{r},t) - \langle\phi\rangle_\beta] + [\phi_s(\mathbf{r}-\mathbf{r_{12}},t) - \langle\phi\rangle_\beta] + \langle\phi\rangle_\beta \qquad (5.18)$$
$$\text{for } D = |\mathbf{r_{12}}| - 2R \to \infty,$$

where $\mathbf{r_{12}}$ is the vector connecting the centers of the two colloids; note that $\phi_s(|\mathbf{r}| \to \infty, t) = \langle\phi\rangle_\beta$. For finite distances, even in the separated state the halos around the two colloids still interact with each other via mutual deformation of the halos. This is not captured by Eq. (5.18). However, this interaction is exponentially small away from $T_c$. As it turns out, for $\Theta_- \gg 1$ this decomposition into two *single*-particle profiles is valid down to the transition distance $D_t$. In this non-critical regime, $D = D_t$ is large compared to the extension of the halos in the *single*-particle profiles.

The order parameter profile $\phi_s(\mathbf{r},t)$ around a *single* cylindrical colloid exhibits the scaling form

$$\phi_s(\mathbf{r} = \{x,y,z\},t) = \mathcal{B}\,|t|^\beta\, P_-^{(s)}\left(s = \frac{\sqrt{x^2+z^2}-R}{\xi_-}; \Theta_- = \frac{R}{\xi_-}\right), \qquad (5.19)$$

with the origin $(x = 0, z = 0)$ located at the center of the colloid. Using the relations $u/6 = 1/(\mathcal{B}\xi_0^+)^2$, $\tau = -|t|/(\sqrt{2}\,\xi_0^-)^2$, and $\xi_0^+ = \sqrt{2}\,\xi_0^-$ (see Sec. 2.1.3) the scaling function $P_-^{(s)}$ can be expressed in terms of $m_-$ as $P_-^{(s)} = m_-/\sqrt{|\tau|}$ which does not depend on the non-universal MFT parameter $u$. In order to proceed, we have to analyze as a function of temperature the thickness of the wetting layer formed by the $\alpha$ phase, which encapsulates the single colloid. Without loss of generality, we can simplify the notation by considering the scaling function $P_-^{(s)}(s = (z-R)/\xi_-; \Theta_- = R/\xi_-)$ at a given rescaled temperature $\Theta_-$ along the $z$ axis at $x = 0$.

In Fig. 5.5 we show this cut of the MFT scaling function $P_-^{(s)}(s;\Theta_-)$ for a *single* particle as a function of the rescaled temperature $\Theta_-$. The surface of the particle strongly prefers the $\alpha$ phase, so that $P_-^{(s)}(s \to 0; \Theta_-) = +\infty$. Far away from the particle surface, i.e., for $z \gg R$, the order parameter $\phi_s$ smoothly approaches its bulk value corresponding to the $\beta$ phase, which implies a decay of the scaling function towards $P_-^{(s)}(s \to \infty; \Theta_-) = -1$. In Fig. 5.5(a), the scaling function $P_-^{(s)}$ is shown as a function of the scaling variable $v = z/R$. Closer to the critical point, i.e., for smaller values of $\Theta_-$, the length scale on which the order parameter approaches its bulk value $P_-^{(s)} = -1$ increases significantly, illustrating that the thickness of the wetting layer around the colloid increases as the temperature approaches $T_c$. This is accompanied by a decrease of the slope of the scaling function as a function of $z$, so that the bulk value corresponding to the $\beta$ phase is also attained more slowly upon approaching $T_c$. In contrast, Fig. 5.5(b) depicts the spatial variation of $P_-^{(s)}$ in terms of the correlation length $\xi_-$ using the scaling variable $s = (z - R)/\xi_-$. In the regime dominated by the strong adsorption close to the surface of the particle, the family of scaling functions for different rescaled temperatures $\Theta_-$ collapses onto a single curve. This regime is well captured by the short-distance approximation for the normalized MFT order parameter $m(z \to 0, R, \tau)$ [36, 99]. For the scaling function $P_-^{(s)} = m_-/\sqrt{|\tau|}$ of a *single* cylinder embedded in spatial dimensions $d = 4$ one has

$$P_-^{(s)} \left( s = \frac{z - R}{\xi_-} \to 0; \Theta_- \right) \approx \frac{2}{s} + \frac{s}{6} - \frac{1}{3}\, s/\Theta_- + \frac{5}{36}\,(s/\Theta_-)^2 . \tag{5.20}$$

The leading order of the short distance approximation is $\propto s^{-1}$, so that the range of the strong adsorption behavior scales proportionally to $\xi_-$ (see the black dashed curve in Fig. 5.5(b)).

However, upon approaching $T_c$ the total adsorption layer thickness $l_a$, which takes into account also the thickness of the emerging $\alpha$-$\beta$ interface around the colloid, increases weaker than the bulk correlation length $\xi_-$ (see the numerical data in the upper panel of Fig. 5.6(a)). Divided by $\xi_-$, the extent of the adsorption layer formed by the $\alpha$ phase does not attain a constant but diminishes upon decreasing $\Theta_-$, i.e., moving towards the critical point (see the numerical data in the lower panel of Fig. 5.6(a)). In order to quantify the temperature dependent changes in the adsorption layer, we define the total adsorption layer thickness $l_a$ via the zero-crossing criterion $P_-^{(s)}(s = l_a/\xi_-; \Theta_-) = 0$. The dependence of $l_a$ on $\Theta_-$ is shown in Fig. 5.6(a).

These numerical data can be rationalized analytically by considering the limit $\xi_- \ll R$ or $\Theta_- \gg 1$. In this limit of being further away from $T_c$ the adsorption layer turns into a wetting film with a quasi-sharp $\alpha$-$\beta$ interface. The cost of free energy to keep this interface, at $\alpha$-$\beta$ coexistence, at a prescribed distance from the cylindrical colloid surface is given by the effective interface potential $V_{\text{inter}}(l) = V_{\text{rep}}(l) + V_c(l)$. In leading order $V_{\text{rep}}(l) = v_0\, \mathcal{L}\, e^{-l/\xi_-}$, with an energy per length $v_0 > 0$, describes the effective repulsion of the interface from the surface, in accordance with complete wetting at a planar wall. At curved surfaces, this growth of $l$ is counterbalanced by the free energy cost of extending the area of the interface: [162] $V_c(l) = \sigma[2\pi(R + l) - 2\pi R]\mathcal{L} = 2\pi\sigma\, l\, \mathcal{L}$ where $\sigma$ is the surface tension of the free $\alpha$-$\beta$ interface (Eq. (5.13)). The equilibrium adsorption layer thickness $l_a$ minimizes $V_{\text{inter}}(l)$, resulting in [41, 162, 164]

$$l_a = \xi_-\, \ln(a/\xi_-), \;\text{ or }\; \frac{l_a}{R} = \frac{1}{\Theta_-}\, \ln\left(\Theta_- \frac{a}{R}\right), \;\text{ for }\; \xi_- < a, \Theta_- \gg 1, \tag{5.21}$$

with the length $a = v_0/(2\pi\sigma)$ [162]. Figure 5.6(a) demonstrates that in the limit $\Theta \gg 1$, the numerical data indeed approach the result in Eq. (5.21) (see the dashed green lines).

Interestingly, Fig. 5.6(b) shows that within the region $(z - R)/l_a \gtrsim 0.5$ the order parameter profile exhibits features which strongly resemble those of the order parameter profile of the free $\alpha$-$\beta$ interface. Inserting the mean field interface $m$ between the two coexisting bulk phases [143, 159], with the interface positioned at $z = R + l_a$, into the scaling function $P_- = m_-/\sqrt{|\tau|}$ yields the form

$$P_-(z) = -\tanh\left(\frac{z - (R + l_a)}{2\xi_-}\right) = -\tanh\left(\frac{l_a}{2\,\xi_-}\left(\frac{z - R}{l_a} - 1\right)\right). \tag{5.22}$$

Note that $P_- = \pm 1$ corresponds to the two coexisting bulk phases. In Fig. 5.6(b), Eq. (5.22) is indicated by a black dashed line, which follows closely the profile of the adsorption layer around a *single* colloid. The second expression in Eq. (5.22) indicates that in terms of $(z - R)/l_a$ in Fig. 5.6(b), $l_a$ does not only determine the position of the adsorption layer interface, but also the width of the interface profile via $l_a/\xi_-$. However, as seen in the lower panel of Fig. 5.6(a), the logarithmic corrections turn out to vary only slightly within the inspected range of the rescaled temperature $\Theta_-$, so that in Fig. 5.6(b) the width of the total adsorption layer remains rather similar. For $\Theta_- \to 0$, it is expected that $l_a \propto \xi_-$ without logarithmic correction [162, 164], which is in line with the deviations of $l_a$ from Eq. (5.21) closer to the critical temperature (see Fig. 5.6(a)). However, due to numerical constraints we cannot fully resolve this change in behavior for $\Theta_- \ll 1$.

Thus, the *single*-particle profile can be viewed as being composed of the profile corresponding to the wall-$\alpha$ interface, dominated by the boundary condition and the corresponding short distance approximation (Eq. (5.20)), and the free $\alpha$-$\beta$ interface profile (Eq. (5.22)). At this stage, by using the total adsorption layer thickness $l_a$ taken from the *single* colloidal system, the issue arises whether this composite profile allows one to predict the distance $D_t$ at which the liquid bridge between two colloids breaks.

## 5.5 Bridging transition

Having discussed the *two*-colloid order parameter profiles for the bridged and the separated state as well as the *single*-colloid profile, which approximates the separated *two*-colloid state (see Eq. (5.18)), we turn to the analysis of the transition distance $D_t$ between the two configurations. Considering the scaling function $G$ of the effective potential (see Fig. 5.4), it is evident that for each rescaled temperature $\Theta_-$, there is a single separation $D_t$, for which the free energy of the bridged and the separated state are equal, leading to a first-order bridging transition. According to Fig. 5.4, the transition distance $D_t$ is determined by the zero of $G(D_t/R, \Theta_-) = 0$. (Strictly speaking, $G = 0$ corresponds to the completely separated state with macroscopically large distances $D$. At the finite distance $D = D_t$, $G = 0$ corresponds only approximately to the separated state, equivalent in

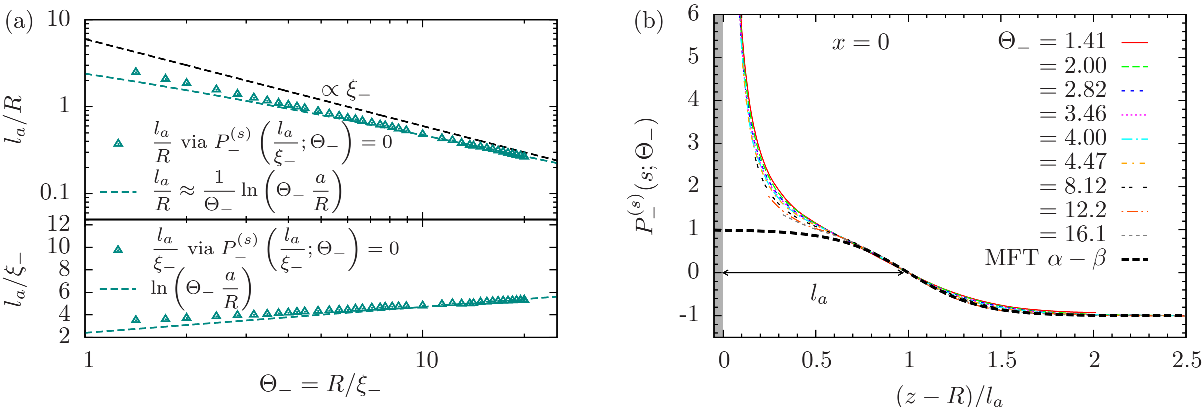

Figure 5.6: (a) The adsorption layer thickness $l_a$ as determined via $P_-^{(s)}(s = l_a/\xi_-;\Theta_-) = 0$ from the OP profiles of a *single* particle (green triangles), shown in units of the radius $R$ in the upper panel and in units of the correlation length $\xi_-$ in the lower panel. Away from the critical point, i.e., for $\Theta_- \gg 1$, the adsorption layer thickness increases as $l_a/R \approx (1/\Theta_-)\ln(\Theta_-\, a/R)$ (dashed green curve; see Eq. (5.21)). The length $a$ depends on the system-specific repulsion strength and interface tension (see the derivation in the main text). We have found $a/R = 11.15$ from a fit to the adsorption layer thickness. The thickness $l_a$ deviates from a linear dependence on the correlation length $\xi_-$ (dashed black line in the upper panel or a constant in the lower panel) by a logarithmic correction highlighted in the lower panel. This reinforces the expected observation that the scaling variable $s = (z-R)/\xi_-$ is not sufficient to describe the full *single*-particle profile. (b) The *single*-colloid profiles as in Fig. 5.5, but scaled in units of the adsorption layer thickness $l_a$. By construction, the interface crosses zero at $(z-R)/l_a = 1$ for all rescaled temperatures $\Theta_-$. Notably, in these units the width of the interface is very similar for a wide range of values of $\Theta_-$. For distances not too close to the surface the adsorption layer strongly resembles the free $\alpha$-$\beta$ interface profile (dashed black curve), which has a tanh functional form and a width of $l_a/\xi_-$ (see Eq. (5.22)). The weak dependence of $l_a/\xi_-$ on $\Theta_-$ leaves the width of the adsorption layer profile to be very similar within the range of temperatures shown here.

spirit to Eq. (5.18), which holds for $\Theta_- \gg 1$.) Upon decreasing $\Theta_-$, the intersection of $G$ with the abscissa moves to larger values of $\Delta = D/R$, which poses an issue as the size of the numeric calculation box has to be increased accordingly. However, even in the case that the transition distance $D_t$ between the bridged and the separated state exceeds the chosen size of the calculation box, it nonetheless can readily be obtained also for values of the rescaled temperature $\Theta_- \gtrsim 1$ by extrapolating linearly the regime dominated by the interfacial tension and thus finding the zero of $G(D_t/R,\Theta_t) = 0$.

By employing this procedure, we have obtained the transitions distances $D_t(\Theta_-)$ in Fig. 5.7(a), which constitute a phase diagram: At a fixed rescaled temperature (vertical dashed line), for small distances $D < D_t$, the two colloids are connected by a bridge. Upon increasing the distance $D$ beyond $D_t$, a first-order transition to the separated state occurs. On the other hand, for a fixed distance (dashed horizontal line), far away from $T_c$, i.e., $\Theta_- \gg 1$, one finds two separate particle profiles (if $D > D_{\min}$, which is discussed

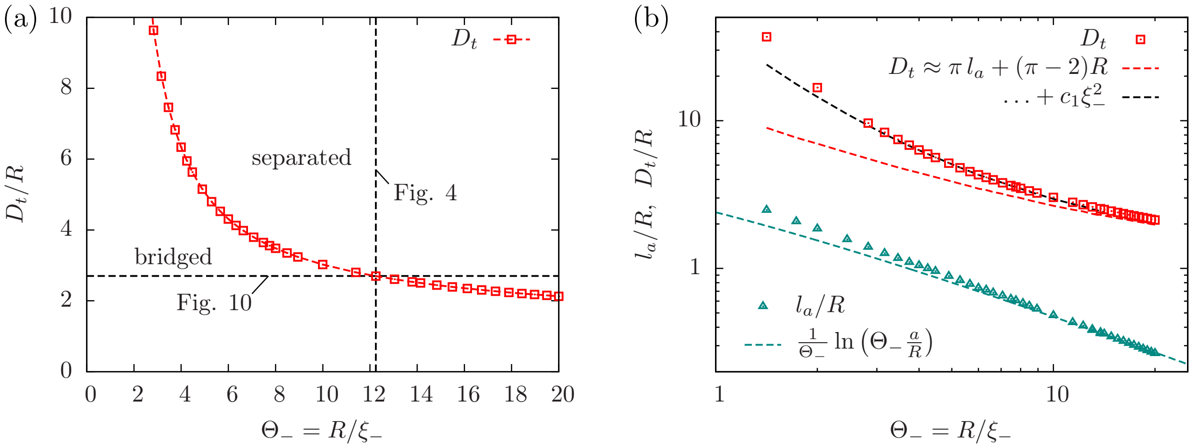

Figure 5.7: (a) Phase diagram with the transition distance $D_t(\Theta_-)$ marking the first-order transition between the separated and the bridged states. Upon varying the rescaled temperature $\Theta_- \to 0$, a bridge forms between two colloids upon crossing $D_t$. However, for small separations $D < D_{\text{min}}$, the bridged state occurs independent of the temperature around $T_c$. The vertical dashed line indicates the case $\Theta_- = 12.25$ studied in Fig. 5.4 and the horizontal dashed line indicates the case $\Delta = 2.7$ studied in Fig. 5.10. (b) The transition distance $D_t(\Theta_-)$ (red symbols) and the adsorption layer thickness $l_a$ (green symbols; the green dashed line represents Eq. (5.21)) as a function of $\Theta_-$ in a double-logarithmic plot. In the non-critical limit $\Theta_- \gg 1$, $D_t$ tends to follow the geometric prediction of $D_t \approx \pi\, l_a + (\pi - 2)R$ (dashed red curve). The geometric model is expected to break down close to $T_c$. An additional argument valid in the critical regime of small $\Theta_-$ limits the highest order of an expansion of $D_t$ in terms of $\Theta_- = R/\xi_-$ to the second order (see the blacked dashed line and the main text).

below). Upon approaching the critical temperature, as the correlation length $\xi_-$ grows, a first-order transition occurs to the bridged state. Of course, both realizations can be performed in reverse, i.e., decreasing the distance $D$ at fixed $\Theta_-$ and moving away from $\Theta_- = 0$ at a fixed distance $D$. The two directions for changing the temperature correspond to the two thermodynamic paths actually used (see the main text devoted to Fig. 5.4) in order to obtain the metastable branches seen in Fig. 5.4(a).

There is a minimum distance $D_{\text{min}}$, below which only the bridged state occurs. This corresponds to a non-critical, geometric situation in which close to contact of the two cylinders, i.e., for $D \to 0$, due to their curvature an inward groove is formed on each side of the composite body, which is bridged and filled completely by the phase favored by the colloids, reminiscent of capillary condensation and wedge wetting [165, 166]. For near-critical order parameter distributions in such structures see Refs. [167, 168].

In Fig. 5.7(b) we show the transition distance $D_t$, and for comparison the adsorption layer thickness $l_a$, on double-logarithmic scales. At non-critical conditions away from $T_c$, it is possible to construct a geometric model for the bridging transition: For two *single*-particle profiles, the adsorption layers generate an interfacial area of $A_{\text{sep}} = 2{\times}2\pi(R{+}l_a)\mathcal{L}$, where $\mathcal{L}$ is the length of the cylindrical particles and where the acronym sep stands for "separated". On the other hand, for the bridged state seen in Figs. 5.2(a) and 5.3(a), the structure of the two outer halves is still very similar to the adsorption layer halos around the separated particles, which amounts to an area $A_{b,1} \approx A_{\mathrm{sep}}/2$; the acronym b stands for "bridged". The difference is only the straight bridge, which has an interfacial area of $A_{b,2} = 2 \times (D + 2\,R)\mathcal{L}$. For $D = D_t$, the free energy of the bridged and the separated state are required to be equal. If we attribute this free energy solely to the interfacial free energies $\sigma(A_{b,1} + A_{b,2})$ and $\sigma A_{\mathrm{sep}}$, respectively, this leads to $2 \times (D_t + 2\,R)\mathcal{L} = 2\pi(R + l_a)\mathcal{L}$, so that

$$D_t = \pi\, l_a + (\pi - 2)R. \tag{5.23}$$

We note that this relation has been obtained similarly in Ref. [45] also for two cylinders and that Eq. (4.2) in Ref. [43] provides a related expression for the case of two spheres. Furthermore, Ref. [48] derives an analogue of the Kelvin equation based on a macroscopic thermodynamic picture, which holds more generally for any contact angle and bulk field $h \neq 0$ (i.e., chemical potential difference $\Delta\mu \neq 0$), but is specific to block-shaped particles. In comparison with our results, the effective block size $b^*$ in Ref. [48] can be identified with half the circumference $\pi(R + l_a)$ formed by the adsorption layer around one colloid.

We emphasize that the transition distance $D_t$ distinguishes the two possible configurations of the *two*-colloid state. Within the geometric estimate of Eq. (5.23), $D_t$ is determined solely by properties of the *single*-particle profile, namely the adsorption layer thickness $l_a$ and the radius $R$. This estimate is indicated by the dashed red line in Fig. 5.7(b), which is asymptotically approached by $D_t$ (red symbols) for $\Theta_- \gg 1$. Away from criticality, i.e., for $\Theta_- \to \infty$ the adsorption layer thickness $l_a$ becomes microscopically small, i.e., $l_a \to 0$, but the surfaces remain strongly adsorbing. Within this approximation and in this limit, we arrive at $D_{\min} = \lim_{l_a \to 0} D_t = (\pi - 2)R$. Thus, having the two colloids in contact, i.e., $D = 0$, amounts to being below the bridging transition, corresponding to the filling of a completely wetted wedge (with contact angle $\theta = 0$). For comparison, $l_a$ (green symbols) and its approximated expression in Eq. (5.21) (green dashed line) are also shown in Fig. 5.7(b). Thus, the surprising answer to the pending question of the previous section is, that it is possible to predict the transition distance based on *single*-particle properties, at least in a low-order estimate.

In contrast, for $\Theta_- \to 0$ as expected the geometric interpretation fails. Upon approaching the critical point, the surface tension $\sigma$ decreases as $\sigma \propto \xi_-^{-(d-1)} \propto |t|^{(d-1)\nu}$ (see Eq. (5.13)), so that for $t \to 0$ the contributions to the free energy from the interfacial tension vanish. Accordingly, another contribution to the free energy takes over. Even though the profiles lack a clear interface at $T = T_c$, the *single*-order parameter profiles of two colloids cannot be brought too close without raising an energetically unfavorable overlap.

In view of the linear variation of $G$ in Fig. 5.4, we determine $D_t$ by linearly extrapolating $\Omega_i \sim G$. From $G(D_t/R, \Theta_-) = 0$, it follows that

$$(-F_\sigma)D_t + \Omega_0^{(b)} = 2\,\Omega_{s,c}^{(\beta)}, \tag{5.24}$$

with the force $F_\sigma = k_B T\,\mathcal{L}\,R^{-(d-1)}\mathcal{K}_\sigma$ (see Eq. (5.10)) and an extrapolated offset contribution $\Omega_0^{(b)}$ for the *b*ridged configuration.

Equation (5.24) implies (see Eq. (5.14))

$$D_t = \frac{2\,\Omega_{s,c}^{(\beta)} - \Omega_0^{(b)}}{(-F_\sigma)} \sim \Theta_-^{-(d-1)}(2\,\Omega_{s,c}^{(\beta)} - \Omega_0^{(b)}). \tag{5.25}$$

Since the slope of $\Omega_i$ with respect to $D$ in the bridged state decreases to zero for $t \to 0$, the extrapolated offset $\Omega_0^{(b)}$ acquires a physical meaning because it attains the same value as the free energy of the bridged state at infinite separation, i.e., $\Omega_i(D \to \infty, \Theta_- = 0) = \Omega_0^{(b)}$. Furthermore, at infinite separation and at $t = 0$, the separated and the bridged state have the same free energy because the break in symmetry disappears at $T = T_c$ and the $\alpha$ and $\beta$-phases become indistinguishable. Thus, it follows that $2\,\Omega_{s,c}^{(\beta)} - \Omega_0^{(b)} \to 0$ for $t \to 0$ so that one can propose the expansion ansatz $2\,\Omega_{s,c}^{(\beta)} - \Omega_0^{(b)} = d_1\,\Theta_- + d_2\,\Theta_-^2 + d_3\,\Theta_-^3 + \mathcal{O}\left(\Theta_-^4\right)$ which fulfills this limiting behavior. For $d = 4$, this leads to the expansion

$$D_t = c_1\,\Theta_-^{-2} + c_2\,\Theta_-^{-1} + c_3 + \mathcal{O}\left(\Theta_-\right), \quad \Theta_- \to 0, \tag{5.26}$$

for the transition distance $D_t$. Thus, it follows that in leading order the divergence of the transition distance is proportional to $\Theta_-^{-2}$. Note that one expects for the adsorption layer thickness $l_a \propto \xi_- \propto \Theta_-^{-1}$ for $\Theta_- \to 0$, so that the next-to-leading order term $\propto \Theta_-^{-1}$ of $D_t$ corresponds to $l_a$. In this sense, Eq. (5.26) is a generalization of the geometrical approximation in Eq. (5.23), but limited to the next higher order $\propto \Theta_-^{-2}$. This is shown by the black dashed line in Fig. 5.7(b), in excellent agreement with the enhancement of $D_t$ for $\Theta_- \to 0$. Still, we must remark that the argument based on the vanishing break in symmetry at $T = T_c$ assumes the bulk behavior for the surrounding liquid which, however, is only an approximation. The asymptotic limit $R/\xi_- \to 0$ is tantamount to the case of the vanishing radius $R$ of the cylindrical particles. However, one does not obtain the bulk system for infinitely thin cylinders. The presence of the two particles effectively alters the critical point of the surrounding liquid and the order parameter deviations near the surfaces do not vanish in the limit $R/\xi_- \to 0$ [143].

In sum, the behavior of the transition distance $D_t$ provides the phase diagram of the bridging transition. Generally, for large separations $D$ and large deviations from $T_c$, the separated state is the thermodynamically stable configuration. For close distances and close to $T_c$, the two colloids are connected by a bridge consisting of the preferred phase. In principle, within MFT the transition between the two states is always first order. A specific feature of cylindrical colloids is that even away from $T_c$, with microscopically thin adsorption layers around the colloids, but at bulk coexistence, this bridge is stable for *all* $\Theta_- > 0$ if the separation is smaller than $D_{\min} = (\pi - 2)R$. According to Ref. [45], a deviation from bulk coexistence alters the slope of $D_{\min}$ with respect to $R$.

## 5.6 Fluctuation effects

As mentioned before, MFT neglects fluctuation effects, which will smear out the first-order bridging transition [43, 161–163]. The excess adsorption is an adequate order parameter for the first-order bridge-separation transition. It is given by the integrated density of component A around the two colloids, relative to the density of the separated configuration. Thus, the OP is zero in the separated state and attains a finite value (depending on the rescaled temperature) upon bridge formation. The adsorbed volume forming the bridge between the particles scales with the $(d-2)$ dimensional length of the cylindrical particles; thus it is quasi-two-dimensional for $d = 4$ and quasi-one-dimensional in $d = 3$. Within the Ising universality class, for $d \leq d_{lc}$, i.e., below the lower critical dimension $d_{lc} = 2$, finite size effects destroy long-ranged order. Following Privman and Fisher [161], in an effectively cylindrical geometry of finite size, at the pseudo-coexistence of the macroscopically-sized separated and bridged states, one has to account for configurations in which the bridge along the length $L$ of the cylinders ($d = 3$) disintegrates into alternating domains of the bridged and separated phases, correlated over a length $\xi_{\|} \ll L$ (see Fig. 5.8). For such an inhomogeneous system the OP for the bridge-separation transition varies sharply, but continuously upon approaching the transition line $D_t(\Theta_-)$ in Fig. 5.7(a), smearing out the first-order bridging transition.

Even though in principle the first-order transition is rounded and shifted, this may experimentally be not detectable. Here we briefly discuss the expected implications in the experimentally relevant case $d = 3$ (which is also more severely affected by fluctuations than the case $d = 4$; for $d > 4$ fluctuation effects become negligible). In this context, based on Ref. [161], one has to take into account terms in the partition function which correspond to configurations which are neglected within mean field theory and thus give rise to subdominant contributions to the partition function. To this end we assume that the (partially) bridged state is the configuration which is energetically disfavored and neglected by MFT, and we adopt a simple two-state description with the partition sum

$$\tilde{Z} = e^{-\tilde{\Omega}_s/k_BT} + e^{-\tilde{\Omega}_b/(k_BT)}, \tag{5.27}$$

where $\tilde{\Omega}_s \approx 2\,\Omega_{s,c}^{(\beta)}$ (compare Eqs. (5.5) and (5.6)) is the geometric approximation of the free energy of the separated state and likewise $\tilde{\Omega}_b$ is that of the (partially) bridged state. Note that in this section, all quantities with a tilde correspond to the respective, purely

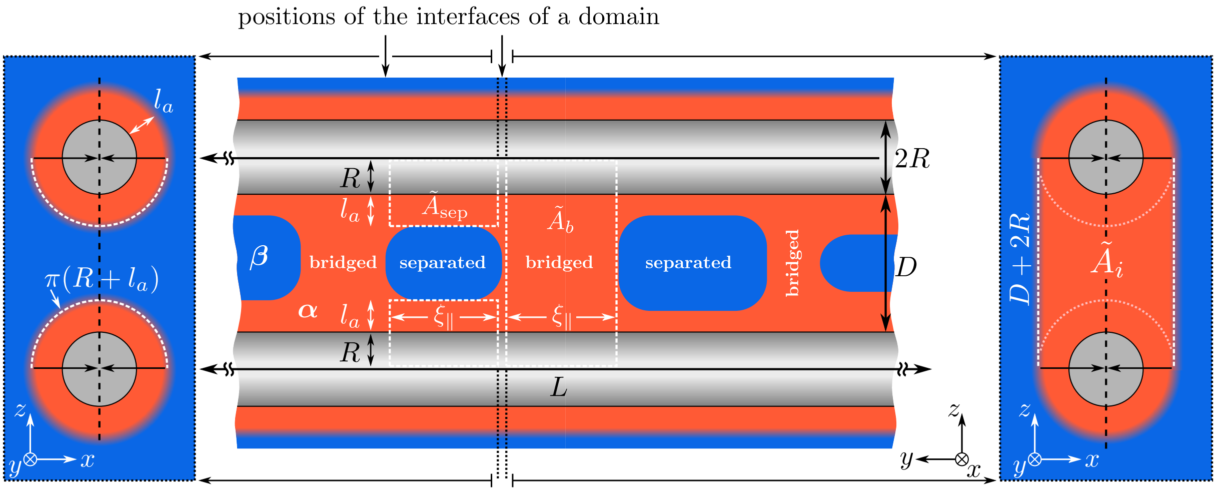

Figure 5.8: Idealized schematic cut along the vertical midplane containing the axes of the two colloids. The $\alpha$-like bridge (red) between the macroscopically large cylindrical colloids (gray) is segregated into domains of partially bridged configurations and of partially separated configurations. The latter ones are indicated as blue inclusions of varying sizes with a mean length $\xi_\parallel$. The length $L$ of the cylinders is much larger than the depicted section. On the left and on the right panels, the two different domains are compared with each other in the plane normal to the axes of the cylinders. The symmetry axes of the colloids, spanning the image plane of the central panel, are indicated by black lines. The two competing areas $\tilde{A}_{\rm sep}$ (to the left of the center, consisting of two separated, equal-sized parts) and $\tilde{A}_b$ (to the right of the center) are indicated in all three views by white dashed border lines. $\tilde{A}_{\rm sep}$ consists of two semi-cylinders of length $\xi_\parallel$ and with arc length $\pi(R+l_a)$. The projection (black arrows in the outer panels) of the two semi-cylinders onto the midplane (vertical dashed line) renders two white rectangles of projected size $\xi_\parallel \times (R+l_a)$ in the central panel. The area $\tilde{A}_b$ consists of two rectangles of size $\xi_\parallel \times (D+2R)$ which translates into one white rectangle of projected size $\xi_\parallel \times (D+2R)$ in the central panel. $\tilde{A}_{\rm sep}$ and $\tilde{A}_b$ are areas extending along the colloid axes. The cross-sectional area $\tilde{A}_i$ of the interface, which is normal to the colloid axes, between the domains is the one enclosed by the dashed full white and the dotted pale white border lines in the right panel. In the side panels, $\tilde{A}_i$ consists of a back and a front side as well, corresponding, however, to the left and the right domain interface, respectively. For $\tilde{A}_i$, the positions of the front and the back side are marked by the two arrows at the top of the central panel.

geometric, approximation illustrated in Fig. 5.8. Accordingly, the relative probability $\tilde{p}_b$ of the bridged state is

$$\tilde{p}_b = \frac{e^{-\tilde{\Omega}_b/(k_BT)}}{\tilde{Z}} = \frac{e^{-(\tilde{\Omega}_b-\tilde{\Omega}_s)/(k_BT)}}{1+e^{-(\tilde{\Omega}_b-\tilde{\Omega}_s)/(k_BT)}} = \frac{e^{-\Delta\tilde{A}\,\sigma/(k_BT)}}{1+e^{-\Delta\tilde{A}\,\sigma/(k_BT)}}, \tag{5.28}$$

with a Boltzmann factor $\exp(-(\tilde{\Omega}_b-\tilde{\Omega}_s)/(k_BT))=\exp(-\Delta\tilde{A}\,\sigma/(k_BT))$ giving the probability of forming finite domains of $\alpha$-like bridges along the cylinders (instead of a single, fully connected bridge consisting of the $\alpha$ phase); $\Delta\tilde{A}$ is the change of the interfacial area upon forming an $\alpha$-like domain of length $\xi_\parallel$ within an otherwise $\beta$-filled, separated configuration; $\sigma$ is the $\alpha$-$\beta$ surface tension. Following the same geometric argument which preceded Eq. (5.23) (such as considering only the inward oriented parts of the adsorption layers), a separated domain has an interfacial area $\tilde{A}_{\text{sep}} = 2 \times \pi(R + l_a)\xi_\parallel$ around the colloids (see the correspondingly labeled area in Fig. 5.8; the factor two accounts for both colloids). A bridged domain has an area $\tilde{A}_b = 2 \times (D + 2R)\xi_\parallel$ accounting for both sides of the bridge volume (see Fig. 5.8). The presence of a domain generates two $\alpha$-$\beta$ interfaces normal to the axial direction. Its corresponding surface area is $\tilde{A}_i = 2 \times [(D + 2R)(2(R + l_a)) - \pi(R + l_a)^2]$ (see the indented area with dashed full white and dotted pale white border lines in the right panel of Fig. 5.8; this is the difference of area between a rectangle and two semi-circular discs). Thus the insertion of a domain of length $\xi_\parallel$ is accompanied by a change in area given by $\Delta\tilde{A} = \tilde{A}_b - \tilde{A}_{\text{sep}} + \tilde{A}_i$.

Specifically, at the transition distance $D = D_t$ (Eq. (5.23)), the Boltzmann factor reduces to $\exp(-2\pi(R+l_a)^2\sigma/(k_BT))$. Far away from the critical point, $l_a$ is microscopically small, so that one arrives at the “simple macroscopic” estimate $\exp(-2\pi R^2\sigma/(k_BT))$ (see Malijevsky and Parry [45]). In the vicinity of the bridging transition $D = D_t \pm \Delta D$, the Boltzmann factor amounts to $\exp(-(2\,\Delta D\,\xi_\parallel + 2\pi(R + l_a)^2 + 4(R + l_a)\Delta D)\sigma/(k_BT))$. In the relevant case in which the length scales are of order $\Delta D \ll R \ll \xi_\parallel$, the last term $4(R + l_a)\Delta D$ represents a small correction which depends also on the precise shape of the domains, which we will neglect. This implies that the probability of the bridged state $\tilde{p}_b$ follows a Fermi function (or logistic function)

$$\tilde{p}_b = \frac{e^{-(2\Delta D\xi_\parallel + 2\pi(R+l_a)^2)\sigma/(k_BT)}}{1 + e^{-(2\Delta D\xi_\parallel + 2\pi(R+l_a)^2)\sigma/(k_BT)}} =: \frac{e^{-(\Delta D+\omega)/\delta}}{1 + e^{-(\Delta D+\omega)/\delta}}, \tag{5.29}$$

from which one can infer a rounding $\delta := (k_BT)/(2\sigma\xi_\parallel)$, which is the distance between the position of the inflection point at $(\Delta D = -\omega, \tilde{p}_b = 1/2)$ and the position of the point at which the probability has dropped to $(1 + e)^{-1}$ or has risen to $e(1 + e)^{-1}$, and a shift $\omega := \pi(R + l_a)^2/\xi_\parallel$ of the transition point (see the solid curve in Fig. 5.9). On the other hand, one can reverse the argument and consider the probability $\propto \exp(-(\tilde{\Omega}_s - \tilde{\Omega}_b)/(k_BT))$ of interstitial, $\beta$-like domains within a bridged state. The change of the interfacial area upon forming a $\beta$-like domain of length $\xi_\parallel$ embedded in an $\alpha$-like bridge configuration is $\Delta\tilde{A} = \tilde{A}_{\text{sep}} - \tilde{A}_{\text{b}} + \tilde{A}_i$; note that the areas $\tilde{A}_i$ of the two domain walls do not change sign. The resulting probability of interstitial domains is $\tilde{p}_i = (e^{(\Delta D-\omega)/\delta})/(1 + e^{(\Delta D-\omega)/\delta})$. Thus the probability to observe an unperturbed bridge is $\tilde{p}_b = 1 - \tilde{p}_i = (e^{-(\Delta D-\omega)/\delta})/(1 + e^{-(\Delta D-\omega)/\delta})$, which features an inverse shift of $-\omega$, so that, due to the finite-size fluctuations, the transition exhibits hysteresis (see the dashed curve in Fig. 5.9). This has been found before in simulations, e.g., in Ref. [163]. It has also been found that the hysteresis is much more important than the rounding.

In order to give an estimate, we consider the ratio $\epsilon = (2\pi R^2\sigma)/(k_BT)$ of the domain interface energy at $D_t$ and the thermal energy; note that $\epsilon \approx \omega/\delta$ for $l_a \to 0$, i.e., far away from $T_c$. Using Eq. (5.13) for $\sigma$ with $R_\sigma = 0.377$ in $d = 3$ [169], $R_\xi = 1.96$ [82],

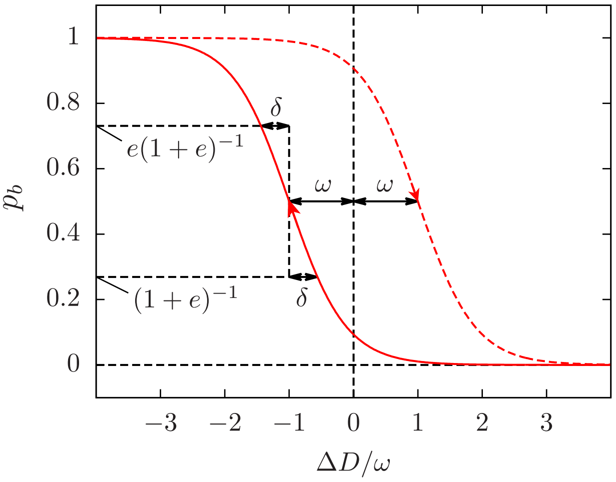

Figure 5.9: Probability distribution $\tilde{p}_b$ of the bridged configuration as a function of the separation $\Delta D = D - D_t$ around the bridging transition at $D_t$. The hysteretic shift $\omega$ and the rounding $\delta$ are defined in the main text. Starting with a large separation $\Delta D \gg \omega$ (solid red curve), i.e., deeply in the separated state, the probability of forming a bridge is vanishingly small and increases only after passing the transition distance $\Delta D = 0$ due to the additional cost of forming the interfaces between the $\alpha$ and $\beta$-like domains. In reverse, starting with two particles close to each other ($\Delta D \ll -\omega$), the probability of the bridged state is effectively one (dashed red curve). The $\alpha$-filled bridge disintegrates for $\Delta D > 0$, also retarded due to the cost of forming the interfaces between the domains.

and, e.g., a moderate value of $\Theta_- = 3$ for the rescaled temperature, the energy cost for interstitial domains within the liquid bridge amounts to $5.4\,k_BT$, so that further away from $T_c$, the hysteresis shift is much larger than the rounding, i.e., $\omega \gg \delta$ for $\Theta_- \gg 1$. The shift $\omega$ scales inversely with the correlation length $\xi_\parallel$ along the axes of the cylinders. Using the transfer matrix method for a cylindrical Ising spin system, it has been shown that $\xi_\parallel = \xi_- \exp\Big((\tilde{A}_i\,\sigma)/(k_BT)\Big)$ for $\tilde{A}_i/\xi_-^{d-1} \gg 1$ [161, 170], i.e., the parallel correlation length $\xi_\parallel$ scales exponentially with the cross-sectional area $\tilde{A}_i$. From this, the hysteresis shift is estimated to be

$$\frac{\omega}{R} = \frac{\pi R}{\xi_-} e^{-(\tilde{A}_i\sigma)/(k_BT)} = \frac{\pi}{\Theta_-}\, e^{-\epsilon} \approx 4.7 \times 10^{-3} \text{ for } \Theta_- = 3. \tag{5.30}$$

Thus, for particles with radii of the order of micrometer, the transition as a function of distance $D$ is rounded on the scale of nanometers. Thus the transition is still expected to appear to be sharp for $\Theta_- > 3$.

Upon approaching $T_c$, the energy cost $\epsilon$ is expected to decrease due to the vanishing of the surface tension $\sigma(\Theta \to 0) \propto \Theta_-^2$. Furthermore the adsorption layer thickness $l_a \propto \xi_- \propto \Theta_-^{-1}$ is expected to grow algebraically for $\Theta_- \to 0$ whereas $\xi_\parallel$ is known to attain a constant at $T = T_c$ [161]. However, these scaling behaviors will not hold once, e.g., the adsorption layer thickness reaches the size of the system. In this case, the finite-size effects will play a dominant role. It has been found beyond mean field theory as well as experimentally (see Ref. [171] and references therein) that the power-law behavior of critical adsorption is pre-empted by capillary condensation. Therefore we conclude that in order to fully resolve the nature of the bridging transition very close to the bulk critical point, it is necessary to improve the present analysis beyond mean field theory. This is left to further research.

## 5.7 Dependence of the scaling functions on rescaled temperature

Finally, it is worthwhile to study in more detail the dependence of the scaling functions $G(\Delta, \Theta_-)$ of the effective potential and $\mathcal{K}(\Delta, \Theta_-)$ of the force as a function of the rescaled temperature $\Theta_- = R/\xi_-$. The discussion of these scaling functions as functions of $\Delta = D/R$ (see Fig. 5.4) corresponds to paths along a vertical line in the phase diagram shown in Fig. 5.7(a). Instead, we now consider horizontal paths through the phase diagram.

There are still similarities between the two representations. Again, by definition, the surface free energy $2\,\Omega_{s,c}^{(\beta)}$ of two single colloids is subtracted from the scaling function $G$ of the effective potential, so that the separated state corresponds to $G = 0$ (apart from exponentially small interaction contributions in the separated state). $\Omega_{s,c}^{(\beta)}$ is independent of the distance $\Delta$, but does depend on the rescaled temperature $\Theta_-$.

In Fig. 5.10 we show the scaling function $G$ in the bridged state for three rescaled separations $\Delta = 3.2$, $2.7$, and $1.5$. For all three curves one has $G < 0$ for $\Theta_- \to 0$, so that the bridge state turns out to be energetically stable close to the critical point. For the smallest rescaled separation $\Delta = 1.5$ considered in Fig. 5.10, the scaling function $G$ remains negative throughout and no transition to the separated state is observed. For $\Delta = 2.7$, the curve of the scaling function $G$ bends upwards, resulting in a zero $G(\Delta, \Theta_-^{(t)}) = 0$ at $\Theta_-^{(t)} = 12.25$, for which a first-order transition to the separated state occurs (see Fig. 5.4(a) for $\Theta_- = 12.25$). For $\Theta_- > 12.25$, following this thermodynamic path, the bridged state remains meta-stable with $G > 0$. The same holds for $\Delta = 3.2$, only with a lower transition temperature $\Theta_-^{(t)} \approx 10$. Upon increasing the separation $\Delta$, $\Theta_-^{(t)}$ shifts to smaller values.

The scaling function $\mathcal{K} = -\partial G/\partial\Delta$ of the force has already been introduced in the discussion of Fig. 5.4. There, it has been demonstrated that for $\Delta > 1$ the force is dominated by the interfacial surface tension and not by the critical Casimir force. Now, we focus on the crossover between these two forces. Thus, in Fig. 5.11 we show the scaling function $\mathcal{K}$ as a function of the rescaled temperature $\Theta_-$ for several small separations $\Delta < 1$. As expected, far away from criticality, i.e., for $\Theta_- \gg 1$, the interfacial tension plays the dominant role, which leads to the behavior $\mathcal{K} \sim (\Theta_-)^3$ in $d = 4$ (see Eq. (5.14) and the black dashed line in Fig. 5.11). Upon increasing $\Delta$, this behavior prevails even

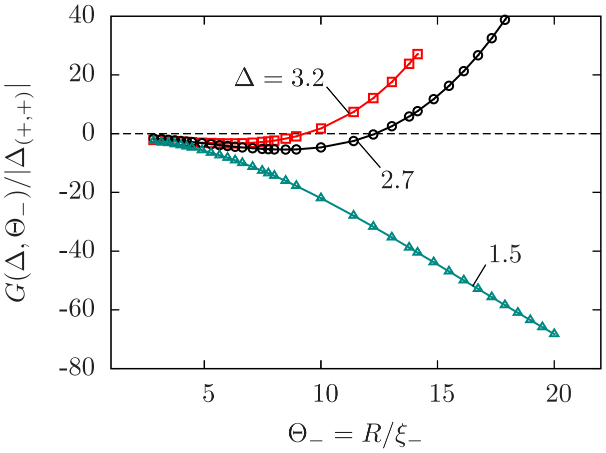

Figure 5.10: Normalized scaling function $G$ of the effective potential between two cylindrical, parallel colloids connected by a liquid bridge as a function of the rescaled temperature $\Theta_-$. Note that also the surface free energy of two separated colloids $2\,\Omega_{s,c}^{(\beta)}$ depends on $\Theta_-$. However, according to the definition of $G$ (Eqs. (5.1) and (5.9)), this contribution is subtracted and corresponds to the dashed line $G = 0$. This is similar to Fig. 5.4, although there $2\,\Omega_{s,c}^{(\beta)}$ is constant as function of $\Delta$. For small separations $\Delta = D/R$, e.g., for the green curve with $\Delta = 1.5$, the bridged state has a significantly lower free energy than the state forming two separate adsorption layers; for cylinder separations $D < D_{\min} = (\pi - 2)R$, i.e., if close to contact, one has $G(\Delta < (\pi - 2), \Theta_-) < 0$ for *all* rescaled temperatures $\Theta_-$. For increasing separations $\Delta$ (black and red curve), the bridged state has a lower free energy ($G < 0$) only within a range $0 < \Theta_- < \Theta_-^{(t)}$, where $\Theta_-^{(t)}$ is defined by $G(\Delta, \Theta_-^{(t)}) = 0$. For rescaled temperatures $\Theta_- > \Theta_-^{(t)}$, the bridged state has a higher free energy than the separated state. The black curve $\Delta = 2.7$ corresponds to the horizontal dashed line in Fig. 5.7(a). The free energy branches with $G > 0$ correspond to metastable bridge states.

down to values of $\Theta_-$ less than 10. Note that here we have chosen the scaling variables $\Delta = D/R$ and $\Theta_- = R/\xi_-$ in view of potential experimental realizations. Equivalent choices are $\Delta = D/R$ and $\tilde{\Theta} = D/\xi$ (used, e.g., in Refs. [29, 36, 103]), in terms of which $D \to 0$ and $\xi \to \infty$ correspond to the same limit $\tilde{\Theta} \to 0$. Conversely, the interfacial tension dominates over the critical Casimir effect away from criticality, i.e., for $\tilde{\Theta} \gg 1$, which we have discussed already twice for $\Delta \gg 1$ (see Sec. 5.3) and for $\Theta_- \gg 1$ here in Sec. 5.7.

On the other hand, for $\Theta_- \to 0$ the interfacial tension $\sigma$ vanishes so that for small $\Delta$ the critical Casimir force $\mathcal{K}(\Delta, \Theta_-) = \Delta^{-(d-1/2)} K_{(+,+)}^{(cc)}$, as obtained from the Derjaguin approximation (see Eq. (A.2) in Appendix A) becomes dominant. The solid color lines in Fig. 5.11 point out that for $\Theta_- \to 0$ the signature of the critical Casimir force clearly emerges. Specifically, as a function of $\Theta_-$, the scaling function attains a constant value $-\mathcal{K}(\Delta \to 0, \Theta_- = 0)/|\Delta_{(+,+)}| = \Delta^{-7/2} \int_1^\infty \mathrm{d}\beta\,(\beta - 1)^{-1/2}\,\beta^{-d} = (5\pi/16)\,\Delta^{-7/2}$ (see Eq. (A.2)), which depends on $\Delta$ only. As stated in Sec. 2.1.3, the stress tensor method is not suitable for the present case, and $\mathcal{K}$ is simply calculated by taking the numerical

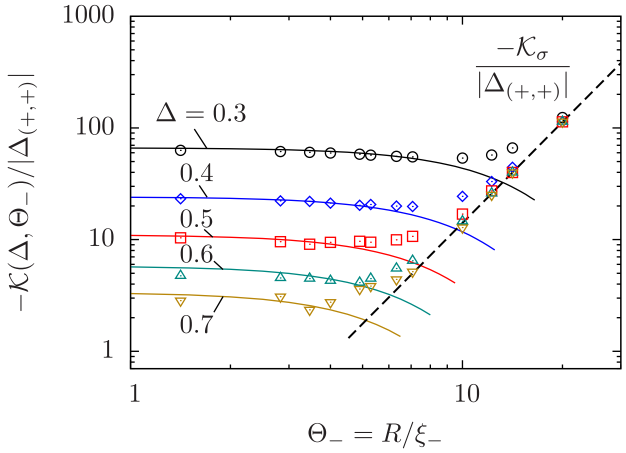

Figure 5.11: Scaling function $\mathcal{K}$ of the force (Eq. (5.10)) between two cylindrical, parallel colloids in close proximity to each other (i.e., $\Delta = D/R < 1$). In this case, a liquid bridge is always formed. Thus, the force is attractive (i.e., $-\mathcal{K}$ is positive). It is shown normalized by the critical Casimir amplitude $\Delta_{(+,+)}$ of the slab geometry. The symbols represent the numerical MFT data and the dashed black line shows the expected interfacial contribution as given by Eq. (5.14), which is proportional to $(\Theta_-)^3$ for $d = 4$. Upon increasing the intercolloidal separation $\Delta$, the force is under the dominant influence of the interfacial tension $\sigma$ even down to values of $\Theta_-$ less than 10. For small $\Theta_-$ and $\Delta < 1$, the critical Casimir force (solid curves) starts to emerge and becomes dominant, with the force saturating at the values $-\mathcal{K}(\Delta \to 0, \Theta_- = 0)/|\Delta_{(+,+)}| = (5\pi/16)\,\Delta^{-7/2}$ at criticality. In the limit $\Theta_- \to 0$ we find very good agreement between the DA of the critical Casimir force (solid lines) and our fully numerical calculations.

derivative of the free energy with respect to $D$. We note that $\mathcal{K}_{DA}$ does not contain any adjustable free parameters; nonetheless there is excellent agreement with the numerical MFT calculations, providing a stringent test of the latter.

## 5.8 Conclusions

We have analyzed within MFT ($d = 4$) the effective interactions between two parallel, cylindrical colloids of radius $R$ immersed in a binary liquid mixture (consisting of A and B particles) close to and below its critical consolute point, i.e., at coexistence of the phases $\alpha$ and $\beta$ rich in A and B particles, respectively. Generically, the two identical colloids have a preference for one of the two species of the binary liquid mixture. This leads to strong critical adsorption of, say, the $\alpha$ phase at the surface of the colloid. Here, we have considered the largely stable local minimum in which the colloids are engulfed by the less preferred $\beta$ phase, far away from the *free* $\alpha$-$\beta$ interface (which can form but outside of our numerical calculation box). Instead, the $\alpha$-$\beta$ interface forms an adsorption layer which remains *bound* to the colloid surface or to a pair of colloids (see Fig. 5.1).

Using finite-size scaling theory, in Sec. 5.1 we have decomposed the free energy of the system into bulk, surface, and interaction contributions, each characterized by a universal scaling function. We have calculated the singular contribution to the free energy in the vicinity of the critical point by varying the rescaled temperature $\Theta_- = R/\xi_-$, where $\xi_-$ is the bulk correlation length, and numerically minimizing the Hamiltonian in Eq. (2.27), from which we concomitantly obtain the equilibrium MFT order parameter profile. Via analyzing the free energy of the system, we have calculated the effective potential and the force between the colloids mediated by the near critical solvent. In this context, our main findings are as follows:

The scaling function $P_-$ (Eq. (5.11)) of the *two*-particle order parameter profiles depends sensitively on the surface-to-surface distance $D$ between the particles and temperature (see Figs. 5.2 and 5.3), exhibiting a local $\alpha$-$\beta$ interface that encapsulates both particles either individually (separated state) or as a pair (bridged state).

By analyzing the dependence of the scaling function $G$ of the effective interaction potential on the distance between the two colloids (shown in Fig. 5.4), we find that there are three regimes: At close separations, critical Casimir forces dominate; at intermediate separations the extension of the liquid bridge leads to a region in which the influence of the $\alpha$-$\beta$ interfacial tension dominates; and finally a third regime in which the liquid bridge is meta-stable compared to the separated state and eventually ruptures. We have analytically derived the Derjaguin approximation for the interaction between two cylinders, which is in very good agreement with the numerical MFT results and confirms that at small separations $\Delta = D/R < 1$ critical Casimir forces dominate. Additionally, for various rescaled temperatures $\Theta_-$ the slope of $G$ with respect to $\Delta$, in the region dominated by the interfacial tension effect, agrees very well with the decrease of the surface tension $\sigma$ upon decreasing $\Theta_- = R/\xi_- \to 0$.

To a large extent, in the less-critical regime $\Theta_- \gg 1$, the transition distance $D_t$ of the liquid bridge can be expressed in terms of *single*-colloid profiles (see Figs. 5.5 and 5.6). To this end, the features of the *single*-particle order parameter profiles, captured by the scaling function $P_-^{(s)}(z)$ (Eq. (5.19)), have been investigated. We have found that the adsorption layer in *single*-particle profiles essentially consists of the wall-$\alpha$ interface, well described by a short distance approximation (Eq. (5.20)), joint together with the free $\alpha$-$\beta$ interface profile (Eq. (5.22)). The adsorption layer thickness $l_a$ turns out to be the relevant quantity to describe the *single*-colloid state.

We have determined the transition distance $D_t$ unambiguously from the zero of the scaling function $G$ of the effective potential in the bridged state, which in the relevant range depends linearly on the separation $\Delta = D/R$. The transition distance $D_t$ divides the phase diagram in Fig. 5.7(a) into two distinct domains: For large $D$ and away from $T_c$, the separated state is the stable configuration. For small separations $\Delta$ or close to $T_c$, the colloids are connected by a bridge formed by the preferred $\alpha$ phase. Away from criticality, i.e., for $\Theta_- \gg 1$, a geometric model based on the adsorption layer thickness $l_a$

yields a reasonable approximation for the transition distance $D_t$ (see Fig. 5.7(b)).

The influence of finite-size induced fluctuation effects, which are not captured within our MFT approach, has been discussed. Inter alia, finite size causes a shift and rounding of phase transitions. In the present context this implies that the excess adsorption of the species favored by the colloids is expected to increase sharply, but continuously. This is due to the entropically favored presence of alternating domains of the two coexisting phases instead of having a macroscopically large single phase, as shown schematically in Fig. 5.8. According to our estimates this rounding and the shift of the transition probability (Fig. 5.9) are too small to be experimentally detectable for rescaled temperatures $\Theta_- \gtrsim 3$. This range still features the discussed critical Casimir contribution.

We have also studied the scaling function $G$ of the effective potential for the bridged state as a function of the rescaled temperature $\Theta_-$ (see Fig. 5.10). For small distances $\Delta$, the bridged state is stable, i.e, $G < 0$, for all rescaled temperatures $\Theta_-$. Upon increasing $\Delta$, the bridged state becomes meta-stable compared to the separated state at a transition temperature $\Theta_-^{(t)}$. Finally, we have studied the temperature dependence of the effective force $\mathcal{K}$ between two colloids for various small separations $D$ whilst they are still connected by a liquid bridge (see Fig. 5.11). Far from the critical point, the influence of the interfacial tension resulting from the extension of the interface dominates the overall force. As the temperature approaches $T_c$, critical Casimir forces start to emerge and, as a function of $\Theta_- \to 0$, the overall force levels off at a constant value, which is in very good agreement with the Derjaguin approximation for $\mathcal{K}(\Delta \to 0, \Theta_- = 0)$.

# Chapter 6

# Colloidal aggregation in terms of pair potentials

In an experiment realization, several attractive and repulsive forces may affect the colloids and the source of an aggregation force may not straightforwardly attributed to the critical Casimir effect alone. These forces include direct interactions and other solvent-mediated forces besides the critical Casimir interaction. A regime of colloidal aggregation around the critical point, in terms of temperature $T$ and concentration $c$, was already observed in early experiments in Refs. [49–51], and found to be asymmetric with strong aggregation occurring on that side of the critical composition $c_c$ poor in the component preferred by the colloids. The critical Casimir potential is theoretically known to depend strongly on the composition of the solvent [93], as well as on the strength of the surface fields [73]. The adsorption preference of the colloids leads to the formation adsorption layers around the particles, which may also interact and form liquid bridges. As seen in chapter 5, critical Casimir forces and adsorption layers occur simultaneously; for certain configurations in terms distance, temperature, and additionally the strength of the bulk and surface fields, either the interaction between adsorption layers or the critical Casimir interaction dominate, and the cross-over between them is continuous. However, the critical Casimir interaction can be distinguished by its scaling behavior as obtained from finite-size theory. Similar to pre-wetting, a bridging transition is known to occur also below the phase-coexistence in the homogeneous solvent phase at off-critical concentrations, see Refs. [28, 29] in the context of critical Casimir forces, Refs. [49–51, 54] for early reports, Refs. [53, 54] for reviews and, e.g., [172, 173] for more recent experimental studies. Note that some studies refer to the collective forces in the vicinity of the solvent phase separation as solvent-mediated forces, and that the term "critical Casimir force" has not been in use at the time of the earlier references, as mentioned in Ref. [54].

As such, the influence of the critical Casimir interaction at off-critical compositions is not well-established experimentally. Recent experiments [115, 174] directed at the critical Casimir interaction in dilute suspensions of microgel particles showed the effect of solvent composition for two representative off-critical compositions. The theoretical modeling within these studies accounted only for the asymptotic exponential form of the critical Casimir potential, valid for large ratios $r/\xi$, and the fitted correlation length was in large disagreement with values expected from literature (e.g., Refs. [175,176]). Mohry et al. [93] improved on this by accounting for the solvent-composition dependence of the critical Casimir potential and using $\xi_t^{(0)}$ extracted from data for the same solvent in Ref. [105].

At this stage, it became evident that an accurate comparison of experimental measurements for the colloidal interaction and theoretical predictions needed appropriate knowledge of the solvent phase diagram and correlation length. Hence, we conducted a theoretical study of an experimental realization performed by S. Stuij, T. Kodger, and P. Schall in a coordinated effort. Here, only those experimental details necessary for the theoretical description will be introduced; for more details the reader is referred to the joint work in Ref. [76].

## 6.1 Description of the experiment

The colloidal particles are copolymer particles which match the density of the binary liquid mixture, so that the influence of gravity is negligible. The polymer particles are rigid with a hydrophilic surface. The particle diameter is determined to be $d = 2.12\,\mu\text{m}$ by confocal microscopy, with a polydispersity of $\sim 3\%$. The surface charge density was determined independently by electrophoresis measurements to be $\Upsilon = -0.17\,e\,\text{nm}^{-1}$. The colloidal particles are suspended in a binary liquid mixture of 3-methylpyridine (3MP) and heavy water ($D_2O$) with different weight fraction $c$ of 3MP in the range of 23.5% to 33%. In order to have a well-defined ion concentration, 1 mM KCl salt was added. The Debye screening lengths of each composition is determined using the Clausius-Mossotti relation to calculate the relative permittivity and the known ion concentration, and found to vary only slightly around a value of $\kappa^{-1} = 6\,\text{nm}$. The colloid volume fraction was kept at a low value of $\sim 0.5\%$.

## 6.2 Radial distribution function

Confocal microscopy is used to image the particles and study the temperature and composition dependent particle pair correlation function $g(r)$ that indicates the probability of finding a particle at a distance $r$ from a reference particle relative to the ideal gas distribution. For calibration, the aggregation temperature $T_a$ for each composition was first determined by increasing the temperature in steps of 0.1 °C, noting when aggregation occurs and then taking the average of the last two temperatures for $T_a$.

Particle centers are then located in the horizontal plane using a Python adaptation of a standard particle tracking algorithm [177, 178]. Though confocal microscopy allows to scan a three-dimensional sample through consecutive focus layers, particles would diffuse significantly during during the scanning time of a layer and thus tracking was restricted to two dimensions. It was shown in [179] that if care is taken to discriminate out-of-plane features, 2D data is able to reproduce the actual $g(r)$ as accurately as 3D data. Further concerns are noted in Ref. [76].

To study particle pair potentials, we link experimental and predicted pair correlation functions via the low-density relation $g(r) \approx e^{-U(r)}$, i.e., we approximate the potential of mean force with the effective pair potential. Focus is set first on data taken at 3 K below the critical temperature, where critical Casimir interactions are vanishingly small and the pair potential is dominated by the electrostatic repulsion. The inverse Debye screening length $\kappa$ estimated from the added 1mM salt and the dissociated particle surface charges is $\kappa^{-1} \sim 6\,\mathrm{nm}$ (varying slightly with temperature and composition, which we take into account), which should yield a sharp increase in the $g(r)$ as shown in Fig. 6.1(a) (green curve). In contrast, the experimental $g(r)$ determined from particle tracking is much softer. This softness arises from the locating uncertainty, the polydispersity of the particles, and the effective slice thickness. To incorporate these effects we compare the experimental pair correlation function with the *projected* theoretical function $g_{\text{proj}}(r' = \{x', y', z'\})$

$$g_{\text{proj}}(r') = \int_{-\infty}^{\infty} \mathrm{d}z \int_{-\infty}^{\infty} \mathrm{d}y \int_{-\infty}^{\infty} \mathrm{d}x\, f_{\{0,\sigma_z\}}(z) f_{\{y',\sigma\}}(y) f_{\{x',\sigma\}}(x) g(\sqrt{x^2+y^2+z^2}), \qquad (6.1)$$

in which the probability distributions $f_{\{x',\sigma\}}(x)$, $f_{\{y',\sigma\}}(y)$ and $f_{\{0,\sigma_z\}}(z)$ account for the uncertainty in the two horizontal directions and the vertical direction, respectively, with the in-plane spreads $\sigma = \sigma_x = \sigma_y$ being equal. To incorporate the different sources of uncertainty, we model them using the normal distributions

$$f_{\{\mu,\sigma\}}(x) = \frac{1}{\sqrt{2\pi}\sigma} e^{-\frac{(x-\mu)^2}{2\sigma^2}} \qquad (6.2)$$

with mean $\mu$ and width $\sigma$. Note that we enforce $g(r < d) = 0$, so that no configurations with physically overlapping pairs contribute to the integral, though the *projected* result may appear to have particle overlap. The three-dimensional integral in Eq. (6.1) can be straightforwardly evaluated numerically, yet, the kernel of three normal distributions lends itself to apply a Monte-Carlo integration, where each set of random numbers can be interpreted as one realization in the experiment.

As seen in Fig. 6.1(a), this uncertainty indeed makes the $g(r)$ look much softer. We determine the values of the broadening parameters by fixing $\sigma_z = 6\sigma$ based on the optical spreads and varying $\sigma$ till a good agreement is obtained for Fig. 6.1(a). For a vanishing critical Casimir interaction this seems to be $\sigma/d = 0.067$. This number is very reasonable given the horizontal locating uncertainty of 75 nm and the particle size variation due to

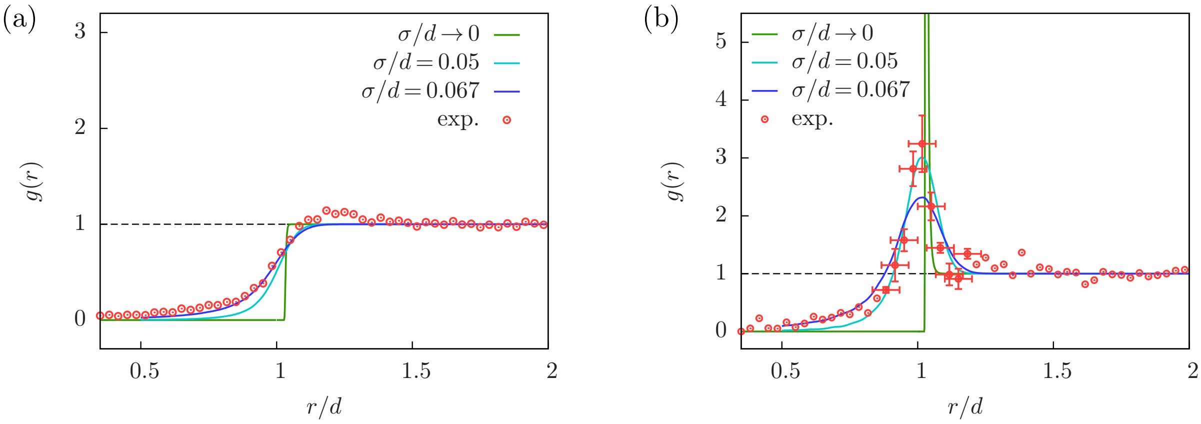

Figure 6.1: Influence of the positional uncertainty in particle tracking on the pair correlation function $g(r)$. The experimental tracking results (red points) are for $c = 28\,\%$. (a) $\Delta T = 3$ K, for which the interaction is dominated by the electrostatic repulsion. The green curve $\Sigma/d \to 0$ represents the electrostatic repulsion as modeled by Eq. (2.41), with the inverse Debye length $\kappa$ being $\sim 6\,\mathrm{nm}$. The theory predicts a much sharper step than indicated by the experimental results. However, incorporating positional uncertainties due to polydispersity, optical shifts and the limited resolution of the digitized images, using Eq. (6.1) with an uncertainty $\sigma = \sigma_x = \sigma_y$ in the image plane and $\sigma_z = 6\sigma$ for the vertical resolution, results in a good agreement for $\sigma/d = 0.05$ (cyan curve) and $\sigma/d = 0.067$ ($\widehat{=}1$ px; blue curve). (b) Close to the critical point (red points: $\Delta T = 0.4\,\mathrm{K}$), the strong critical Casimir attraction results in a peak of the pair correlation function $g(r)$ at $r/d \simeq 1$. The theoretical model Eq. (2.41) ($\sigma/d \to 0$; green curve) shows only some agreement for $r/d > 1$. When incorporating the positional uncertainties with $\sigma/d = 0.05$ and $\sigma/d = 0.067$ (cyan and blue curve), the shape of the peak changes and resembles more closely the experimental results. Around the peak, we indicate the estimated error. The lateral error in the plot represents $\Delta r = 1\,\mathrm{px}$ and the error $\Delta g$ is given by the standard deviation of the $g(r)$ values between sets calculated using different cutoffs for the brightness in the algorithm.

polydispersity of $\sim 60\,\mathrm{nm}$, giving a total variance of $\sim 135\mathrm{nm}$ corresponding to $\sigma/d \sim 0.0675$. Also $\sigma_z = 6\sigma \sim 0.8\,\mu\mathrm{m}$ is smaller than the limit for the half-width of the effective slice thickness of $1.6\mu\mathrm{m}$, but comparable to the particle radius. More accurate fitting of the tracking uncertainties is hardly justified given the limited statistics and noise affecting the pair correlation function $g(r)$.

The broadening of the $g(r)$ holds also when critical Casimir forces act between the particles. As an example, we show pair correlations at temperatures close to $T_c$ in Fig. 6.1(b) (red points), where we compare the experimental data with pair correlations computed from the full pair potential of Eq. (2.41). Due to the critical Casimir attraction, the pair correlation function develops a strong peak close to $r/d = 1$ (green curve). When incorporating the tracking uncertainty with $\sigma/d = 0.05$ (light blue), and $\sigma/d = 0.067$ (dark blue), the correlation peak broadens, yielding good agreement with the experimental data. The figure suggests that the smaller uncertainty $\sigma \lesssim 0.05d = 106\,\mathrm{nm}$ leads to better fit, while Fig. 6.1(a) suggested that far below $T_c$, when the repulsion is dominant, the larger

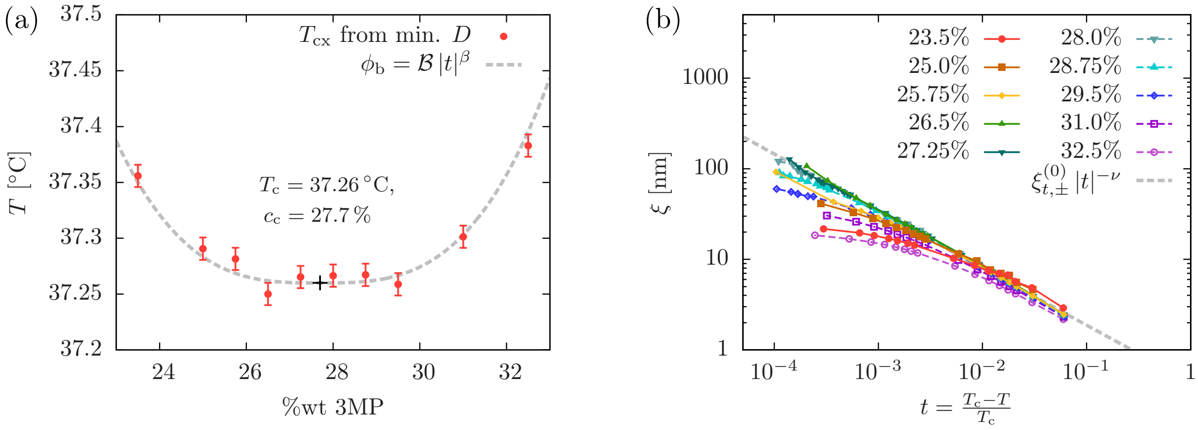

Figure 6.2: Coexistence curve and correlation length of the binary solvent determined by dynamic light scattering. (a) Phase separation temperature as defined from the minimum of the diffusion coefficient. The coexistence curve is theoretically expected to follow $\phi_b = \mathcal{B}\,|t|^{\beta}$ from Eq. (2.16), where $\mathcal{B}$ is a non-universal amplitude specific to the solvent. The error bars indicate the limited temperature resolution given by $\Delta T$. We find good agreement for $\mathcal{B} = 0.6$ and for the critical point at $T_c = 37.26\,°\mathrm{C}$, $c = 27.7\,\%$ (cross symbol). (b) Correlation length $\xi$ as a function of $t = (T_{\mathrm{c}} - T)/T_{\mathrm{c}}$ for various compositions. For compositions around $c_c \approx 28\%$, the correlation length clearly follows the power law $\xi^{(0)}_{t,\pm}\,|t|^{-\nu}$, with $\xi^{(0)}_{t,+} = 0.44\,\mathrm{nm}$ found from the numerical minimization. Curves for off-critical compositions bend downwards, as expected.

uncertainty of $\sigma = 0.067d = 141\,\mathrm{nm}$ describes the data best. Since our interest lies in capturing the critical Casimir attraction, in the following, we generally adopt a value of $\sigma/d = 0.05$ for comparison with the experimental results.

We note that a measure insensitive to these experimental inaccuracies is given by the virial coefficient that is unaffected by the experimental broadening: In the low-density limit where $g(r) \approx e^{-U(r)}$, the second virial coefficient is related to the radial distribution function via $B_2 = \int_V \mathrm{d}\mathbf{r}\,[1 - g(\mathbf{r})]$. One can verify that for any normalized and symmetric distribution function for $f_{\{\mu,\sigma\}}$ in Eq. (6.1), the virial coefficient of the broadened distribution $g_{\mathrm{proj}}$, $B_{2,\mathrm{proj}} = \int_V \mathrm{d}\mathbf{r}\,[1 - g_{\mathrm{proj}}(\mathbf{r})]$, is identical to $B_2$. Hence, despite the choice and disparity between $g(r)$ and $g_{\mathrm{proj}}(r)$ as input, there is only one unique thermodynamically relevant $B_2$. We have also confirmed this numerically.

## 6.3 Solvent phase diagram and correlation length

The solvent phase diagram extracted from dynamic light scattering is shown in Fig. 6.2(a). The phase separation temperatures can indeed be fitted with the bulk coexistence relation $\phi_b = c - c_c = \mathcal{B}\,|t|^{\beta}$ from Eq. (2.16). For the fit, we have fixed the critical exponent $\beta = 0.3265$ to its theoretical value [82], and left the amplitude $\mathcal{B}$ and the coordinates of the critical point $(c_c, T_c)$ as adjustable parameters. Note that the values presented here are not based solely on fitting of the experimental coexistence data, but from a combination

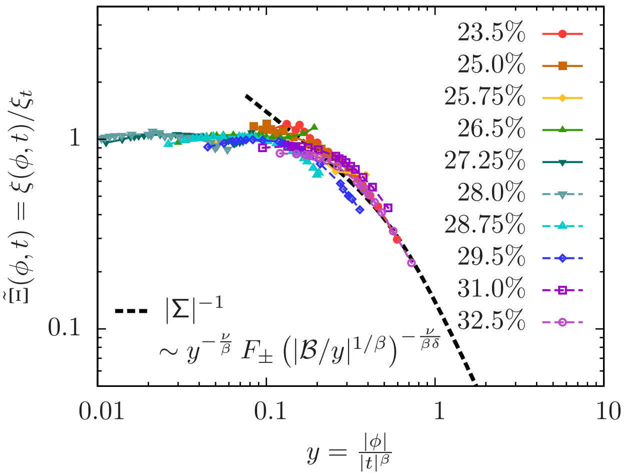

Figure 6.3: The ratio $\tilde{\Xi}(\phi,t)=\xi(\phi,t)/\xi_t$, i.e. the correlation length $\xi(\phi,t)$ normalized by the scaling law $\xi_t=\xi_{t,\pm}^{(0)}\,|t|^{-\nu}$. This is analogous to the scaling function $\Xi(|\Sigma|)$ in Eq. (2.14), except plotted for $y=|\phi|/|t|^\beta$ instead of the scaling variable $\Sigma$. There are two limiting cases, $\tilde{\Xi}(y\to 0)=1$ and $\tilde{\Xi}(y\to\infty)=|\Sigma|^{-1}$. For the latter, $y\to\infty$, the experimental results of $\tilde{\Xi}$ are in good agreement with the linear approximation of the EOS for $\Sigma$ in Eq. (6.3) (black dashed curve), even for intermediate values of $y$.

with further analysis below. We find $\mathcal{B}=0.6$, close to the amplitude $\mathcal{B}\simeq 0.5$ [93] derived from the phase diagram of the pure 3MP-$D_2O$ binary mixture [180]. The coordinates of the critical point $c_c=0.277$, $T_c=37.26\,°\mathrm{C}$ are slightly shifted from the literature values of $c_c=0.28$ and $T_c\approx 38.5\,°\mathrm{C}$ [105, 111, 180] due to the presence of salt [181, 182], which is known to lower the phase separation temperature.

We show the scaling of the correlation length upon approaching the critical temperature in Fig. 6.2(b). At the critical composition $c_c$, the correlation length follows the Ising power-law scaling, while for $c\neq c_c$ it deviates increasingly from this divergence, as expected. Although the divergence at the critical composition was achieved by construction (as explained in Section 2.2.1 and Appendix 6.A), nevertheless the success of the method is still compelling since the hereby calculated correlation length $\xi(\phi(h,t),t)$ reproduces the full scaling behavior with respect to solvent composition.

To show this, we consider the correlation length $\xi(\phi,t)$ normalized by that at the critical composition, $\tilde{\Xi}(\phi,t)=\xi(\phi,t)/\xi_t$; this ratio is analogous to the scaling function $\Xi(|\Sigma|)$ in Eq. (2.14), but with $\phi$ and $t$ as independent variables. Note that the relation $\Sigma(\phi,t)$, such that $\tilde{\Xi}(\phi,t)=\Xi(|\Sigma(\phi,t)|)$, corresponds to knowing the equation of state. In the linear form in Eq. (2.17), $\Sigma$ depends only on $X=t|\mathcal{B}/\phi|^{1/\beta}$. By introducing the variable $y=|\phi|/|t|^\beta$ given directly by the experimental state, we recast this as $X=\pm|\mathcal{B}/y|^{1/\beta}$, where the sign depends on $t$. This variable allows us to approach the critical point along the two relevant thermodynamic paths: for $y\to 0$, i.e., $|\phi|\ll|t|^\beta$, the critical point is approached along the critical composition ($\phi$=0) by varying the temperature $t\to 0$; in this case one expects $\xi(\phi{=}0,t)=\xi_t$ and $\tilde{\Xi}(y\to 0)=1$. For $y\to\infty$, where

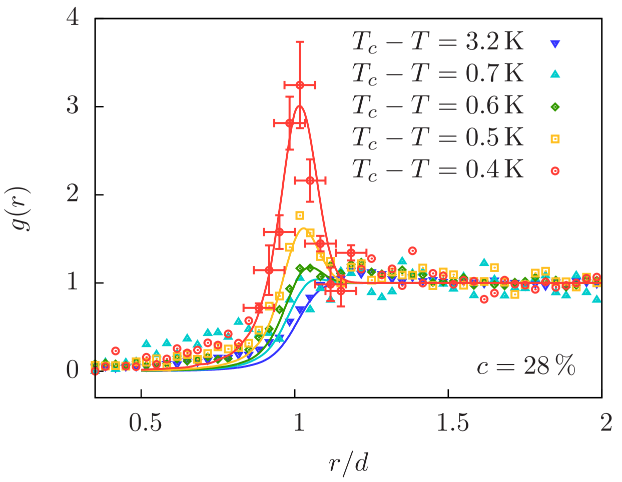

Figure 6.4: Pair correlation function $g(r)$ for solvent composition $c = 28\,\%$, close to the critical composition, for different temperatures. The experimental results (symbols and error bars) are compared to results of the pair potential model Eq. (2.41) using the dimensional approximation for the scaling function $\Theta^{(d=3,Derj)}$, and using Eq. (6.1) to account for the experimental broadening (solid lines). A temperature offset of $\Delta T_{\mathrm{off}} \approx 0.55\,\mathrm{K}$ was used to account for the weak hydrophilic adsorption preference of the particles.

$|\phi| \gg |t|^\beta$, the critical point is approached along the critical isotherm ($t$=0) through variations of composition $\phi \to 0$. One expects that in this limit (see Eq. (2.17))

$$\tilde{\Xi}(y \to \infty) = |\Sigma|^{-1} = \tilde{B}\, y^{-\frac{\nu}{\beta}}\, F_\pm \left(|\mathcal{B}/y|^{1/\beta}\right)^{-\frac{\nu}{\beta\delta}} \tag{6.3}$$

with the amplitude [92]

$$\tilde{B} = (R_\chi \delta / Q_2)^{-\frac{\nu}{\beta(\delta-1)}} \left(Q_\xi^c / Q_\xi^+\right) \mathcal{B}^{\frac{\nu}{\beta}}$$

that contains a combination of several universal amplitude ratios. We check these predictions by plotting $\tilde{\Xi}$ as a function of $y$ in Fig. 6.3, and find very good agreement in both limits. While we cannot fully follow the limit $y \to \infty$ as this thermodynamic path is not practical in the experiment, we find that already $y > 0.1$ is sufficiently large for $\tilde{\Xi}(y)$ to start approaching the linear approximation of $|\Sigma|^{-1}$. The scaling function $F_\pm(|\mathcal{B}/y|^{1/\beta})$ in this approximation contains the non-universal amplitude $\mathcal{B}$, which we take as $\mathcal{B} = 0.6$ as determined from the coexistence curve, indicating the fundamental correspondence based on the EOS. For the amplitude $\tilde{B}$ we obtain from simple fitting $\tilde{B} = 0.15$, in good agreement with the value $\tilde{B} = 0.145$ obtained with $\mathcal{B} = 0.6$ and the amplitude ratios given in Ref. [82].

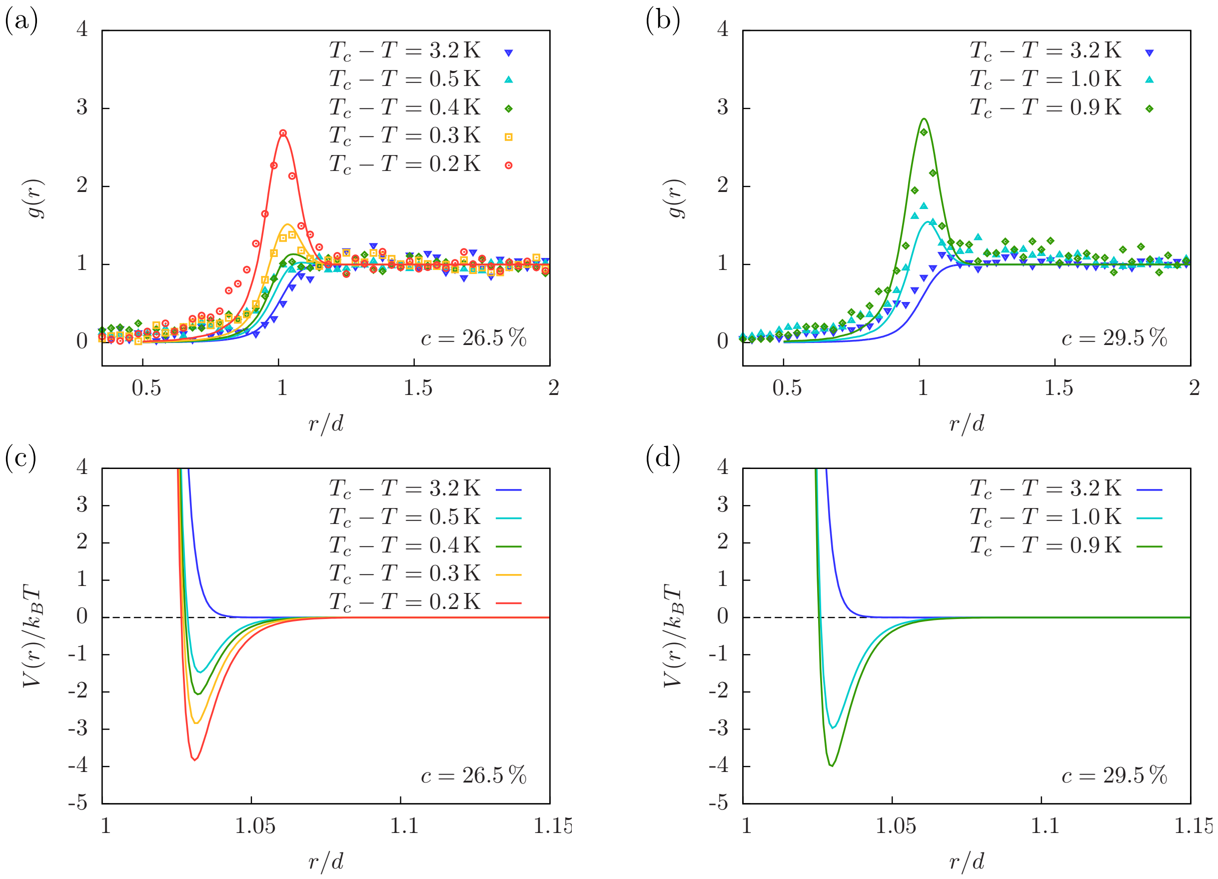

Figure 6.5: (a) and (b): Pair correlation function $g(r)$ for the off-critical compositions $c = 26.5\,\%$ (with $\Delta T_{\mathrm{off}} = 0.7\,\mathrm{K}$) and $c = 29.5\,\%$ (with $\Delta T_{\mathrm{off}} = 0.18\,\mathrm{K}$). The experimental results (points) are compared to the dimensional approximation (solid lines). (c) and (d) Theoretically predicted pair potentials $V(r)$ for the same composition.

## 6.4 Pair potential and virial coefficient

Building upon this consistent description of the bulk properties of the liquid mixture, we now turn to the critical Casimir interactions between suspended particles. We first focus on the critical composition. Particle pair correlation functions for various temperatures are shown in Fig. 6.4. For this critical composition, we can fit all pair correlations with a single parameter $\Delta T_{\mathrm{off}}$ that accounts for the finite surface fields, as explained in section 2.2.2. Best agreement with the dimensional approximation model (solid lines) is obtained for $\Delta T_{\mathrm{off}} = 0.55\,\mathrm{K}$ or a rescaling parameter $s = 0.78$, corresponding to a value of $h_s \approx 70$ for the the scaling variable of the surface field based on the short distance approximation described in Ref. [73] (see also footnote 1 on page 27). Since this approximation is valid for $h_s \gtrsim 10$ and the universality class of the surface boundary conditions switches from the normal to the special transition for $h_s \to 0$, it appears the observed particles are moderately weak and still adhere to the normal universality class.

We now exploit the full solvent-composition dependence. For 3MP-rich compositions ($c > c_c$), the particles aggregate as far as $1\,^\circ\mathrm{C}$ below the critical temperature, indicating

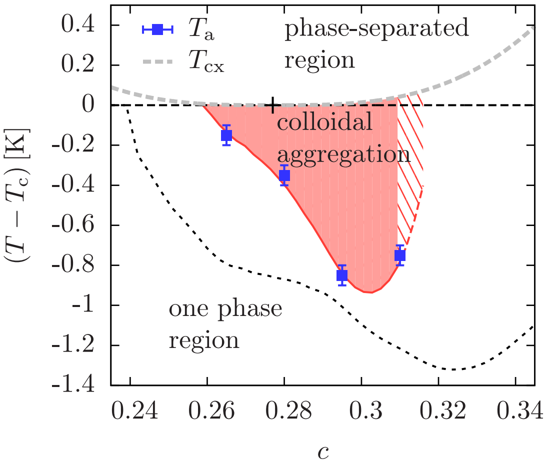

Figure 6.6: Phase diagram showing the coexistence curve $T_{cx}$ and the experimentally observed aggregation points $T_a$, compared to the $B_2$ isoline with the critical value $B^*_{2,\mathrm{crit}} = -1.2$ of the sticky sphere model. The critical point is marked by a cross symbol. Within the shaded area, colloids aggregate and the pair potential cannot be measured experimentally. In the hatched part, $B^*_2$ is determined based on a polynomial extrapolation of $t_{\mathrm{off}}$ beyond the experimental range, which may not resemble the actual shape of the colloidal aggregation region. The black dotted curve indicates the aggregation line predicted for strongly adsorbing particles.

strong attraction, while for 3MP poor compositions ($c < c_c$), this temperature interval of aggregation is very small and diminishes until aggregation is no longer observed. This is in agreement with the well-known fact that the attraction is strong in solvents poor in the component preferred by the particles. To compare with theoretical predictions, we take advantage of the internally calibrated correlation length to compute the critical Casimir attraction, and we add the electrostatic repulsion obtained from pair correlation measurements sufficiently far from $T_c$. In principle, there are no other remaining parameters in the case of strong adsorption. To account for the weak hydrophilic adsorption preferences of our particles, we again use the effective temperature offset $t_{\mathrm{off}}$, which depends on the solvent composition. We find that even for off-critical compositions we can fit all pair correlation functions for the different temperatures using the single parameter $t_{\mathrm{off}}$ varying systematically with composition. We show examples of measured and predicted pair correlation functions for a composition to the left and right of the critical point in Fig. 6.5. In both cases, good agreement is observed for all temperatures. The resulting predicted pair potentials are also shown. Note the difference in horizontal scale between the observed radial distributions and the predicted pair potentials due to the experimental broadening.

The particle aggregation behavior provides an independent check of the validity of the model based on the colloidal state not affected by any quantitative uncertainties of particle tracking. Theoretically, we can predict where aggregation occurs from the second virial coefficient $B_2$ (see Sec. 2.2.3) following the argument in Ref. [92], while experimentally,

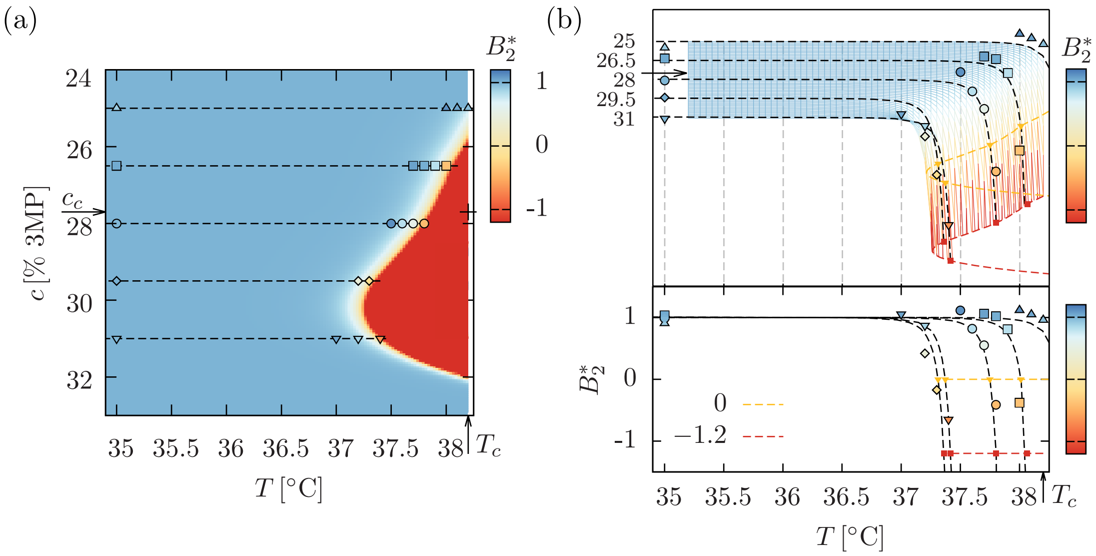

Figure 6.7: Composition and temperature dependence of the reduced second virial coefficient from measured $g(r)$ (symbols) and from theory (lines and colored surface). (a) Color map in the temperature-composition plane indicates theoretically predicted, and colored symbols experimental $B_2^*$ values. Values $B_2^* \sim 1$ depicted in blue indicate a significant repulsion, while values $B_2^* \sim -1$ depicted in red indicate strong attraction. Yellow marks the crossover. Also indicated by arrows are the critical temperature $T_c$ and composition $c_c$, and the critical point (cross symbol). (b) $B_2^*$ values as a function of temperature along the experimental solvent compositions (dashed lines in (a)). Values in the top panel are shifted vertically, providing a perspective view on the temperature-composition plane in (a). Dashed yellow and red lines indicate isolines of $B_2^* = 0$ and $B_2^* = -1.2$, marking, respectively, the crossover from repulsion to attraction, and the critical value of the sticky spheres model.

we can observe the onset of aggregation directly. We compare the theoretical curve for the onset of aggregation, as obtained from the critical value $B_2^* = -1.2$ of the sticky sphere model, with the experimental aggregation points in Fig. 6.6. Very good agreement is observed. In particular, the asymmetry of the aggregation region is very well reproduced. We also indicate the aggregation region predicted for the case of strong adsorption, i.e. for vanishing $t_{\text{off}}$ (black dashed curve). As expected, it extends further below $T_c$, as strongly adsorbing particles exhibit a stronger attraction. Yet, the shape of the aggregation region, especially its pronounced asymmetry, does not change qualitatively.

We investigated particle pair interactions just below aggregation in more detail. Taking advantage of the fact that the virial coefficient is unaffected by the experimental broadening as it is based on the integrated pair potential, we can compare virial coefficients computed from the raw measured $g(r)$ directly with theoretical predictions without any need to account for experimental inaccuracy and particle polydispersity. In fact, one can show that any distorting influence described by normalized symmetric distribution functions, such as the optical broadening, leaves the second virial coefficient unchanged (see Sec. 6.2). We therefore compute experimental $B_2$ values directly by numerically inte-

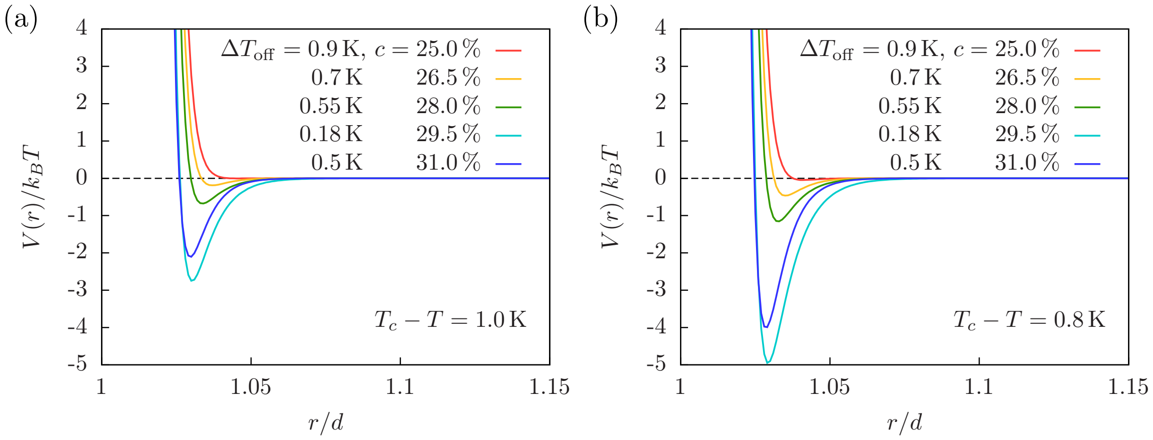

Figure 6.8: Pair potential $u(r)$ predicted by the dimensional approximation, for different compositions at fixed temperature $T_c - T = 1.0\,$K (a) and $T_c - T = 0.8\,$K (b).

grating the measured $g(r)$. Specifically, we calculate the reduced second virial coefficient $B_2^* = B_2/B_2^{(hs)}$ (see Sections 2.2.3 and 6.2) in the low-density limit, by numerically integrating $B_2 = 2\pi \int_0^\infty \mathrm{d}r\, r^2\,(1 - g(r))$. In order to treat the limited experimental data range, we assume $g(r < r_0) = 0$ below the smallest distance $r_0$ of the data set, and we apply a smoothing factor to $g(r)$ for large separations.

Experimental and theoretical values of $B_2^*$ in the entire temperature-composition plane are compared in Fig. 6.7(a). The color map indicates the theoretically predicted values, while colored dots along the experimental compositions (dashed lines) indicate the measured values. Good qualitative agreement is observed. For quantitative comparison, we plot $B_2^*$ values as a function of temperature in Fig. 6.7(b). The bottom panel shows $B_2^*$ values superimposed for the different solvent compositions, while the top panel shows the same data shifted vertically for clarity, providing a perspective view of the $B_2^*$ values above the temperature-composition plane. Experimental data (dots) and theoretical predictions (lines) show very good agreement for all compositions. The values $B_2^* = 1$ far below the critical temperature indicate the system is dominated by a short-range repulsion, described by an effective hard-core model. Starting from $T - T_c \sim 1\,$K at solvent compositions of around $c \sim 30\,\%$, $B_2^*$ quickly drops to negative values, indicating the rise of an attractive critical Casimir interaction. This is in line with previous studies of the virial coefficient close to the critical point [183]. The comparison based directly on the raw measurements provides good evidence that it is indeed the critical Casimir interactions that underlie the colloidal attraction in the investigated solvent composition range. Hence, this direct comparison suggests that not only at the critical composition, but also at these off-critical compositions, the attraction is described in terms of a critical Casimir force rather than by wetting effects. Yet, at even higher off-critical compositions, wetting effects are expected to eventually take over and dominate the attraction as clearly observed in Ref. [28].

We finally highlight the composition dependence of particle interactions by showing the theoretically calculated pair potentials for two fixed temperatures in Fig. 6.8. As already observed for the virial coefficients, the strongest attraction occurs for compositions $c = 29.5 - 31\,\%$, well above the critical composition $c_c = 27.7\,\%$. For $\Delta T = 1.0\,\mathrm{K}$ (Fig. 6.8(a)), the interaction is still small at $c = 28\,\% \approx c_c$ and below, whereas at higher composition $c > c_c$, the critical Casimir force leads to a notable attractive potential well. The depth of the potential minimum for $c = 29.5\,\%$ becomes close to $-3\,k_BT$, but no aggregation is yet observed (compare Fig. 6.6). For $\Delta T = 0.8\,\mathrm{K}$ (Fig. 6.8(b)), the depth of the potential minimum has increased considerably, exceeding $-3\,k_BT$ for $c = 29.5\,\%$ and $c = 31.0\,\%$, leading to aggregation in the experiment. For the critical composition $c = 28\,\%$ and below, the attraction is still small. We find that the criteria $B_2^* \lesssim 1.2$ of the sticky sphere model provides a quantitatively good estimate for the onset of aggregation, while the earlier, simple criteria that the depth of the potential minimum exceeds $-3\,k_BT$ [84], is qualitatively in line with our findings, but may not provide a quantitatively reliable estimate.

Furthermore, Fig. 6.8 reports the parameters $\Delta T_{\mathrm{off}}$ for each composition for which we have obtained the best agreement between the experimental $g(r)$ and the theoretical predictions. As discussed in section 2.2.2, $\Delta T_{\mathrm{off}}$ is an effective rescaling in the case of weakly adsorbing particles. Thus, the same systematic trend carries over to the scaling parameter $s(h_s, h)$. To our knowledge, the dependence of $s$ on $h$ has not been studied yet (see Ref. [73] for $s(h_s) = s(h_s, h = 0)$). Our measurements indicate a systematic dependence that itself is asymmetric around the critical composition, i.e., the behavior depends strongly on the signs of $h_s$ and $h$. Further studies could focus on the dependence of colloidal aggregation on the strength of the surface adsorption.

## 6.5 Conclusions

As a field test for the theoretical pair potential model in Eq. (2.41), we have investigated the interactions of colloidal particles in near-critical binary solvent at off-critical compositions in the context of an actual experimental realization. Experimentally, the colloids have been monitored through a laser-scanning confocal microscope, which takes two-dimensional images of an illuminated focal plane within the three-dimensional sample cell. The particle centers have then been located in the horizontal plane by a standard tracking algorithm [178]. The pair correlation function $g(r)$ is inferred from the probability of finding a particle at distance $r$ from a reference particle. A number of optical and experimental limitations have affected the resulting pair correlation function (diffusion of particles during scanning time, noise, accuracy of the algorithm, poly-dispersity, and the effect of the non-zero focal thickness in vertical direction). As these effects are expected to be independent of temperature, at least within the range of a few degrees, a measurement $3\,\mathrm{K}$ below the lower critical point serves as a reference of the repulsive interactions, without the influence of the critical Casimir attraction (Fig. 6.1). The determined $g(r)$ has been much smoother than expected, in contrast to the model with hard-core repulsion and electrostatic repulsion. For that, the Debye length $\kappa^{-1}$ for the binary liquid mixture of 3-methylpyridine and heavy water with 1 mM salt was estimated to be around 6 nm and the surface charge density was determined independently by electrophoresis measurements to be $\Upsilon = -0.17\, e\, \mathrm{nm}^{-1}$. The discrepancy can be resolved by considering a projected $g_{\mathrm{proj}}(r')$ (Eq. (6.1)) which accounts for the uncertainties in $x$, $y$, and $z$ direction using normal probability distributions around the *true* particle position, with standard deviations $\sigma = \sigma_x = \sigma_y$ within the plane and $\sigma_z$ perpendicular to the focal plane. An in-plane distribution width between $\sigma/d = 0.05$ and 0.067, i.e., $\sigma = (106\text{–}141)$ nm based on the diameter $d = 2.012\,\mu$m of the colloids, corresponds well to the observed pair correlation function. This is also in agreement with the sum of the individual estimates of the experimental uncertainties, amounting to 135 nm.

Thus, for a robust comparison between theory and experiment which avoids fitting, we have followed the strategy to determine independently all parameters entering the scaling variables of the dimensionless effective potential $U(r)$ (Eq. (2.41)), to assume the low-density limit $g(r) = e^{-U(r)}$, and then to apply the same broadening effect to the theoretical pair potential via $g_{\mathrm{proj}}(r')$.

The equation of state for the critical solvent depends only on two non-universal amplitudes, as other non-universal amplitudes are related to each other via universal amplitude ratios. A purposeful choice is the amplitude $\xi_t^{(0)}$ of the correlation length $\xi_t(t) = \xi_t^{(0)}\,|t|^{-\nu}$ at the critical concentration, and the amplitude $\mathcal{B}$ which enters into the shape of the coexistence curve $\phi_b(t) = \mathcal{B}\,|t|^{\beta}$. The values of these amplitudes are determined from dynamic light scattering (DLS) measurements of the solvent without colloids and from observing the phase separation of the solvent, respectively (see Figs. 6.2 and 6.3). Note that DLS in fact provides the self-diffusion coefficient, which is related to the correlation length via the intricate relations presented in Appendix 6.A.

Finally, it was required to incorporate the weak adsorption preference of the colloids. It is known that, at the critical concentration, the profiles for weak surface fields can be mapped to the strong adsorption case by rescaling of the scaling function [73]. However, to the best of our knowledge it has not been studied how such a relation is modified for being at off-critical concentrations. Within the experimentally accessible range, an effective temperature offset approximates the weak adsorption to a good degree (see the discussion in Sec. 2.2.2).

Thus having established the values of all scaling variables, we have been able to compare the projected pair correlation functions from the experiment and theory close to the critical point, for different temperatures and concentrations in Figs. 6.4 and 6.5(a,b). The unmodified theoretical pair potentials are shown in Fig. 6.5(c,d).

The second virial coefficient $B_2$ is found to be a more accurate quantity, which is largely insensitive to the experimental inaccuracies, see the discussion in Sec. 6.2. The law of corresponding states can be applied in order to compare this with the critical, normalized value $B_2^* = -1.2$ of the sticky spheres model below which aggregation is observed. This critical value successfully identifies the region of colloidal aggregation induced by the critical Casimir attraction in Fig. 6.6. Furthermore, we have made a comparison in Fig. 6.7 between $B_2^*$ as a function of temperature $T$ and composition $c$ as obtained in theory (colored surface) and from the experiment (data points) in a three-dimensional surface plot, from a top-view in (a), an elevated side perspective in the top panel of (b) and a full side view in the lower panel.

Thus, we conclude it is possible to accurately reproduce the experimentally measured pair correlations in the vicinity the critical point based on a simple effective pair potential comprised of hard-core interaction, electrostatic repulsion and the critical Casimir attraction.

# 6.A Appendix: Calculation of the correlation length

## 6.A.1 Implementation

The computational task at hand is determining from Eq. (2.35) inversely the correlation length $\xi$ that yields the same diffusion coefficient as experimentally determined. Apart from the known experimental state $(\phi, T)$, the arguments $Q_0$ and $q_D/q_c$ are unknown and need to be determined simultaneously. In order to find optimal values for $Q_0$ and $q_D/q_c$ we implement an iterative approach inspired by Ref. [105]. In our approach we assume $Q_0$ and $q_D/q_c$ to be independent of $\phi$ and $T$. This means that the dependence of viscosity on the closeness to critical point is fully described by the $\xi$. We then determine the optimal $Q_0$ and $q_D/q_c$ values as the ones that give the best agreement of the resulting $\xi$ with the power law $\xi_t = \xi_{t,+}^{(0)}\,|t|^{-\nu}$ for compositions around $c \approx 0.28$. More specifically, we minimize the least-square deviation of the logarithmic values $\sum_i \left(\log \xi_i - \log\left(\xi_{t,+}^{(0)}\left|\frac{T_c - T_i}{T_c}\right|^{-0.63}\right)\right)^2$, for all $\{\xi_i, T_i\}$ data points of the 27.25% and 28% samples. Note that we fix the critical exponent $\nu = 0.63$ but leave $\xi_{t,+}^{(0)}$ to be optimized. Close to the critical point, as the value of the diffusion coefficient drops, the relative experimental error increases significantly; due to the sensitivity of our procedure to these errors, we disregard samples with $t < 10^{-4}$. One interesting observation is that the procedure becomes more resilient against these experimental errors for $\mathcal{R} > 1$, indicating that the critical part of the diffusion coefficient as given in Eq. (2.33) is different from a simple Stokes-Einstein relation ($\mathcal{R} = 1$). As consistency checks, we have tested three variants: first, we have varied only $Q_0$ for $q_D/q_c = 0$, i.e. for vanishing background, with the additional constrain that $Q_0\,\xi_{t,+}^{(0)} = 0.15$. This value was taken from Ref. [111] where it was found by fitting to experimental data of the critical contribution to the viscosity. We find an optimal fit with $Q_0 = 0.36\text{nm}^{-1}$ and

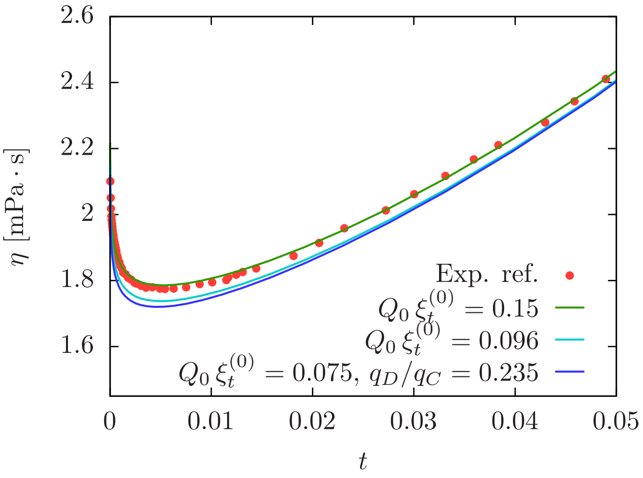

Figure 6.9: Estimated viscosity of the present mixture 3MP / heavy water with 1mM KCl at the critical weight fraction $c \approx 0.28$, based on values from the fitting procedure of the diffusion coefficient (see appendix). The experimental values of Ref. [111] are for the pure binary mixture without salt.

$\xi_{t,+}^{(0)} = 0.42\,\text{nm}$. In the second case, we have minimized for both $Q_0$ and $\xi_{t,+}^{(0)}$, still keeping $q_D/q_c = 0$. This yields $Q_0 = 0.22\,\text{nm}^{-1}$ and $\xi_{t,+}^{(0)} = 0.435\,\text{nm}$, so that $Q_0\,\xi_t^{(0)} = 0.096$. Lastly, we have allowed for a finite value of $q_D/q_c$, yielding the best agreement with $Q_0 = 0.17\,\text{nm}^{-1}$, $\xi_{t,+}^{(0)} = 0.44\,\text{nm}$ and $q_D/q_c = 0.235$, so that $Q_0\,\xi_{t,+}^{(0)} = 0.075$. In order to validate our approach we note that the values for $Q_0\,\xi_{t,+}^{(0)}$ that we obtain in the second and third case are not far removed from this in the first case; small changes can be expected because our mixtures contain salt [105, 182]. The resulting viscosities for the present mixture are shown in Fig. 6.9. Overall our estimates are slightly below the viscosity data of Ref. [111] for the pure binary mixture 3MP-$D_2O$. Still, we find reassurance in the overall agreement, since estimating the viscosity is not the primary focus of this procedure.

### 6.A.2 Corrections to the critical diffusion coefficient

Here, we argue why the expression given by Eq. (2.35), which is dominated by the critical part in Eq. (2.33), reproduces the behavior of the measured diffusion coefficient given in Fig. 2.1(b). In literature, Eq. (2.33) is often called a (pseudo-)Stokes-Einstein relation, especially when setting $\mathcal{R} = 1$ [107]. However, this is more of an analogue than a rigorous statement, as the self-diffusion of the OP is not governed by the same relation as the Brownian motion. If we naïvely assume the Stokes-Einstein relation in which the radius of the Brownian particles is replaced with the size of the correlated scattering features, i.e., the correlation length $\xi$, so that

$$D = \frac{k_B T}{6\pi\eta\xi}, \tag{6.4}$$

we obtain inconsistent results: as we know that $\xi$ is a power law of $t$ close to $T_c$, we would then expect that $D$ also follows a power law, i.e., a straight line in Fig. 2.1. However, we find that instead $D$ flattens out and approaches a constant value upon decreasing $t$. In contrast, saturation of $D$ is captured correctly by Eq. (2.33). In the critical limit $x = q\,\xi \gg 1$ one has $K(x) \propto x$ [184] and $H(Q_0\,\xi \to \infty, q_D/q_c) = \ln(Q_0\,\xi)$ [106], so that

$$\lim_{\xi\to\infty} D_{\mathrm{c}} = \frac{\mathcal{R}\,k_B T}{6\pi\,\eta_{\mathrm{bg}}\,Q_0^z\,\xi^{1+z}}\,b^z(q\,\xi)^{1+z} = \mathrm{const.}, \tag{6.5}$$

leading to a saturation of the diffusion coefficient at $T = T_c$, as observed in the experiments. Note that it is sufficient to look at $D_{\mathrm{c}}$ to explain this saturation since the background $D_{\mathrm{bg}}$ given by Eq. (2.34) becomes negligible for large $\xi$. $D_{\mathrm{bg}}$ contributes to the deviation from a power law that is observed for large $t$, due to effects of the viscosity on a different, non-critical temperature scale.

For our fitting procedure, we have used newer estimates that give as the value of the universal amplitude $\mathcal{R} = 1.05$ [107, 108]. This slight deviation from 1 is of significant importance. Since $\lim\limits_{\xi\to\infty} D_c = \mathrm{const.}$, the diffusion coefficient becomes insensitive to the actual value of the correlation length, but is still proportional to the universal amplitude $\mathcal{R}$. Conversely, in our procedure we find for $\mathcal{R} = 1$ widely varying results for the correlation length $\xi$, amplifying small experimental errors of the diffusion coefficient. These issues are significantly reduced for $\mathcal{R} = 1.05$, supporting the finding that the universal amplitude $\mathcal{R} > 1$. In consequence, there is no particular limit in which the Stokes-Einstein relation in Eq. (6.4) can be obtained from Eq. (2.33).

# Chapter 7

# Summary and Outlook

This thesis presents investigations into *effective interactions between colloidal particles in critical solvents.* In this chapter, in addition to the conclusions at the end of each chapter, the findings are summarized in its entirety. As it seems impossible to cover such a topic exhaustively, a possible outlook to further research is also given.

After a basic introduction in **chapter 1** and a discussion of the necessary theoretical background in **chapter 2**, the main results have been presented. To start off, in **chapter 3**, specific interest has been taken in the critical Casimir interaction between chemically structured colloids and substrates. The chapter is sectioned according to the different geometries sketched out in Fig. 3.1. A distinction between two types of cylindrical Janus particles has been drawn: type A, which features a step in the surface boundary conditions (BCs) along the length of the cylinder, cutting it into two half-cylinders, and type B, which is divided perpendicular to the length of the cylinder, cutting it in two cylinders of half the length. For the type A Janus cylinder, the critical Casimir force acting on a single such particle (see Sec. 3.1) has first been calculated both by using the Derjaguin approximation (DA) and by applying mean field theory (MFT). Figs. 3.2 and 3.3 compare the scaling functions of the force for a Janus cylinder (type A) above a homogeneous substrate with the scaling function for a homogeneous cylinder above a substrate with a chemical step, both in DA and MFT, as a function of the scaled temperature $\Theta = D/\xi(t)$ (Fig. 3.2) and the scaled position $\Xi$ of the particle (Fig. 3.3). The construction principle of the DA suggests that these configuration are analogous to each other, and good agreement is in fact also found within MFT in the DA limit $\Delta \to 0$. This relation has been further studied by inspecting the order parameter (OP) profiles in these configurations as obtained from MFT, see Fig. 3.4. A phenomenological relation for the DA has been proposed, which has been obtained by applying the DA to a fictional, scaled colloid (Fig. 3.5) in order to account for the shape of the OP profiles. The improvement has been demonstrated in Fig. 3.6. Thus, the additive nature of the DA has been further used with the expectation that it holds qualitatively, and to some degree quantitatively, also in MFT. The correspondence of a type A Janus particle and chemical steps on a substrate has been used in section 3.2 for the combination of a cylindrical Janus particle above a chemically stepped substrate. Fig. 3.7 compares the results for the scaling function of the force obtained from DA and within MFT, with good agreement for the smaller distance $\Delta = D/R = 1/5$. Before directly studying the type B Janus particle, the case of a homogeneous cylinder above a substrate with a chemical step (Sec. 3.3) has been revisited, now with a view on the critical Casimir torque acting on the particle, which has been derived from the critical Casimir potential using the DA. The scaling function of the torque, shown in Fig. 3.8, changes sign depending on the lateral distance from the step, the combination of BCs, as well as the aspect ratio of the cylindrical particle. This torque aligns the colloid parallel for positive values or perpendicular for negative values. The orientational order, as seen in Figs. 3.9 and 3.10, has been further investigated for different lengths of the particle, from rod-like particles to disk-like ones, using the planar nematic order parameter $S$. It has been experimentally demonstrated in binary liquid mixtures that homogeneous spherical colloidal particles can be reversibly trapped above a chemically patterned substrate via critical Casimir interactions [68–70,103]. Together with the present study of alignment, this has prompted a particular perspective on the type B Janus particle: In Sec. 3.4, the critical Casimir potential derived within DA has been used in order to study the effective interaction between a cylindrical Janus particle and a chemically striped substrate. The angular and position dependent part of the scaling function of potential $\omega_p$ [Eq. (3.16)] exhibits several maxima and minima (Fig. 3.11). The alignment has been characterized using the standard deviation $\sigma_\alpha$ of the angular probability distribution function, from which a characteristic and well defined rotation angle $\alpha$ followed (Fig. 3.12), so that the Janus particle is preferentially rotated relative to the chemical stripes and shifted laterally with respect to the center of the stripes. Based on this analysis within DA, it should be possible to achieve a controlled, reversible alignment of type B Janus particles using a similar setup as in previous experiments.

In **chapter 4**, the study has been extended to critical Casimir interactions between two Janus particles. The case of two Janus cylinders (type A) had already been worked out before [75,127], but a short reminder has been given for clarity. The focus has then been put on Janus spheres, which have been described in a relative coordinate system as a function of three spherical coordinates $\alpha = \phi_2 - \phi_1$, $\vartheta_1$, and $\vartheta_2$ (see Fig. 4.2). The details of the DA for Janus spheres are given in Appendix B. The resulting scaling function of the force as a function of the scaled temperature $\Theta = D/\xi(t)$ is shown in Fig. 4.3. Depending on the orientation of the two Janus spheres, the critical Casimir force can be attractive or repulsive. The strongest attraction is found in the case of the two Janus spheres facing each other with the same face, whereas the strongest repulsion occurs when they are lined up. The scaling function of the effective pair potential then follows from the force. In order to gain another perspective on the scaling function of the potential, it is presented in Fig. 4.4 as an energy landscape in terms of the particle orientations $\vartheta_1$ and $\vartheta_2$ for the two cases $\alpha = 0$ and $\alpha = \pi$, for fixed temperature and distance. There are two flat and stable minima in the potential energy, which are connected by a narrow valley (which represents counter-rotating orientations of the Janus particles). The large plateaus of repulsive orientational states corresponding to opposing BC yield a checkerboard landscape pattern. Varying the angle $\alpha$ affects the scaling function of the effective potential only around orientations $\vartheta_{1,2} = \pi/2$, but does not alter the structure of plateaus and plains.

The knowledge gained of the scaling function of the effective potential has then been used to study a common experimental situation in which the particle positions and orientations are confined to a plane parallel to the planar surface of a substrate. Fig. 4.5 visualizes the analysis of how the effective influence of the substrate, incorporated as an externally imposed common tilt $\gamma$ of all Janus particles, changes the effective pair interaction among the Janus particles. The deviations turn out to be small for tilts $\gamma \lesssim 30°$ and still acceptable for $\gamma \lesssim 45°$. Under this condition, concerning the interaction among the particles, the substrate induced interaction can be discarded.

In view of the desire to employ the critical Casimir potential in numerical computations (e.g., density functional theory) or simulations (e.g., Monte-Carlo) of the phase behavior, the foundation for an expansion in terms of the Kern-Frenkel (KF) model and a generalized dipole-dipole interaction has been laid out in Sec. 4.3 (compare Fig. 4.6 with Fig. 4.4). The KF model provides clear parameters for the interaction strength, interaction range and the effective patch size (see Fig. 4.7), but turns out to be of limited use close to the critical point. Alternatively, an expansion of the critical Casimir potential in a rotational invariant basis has been introduced, leading to a generalized dipole-dipole interaction in terms of the orientational order (the coefficients are depicted in Fig. 4.8).

Up to this point, explicit calculations of the critical Casimir force and potential have been based solely or additionally on the DA. Now in **chapter 5**, in order to capture effective interactions beyond the critical Casimir interaction, the Hamiltonian in Eq. (2.27) has been minimized numerically for two parallel, cylindrical colloids of radius $R$ in a near-critical solvent at two-phase coexistence, from which one obtains the free energy and the corresponding equilibrium MFT order parameter profiles. In the terminology of binary liquid mixtures, the colloids have a preference for one of the two components of the solvent. This leads to the formation of an adsorption layer of the preferred phase around the colloids, as sketched in Fig. 5.1. In the global minimum of the free energy, the colloids are immersed in the preferred $\alpha$ phase; however, there is a largely stable local minimum in which the colloids are engulfed by the less favored $\beta$ phase and located far away from the $\alpha$-$\beta$ interface. It turns out that the scaling function $P_-$ [Eq. (5.11)] of the *two*-particle order parameter profiles (see Figs. 5.2 and 5.3) features a local $\alpha$-$\beta$ interface that encapsulates both particles either individually (separated state) or as a pair (bridged state), depending on the surface-to-surface distance $D$ and temperature, with a first-order phase transition between the two states. Three regimes clearly manifest themselves in the scaling function $G$ of the effective interaction potential as a function of the distance (shown in Fig. 5.4): At close separations, critical Casimir forces dominate; at intermediate separations the extension of the liquid bridge leads to a region in which the influence of the $\alpha$-$\beta$ interfacial tension dominates; and finally a third regime in which the liquid bridge is meta-stable compared to the separated state and eventually ruptures. By comparison, the first regime at small separations $\Delta = D/R < 1$ is in very good agreement with the DA for the critical Casimir potential between two cylinders. In the second regime, the slope of $G$ with respect to $\Delta$ matches the surface tension contribution to the force, confirming that the effective potential is dominated by the cost of extending the interfacial area. Finally, the liquid bridge ruptures and the third regime corresponds to two separated particles, with the scaling function $G$ being de facto independent of distance. To a large extent, in the less-critical regime $\Theta_- \gg 1$, the transition distance $D_t$ of the liquid bridge can be expressed in terms of *single*-colloid profiles (see Figs. 5.5 and 5.6). It turns out that the adsorption layer in *single*-particle profiles essentially consists of the wall-$\alpha$ interface, well described by a short distance approximation [Eq. (5.20)], joint together with the free $\alpha$-$\beta$ interface profile [Eq. (5.22)] for which the adsorption layer thickness $l_a$ is the relevant quantity. The transition distance $D_t$ has been unambiguously determined from the zero-crossing of the scaling function $G$ of the effective potential in the bridged state. Fig. 5.7(a) presents the phase diagram of the liquid bridge, which is divided by $D_t$ into two distinct domains: For large $\Delta$ and away from $T_c$, the separated state is the stable configuration. For small separations $\Delta$ or close to $T_c$, the colloids are connected by a bridge formed by the preferred $\alpha$ phase. Away from criticality, i.e., for $\Theta_- \gg 1$, a geometric model based on the adsorption layer thickness $l_a$ yields a reasonable approximation for the transition distance $D_t$ [see Fig. 5.7(b)]. Beyond the present mean field treatment, finite-size induced fluctuation are expected to cause a shift and rounding of the phase transition. This has been discussed specifically for the geometry of two parallel cylinders, see Fig. 5.8. According to the presented estimates, the smearing and the shift of the transition probability (Fig. 5.9) are too small to be noticeable in the experiment for rescaled temperatures $\Theta_- \gtrsim 3$. This range still features the critical Casimir contribution discussed above. Furthermore, the scaling function $G$ of the effective potential for the bridged state has been studied as a function of the rescaled temperature $\Theta_-$ (see Fig. 5.10), reproducing the phase transition temperature $\Theta_-^{(t)}$, as well as the temperature dependence of the scaling function $\mathcal{K}$ of the effective force between two colloids for various small separations $D$ (see Fig. 5.11). The latter has highlighted again both the influence of the interfacial tension resulting from extending the liquid bridge as well as the critical Casimir force for $\Theta_- \to 0$.

As a field test for the theoretical pair potential model in Eq. (2.41), in **chapter 6** the interactions of colloidal particles in near-critical binary solvent at off-critical compositions have been investigated in comparison with an actual experimental realization. Experimentally, the colloids have been monitored through a laser-scanning confocal microscope, which takes two-dimensional images of an illuminated focal plane within the three-dimensional sample cell. The pair correlation function $g(r)$ is inferred from the probability of finding a particle at distance $r$ from a reference particle. A number of optical and experimental limitations have affected the resulting pair correlation function (diffusion of particles during scanning time, noise, accuracy of the algorithm, poly-dispersity, and the non-zero focal thickness in vertical direction). The influence on the pair correlation function has briefly been studied in Fig. 6.1. The determined $g(r)$ has been much smoother than expected, in contrast to the model with hard-core repulsion and electrostatic repulsion. The discrepancy can be resolved by considering a projected $g_{\text{proj}}(r')$ [Eq. (6.1)] which accounts for the uncertainties in $x$, $y$, and $z$ direction using normal probability distributions around the *true* particle position, with standard deviations $\sigma = \sigma_x = \sigma_y$ within the plane and $\sigma_z$ perpendicular to the focal plane. An in-plane distribution width between $\sigma/d = 0.05$ and 0.067, i.e., $\sigma = (106\text{–}141)\,\text{nm}$ based on the diameter $d = 2.012\,\mu\text{m}$ of the colloids, corresponds well to the observed pair correlation function. This is also in agreement with the sum of the individual estimates of the experimental uncertainties, amounting to 135 nm. Thus, for a robust comparison between theory and experiment which avoids fitting, the strategy was to determine independently all parameters entering the scaling variables of the dimensionless effective potential $U(r)$ [Eq. (2.41)], to assume the low-density limit $g(r) = e^{-U(r)}$, and then to apply the same broadening effect to the theoretical pair potential via $g_{\text{proj}}(r')$.

The equation of state for the critical solvent depends only on two non-universal amplitudes, as other non-universal amplitudes are related to each other via universal amplitude ratios. A purposeful choice is the amplitude $\xi_t^{(0)}$ of the correlation length $\xi_t(t) = \xi_t^{(0)}\,|t|^{-\nu}$ at the critical concentration, and the amplitude $\mathcal{B}$ which enters into the shape of the coexistence curve $\phi_b(t) = \mathcal{B}\,|t|^{\beta}$ ($\nu$ and $\beta$ are standard bulk critical exponents). The values of these amplitudes are determined from dynamic light scattering (DLS) measurements of the solvent without colloids and from observing the phase separation of the solvent, respectively (see Figs. 6.2 and 6.3). Note that DLS actually yields the self-diffusion coefficient, which is related to the correlation length via the intricate relations presented in Appendix 6.A. Finally, it has been necessary to incorporate the weak adsorption preference of the colloids. It is known that at the critical concentration the profiles for weak surface fields can be mapped to the strong adsorption case by rescaling of the scaling function [73]. However, as far as presently known, it has not been studied how such a relation is modified for being at off-critical concentrations. Within the experimentally accessible range, an effective temperature offset describes approximately the weak adsorption, see the discussion in Sec. 2.2.2. Thus having established the values of all scaling variables, it was possible to compare the projected pair correlation functions from the experiment and from theory close to the critical point, for different temperatures and concentrations in Figs. 6.4 and 6.5(a,b). The unmodified theoretical pair potentials are shown in Fig. 6.5(c,d). A more accurate measure, which is rather insensitive to the experimental inaccuracies, is found in the second virial coefficient $B_2$, see the discussion in Sec. 6.2. The law of corresponding states can be applied in order to make a comparison with the critical, normalized value $B_2^* = -1.2$ of the sticky spheres model below which aggregation is observed. This critical value successfully identifies the region of colloidal aggregation induced by the critical Casimir attraction in Fig. 6.6. Furthermore, a comparison between the values $B_2^*$ of theory (colored surface) and experiment (data points) has been made in the form of a three-dimensional surface plot (Fig. 6.7).

As listed before, the results have been published ahead of this thesis. In order to present a more coherent train of thought, the content in this thesis has been rearranged compared to the chronological publication list: **Sections 3.1** and **3.2** can be found in Ref. [75], **sections 3.3** and **3.4** in Ref. [74]. **Chapter 4** is also part of Ref. [75]. **Chapter 5** is published as Ref. [77]. **Chapter 6** is based on Ref. [76], which contains additional details about the experimental setup.

In conclusion, all studies performed during this thesis corroborate that *effective interactions* are capable to accurately describe the behavior of *colloidal particles in critical solvents*. Within the description of *effective interactions*, the solvent is not considered explicitly, but rather as an effective background captured by the parameters of the effective pair potential, and there is no coupling between individual interactions, such as the critical Casimir interactions and electrostatic repulsion. The resulting forces are assumed to be additive. Note that the geometries under consideration have been simple pairs (**chapters 3**, **4**, and **5**), or at most dilute suspension dominated by pairwise interactions (**chapter 6**). It is known that for the critical Casimir force, many-body contributions can amount up to 25% of the total force [185–187]. It has also been found that ion-solvent coupling plays an important role in the case of electrostatic interactions and critical Casimir interactions [188, 189]. In the case of opposing BCs on the particle surfaces, the coupling gives rise to an attractive contribution to the otherwise repulsive interactions. This does not influence the experiment presented in **chapter 6** which employs only one type of particle with a uniform BC. However, one expects such deviations to be relevant for Janus particles.

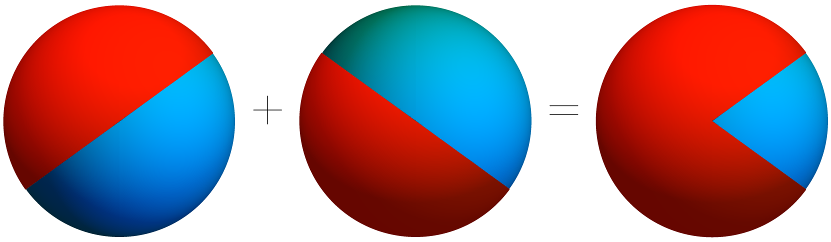

Figure 7.1: Sketch of a pistachio or pacman particle, imagined as a continuation of the present research by superimposing tilted Janus spheres on top of each other and combining their effective interactions.

Nonetheless, considering that highly sophisticated particle “designs” are experimentally available (triblock Janus spheres [56], variations of patchy particles [63], raspberry-like particles [190], Mickey Mouse particles [191], and dumbbells [192]), *effective interactions* remain important for the basic assessment of the phase behavior in dilute systems. Due to the additive nature of the Derjaguin approximation, new particle types can be constructed from already known geometries. As an outlook, consider the pistachio or pacman particle depicted in Fig. 7.1. It can be viewed as consisting of two (graphically) superimposed Janus particles. By correct summation of surface elements, an additive effective interaction can be constructed again. Experimentally, the fabrication of such a particle can be achieved using evaporation techniques, by which half of an originally homogeneous particle is coated with another surface layer (boundary condition). Tilting the particle, e.g., by alignment in an external magnetic field, and depositing a second, rotated hemisphere is expected to produce a surface structure as depicted. In this rare case, the theoretic model of combining the interaction of Janus particles is actually an imitation of the manufacturing step.

It appears that further research is not limited by imagination, but only by the increasing complexity both in the theoretical models and the experimental fabrication. Thus, every incremental addition to the knowledge of *effective interactions* between structured *colloidal particles* may serve as the basis for further investigations.

# Zusammenfassung und Ausblick

Diese Doktorarbeit behandelt *effektive Wechselwirkungen zwischen kolloidalen Teilchen in kritischen Lösungen*. In diesem Kapitel werden die Ergebnisse, zusätzlich zu den Schlussfolgerungen (Conclusions) am Ende jedes Kapitels, in ihrer Gesamtheit zusammengefasst. Da es ausgeschlossen scheint ein solches Thema erschöpfend wiederzugeben, wird auch ein möglicher Ausblick auf weitere Forschung gegeben.

Nach einer grundsätzlichen Einführung in **Kapitel 1** und einer Diskussion des notwendigen theoretischen Hintergrundes in **Kapitel 2**, wurden die wesentlichen Ergebnisse präsentiert. Zum Einstieg wurde in **Kapitel 3** das Augenmerk auf die kritische Casimir Wechselwirkung zwischen chemisch strukturierten Kolloiden und Substraten gelegt. Das Kapitel teilt sich gemäß der verschiedenen Geometrien auf, die in Abb. 3.1 skizziert sind. Es wurde zwischen zwei Typen von zylindrischen Janus-Teilchen unterschieden: Typ A besitzt eine Stufe in den Randbedingungen (boundary conditions; BCs) entlang der Längsachse des Zylinders, unterteilt ihn also in zwei Halbzylinder. Typ B ist quer zur Längsachse des Zylinders geteilt, ist also aus zwei Zylindern der halben Länge zusammengesetzt. Für den Typ A Janus-Zylinder wurde zunächst die kritische Casimir-Kraft, die auf einzelnes Teilchen wirkt, berechnet (siehe Abschnitt 3.1), sowohl mit der Derjaguin-Näherung (DA) als auch mittels der Molekularfeldtheorie (MFT). Abb. 3.2 und 3.3 vergleichen die Skalenfunktionen der Kraft für einen Janus-Zylinder (Typ A) über einem homogenen Substrat mit der Skalenfunktion für einen homogenen Zylinder über einem Substrat mit einer chemischen Stufe, sowohl in DA als auch MFT, als Funktion der skalierten Temperatur $\Theta = D/\xi(t)$ (Abb. 3.2) und der skalierten Position $\Xi$ des Teilchens (Abb. 3.3). Das Konstruktionsprinzip der DA legte nahe, dass diese Konfigurationen analog zueinander sind und tatsächlich fand sich eine gute Übereinstimmung auch mit der MFT im Grenzfall $\Delta \to 0$ der DA. Dieser Zusammenhang wurde weiterhin anhand der aus der MFT gewonnenen Profile des Ordnungsparameters (OP) in den betreffenden Konfigurationen untersucht, siehe Abb. 3.4. Es wurde eine phänomenologische Relation angeregt, die der Form der OP-Profile Rechnung trägt, und die sich ergibt, wenn man die DA auf ein fiktives, skaliertes Kolloid (Abb. 3.5) anwendet. Die Verbesserung wurde in Abb. 3.6 demonstriert. Folglich konnte die additive Natur der DA im Weiteren ausgenutzt werden, in der Erwartung, dass sie auch für MFT qualitativ zutrifft und im begrenzten Maße auch quantitativ. Die Übereinstimmung zwischen Typ A Janus-Zylindern und chemischen Stufen auf einem Substrat wurde anschließend in Abschnitt 3.2 für die Kombination eines zylindrischen Janus-Teilchens über einem chemisch abgestuften Substrat verwendet. Abb. 3.7 vergleicht die sich aus DA und MFT ergebenden Skalenfunktionen der Kraft und zeigt gute Übereinstimmung bei dem kleineren Abstand von $\Delta = D/R = 1/5$. Vor den Typ B Janus-Teilchen wurde zunächst noch einmal der Fall eines homogenen Zylinders über einem Substrat mit einer chemischen Stufe betrachtet (Abschnitt 3.3). Diesmal wurde das kritische Casimir-Drehmoment ausgewertet, das auf ein Teilchen wirkt, und das aus dem kritischen Casimir-Potential in DA abgeleitet wurde. Die Skalenfunktion des Drehmoments, wie in Abb. 3.8 zu sehen, wechselt das Vorzeichen in Abhängigkeit des lateralen Abstands von der Stufe, von der Kombination der BCs und dem Längenverhältnis der zylindrischen Teilchen. Das Drehmoment richtet das Kolloid für positive Werte parallel aus und senkrecht für negative Werte. Weiterhin wurde, wie in Abb. 3.9 und 3.10 zu sehen, die Orientierungsordnung mittels des nematischen Ordnungsparameters $S$ für verschiedene Längen des Teilchens (stäbchenförmig bis hin zu Scheiben) untersucht. Zuvor war schon in binären Flüssigkeitsmischungen experimentell gezeigt worden, dass sich homogene, kugelförmige kolloidale Teilchen über chemisch gestreiften Substraten mit kritischen Casimir-Kräften reversibel einfangen lassen [68–70, 103]. Zusammen mit der vorliegenden Untersuchung gab dies den Anlass, Janus-Teilchen des Typs B gezielt nach diesem Gesichtspunkt zu untersuchen: In Abschnitt 3.4 wurde das kritische Casimir-Potential in DA abgeleitet, um die effektiven Wechselwirkungen zwischen einem zylindrischen Janus-Teilchen und einem chemisch gestreiften Substrat zu untersuchen. Die Winkel- und Positionsabhängigkeit der Skalenfunktion des Potentials $\omega_p$ [Gl. (3.16)] weist mehrere Maxima und Minima auf (Abb. 3.11). Das Ausrichtungsverhalten wurde über die Standardabweichung $\sigma_\alpha$ der Winkelverteilung charakterisiert, woraus sich ein kennzeichnender Winkel $\alpha$ ergab (Abb. 3.12), so dass sich das Janus-Teilchen in Bezug auf die chemische Stufe bevorzugt in diesem Winkel ausrichtet und sich zur Mitte der Stufe lateral verschoben aufhält. Aus dieser Analyse auf Basis der DA folgt der Schluss, dass es möglich wäre in einem ähnlichen Aufbau wie in früheren Experimenten auch eine kontrollierte, reversible Ausrichtung von Janus-Teilchen des Typs B zu erzielen.

In **Kapitel 4** wurden die Untersuchungen auf kritische Casimir-Wechselwirkungen zwischen zwei Janus-Teilchen erweitert. Der Fall zweier Janus-Zylinder (Typ A) war bereits zuvor ausgearbeitet worden [75,127]. Der Fokus lag anschließend auf Janus-Kugeln, welche in einem relativen Koordinatensystem beschrieben wurden, das von drei Kugelkoordinaten $\alpha = \phi_2 - \phi_1$, $\vartheta_1$ und $\vartheta_2$ abhängt (siehe Abb. 4.2). Die Details der DA für Janus-Kugeln wurden in Appendix B abgehandelt. Die resultierende Skalenfunktion der Kraft als Funktion der skalierten Temperatur $\Theta = D/\xi(t)$ wurde in Abb. 4.3 gezeigt. Abhängig von der Ausrichtung der beiden Janus-Kugeln kann die kritische Casimir-Kraft attraktiv oder repulsiv ausfallen. Die stärkste Attraktion ergibt sich im Fall, dass sich die beiden Kugeln mit derselben Seite gegenüberstehen, während die stärkste Repulsion dann auftritt, wenn sie in einer Linie ausgerichtet sind. Die Skalenfunktion des effektiven Paarpotentials folgt dann aus der Kraft. Um eine weitere Sichtweise auf die Skalenfunktion des Potentials zu gewinnen, ist selbige in Abb. 4.4 als Energielandschaft bezüglich der Winkel $\vartheta_1$ und $\vartheta_2$ für die beiden Fälle $\alpha = 0$ und $\alpha = \pi$ dargestellt, bei konstanter Temperatur und konstantem Abstand. Es zeigten sich zwei flache und stabile Minima in der potentiellen Energie, die durch ein schmales Tal verbunden sind (welches gegenläufig rotierende Orientierungen der Janus-Teilchen darstellt). Die großen Plateaus entsprechen repulsiven Ausrichtungen mit gegensätzlichen BCs, woraus sich ein Schachbrettmuster in der Energielandschaft ergibt. Eine Veränderung des Winkels $\alpha$ beeinflusst die Skalenfunktion des effektiven Potentials nur bei Ausrichtungen in der Nähe von $\vartheta_{1,2} = \pi/2$, verändert die grundsätzliche Struktur von Plateaus und Talflächen allerdings nicht.

Das gewonnene Wissen über die Skalenfunktion des effektiven Potentials wurde dann angewendet, um eine verbreitete experimentelle Situation zu studieren, bei der die Teilchenposition und Orientierungen auf eine Ebene beschränkt sind, die parallel zur Substratoberfläche liegt. Abb. 4.5 visualisiert die Analyse über den effektiven Einfluss des Substrats auf die Wechselwirkung, der als von außen erzwungene Neigung $\gamma$ aller Janus-Teilchen beschrieben wird. Die Abweichung des effektiven Paarpotentials erweist sich als klein für Neigungen $\gamma \lesssim 30°$ und als vertretbar für $\gamma \lesssim 45°$. Unter dieser Bedingung kann die Wechselwirkung des Substrats bei Betrachtungen der Paarwechselwirkungen vernachlässigt werden.

Mit dem Anliegen, das kritische Casimir-Potential auch in numerischen Berechnungen (z.B. in der Dichtefunktionaltheorie) oder in Simulationen (z.B. Monte-Carlo) einsetzten zu können, um das Phasenverhalten auszuwerten, wurde in Abschnitt 4.3 die Grundlage für eine Entwicklung im Sinne des Kern-Frenkel (KF) Modells und im Sinne eines verallgemeinerten Dipol-Potentials gelegt (vgl. Abb. 4.6 mit Abb. 4.4). Das KF-Modell liefert eindeutige Parameter für die Wechselwirkungsstärke und -reichweite sowie die effektive Patch-Größe (siehe Abb. 4.7), weist jedoch Einschränkungen in der Nähe des kritischen Punkts auf. Als Alternative wurde die Entwicklung des kritischen Casimir-Potentials in eine rotationsinvariante Basis vorgestellt, welche zu einem verallgemeinerten Dipol-Potential bezüglich der Orientierungsordnung führt (die Koeffizienten sind in Abb. 4.8 dargestellt).

Bis zu diesem Punkt wurden explizite Berechnungen der kritischen Casimir-Kraft oder des Potentials stets vollständig oder zusätzlich mit der DA durchgeführt. Um effektive Wechselwirkungen über die Casimir-Wechselwirkungen hinaus zu erfassen, wurde in **Kapitel 5** der Hamiltonian in Gl. (2.27) numerisch für zwei parallele, zylindrische Kolloide mit Radius $R$ in einer nahezu kritischen Lösung bei Zweiphasenkoexistenz minimiert, wodurch man die Freie Energie und die entsprechenden MFT Gleichgewichtsprofile des OP erhält. Mit den Begrifflichkeiten von binären Flüssigkeitsmischungen gesprochen, besitzen die Kolloide eine Präferenz für eine der beiden Komponenten der Lösung. Das führt zur Ausbildung einer Adsorptionsschicht der bevorzugten Phase um die Kolloide herum, wie in Abb. 5.1 skizziert. Im globalen Minimum der Freien Energie sind die Kolloide in der bevorzugten $\alpha$-Phase gelöst, allerdings existiert ein weitgehend stabiles, lokales Minimum in dem die Kolloide in der missliebigen $\beta$-Phase, weit von der $\alpha$-$\beta$ Grenzfläche entfernt, eingeschlossen sind. Es zeigte sich, dass die Skalenfunktion $P_{-}$ [Gl. (5.11)] des Zwei-Teilchen-Profils des Ordnungsparameters (siehe Abb. 5.2 und 5.3) eine lokale $\alpha$-$\beta$ Grenzfläche aufweist, die entweder beide Teilchen einzeln (getrennter Zustand) oder als Paar (Brückenzustand) umschließt, je nach Oberflächenabstand $D$ und Temperatur. Dazwischen tritt ein Phasenübergang erster Ordnung auf. In der Skalenfunktion $G$ des effektiven Wechselwirkungspotentials zeigten sich drei eindeutige Bereiche als Funktion des Abstands (siehe Abb. 5.4): Bei kleinen Abständen überwiegen die kritischen Casimir-Kräfte; bei mittleren Abständen führt die Dehnung der Flüssigkeitsbrücke zu einem Bereich, in dem die $\alpha$-$\beta$ Grenzflächenspannung dominiert; und zuletzt ein dritter Bereich in dem die Flüssigkeitsbrücke nur noch metastabil gegenüber dem getrennten Zustand ist und reißt. Im Vergleich stimmt der erste Bereich mit kleinen Abständen $\Delta = D/R < 1$ hervorragend mit der DA des kritischen Casimir-Potentials überein. Im zweiten Bereich entspricht die Steigung von $G$ bezüglich $\Delta$ genau dem Beitrag der Grenzflächenspannung zur Kraft, was bestätigt, dass das effektive Potential von der Dehnung der Grenzfläche bestimmt wird. Schließlich reißt die Flüssigkeitsbrücke und der dritte Bereich entspricht zwei einzelnen Teilchen; dort ist die Skalenfunktion $G$ faktisch nicht mehr vom Abstand abhängig. Im weniger kritischen Bereich $\Theta_{-} \gg 1$ ließ sich der Übergangsabstand $D_t$, bei dem die Flüssigkeitsbrücke ausgebildet wird, größtenteils durch Ein-Teilchen-Profile vorhersagen (siehe Abb. 5.5 und 5.6). Es zeigte sich, dass die Adsorptionsschicht in den Ein-Teilchen-Profilen im Wesentlichen aus einer Wand-$\alpha$ Grenzfläche besteht, die gut durch die Short-Distance-Approximation beschrieben wird [Gl. (5.20)], in Verbindung mit einer freien $\alpha$-$\beta$-Grenzfläche [Gl. (5.22)], welche durch die Adsorptionsschichtdicke $l_a$ gekennzeichnet ist. Der Übergangsabstand $D_t$ wurde eindeutig aus dem Nulldurchgang der Skalenfunktion $G$ mit Flüssigkeitsbrücke bestimmt. Abb. 5.7(a) zeigt das Phasendiagramm mit den, durch $D_t$ aufgeteilten, zwei Zuständen der Flüssigkeitsbrücke: Für große $\Delta$ und abseits von $T_c$ ist der getrennte Zustand der stabile. Für kleine Abstände $\Delta$ oder nahe bei $T_c$ sind die Kolloide durch eine Flüssigkeitsbrücke, bestehend aus der bevorzugten $\alpha$-Phase, verbunden. Abseits vom kritischen Punkt, d.h. wenn $\Theta_{-} \gg 1$, ließ sich $D_t$ sinnvoll durch ein geometrisches Model nähern, das auf der Adsorptionsschichtdicke $l_a$ basiert [siehe Abb. 5.7(b)]. Über die gegenwärtige Molekularfeldtheorie hinaus steht zu erwarten, dass Fluktuationen, die aus der endlichen Größe des Volumens resultieren (Finite-Size Effekte), den Phasenübergang verschieben und ausschmieren. Dies wurde konkret für diese Geometrie mit zwei parallelen Zylindern diskutiert, siehe Abb. 5.8. Den dargelegten Abschätzungen zu Folge, sind die Aufweichung und die Verschiebung der Übergangswahrscheinlichkeit bei Temperaturen $\Theta_- \gtrsim 3$ zu klein, um experimentell beobachtbar zu sein. Dieser Temperaturbereich weist dennoch die angesprochenen Beiträge der kritischen Casimir-Kraft auf. Des Weiteren wurde die Skalenfunktion $G$ des effektiven Potentials noch als Funktion der skalierten Temperatur $\Theta_-$ im Brückenzustand (Abb. 5.10) untersucht, wobei sich die Übergangstemperatur $\Theta_-^{(t)}$ abbildete, sowie für verschiedene, kleine Abstände $D$ die Temperaturabhängigkeit der Skalenfunktion $\mathcal{K}$ der effektiven Kraft zwischen zwei Teilchen (Abb. 5.11). Letzteres verdeutlichte erneut den Einfluss der Grenzflächenspannung durch Dehnung der Flüssigkeitsbrücke, als auch die kritische Casimir-Kraft für $\Theta_- \to 0$.

Als Praxistest für das theoretische Paarpotential aus Gl. (2.41) wurden in **Kapitel 6** die Wechselwirkungen zwischen kolloidalen Teilchen in einer kritischen binären Mischung bei nicht-kritischen Zusammensetzungen mit einer tatsächlichen experimentellen Realisierung verglichen. Im Experiment wurden die Kolloide durch ein Laser-Konfokalmikroskop beobachtet, welches zweidimensionale Bilder aus einer beleuchteten Fokusebene innerhalb der dreidimensionalen Probe aufnahm. Die Paarkorrelationsfunktion $g(r)$ ist durch die Wahrscheinlichkeit bestimmt, ein Teilchen in einem Abstand $r$ von einem Referenzteilchen zu finden. Eine Reihe von optischen und experimentellen Einschränkungen beeinträchtigten die resultierende Paarkorrelationsfunktion (Diffusion der Teilchen während der Aufnahme, Rauschen, Genauigkeit des Algorithmus, Polydispersität und die endliche Fokusbreite in vertikaler Richtung). Der Einfluss auf die Paarkorrelationsfunktion wurde anhand Abb. 6.1 besprochen. Die beobachtete $g(r)$ Funktion fiel deutlich weicher aus, als aufgrund der harten Wechselwirkung und der elektrostatischen Abstoßung zu erwarten war. Diese Diskrepanz erklärt sich, wenn man eine Projektion $g_{\mathrm{proj}}(r')$ [Gl. (6.1)] betrachtet, welche die Unsicherheiten in $x$, $y$ und $z$-Richtung mit Normalverteilungen um die *wahre* Teilchenposition beschreibt, samt Standardabweichungen $\sigma = \sigma_x = \sigma_y$ innerhalb der Fokusebene und $\sigma_z$ vertikal dazu. In der Ebene stimmt eine Verteilungsbreite von $\sigma/d = 0{,}05$ und 0,067, was bei einem Durchmesser $d = 2{,}012\,\mu$m der Kolloide $\sigma = (106–141)$ nm entspricht, gut mit der beobachteten Paarkorrelationsfunktion überein. Diese passt auch zur Summe der einzelnen, geschätzten experimentellen Unsicherheiten, die sich auf 135 nm beläuft.

In der Absicht einen robusten Vergleich zwischen Theorie und Experiment ohne Fitting zu schaffen, bestand die Strategie darin, unabhängig alle Parameter zu bestimmen, die in Skalenvariablen des dimensionslosen effektiven Potentials $U(r)$ [Gl. (2.41)] eingehen, den Grenzfall $g(r) = e^{-U(r)}$ kleiner Dichte anzunehmen und dann mittels $g_{\mathrm{proj}}(r')$ denselben Aufweichungseffekt auf das theoretische Paarpotential anzuwenden. Die Zustandsgleichung des kritischen Lösungsmittels hängt nur von zwei nicht-universellen Amplituden ab, da weitere nicht-universelle Amplituden über universelle Verhältnisse in Relation zueinander stehen. Eine zweckdienliche Wahl besteht in den Größen $\xi_t^{(0)}$, welches die Amplitude der Korrelationslänge $\xi_t(t) = \xi_t^{(0)}\,|t|^{-\nu}$ an der kritischen Konzentration darstellt, und $\mathcal{B}$, welches die Breite der Koexistenzkurve $\phi_b(t) = \mathcal{B}\,|t|^{\beta}$ festlegt ($\nu$ und $\beta$ sind dabei kritische Exponenten). Die Werte dieser Amplituden wurden mit Dynamischer Lichtstreuung (Dynamic light scattering; DLS) in der Lösung ohne Kolloide gemessen, respektive durch Messung der Phasenseparation der Mischung (siehe Abb. 6.2 und 6.3). Genauer gesagt lieferten die DLS Messungen den Selbstdiffusionskoeffizienten, der mit der Korrelationslänge über die etwas verschlungenen Formeln in Appendix 6.A verbunden ist. Schließlich war es noch erforderlich, die schwache Adsorptionspräferenz der Kolloide zu berücksichtigen. Für die kritische Konzentration ist bekannt, dass sich die Profile bei schwachen Oberflächenfeldern auf den Fall starker Adsorption durch eine Umskalierung der Skalenfunktion abbilden lassen [73]. Allerdings wurde es, soweit bekannt, noch nicht untersucht, wie sich der Zusammenhang bei Zusammensetzungen abseits der kritischen Konzentration verhält. Innerhalb des experimentell zugänglichen Temperaturbereichs genügte ein Temperaturoffset, um die schwache Adsorption zu berücksichtigen, wie in Abschnitt 2.2.2 beschrieben. Mittels der so bestimmten Werte aller Skalenvariablen war es möglich, die projizierte Paarkorrelationsfunktion aus der Theorie mit dem Experiment für verschiedene Temperaturen und Konzentrationen nahe dem kritischen Punkt in den Abbildungen 6.4 und 6.5(a,b) zu vergleichen. Die reinen, theoretischen Paarpotentiale werden in Abb. 6.5(c,d) gezeigt. Eine präzisere Größe, die wenig von den experimentellen Ungenauigkeiten abhängt, fand sich in dem zweiten Virialkoeffizienten $B_2$, wie in Abschnitt 6.2 geschildert. Das Gesetz der übereinstimmenden Zustände (law of corresponding states) konnte hier angewendet werden und erlaubte den Vergleich mit dem kritischen, normierten Wert $B_2^* = -1.2$ aus dem Model haftender harter Kugeln, unterhalb dessen Aggregation auftritt. Wie in Abb. 6.6 zu sehen, ermöglicht es der kritische Wert, den Bereich der kolloidalen Aggregation zu bestimmen. Darüber hinaus wurden in Abb. 6.7 die Werte von $B_2^*$ aus der Theorie (farbige Fläche) und dem Experiment (Datenpunkte) in einem dreidimensionalen Oberflächenplot verglichen.

Wie angegeben wurden diese Ergebnisse bereits wissenschaftlich veröffentlicht. Im Sinne einer stringenteren Darstellung wurde die Reihenfolge in dieser Abhandlung jedoch gegenüber der chronologischen Veröffentlichung umgestellt: **Abschnitte 3.1** und **3.2** finden sich in Referenz [75] wieder, die **Abschnitte 3.3** und **3.4** in Ref. [74]. **Kapitel 4** ist ebenso Teil von Ref. [75]. **Kapitel 5** wurde als Ref. [77] veröffentlicht. **Kapitel 6** entstammt Referenz [76], die noch weitere Details über den experimentellen Aufbau enthält.

Im Rückblick unterstreichen die innerhalb dieser Arbeit durchgeführten Untersuchungen, dass *effektive Wechselwirkungen* zur Beschreibung von *kolloidalen Teilchen in kritischen*

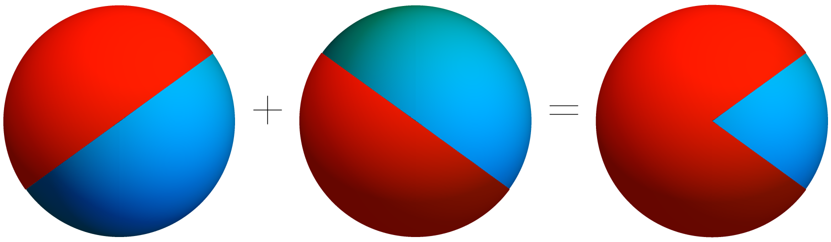

Abbildung 7.1: Zeichnung eines Pistazien- oder Pacman-Teilchens, das als Erweiterung dieser Arbeit gesehen werden kann, indem man zwei gedrehte Janus-Teilchen bildlich übereinander legt und ihre effektiven Wechselwirkungen kombiniert.

*Lösungen* geeignet sind. Bei der Beschreibung durch *effektive Wechselwirkungen* wird das Lösungsmittel nicht explizit berücksichtigt, sondern nur als effektiver Hintergrund, der durch die Parameter des effektiven Potentials erfasst wird. Darüber hinaus besteht keine Kopplung zwischen den einzelnen Wechselwirkungen, wie zum Beispiel zwischen der kritischen Casimir-Wechselwirkung und der elektrostatischen Repulsion. Die resultierenden Kräfte wurden als additiv angenommen. Bei den besprochenen Geometrien handelt es sich entsprechend um einfache Paare (**Kapitel 3**, **4**, und **5**) oder um eine verdünnte Suspension, bei denen die paarweise Wechselwirkung dominiert (**Kapitel 6**). Für die kritische Casimir-Kraft ist bekannt, dass die Mehrteilchen-Wechselwirkung bis zu 25% der gesamten Kraft ausmachen kann [185–187]. Es hat sich auch gezeigt, dass die Kopplung von Ionen und Lösungsmittelteilchen eine bedeutende Rolle zwischen der elektrostatischen Repulsion und der kritischen Casimir-Kraft spielt [188, 189]. Bei gegensätzlichen Randbedingungen auf den Teilchenoberflächen kommt es zu einem attraktiven Beitrag zu den ansonsten repulsiven Kräften. Dies hat allerdings keinen Einfluss auf das Experiment in **Kapitel 6**, in dem nur ein einziger Teilchentyp mit einheitlicher Oberfläche verwendet wurde. Für Janus-Teilchen können solche Abweichungen dagegen relevant sein.

Nichtsdestotrotz bleiben *effektive Wechselwirkungen* wertvoll für grundlegende Einschätzungen des Phasenverhaltens in verdünnten Systemen, besonders für hochkomplexe "Designer"-Teilchen, die es schon experimentell gibt (Triblock Janus-Kugeln [56], vers. Varianten von Patchy-Teilchen [63], Himbeer-Teilchen [190], Mickey-Mouse-Teilchen [191] und Hanteln [192]). Aufgrund der additiven Herangehensweise bei der Derjaguin-Näherung lassen sich neue Teilchenformen aus bereits bekannten Geometrien konstruieren. Als Ausblick sei auf das in Abb. 7.1 dargestellte Pistazien- oder Pacman-Teilchen verwiesen. Es lässt sich auch als graphische Übereinanderlagerung zweier Janus-Teilchen sehen. Mittels der richtigen Abzählung von Oberflächenelementen lässt sich erneut eine additive, effektive Wechselwirkung konstruieren. Für Experimente lässt sich ein solches Teilchen mit Aufdampftechniken herstellen; dabei wird die Hälfte eines ursprünglich homogenen Teilchens mit einer anderen Oberflächenschicht (Randbedingung) überzogen. Neigt man das Teilchen, zum Beispiel mit Hilfe eines äußeren Magnetfeldes, und trägt dann eine zweite halbkugelförmige Schicht auf, erhält man die dargestellte Form. In diesem seltenen Fall imitiert die theoretische Herleitung der kombinierten Wechselwirkung sogar die reale Anfertigung.

Es scheint gar so, als ob die zukünftige Forschung nicht durch die Vorstellungskraft beschränkt wird, sondern nur durch die zunehmende Komplexität der theoretischen Modelle und der experimentellen Herstellung. Daher stellt auch jede schrittweise Erweiterung des Wissens um *effektive Wechselwirkungen* zwischen strukturierten *kolloidalen Teilchen* eine mögliche Basis weiterer Forschung dar.

# Appendix A

# Derjaguin approximation for two cylinders

The Derjaguin approximation (DA) allows one to determine the force between two close objects with curved surfaces in terms of the corresponding forces between parallel, planar plates. To this end the surfaces are subdivided into infinitesimal, flat surface elements. Assuming additivity of the forces between these elements provides an integral expression for the force between curved objects in terms of the force between two planar walls.

In the case of two parallel cylinders, the DA cuts the two surfaces into parallel, infinitesimally thin stripes [74, 103]. Thus, each surface is parameterized by a continuous parameter $\rho$, tracking two parallel stripes at positions $\pm\rho$ from the axis of each particle. The distance between two adjacent surface elements on two colloids is given by $L(\rho) = D + 2R - 2\sqrt{R^2 - \rho^2}$, where $D$ is the shortest surface-to-surface distance between the two cylinders and $R$ is the radius common to both particles. The DA is valid for $D \ll R$, i.e., $\Delta = D/R \to 0$. In this limit one can employ the so-called "parabolic distance approximation" [29, 35, 103] $L(\rho) \approx D\,(1 + \rho^2/(RD))$.

A visualization of these two distance formulae is shown in Fig. A.1(a) for a fixed distance $\Delta = D/R = 0.3$. For this medium-sized distance, which is not particularly close to the DA limit $\Delta \to 0$, the resulting difference for the scaling functions $K^{(cc)}_{(a,b)}$ between the above two distance formulae is still small (see Fig. A.1(b) and details below), even close to $T_c$, i.e., for $\Theta_\pm \to 0$, where the underlying interaction is long ranged. The deviations are more noticeable in the case of opposing boundary conditions $(+,-)$ at the surfaces of the particles. Here, however, we focus on particles with equal boundary conditions $(+,+)$, for which the agreement is very good.

Based on the scaling functions $k_{(a,b)}$ of the critical Casimir force between two planar walls with boundary characteristics $a$ and $b$, respectively, the force between two cylinders follows from integrating the force acting on each surface area element $\mathrm{d}s(\rho) = 2\mathrm{d}\rho$, per

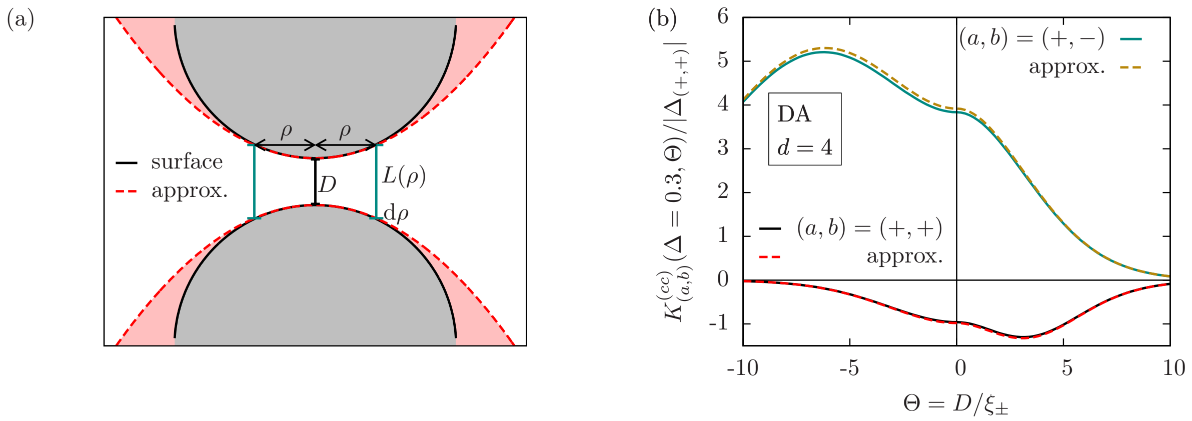

Figure A.1: (a) Sketch of the geometrical aspects of the DA. The force between two cylindrical colloids (gray areas with surfaces as black lines) is calculated by assuming additivity of the forces between infinitesimally small and planar surface elements. Additionally, we approximate the true distance $L(\rho)$ between the surface elements by the so-called "parabolic distance approximation" indicated by the dashed red curves and the light red areas. (b) The normalized DA scaling function $K^{(cyl)}_{(a,b)}$ of the force between two cylinders (see Eq. (A.2)), in $d = 4$ for the boundary conditions $(a, b) = (+, \pm)$, as obtained either via the true distance formula $L(\rho) = D + 2R - 2\sqrt{R^2 - \rho^2}$ (black and green solid lines), or via the "parabolic distance approximation" $L(\rho) \approx D\,(1 + \rho^2/(RD))$ (red and golden dashed lines) for a fixed scaled surface-to-surface distance $\Delta = D/R = 0.3$.

generalized length $\mathcal{L}$ of the cylinders,

$$F^{(cc)}_{(a,b)}(D, R, T) = k_B T \mathcal{L} \int\limits_0^R \frac{2\mathrm{d}\rho}{L(\rho)^d}\, k_{(a,b)}\left(\pm \frac{L(\rho)}{\xi_\pm}\right), \tag{A.1}$$

where the sign in the argument of $k_{(a,b)}$ and the index of $\xi_\pm$ are given by the sign of $t = (T - T_c)/T_c$ (for an upper critical point).

Inserting $L(\rho) \approx D\,(1 + \rho^2/(RD))$ into Eq. (A.1), together with two consecutive integral substitutions $\rho \to \alpha = \rho/\sqrt{RD}$ and $\alpha \to \beta = 1 + \alpha^2$, results in

$$\begin{aligned} &F^{(cc)}_{(a,b)}(D, R, T) \\ &\quad = k_B T \mathcal{L}\, \frac{R^{1/2}}{D^{d-1/2}} \int_1^{1+\Delta^{-1}} \mathrm{d}\beta\, (\beta - 1)^{-1/2}\, \beta^{-d}\, k_{(a,b)}\left(\pm\beta\, \frac{D}{\xi_\pm}\right) \\ &\quad = \frac{k_B T \mathcal{L}}{R^{d-1}}\, \frac{1}{\Delta^{d-1/2}} \underbrace{\int_1^{1+\Delta^{-1}} \mathrm{d}\beta\, (\beta - 1)^{-1/2}\, \beta^{-d}\, k_{(a,b)}(\pm\beta\Theta)}_{K^{(cc)}_{(a,b)}(\Delta,\Theta)} \end{aligned} \tag{A.2}$$

where $K^{(cc)}_{(a,b)}(\Delta, \Theta)$ is the DA scaling function of the force and $\Theta = D/\xi_\pm$ is the rescaled temperature. The results of the numerical integrations, based on the MFT data in $d = 4$

for the film scaling function $k_{(a,b)}$ [91], are shown in Fig. A.1(b).

The effective potential $V^{(cc)}_{(a,b)}$ can be obtained from the force according to the relation

$$V^{(cc)}_{(a,b)}(D,R,T) = \int_D^\infty \mathrm{d}z\, F^{(cc)}_{(a,b)}(z,R,T) \tag{A.3}$$

and expressed in the scaling form

$$\frac{V^{(cc)}_{(a,b)}(D,R,T)}{k_B T} = \frac{\mathcal{L}}{R^{d-2}}\,\frac{\Phi^{(cc)}_{(a,b)}\left(\Delta = \frac{D}{R}, \Theta = \frac{D}{\xi_\pm}\right)}{\Delta^{d-3/2}} \tag{A.4}$$

with the scaling function $\Phi^{(cc)}_{(a,b)}$ of the potential within DA

$$\Phi^{(cc)}_{(a,b)}(\Delta,\Theta) = \Delta^{d-3/2} \int_\Delta^\infty \mathrm{d}\Delta'\, \frac{K^{(cc)}_{(a,b)}(\Delta', (\Delta'/\Delta)\Theta)}{(\Delta')^{d-1/2}} = \int_1^\infty \mathrm{d}\zeta\, \frac{K^{(cc)}_{(a,b)}(\zeta\Delta, \zeta\Theta)}{\zeta^{d-1/2}}. \tag{A.5}$$

We insert the scaling function of the critical Casimir force $K^{(cc)}_{(a,b)}$ from Eq. (A.2) into Eq. (A.5) and consider the limit $\Delta \to 0$ in the upper limit of integration. This renders the scaling function of the potential

$$\Phi^{(cc)}_{(a,b)}(\Delta \to 0,\Theta) = \int_1^\infty \mathrm{d}\zeta \int_1^\infty \mathrm{d}\beta\, \frac{1}{\zeta^{d-1/2}} (\beta-1)^{-1/2}\, \beta^{-d}\, k_{(a,b)}(\pm\beta\,\zeta\,\Theta). \tag{A.6}$$

This expression can be simplified by employing the substitution $\beta \to \eta = \beta\,\zeta$. After changing the order of integration and by using the relation $\int_1^\infty \mathrm{d}\zeta \int_\zeta^\infty \mathrm{d}\eta = \int_1^\infty \mathrm{d}\eta \int_1^\eta \mathrm{d}\zeta$, the result of the second integration is $\int_1^\eta \mathrm{d}\zeta\,(\eta-\zeta)^{-1/2} = 2\sqrt{\eta-1}$, so that

$$\Phi^{(cc)}_{(a,b)}(\Delta \to 0,\Theta) = 2\int_1^\infty \mathrm{d}\eta\, \sqrt{\eta-1}\,\eta^{-d} k_{(a,b)}(\pm\eta\,\Theta). \tag{A.7}$$

If, instead, the finite integration limit $1+\Delta^{-1}$ in Eq. (A.2) is kept, the calculation of the potential can be performed similarly, but with an additional term in the scaling function $\Phi^{(cc)}_{(a,b)}$ of the potential, resulting in the scaling function

$$\begin{aligned}\Phi^{(cc)}_{(a,b)}(\Delta,\Theta) = 2\int_1^\infty \mathrm{d}\eta\, \sqrt{\eta-1}\,\eta^{-d}\, k_{(a,b)}(\eta\,\Theta) \\ - 2\int_{1+\Delta^{-1}}^\infty \mathrm{d}\eta\, \left(\sqrt{\eta-1} - \Delta^{-1/2}\right)\, \eta^{-d}\, k_{(a,b)}(\eta\,\Theta).\end{aligned} \tag{A.8}$$

# Appendix B

# Derjaguin approximation for two Janus spheres

## B.1 Scaling function of the effective force

Concerning the geometry of two homogeneous, i.e., isotropic spheres, the Derjaguin approximation consists of subdividing their surfaces into infinitesimal thin rings of area $2\pi\rho\,\mathrm{d}\rho$, parameterized by their radius $\rho$ [29]. This has been used successfully in several studies, such as Refs. [29, 35, 103], generally in conjunction with the so-called "parabolic distance approximation" for the local distance $L(\rho)$ between surface elements of the two colloids:

$$L(\rho) = D + 2R - 2\sqrt{R^2 - \rho^2} \approx D\left(1 + \frac{\rho^2}{RD}\right). \tag{B.1}$$

Building on that, for Janus spheres the corresponding step in BC has to be incorporated additionally, depending on the particle orientations. Within DA, the overlap of pairs of surface elements on both spheres is determined after the projection along the vector $\mathbf{r}_{12}$ connecting the centers of the two spheres. We choose to express this geometry in terms of a local coordinate system, the $z$ axis of which passes through the centers of the two colloids, so that $\mathbf{r}_{12} = (D + 2R)\,\hat{\mathbf{r}}_{12}$ with $\hat{\mathbf{r}}_{12} = (0, 0, 1)$ (see Fig. 4.2). The orientations of the colloids can be represented by orientation vectors $\mathbf{n}_1$ and $\mathbf{n}_2$, which can be chosen to point either into the direction of the (+) (red) or the (−) (blue) side. As far as the figures in the main text are concerned, the orientation vector is chosen to point towards the (−) (blue) cap. However, regarding the general approach in the present appendix, we shall use the more abstract notions of "north" and "south", which are supposed to underscore the arbitrariness of this choice.

Without loss of generality, we define the coordinate system such that the orientation of the first particle has an azimuthal angle $\phi_1 = 0$ and a polar angle $\vartheta_1$; the orientation $(\alpha, \vartheta_2)$ of the second particle is taken relative to the "prime meridian" of the first (i.e., $\alpha = \phi_2 - \phi_1$). Rotations of the coordinate system while keeping $(\alpha, \vartheta_1, \vartheta_2)$ fixed do not change the interaction between the particles. Still, there remains a choice in the numbering of the particles. We implement this such that $|\cos\vartheta_1| < |\cos\vartheta_2|$, as it shortens the notation below; otherwise one can exchange the labels (1) and (2) and rotate the frame of reference around the $y$ axis by 180° (see Fig. 4.2).

The orientations $\mathbf{n}_{1,2}$ and two mirror points $\mathbf{r}_1$ and $\mathbf{r}_2$ on the surface of colloid 1 and 2, respectively, are parameterized within the relative coordinate system by

$$\mathbf{n}_1 = \begin{pmatrix} \sin\vartheta_1 \\ 0 \\ \cos\vartheta_1 \end{pmatrix}, \qquad \mathbf{n}_2 = \begin{pmatrix} \cos\alpha\sin\vartheta_2 \\ \sin\alpha\sin\vartheta_2 \\ \cos\vartheta_2 \end{pmatrix}, \tag{B.2}$$

$$\mathbf{r}_1 = R\begin{pmatrix} \cos\phi\sin\vartheta \\ \sin\phi\sin\vartheta \\ -\cos\vartheta \end{pmatrix}, \qquad \mathbf{r}_2 = R\begin{pmatrix} \cos\phi\sin\vartheta \\ \sin\phi\sin\vartheta \\ \cos\vartheta \end{pmatrix}, \tag{B.3}$$

where $\vartheta_1$ is the polar angle of the first particle, $(\alpha, \vartheta_2)$ are the azimuthal and polar angle of the second particle, and $(\phi, \vartheta)$ are the spherical coordinates of the vectors $\mathbf{r}_1$ and $\mathbf{r}_2$ of a pair of surface elements, where $\mathbf{r}_1$ and $\mathbf{r}_2$ are mirror images of each other with respect to the midplane orthogonal to $\hat{\mathbf{r}}_{12} = \mathbf{e}_z$, such that $(\mathbf{r}_1)_z = -(\mathbf{r}_2)_z$ (see Fig. B.1). After the projection into the midplane by using the orthogonal projection matrix

$$\mathbf{P}_z = \begin{pmatrix} 1 & 0 & 0 \\ 0 & 1 & 0 \\ 0 & 0 & 0 \end{pmatrix}, \tag{B.4}$$

surface elements with equal distance from their mirror element on the other particle form a ring with polar coordinates $(\rho = R\sin\vartheta, \phi)$ and a fixed value of $\vartheta$.

The force between the Janus spheres, as constructed within DA, depends on the combination of BC for a pair of surface elements. A selected pair of of surface elements will share the "northern" BC if $\mathbf{r}_1 \cdot \mathbf{n}_1 > 0$ and $\mathbf{r}_2 \cdot \mathbf{n}_2 > 0$. Likewise, they will both have the "southern" BC if $\mathbf{r}_1 \cdot \mathbf{n}_1 < 0$ and $\mathbf{r}_2 \cdot \mathbf{n}_2 < 0$, otherwise the surface elements have different BCs.

In our parameterization and with $f_1(\phi) := \mathbf{r_1} \cdot \mathbf{n_1} = -\cos\vartheta\cos\vartheta_1 + \cos\phi\sin\vartheta\sin\vartheta_1$ and $f_2(\phi) := \mathbf{r_2} \cdot \mathbf{n_2} = \cos\vartheta\cos\vartheta_2 + \cos(\alpha - \phi)\sin\vartheta\sin\vartheta_2$, the two conditions above read

$$\text{same BC ("north")} \Leftrightarrow \; f_1(\phi) > 0 \;\wedge\; f_2(\phi) > 0 \quad \text{or} \tag{B.5a}$$

$$\text{same BC ("south")} \Leftrightarrow \; f_1(\phi) < 0 \;\wedge\; f_2(\phi) < 0. \tag{B.5b}$$

There are two more conditions representing opposing BC, with opposite signs of $f_1(\phi) \gtrless 0$ and $f_2(\phi) \lessgtr 0$. For any value of $\phi$, one and only one of these four conditions is fulfilled. Thus, these four conditions hold in four intervals. Determining the zeroes of $f_1$ and $f_2$ as

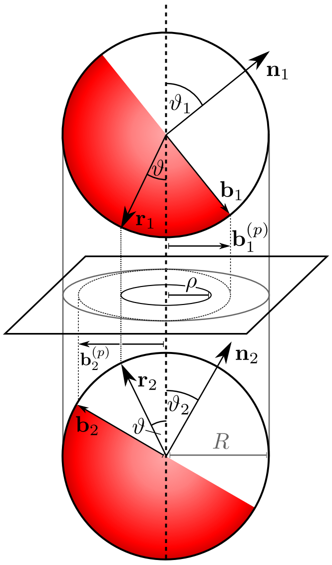

Figure B.1: Two Janus spheres within the Derjaguin approximation. The two orientations of the two particles are given by the direction vectors $\mathbf{n}_1$ and $\mathbf{n}_2$ which are normals of the respective equatorial planes. In the relative coordinate system, given by the axis through the centers of both particles, the orientations can be represented by the two polar angles $\vartheta_1$ and $\vartheta_2$ and the relative azimuthal angle $\alpha$; for simplicity, here we depict the case $\alpha = 0$ in which the two equatorial planes are rotated with respect to each other but not tilted (see Fig. 4.2 for a reduced schematic drawing with $\alpha \neq 0$). A pair of surface elements at $\mathbf{r}_1(\phi, \vartheta)$ and $\mathbf{r}_2(\phi, \vartheta)$ on the two Janus spheres, such that they are mirror images of each other, i.e., $(\mathbf{r}_1)_z = -(\mathbf{r}_2)_z$, share the same "northern" BC if $\mathbf{r}_1 \cdot \mathbf{n}_1 > 0$ and $\mathbf{r}_2 \cdot \mathbf{n}_2 > 0$. Likewise, two surface elements share the same "southern" BC if $\mathbf{r}_1 \cdot \mathbf{n}_1 < 0$ and $\mathbf{r}_2 \cdot \mathbf{n}_2 < 0$; otherwise for the selected pair of surface elements the BC on the two Janus spheres differ. Surface elements at $\mathbf{r}_1$ and $\mathbf{r}_2$ with equal distance between them (dotted line parallel to the axis through the centers of both particles and connecting the tips of $\mathbf{r}_1$ and $\mathbf{r}_2$) form a ring with radius $\rho = R \cos \vartheta$ (here, the inner black circle) which is shown in the midplane between the particles. The equatorial steps of the Janus spheres ① and ② form half-ellipses when projected onto the same midplane. The vectors $\mathbf{b}_1$ and $\mathbf{b}_2$ lie in the equatorial plane of the corresponding particles and thus are orthogonal to $\mathbf{n}_1$ and $\mathbf{n}_2$, respectively. Their direction is chosen to point to that point on each equator which is closest in sight of the opposite particle. The projections $\mathbf{b}_1^{(p)}$ and $\mathbf{b}_2^{(p)}$ of the vectors $\mathbf{b}_1$ and $\mathbf{b}_2$, respectively, onto the midplane render the semi-minor axes of the half-ellipses.

functions of $\phi$ renders four possible values, separating the intervals (note that four points naturally enclose three closed intervals, and one more interval due to the periodicity in $\phi$):

$$f_1(\phi) = 0 \quad \Rightarrow \quad \begin{cases} \phi_1 = \arccos(\cot\vartheta \cot\vartheta_1), & \text{(B.6a)} \\ \phi_2 = -\arccos(\cot\vartheta \cot\vartheta_1) \quad (+2\pi); & \text{(B.6b)} \end{cases}$$

$$f_2(\phi) = 0 \quad \Rightarrow \quad \begin{cases} \phi_3 = \alpha - \arccos(-\cot\vartheta \cot\vartheta_2) \quad (+2\pi), & \text{(B.6c)} \\ \phi_4 = \alpha + \arccos(-\cot\vartheta \cot\vartheta_2). & \text{(B.6d)} \end{cases}$$

Strictly speaking, Eq. (B.5) has an infinite number of solutions, because any solution shifted by $\pm 2\pi$ is also a solution. With $(+2\pi)$ we indicate that $\phi_2$ and $\phi_3$ may need to be shifted such that all four given solutions are the relevant ones within the principal interval $[0, 2\pi]$.

Figure B.2 puts the meaning of these four values of $\phi$ given by Eq. (B.6) into proper perspectives. Figure B.2 shows a schematic (top-down) plan view of the geometry shown in Fig. B.1 which is rendered by the projection matrix $\mathbf{P}_z$ for four different values of $\alpha$ and with additional details, visualizing how the projected surface elements entering the DA are partitioned by Eq. (B.6) (compare also Fig. 4.2). The spherical colloids are drawn with non-occluding outlines and the equatorial step is indicated only partially. The projection of the equatorial steps between the "north" and the "south" Janus BC on each sphere results in two ellipses. This follows from noting that the two equators can be parameterized as circles $\mathbf{p}_i = (\cos\phi_i, \sin\phi_i, 0)$, tilted by a rotation matrix

$$\mathbf{R}_i = \begin{pmatrix} 1 & 0 & 0 \\ 0 & \cos\vartheta_i & -\sin\vartheta_i \\ 0 & \sin\vartheta_i & \cos\vartheta_i \end{pmatrix}. \tag{B.7}$$

One finds that $\mathbf{P}_z \cdot \mathbf{R}_i \cdot \mathbf{p}_i = (\cos\phi_i, \cos\vartheta_i \sin\phi_i, 0)$ fulfills the ellipse equation $\frac{x^2}{a^2} + \frac{y^2}{b^2} = 1$ for $a = 1$ and $b = |\cos\vartheta_i|$. Of the two elliptical projections, we draw only that half facing the other colloid, resulting in two half-elliptical curves, which are intersecting for $0 < \alpha < \pi$ (i.e., they do not intersect for $\alpha = 0$ and $\alpha = \pi$). The semi-minor axes of the half-ellipses are indicated by the projections $\mathbf{b}_1^{(p)}$ and $\mathbf{b}_2^{(p)}$ of the vectors $\mathbf{b}_1$ and $\mathbf{b}_2$, respectively, which have a projected length of $R\cos\vartheta_{1,2}$ and form the angle $\pi - \alpha$ between them. The projected Janus steps divide the circular area of radius $R$ into four regions (blue, white, red, white); a selected ring of fixed radius $\rho = R\sin\vartheta$ (corresponding to the color colored circle in Fig. B.2) is divided into four arcs by points with the polar coordinates $(\rho, \phi_1)$ to $(\rho, \phi_4)$. In the case of small $\alpha$ as shown in Fig. B.2(a), the numbering of the values $\phi_1$ to $\phi_4$ given in Eq. (B.6) corresponds to a clockwise counting of the intersections of the ring with the projected Janus steps (i.e., the half-ellipses). However, the order of their occurrence changes upon increasing $\alpha$ towards $\pi$ (see Figs. B.2(a)–(d)).

Within DA, the force due to each ring of surface elements of equal distance between them is proportional to its arc length and to the force between parallel walls corresponding to the respective combination of the BC. In Fig. B.2(a), the blue curve, representing a common "northern" BC, has an arc length of $(\phi_2 - \phi_1)\rho$, whereas the red arc represents a common "southern" BC with an arc length of $(\phi_4 - \phi_3)\rho$. In this case, using the relation $\arccos(-x) = \pi - \arccos(x)$, the total arc length of equal BC amounts to $[2\pi - 2\arccos(\cot\vartheta\cot\vartheta_1) - 2\arccos(\cot\vartheta\cot\vartheta_2)]\,\rho$.

The number and the order of the intersections between a ring of equidistant surface

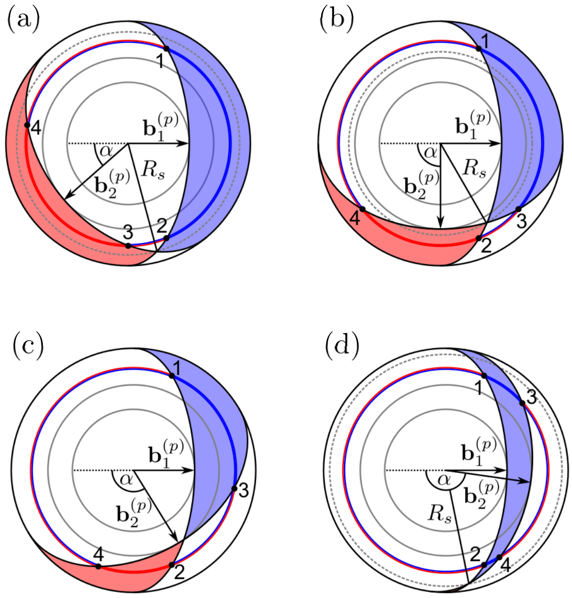

Figure B.2: A top-down plan view, as rendered by the projection matrix $\mathbf{P}_z$, of the geometry of two Janus spheres, which is the same as in Fig. B.1, but highlights the significance of the angles $\phi_1$ to $\phi_4$ of the DA procedure given in Eq. (B.6). The two half-elliptical curves running through 1 and 2 and through 3 and 4, respectively, represent the projection of the Janus equators onto the midplane. Their semi-minor axes are given by the projections $\mathbf{b}_1^{(p)}$ and $\mathbf{b}_2^{(p)}$ of the vectors $\mathbf{b}_1$ and $\mathbf{b}_2$, respectively, shown in Fig. B.1, which enclose the angle $\pi - \alpha$. The full gray circles have radii $|\mathbf{b}_i^{(p)}|$. Here, the parameters of the particle orientations $\mathbf{n}_{1,2}$ ($\perp$ $\mathbf{b}_{1,2}$) are $\vartheta_1 = \pi/3$ and $\vartheta_2 = \pi/4$, and $\alpha$ is varied from (a) $\alpha = 0.7$, (b) $\alpha = \pi/2$, and (c) $\alpha = 2.1$ to (d) $\alpha = 3.0$. In this projection, two surface elements forming a pair at $\mathbf{r}_1$ and $\mathbf{r}_2$ lie on top of each other, rendering a single point within the circular area. The projected area, indicated in blue, corresponds to those pairs of surface elements which share the "northern" BC. Likewise, the projected area within which both surface elements feature the "southern" BC is indicated in red. The white areas correspond to pairs of surface elements with opposite BC. As a function of $\phi$ and for a fixed value of $\vartheta$, in projection the pairs of surface elements form a ring of radius $\rho = R\sin(\vartheta)$ (see Fig. B.1). We depict the case $\vartheta = 1$ so that $\rho = 0.84\,R$ (color-coded ring). The points 1 to 4 mark the intersections of the color-coded ring with the projected equatorial steps of the BC, which are given by the polar coordinates $(\rho, \phi_1)$ through $(\rho, \phi_4)$. Both the thick red and the thick blue arcs of this ring represent equal BC on both particle surfaces, whereas those arcs being half blue and half red correspond to opposite BC. Additional explanations, such as the meaning of $R_s$, are given in the main text.

element pairs and the projected Janus equators depends on the radius of the ring. For $\rho < R\cos\vartheta_1$ (the inner gray circle in Fig. B.2 indicates $\rho = R\cos\vartheta_1$), the ring does not cross the projected steps in BC at all. For $R\cos\vartheta_1 < \rho < R\cos\vartheta_2$, there are two points of intersection (we recall that the labels ① and ② are chosen such that $|\cos\vartheta_1| < |\cos\vartheta_2|$). Starting from $\rho = R\cos\vartheta_2$ (indicated by the outer gray circle), for $\rho > R\cos\vartheta_2$ there are four points of intersection. However, at a specific radius $\rho = R_s$ (gray dashed line in Fig. B.2), the two half-ellipses intersect and the order of the values $\phi_1 \ldots \phi_4$ changes (e.g., compare the order of the intersections in Figs. B.2(a) and (b)).

The dimensionless radius $r_s = R_s/R = \sqrt{x^2+y^2}$ is determined by the intersection point $(x, y)$ of the two semi-ellipses, which is found from a solution of the general problem of the intersection between two co-centric ellipses: the first ellipse $(x/a_1)^2 + (y/b_1)^2 = 1$ and the second ellipse $(x/a_2)^2+(y/b_2)^2 = 1$ rotated by an angle $\alpha$. Within their parametric representations the intersections follow from

$$\begin{pmatrix} x \\ y \end{pmatrix} = \begin{pmatrix} a_1 \cos t_1 \\ b_1 \sin t_1 \end{pmatrix} \overset{!}{=} \begin{pmatrix} a_2 \cos t_2 \cos\alpha - b_2 \sin t_2 \sin\alpha \\ a_2 \cos t_2 \sin\alpha + b_2 \sin t_2 \cos\alpha \end{pmatrix}. \tag{B.8}$$

Equation (B.8) is a system of two equations for the two unknowns $t_1$ and $t_2$, which become functions of $a_1, b_1, a_2, b_2$, and $\alpha$. For the present situation, and with $x$ and $y$ giving rise to a dimensionless factor $\sqrt{x^2+y^2}$ of the radius $R$, the problem reduces to the special case in which the semi-major axes are $a_1 = a_2 = 1$ (i.e., the semi-major axes are touching the circle of radius $R$) and the semi-minor axes are the projected lengths $b_1 = \left|\mathbf{b}_1^{(p)}\right|/R = |\cos(\vartheta_1)|$ and $b_2 = \left|\mathbf{b}_2^{(p)}\right|/R = |\cos(\vartheta_2)|$. While in principle this system of equations can be solved analytically, it is not guaranteed that all solutions are real, because in degenerate cases (e.g., for $\alpha = 0$ or $\alpha = \pi$ and $b_1 = b_2$, or $b_1 = b_2 = 1$, or $b_1 = b_2 = 0$) the number of physically acceptable solutions can be less than four. In the non-degenerate cases, out of these four general solutions of the intersection of two ellipses, only one gives the intersection of two half-ellipses. We have followed a pragmatic approach by solving Eq. (B.8) numerically within an *a priori* chosen interval of $t_2$ in order to preselect the appropriate solution for the half-ellipses [1]. We note that our definition enforces the relation $|\cos\vartheta_1| < |\cos\vartheta_2|$, so that the dimensionless radius $r_s$ corresponding to the point of intersection between the two half-ellipses is bounded by $|\cos\vartheta_2| \leq r_s \leq 1$, because any point on the second ellipse has a radial distance from its center, the value of which lies between the semi-minor axis $b_2 = \cos\vartheta_2$ and the semi-major axis $a_2 = 1$, and so does the point of intersection.

Using this procedure, we have constructed the force between two Janus spheres within DA by integrating the force between the rings of surface elements of radius $\rho$, with attractive and repulsive contributions proportional to the respective four arc lengths determined by $\phi_1 \dots \phi_4$ in Eq. (B.6), and using the numerically determined radius $R_s = R_s(\alpha, \vartheta_1, \vartheta_2)$ for each configuration, which governs the occurrence of the attractive and repulsive force contributions (depending on $\rho \lesseqgtr R_s$) by interchanging the order of $\phi_1 \dots \phi_4$. A thorough investigation of all geometric configurations reveals that the excess force takes the

---

[1] This also allows us to use optimized numerical root finding algorithms operating within an interval in which the function changes sign. We have chosen Brent's root finding method, http://mathworld.wolfram.com/BrentsMethod.html, which is implemented in the SciPy library http://docs.scipy.org/doc/scipy-0.16.0/reference/generated/scipy.optimize.brentq.html.

following form

$$\begin{aligned}
&\Delta F^{(ss)}_{\oslash\oslash}(\mathbf{n}_1, \mathbf{n}_2, \mathbf{r}_{12} = (D + 2R)\mathbf{e}_z, R, T)\\
&\quad = \frac{k_B T}{D^d}\left[ \int_0^{R_s} \mathrm{d}\rho\, \rho \frac{2\pi\, H\left((\cos\vartheta_1)\,(\cos\vartheta_2)\right)}{(L(\rho)/D)^d}\, \Delta k\left(\frac{L(\rho)}{\xi_\pm}\right)\right.\\
&\qquad - \operatorname{sign}\left((\cos\vartheta_1)\,(\cos\vartheta_2)\right)\\
&\qquad\quad \times \int_{R\cos\vartheta_1}^{R_s} \mathrm{d}\rho\, \rho \frac{2\arccos\left((\operatorname{sign}(\cos\vartheta_1))(\cot\vartheta)(\cot\vartheta_1)\right)}{(L(\rho)/D)^d}\, \Delta k\left(\frac{L(\rho)}{\xi_\pm}\right)\\
&\qquad - c(\alpha, \vartheta_1, \vartheta_2)\operatorname{sign}\left((\cos\vartheta_1)\,(\cos\vartheta_2)\right)\\
&\qquad\quad \times \int_{R\cos\vartheta_2}^{R_s} \mathrm{d}\rho\, \rho \frac{2\arccos\left((\operatorname{sign}(\cos\vartheta_2))(\cot\vartheta)(\cot\vartheta_2)\right)}{(L(\rho)/D)^d}\, \Delta k\left(\frac{L(\rho)}{\xi_\pm}\right)\\
&\qquad \left. + \int_{R_s}^{R} \mathrm{d}\rho\, \rho \frac{2\alpha}{(L(\rho)/D)^d}\, \Delta k\left(\frac{L(\rho)}{\xi_\pm}\right)\right],
\end{aligned} \tag{B.9}$$

with $\rho = R\sin\vartheta$ and $\cot\vartheta = \frac{\cos\vartheta}{\sin\vartheta} = \frac{\sqrt{1-\sin^2\vartheta}}{\sin\vartheta} = \frac{R}{\rho}\sqrt{1-\frac{\rho^2}{R^2}}$, for $\mathbf{r}_{12} = (D+2R)\mathbf{e}_z$ and $\mathbf{n}_{1,2}$ in relative coordinates (see Eq. (B.2)). The occurrence of various expressions in Eq. (B.9) can be rationalized as follows: The combined arc length of equal BC is generally of the form $\pm\phi_4 \mp \phi_3 \pm \phi_2 \mp \phi_1$ (i.e., different combinations of the signs). According to Eq. (B.6), additional shifts of $2\pi$ might be required to ensure $\phi_i \in [0, 2\pi)$. In fact the term $2\pi$ occurs only for rings of surface elements with radii $\rho < R_s$, provided $(\cos\vartheta_1)\,(\cos\vartheta_2) \geq 0$, which is expressed by the limits of integration of the first term in Eq. (B.9) (see below also the note regarding the second and third term). Similarly, the azimuthal angle $\alpha$ contributes in total as $2\alpha$ to the arc length if $\rho > R_s$, but it does not contribute if $\rho < R_s$, leading to the fourth and last term in Eq. (B.9). The second and third term reproduce the functional dependence of the arc length on $\vartheta(\rho)$ and $\vartheta_{1,2}$. The changes of sign of the argument in the arccos functions in Eq. (B.6) generalize to $\operatorname{sign}(\cos\vartheta_{1,2})$ in Eq. (B.9) due to the relation $2\arccos(-x) = 2\pi - 2\arccos(x)$. Note that the shift of $2\pi$ re-enters the first term; in Eq. (B.9) the first term reflects the notation in the second and third term. Analogously to the geometry of two Janus cylinders, we find a dependence of the sign of the second and third term on the sign of $(\cos\vartheta_1)\,(\cos\vartheta_2)$. Furthermore, the sign picking function $c(\alpha, \vartheta_1, \vartheta_2)$ is given by

$$c(\alpha, \vartheta_1, \vartheta_2) = \begin{cases} \operatorname{sign}(\cos\alpha), & \text{if } (\cos\vartheta_1)\,(\cos\vartheta_2) = 0,\\ 1, & \text{if } \alpha \leq \arccos\left(-(\tan\vartheta_2)\,(\cot\vartheta_1)\right) \leq \pi H\left((\cos\vartheta_1)\,(\cos\vartheta_2)\right)\\ & \text{or } \pi H\left((\cos\vartheta_1)\,(\cos\vartheta_2)\right) \leq \arccos\left(-(\tan\vartheta_2)\,(\cot\vartheta_1)\right) \leq \alpha,\\ -1 & \text{otherwise,} \end{cases} \tag{B.10}$$

with the restriction that $\alpha$ is replaced by $2\pi - \alpha$ if $\alpha > \pi$.

Finally, the scaling function of the excess force is found from Eq. (B.9) by using the distance function $L(\rho)$ within the "parabolic distance approximation" $L(\rho) = D\left(1 + \frac{\rho^2}{RD}\right)$ and by applying the substitution $\rho \to x = 1 + \frac{\rho^2}{RD}$ with $\mathrm{d}x = \frac{2\rho}{RD}\,\mathrm{d}\rho$, which leads to $L(x) = D\,x$, $\cot\vartheta = \sqrt{\frac{1}{\Delta(x-1)} - 1}$, and

$$\begin{aligned}
\Delta K^{(ss)}_{\oslash\oslash}(\alpha, \vartheta_1, \vartheta_2, \Delta, \Theta) = {} & \pi\, H\left((\cos\vartheta_1)\,(\cos\vartheta_2)\right) \int_1^{1+\Delta^{-1} r_s^2} \mathrm{d}x\, x^{-d}\, \Delta k\,(x\vartheta) \\
& - \operatorname{sign}\left((\cos\vartheta_1)\,(\cos\vartheta_2)\right) \\
& \quad \times \left[ \int_{1+\Delta^{-1}\cos^2\vartheta_1}^{1+\Delta^{-1} r_s^2} \mathrm{d}x\ \arccos\left( |\cot\vartheta_1| \sqrt{\frac{1}{\Delta(x-1)} - 1} \right) x^{-d}\, \Delta k\,(x\Theta) \right. \\
& \quad \left. + c(\alpha, \vartheta_1, \vartheta_2) \int_{1+\Delta^{-1}\cos^2\vartheta_2}^{1+\Delta^{-1} r_s^2} \mathrm{d}x\ \arccos\left( |\cot\vartheta_2| \sqrt{\frac{1}{\Delta(x-1)} - 1} \right) x^{-d}\, \Delta k\,(x\Theta) \right] \\
& + \alpha \int_{1+\Delta^{-1} r_s^2}^{1+\Delta^{-1}} \mathrm{d}x\, x^{-d}\, \Delta k\,(x\Theta)\,. \qquad \text{(B.11)}
\end{aligned}$$

with the abbreviation $r_s = R_s/R$, and the replacement of $(\operatorname{sign}(\cos\vartheta_{1,2}))\cot\vartheta_{1,2} = |\cot\vartheta_{1,2}|$, which holds in the domain of definition of the polar angles, i.e., for $\vartheta_{1,2} \in [0, \pi]$.

## B.2 Scaling function of the effective potential

The effective potential can be determined from the force in the relative coordinate system according to

$$\begin{aligned}
V^{(ss)}_{\bullet\bullet}(\mathbf{n}_1, \mathbf{n}_2, \mathbf{r}_{12} = (D+2R)\mathbf{e}_z, R, T) &= \int_D^\infty \mathrm{d}z\, F^{(ss)}_{\bullet\bullet}(\mathbf{n}_1, \mathbf{n}_2, \mathbf{r}_{12} = (z+2R)\mathbf{e}_z, R, T) \qquad \text{(B.12)} \\
&= k_B T \frac{\mathcal{L}}{R^{d-2}} \int_D^\infty \mathrm{d}z\, \frac{K^{(ss)}_{\bullet\bullet}(\alpha, \vartheta_1, \vartheta_2, z/R, z/\xi_\pm)}{(z/R)^{d-1}}.
\end{aligned}$$

Substitution of $z = D\,\tilde{z}$ with $\mathrm{d}z = D\,\mathrm{d}\tilde{z}$ yields

$$\begin{aligned}
V^{(ss)}_{\bullet\bullet}&(\mathbf{n}_1, \mathbf{n}_2, \mathbf{r}_{12} = (D+2R)\mathbf{e}_z, R, T) \\
&= k_B T \frac{\mathcal{L}}{R^{d-3}}\, \Delta^{-(d-2)} \int_1^\infty \mathrm{d}\tilde{z}\, \frac{K^{(ss)}_{\bullet\bullet}(\alpha, \vartheta_1, \vartheta_2, \tilde{z}\Delta, \tilde{z}\Theta)}{\tilde{z}^{d-1}}. \qquad \text{(B.13)}
\end{aligned}$$

This can be cast into the scaling form

$$V^{(ss)}_{\bullet\bullet}(\mathbf{n}_1, \mathbf{n}_2, \mathbf{r}_{12} = (D+2R)\mathbf{e}_z, R, T) = k_B T\, \frac{\mathcal{L}}{R^{d-3}}\, \frac{\Phi^{(ss)}_{\bullet\bullet}(\alpha, \vartheta_1, \vartheta_2, \Delta, \Theta)}{\Delta^{d-2}}, \qquad \text{(B.14)}$$

with the scaling function $\Phi^{(ss)}_{\oslash\oslash}$ of the effective potential,

$$\Phi^{(ss)}_{\oslash\oslash}(\alpha,\vartheta_1,\vartheta_2,\Delta,\Theta)=\Phi^{(ss)}_{(+,+)}(\Delta,\Theta)-\Delta\Phi^{(ss)}_{\oslash\oslash}(\alpha,\vartheta_1,\vartheta_2,\Delta,\Theta), \tag{B.15}$$

where

$$\begin{aligned}\Phi^{(ss)}_{(+,\pm)}(\Delta,\Theta)=&\pi\int_1^\infty \mathrm{d}x\,(x-1)x^{-d}\,k_{(+,\pm)}(x\,\Theta)\\ &-\pi\int_{1+\Delta^{-1}}^\infty \mathrm{d}x\,(x-1-\Delta^{-1})\,x^{-d}\,k_{(+,\pm)}(x\,\Theta)\end{aligned} \tag{B.16}$$

is the scaling function of the potential between two homogeneous spheres [29], with an explicit dependence on $\Delta$ retained (in spite of the underlying DA limit $\Delta\to 0$) for consistency with the dependence on $\Delta$ of the orientation dependent term $\Delta\Phi^{(ss)}_{\oslash\oslash}$.

In order to obtain the excess scaling function $\Delta\Phi^{(ss)}_{\oslash\oslash}$ one has to integrate $\Delta K^{(ss)}_{\oslash\oslash}$ from Eq. (B.11) in accordance with Eq. (B.13). The integral of $\Delta K^{(ss)}_{\oslash\oslash}$ features two generic types of integrals (here, omitting the tilde of the integration variable):

$$I_1\equiv\int_1^\infty \mathrm{d}z\,\frac{1}{z^{d-1}}\int_{1+b/(z\,\Delta)}^{1+a/(z\,\Delta)}\mathrm{d}x\,x^{-d}\,\Delta k\,(x\,z\,\Theta) \tag{B.17}$$

with the first and last contribution to this integral [compare Eqs. (B.11) and (B.13)] being described by $a=r_s^2,\ b=0$ and $a=1,\ b=r_s^2$, respectively, and

$$\begin{aligned}I_2\equiv&\int_1^\infty \mathrm{d}z\,\frac{1}{z^{d-1}}\\ &\times\int_{1+\cos^2\vartheta_{1,2}/(z\,\Delta)}^{1+r_s^2/(z\,\Delta)}\mathrm{d}x\,\arccos\left(|\cot\vartheta_{1,2}|\sqrt{\frac{1}{(z\,\Delta)(x-1)}-1}\right)\,x^{-d}\,\Delta k\,(x\,z\,\Theta)\,.\end{aligned} \tag{B.18}$$

We represent integral $I_1$ by the function

$$\begin{aligned}I_1&\equiv\Delta u^{(ss)}(a,b,\Delta,\Theta)\\ &=\int_1^\infty \mathrm{d}z\,\frac{1}{z^{d-1}}\left[\int_{1+b/(z\,\Delta)}^\infty \mathrm{d}x\,x^{-d}\,\Delta k\,(x\,z\,\Theta)-\int_{1+a/(z\,\Delta)}^\infty \mathrm{d}x\,x^{-d}\,\Delta k\,(x\,z\,\Theta)\right].\end{aligned} \tag{B.19}$$

With the substitution $x\to w=z\,\Delta\,(x-1)$ so that $\mathrm{d}w=z\,\Delta\,\mathrm{d}x$ one has

$$\begin{aligned}\Delta u^{(ss)}(a,b,\Delta,\Theta)=\Delta^{-1}\int_1^\infty \mathrm{d}z\,\frac{1}{z^{d}}\Bigg[&\int_b^\infty \mathrm{d}w\,\left(1+\frac{w}{z\,\Delta}\right)^{-d}\,\Delta k\left(z\left(1+\frac{w}{z\,\Delta}\right)\Theta\right)\\ &-\int_a^\infty \mathrm{d}w\,\left(1+\frac{w}{z\,\Delta}\right)^{-d}\,\Delta k\left(z\left(1+\frac{w}{z\,\Delta}\right)\Theta\right)\Bigg]\end{aligned} \tag{B.20}$$

and with the substitution $z \to y = z + w/\Delta$ with $\mathrm{d}y = \mathrm{d}z$ one finds

$$\Delta u^{(ss)}(a, b, \Delta, \Theta) = \Delta^{-1} \Bigg[ \int_b^\infty \mathrm{d}w \int_{1+w/\Delta}^\infty \mathrm{d}y \, y^{-d} \, \Delta k\,(y\,\Theta) - \int_a^\infty \mathrm{d}w \int_{1+w/\Delta}^\infty \mathrm{d}y \, y^{-d} \, \Delta k\,(y\,\Theta) \Bigg]. \tag{B.21}$$

After switching the order of the integrations according to

$$\int_b^\infty \mathrm{d}w \int_{1+w/\Delta}^\infty \mathrm{d}y = \int_{1+b/\Delta}^\infty \mathrm{d}y \int_b^{\Delta(y-1)} \mathrm{d}w \tag{B.22}$$

the integration over $w$ can be carried out, resulting in

$$\Delta u^{(ss)}(a, b, \Delta, \Theta) = \int_{1+b/\Delta}^\infty \mathrm{d}y \, (y - 1 - b/\Delta) \, y^{-d} \Delta k(y\,\Theta) - \int_{1+a/\Delta}^\infty \mathrm{d}y \, (y - 1 - a/\Delta) \, y^{-d} \Delta k(y\,\Theta). \tag{B.23}$$

Integral $I_2$ is represented by the function

$$\begin{aligned} I_2 &\equiv \Delta v^{(ss)}(r_s, \vartheta, \Delta, \Theta) \\ &= \int_1^\infty \mathrm{d}z \, \frac{1}{z^{d-1}} \Bigg[ \int_{1+\cos^2\vartheta/(z\,\Delta)}^\infty \mathrm{d}x \, \arccos\left( |\cot\vartheta| \sqrt{\frac{1}{(z\,\Delta)(x-1)} - 1} \right) x^{-d} \, \Delta k\,(x\,z\,\Theta) \\ &\quad - \int_{1+r_s^2/(z\,\Delta)}^\infty \mathrm{d}x \, \arccos\left( |\cot\vartheta| \sqrt{\frac{1}{(z\,\Delta)(x-1)} - 1} \right) x^{-d} \, \Delta k\,(x\,z\,\Theta) \Bigg]. \end{aligned} \tag{B.24}$$

As before, we first use the substitution $x \to w = z\,\Delta\,(x-1)$ with $\mathrm{d}w = z\,\Delta\,\mathrm{d}x$, followed by the substitution $z \to y = z + w/\Delta$ with $\mathrm{d}y = \mathrm{d}z$. This renders

$$\begin{aligned} &\Delta v^{(ss)}(r_s, \vartheta, \Delta, \Theta) \\ &\quad = \Delta^{-1} \Bigg[ \int_{\cos^2\vartheta}^\infty \mathrm{d}w \int_{1+w/\Delta}^\infty \mathrm{d}y \, \arccos\left( |\cot\vartheta| \sqrt{\frac{1}{w} - 1} \right) y^{-d} \, \Delta k\,(y\,\Theta) \\ &\qquad - \int_{r_s^2}^\infty \mathrm{d}w \int_{1+w/\Delta}^\infty \mathrm{d}y \, \arccos\left( |\cot\vartheta| \sqrt{\frac{1}{w} - 1} \right) y^{-d} \, \Delta k\,(y\,\Theta) \Bigg]. \end{aligned} \tag{B.25}$$

We recall that the semi-minor axes of the two half-ellipses are given by $b_{1,2} = |\cos\vartheta_{1,2}|$ and that $r_s$ denotes the distance of the intersection point between the half-ellipses from the symmetry axis of the two particles. Obviously, the intersection point cannot be closer to the common origin than any semi-minor axis, so that $|\cos\vartheta_1| \leq r_s$ and $|\cos\vartheta_2| \leq r_s$. Based on Eq. (B.11), we need to evaluate $\Delta v^{(ss)}(r_s, \vartheta, \Delta, \Theta)$ for $\vartheta = \vartheta_1$ and $\vartheta = \vartheta_2$. For that reason, we consider only the case $|\cos\vartheta| \leq r_s$ and reorder the integrals:

$$\begin{aligned}
&\int_{\cos^2\vartheta}^{\infty} \mathrm{d}w \int_{1+w/\Delta}^{\infty} \mathrm{d}y \; - \int_{r_s^2}^{\infty} \mathrm{d}w \int_{1+w/\Delta}^{\infty} \mathrm{d}y \\
&= \int_{1+\cos^2\vartheta/\Delta}^{\infty} \mathrm{d}y \int_{\cos^2\vartheta}^{\Delta(y-1)} \mathrm{d}w - \int_{1+r_s^2/\Delta}^{\infty} \mathrm{d}y \underbrace{\int_{r_s^2}^{\Delta(y-1)} \mathrm{d}w}_{\int_{\cos^2\vartheta}^{\Delta(y-1)} \mathrm{d}w \; - \int_{\cos^2\vartheta}^{r_s^2} \mathrm{d}w} \qquad \text{(B.26)} \\
&= \int_{1+\cos^2\vartheta/\Delta}^{1+r_s^2/\Delta} \mathrm{d}y \int_{\cos^2\vartheta}^{\Delta(y-1)} \mathrm{d}w \; + \int_{1+r_s^2/\Delta}^{\infty} \mathrm{d}y \int_{\cos^2\vartheta}^{r_s^2} \mathrm{d}w
\end{aligned}$$

so that finally

$$\begin{aligned}
\Delta v^{(ss)}(r_s,\vartheta,\Delta,\Theta) = {}& \Delta^{-1} \int_{1+\cos^2\vartheta/\Delta}^{1+r_s^2/\Delta} \mathrm{d}y \, g\big(\Delta(y-1),\vartheta\big)\, y^{-d}\, \Delta k\,(y\,\Theta) \\
&+ \Delta^{-1} \int_{1+r_s^2/\Delta}^{\infty} \mathrm{d}y \, g(r_s^2,\vartheta)\, y^{-d}\, \Delta k\,(y\,\Theta)\,, \quad |\cos\vartheta| \leq r_s, \qquad \text{(B.27)}
\end{aligned}$$

and

$$\begin{aligned}
g(u,\vartheta) &= \int_{\cos^2\vartheta}^{u} \mathrm{d}w \; \arccos\left(|\cot\vartheta|\sqrt{\frac{1}{w}-1}\right) \qquad \text{(B.28)} \\
&= \left[ w \arccos\left(|\cot\vartheta|\sqrt{\frac{1}{w}-1}\right) + |\cos\vartheta| \arcsin\big(|\csc\vartheta|\sqrt{1-w}\big) \right]_{\cos^2\vartheta}^{u} \\
&= u \arccos\left(|\cot\vartheta|\sqrt{\frac{1}{u}-1}\right) - |\cos\vartheta| \arccos\big(|\csc\vartheta|\sqrt{1-u}\big)\,, \quad \cos^2\vartheta \leq u.
\end{aligned}$$

Note that $g(u=\cos^2\vartheta,\vartheta)=0$. Concerning the derivation of Eq. (B.28) we leave out the detailed case analysis for the sign of $\cot\vartheta$, which in the end, can be subsumed by taking the absolute values as stated in Eq. (B.28). Putting the results together, the excess scaling function of the potential is given by

$$\begin{aligned}
\Delta\Phi^{(ss)}_{\oslash\oslash}(\alpha,\vartheta_1,\vartheta_2,\Delta,\Theta) = {}& \pi\, H\,((\cos\vartheta_1)\,(\cos\vartheta_2))\, \Delta u^{(ss)}(r_s^2,0,\Delta,\Theta) \\
&- \operatorname{sign}\,((\cos\vartheta_1)\,(\cos\vartheta_2)) \Big[\Delta v^{(ss)}(r_s^2,\vartheta_1,\Delta,\Theta) \\
&\qquad + c(\alpha,\vartheta_1,\vartheta_2)\Delta v^{(ss)}(r_s^2,\vartheta_2,\Delta,\Theta)\Big] \\
&+ \alpha\, \Delta u^{(ss)}(1,r_s^2,\Delta,\Theta). \qquad \text{(B.29)}
\end{aligned}$$

# Appendix C

# Theoretical models of critical systems

Much of the work presented in this thesis, aiming at describing behavior near the critical point of a binary liquid mixture, has been obtained using, or at least compared to, results of mean field theory.

In an enlightening discussion with the experimental collaborators that provided the data for chapter 6, the innocent question "How can one obtain a fluctuation-induced force [the critical Casimir force] within mean field theory, which supposedly neglects fluctuations?" popped up. Much of the doubt is rooted in the loose definitions of what mean field means and what fluctuations are. Sometimes in physics, one has to concede that all the elaborate verbal descriptions cannot replace a mathematical precise model. Since certain models are so fundamental to all understanding of critical phenomena, this appendix is devoted to a concise, but sufficient derivation of critical phenomena within, and fluctuations beyond mean field theory.

## C.1 Ising model

The *Ising model* is a mathematical model for the total interaction between $N$ points in a connected graph, which interact via a single property of the points, called spin, that has either the value $+1$ or $-1$, in analogy to the magnetic spin of atoms. The most general Hamiltonian of the Ising model is defined as

$$H = -\frac{1}{2}\sum_{i,j=1}^{N} J_{ij} s_i s_j - h \sum_{i=1}^{N} s_i. \tag{C.1}$$

Here, the points labeled $i$ and $j$ interact via their spin values $s_i = \pm 1$ and exchange energies $J_{ij}$ (a $N \times N$ matrix), the sign of which determines whether pairs with the same spin or pairs with opposing spins lower the energy. The spins may couple to an *external field* $h$ that promotes one spin value. Typically, instead of a general graph, one is interested in the specific Ising model for the $d$-dimensional regular lattice. Furthermore, often only the nearest-neighbor interaction with $J_{ij} = J$ for $i$ and $j$ denoting adjacent points in the lattice, and $J_{ij} = 0$ for non-adjacent points, is considered, so that the name Ising model often stands totum pro parte for the Hamiltonian

$$H = -J \sum_{\langle i,j \rangle} s_i s_j - h \sum_{i=1}^{N} s_i, \tag{C.2}$$

where $\langle i, j \rangle$ denotes all distinct pairs of nearest neighbors. Here, we will also simply refer to Eq. (C.2) as the Ising model.

The thermodynamic behavior of the system follows from the discrete partition sum $Z = \sum_{\{s_i\}} e^{-\beta H}$, where the sum runs over all sets $\{s_i\}$ of combinations of the spin values $s_i$. Of course, the order of the combinatorial sets is not important, so that partition sum can be written more explicitly as

$$Z = \sum_{\{s_i\}} e^{-\beta H} = \sum_{s_1=\pm 1} \sum_{s_2=\pm 1} \cdots \sum_{s_N=\pm 1} \exp\left( \beta J \sum_{\langle i,j \rangle} s_i s_j + \beta h \sum_{i=1}^{N} s_i, \right). \tag{C.3}$$

The Ising model is straightforward to solve analytically in a 1D chain. In two dimensions, an analytic solutions is known only for $h = 0$, as first derived by Onsager [193]. For non-zero field $h \neq 0$ solutions can be obtained numerically. For $d = 3$ dimensions, no exact results are available. For $d \geq 4$, the mean field approximation becomes valid and predicts the exact critical exponents of the Ising model (see Table 2.1).

In order to present a clear notation, we define three closely related but distinct quantities that can be confusing to the unprepared reader:

1. the magnetization of a single realization: $m(\{s_i\}) := \frac{1}{N} \sum\limits_i s_i$.
2. the local magnetization of a specific site $i$: $m_i := \langle s_i \rangle = \sum\limits_{s_i=\pm 1} s_i \, p(s_i)$.
   Note that for an infinite, regular lattice, i.e., with invariance under translation by lattice vectors, all points are equivalent, so that $m_i = m_j \, \forall \, i, j$
3. the equilibrium global magnetization: $\overline{m} = \frac{1}{N} \sum\limits_i m_i = \frac{1}{N} \sum\limits_i \langle s_i \rangle = \langle m(\{s_i\}) \rangle$.
   That means the average of all local magnetizations is the same as averaging the magnetization of all realization.

Let us rewrite the spin values on each site using the deviation $\delta s_j$ from the local magnetization $m_j$, i.e., $s_j = m_j + \delta s_j = \overline{m} + \delta s_j$. For a homogeneous bulk system, the local magnetization is equivalent to the global magnetization $\overline{m}$. In consequence, averaged over all realizations the fluctuations cancel out, i.e., $\langle \delta s_j \rangle = 0$. On the other hand, the average of the fluctuations in a particular realization is $\frac{1}{N} \sum_i \delta s_i = m(\{s_i\}) - \overline{m}$, i.e., the difference between the magnetization of this particular realization and the equilibrium magnetization. The core of the mean field approximation is to assume that the magnetization of all realizations remain close to the equilibrium magnetization, i.e., fluctuations from the equilibrium are small, so that $|m(\{s_i\}) - \overline{m}| \leq \frac{1}{N}\sum_i |\delta s_i| \ll 1$.

Now, the Ising Hamiltonian Eq. (C.2) can be rewritten as a sum over all lattice points indexed by $i$, interacting with its nearest neighbors $j \in \text{n.n.}(i)$, so that

$$H = -\frac{J}{2}\sum_{i}^{N}\sum_{j\in \text{n.n.}(i)} s_i(\overline{m} + \delta s_j) - h\sum_{i=1}^{N} s_i. \tag{C.4}$$

A factor $1/2$ is needed to correct for double counting of pairs. Substituting also $s_i = \overline{m} + \delta s_i$ and $\overline{m}\,\delta s_j = \overline{m}\,s_j - m^2$, one has

$$\begin{aligned} H &= -\frac{J}{2}\sum_{i}^{N}\sum_{j\in \text{n.n.}(i)} (\overline{m}\,s_i + \overline{m}\,s_j - \overline{m}^2 + \delta s_i\,\delta s_j) - h\sum_{i=1}^{N} s_i \\ &= N\,\frac{zJ}{2}\overline{m}^2 - \sum_{i}^{N}(h + zJ\overline{m})s_i - J\sum_{\langle i,j\rangle}\delta s_i\,\delta s_j, \end{aligned} \tag{C.5}$$

where the coordination number $z = 2d$ gives the number of nearest neighbor in a $d$-dimensional lattice. Note that an individual spin fluctuation $\delta s_i$ is limited to $\delta s_i = \pm 1 - \overline{m} \in [-2, 2]$. The quadratic fluctuations can be estimated to be

$$\Big|\sum_{\langle i,j\rangle}\delta s_i \delta s_j\Big| \leq \frac{1}{2}\sum_{i}^{N}|\delta s_i| \underbrace{\Big|\sum_{j\in\text{n.n.}(i)}\delta s_j\Big|}_{\in[-2z,\leq 2z]} < \sum_{i}^{N}|\delta s_i| z \ll Nz, \tag{C.6}$$

by employing the assumption that $\sum_i |\delta s_i| \ll N$. Thus the sum of quadratic fluctuations is small compared to the other two terms.

Accordingly, the approximated mean field Hamiltonian

$$H_{\text{MF}} = N\,\frac{zJ}{2}\overline{m}^2 - \sum_{i}^{N}(h + zJ\overline{m})s_i \tag{C.7}$$

has a form as if each spin $s_i$ interacts independently with an effective mean field $h_{\text{MF}} = h + zJm$, without any interaction between the spins. From this, the mean field partition sum easily follows

$$
\begin{aligned}
Z_{\mathrm{MF}} &= e^{-\beta N z J \overline{m}^2/2} \sum_{\{s_i\}} e^{\beta(h+zJ\overline{m})\sum_i s_i} = e^{-\beta N z J \overline{m}^2/2} \sum_{\{s_i\}} \prod_i e^{\beta(h+zJ\overline{m})s_i} \\
&= e^{-\beta N z J \overline{m}^2/2} \prod_i \left( e^{\beta(h+zJ\overline{m})} + e^{-\beta(h+zJ\overline{m})} \right) \\
&= e^{-\beta N z J \overline{m}^2/2} \left( 2\cosh\left(\beta(h+zJ\overline{m})\right)\right)^N ,
\end{aligned}
\tag{C.8}
$$

and in consequence the free energy of the mean field Ising model

$$
\frac{F_{\mathrm{MF}}}{N} = -\frac{k_B T}{N} \log Z_{\mathrm{MF}} = \frac{zJ}{2}\overline{m}^2 - k_B T \log\left(2\cosh\left(\beta(h+zJ\overline{m})\right)\right). \tag{C.9}
$$

There remains one issue of consistency: The effective field $h_{\mathrm{MF}} = h + zJ\overline{m}$ is on one hand the field generating the equilibrium magnetization $\overline{m}$, but also depending itself on the resulting magnetization. For a physical solution, the self-consistency condition

$$
\begin{aligned}
\overline{m} = \langle s_i \rangle &= \sum_{s_i=\pm 1} s_i\, p(s_i) \quad \text{with } p(s_i) = \frac{e^{\beta(h+zJ\overline{m})s_i}}{\sum_{s_i=\pm1} e^{\beta(h+zJ\overline{m})s_i}} \\
&= \frac{e^{\beta(h+zJ\overline{m})} - e^{-\beta(h+zJ\overline{m})}}{e^{\beta(h+zJ\overline{m})} + e^{-\beta(h+zJ\overline{m})}} = \tanh(\beta(h+zJ\overline{m}))
\end{aligned}
\tag{C.10}
$$

must be fulfilled. Here, the local magnetization was identified to be equal with the global magnetization. Equivalently, the global magnetization as an average over all realizations follows from

$$
\begin{aligned}
\overline{m} = \langle m(\{s_i\}) \rangle &= \frac{1}{Z_{\mathrm{MF}}} \sum_{\{s_i\}} m(\{s_i\})\, e^{-\beta H_{\mathrm{MF}}} \\
&= \frac{1}{\beta N Z_{\mathrm{MF}}} \frac{\partial Z_{\mathrm{MF}}}{\partial h} = \frac{1}{\beta N} \frac{\partial}{\partial h} \log Z_{\mathrm{MF}} = \tanh(\beta(h + Jz\overline{m})),
\end{aligned}
\tag{C.11}
$$

giving the same result. It is worthwhile to note that for the mean field Ising model $0 = (\beta N)^{-1} \frac{\partial}{\partial h} \log Z_{\mathrm{MF}} - \overline{m} \overset{\text{Eq. (C.9)}}{=} (zJ\beta N)^{-1} \frac{\partial}{\partial m} \log Z_{\mathrm{MF}}$. Thus $\frac{\partial}{\partial m} F_{\mathrm{MF}} = 0$ and the mean field magnetization $\overline{m}$ minimizes also the free energy $F_{\mathrm{MF}}$. In turn, fluctuations out of equilibrium raise the free energy.

One can verify that without an external field ($h = 0$), the self-consistency Eq. (C.10) always possesses the trivial solution $m = 0$, which is the only solution for $\beta zJ < 1$. For $\beta zJ > 1$, two symmetric, non-trivial solutions appear. This leads one to define the critical temperature $T_c = zJ/k_B$, above which the system exhibits a homogeneous magnetization $\overline{m} = 0$, and below which a spontaneous symmetry break into one of two configurations with $\overline{m} = \pm|\overline{m}| \neq 0$ occurs. The fundamental result that such a phase transition exists is incorrect in $d = 1$, but correctly predicts the situation in $d \geq 2$. The estimate of the critical temperature via MFT is quantitatively off, but becomes increasingly accurate for higher dimensions $d$. The inaccuracy can be pinpointed to the assumption underlying the mean field approximation: For the lattice Ising model, the number of nearest-neighbors $z = 2d$ increases with the number of dimension $d$. With more neighbors taken into account, the local average of neighboring spins becomes closer to the global average (the mean field). For low dimensionality local fluctuations can be significant and even destroy global order.

## C.2 Landau theory

Interestingly, the equilibrium magnetization $\overline{m}$ turns into a continuous variable in the thermodynamic limit $N \to \infty$. This motivates the search for an *a priori* field-theoretic Hamiltonian, which exhibits the same features as the Ising Hamiltonian, but with a continuous variable $\phi$, the so-called order parameter (OP), which replaces the magnetization. Historically, the structure of such a Hamiltonian was proposed phenomenologically by Landau [5] in 1937 based on the symmetries of the original Hamiltonian to be

$$H = t\phi^2 + u\phi^4 - h\phi + \mathcal{O}[\phi^6] \tag{C.12}$$

for a bulk order parameter $\phi$. This was motivated by the observation that many different systems behave similarly close to critical point, thus microscopic details cannot be important and only the gross features of the system play a role. The Ginzburg-Laundau Hamiltonian includes local variations of the order parameter via gradient terms $\nabla\phi(\mathbf{r})$, leading to the functional

$$\mathcal{H} = \int \mathrm{d}\mathbf{r}\, \left[\frac{s}{2}(\nabla\phi(\mathbf{r}))^2 + t\,\phi(\mathbf{r})^2 + u\,\phi(\mathbf{r})^4 - h\,\phi(\mathbf{r}) + \mathcal{O}\left[(\nabla^2\phi)^2, (\nabla\phi)^2\phi^2, \phi^6\right]\right]. \tag{C.13}$$

Using this ansatz as a working basis is very powerful. However, one does not know a priori how the phenomenological coefficients $s, t, u$ depend on microscopic model parameters, as well as thermodynamic parameters such as temperature and pressure. Therefore, we will take a short detour, which details how to arrive at the Ginzburg-Laundau Hamiltonian starting from the Ising model in order to establish firmly that both Hamiltonians belong to the same universality class.

The partition sum, based on the most general form of the Ising Hamiltonian in Eq. (C.1), can be written in vector and matrix notation as

$$Z = \sum_{\{s_i\}} \exp\left(\frac{1}{2}\mathbf{s}^t\tilde{\mathbf{J}}\mathbf{s} + \tilde{\mathbf{h}}\mathbf{s}\right) \tag{C.14}$$

with an $N \times N$ matrix $\tilde{\mathbf{J}}$ with entries $\tilde{J}_{ij} = \beta J_{ij}$ and a scaled unit vector with all components $\tilde{h}_i = \beta h$. A way towards a continuous OP is provided by the Hubbard-Stratonovich transformation

$$\sqrt{\det(\mathbf{A}^{-1})}\exp\left(\frac{1}{2}\mathbf{s}^t\mathbf{A}^{-1}\mathbf{s}\right) = \prod_{i=1}^{N}\int_{-\infty}^{\infty}\frac{\mathrm{d}x_i}{\sqrt{2\pi}}\exp\left(-\frac{1}{2}\mathbf{x}^t\mathbf{A}\mathbf{x}+\mathbf{x}^t\mathbf{s}\right), \tag{C.15}$$

which allows to write the partition sum as an integral over the auxiliary vector $\mathbf{x}$, with the matrix determinant expressed by

$$\sqrt{\det(\mathbf{A}^{-1})} = \prod_{i=1}^{N}\int_{-\infty}^{\infty}\frac{\mathrm{d}x_i}{\sqrt{2\pi}}\exp\left(-\frac{1}{2}\mathbf{x}^t\mathbf{A}\mathbf{x}\right). \tag{C.16}$$

One may realize that, when read from right to left, this is simply an identity holding for multi-dimensional Gaussian integrals. Here it is not used to solve the integral, but as a transformation from which one obtains the partition function

$$\mathcal{Z} = \frac{\prod\limits_{i=1}^{N}\int\limits_{-\infty}^{\infty}\frac{\mathrm{d}x_i}{\sqrt{2\pi}}\exp\left(-\frac{1}{2}\mathbf{x}^t\tilde{\mathbf{J}}^{-1}\mathbf{x}\right)\sum\limits_{\{s_i\}}\exp\left((\tilde{\mathbf{h}}+\mathbf{x})^t\mathbf{s}\right)}{\sqrt{\det(\tilde{\mathbf{J}})}}. \tag{C.17}$$

The sum over all spin configurations can be exactly evaluated

$$\begin{aligned}\sum_{\{s_i\}}\exp\left((\tilde{\mathbf{h}}+\mathbf{x})^t\mathbf{s}\right) &= \prod_{i=1}^{N}\sum_{\{s_i\}}\exp\left((\beta h + x_i)s_i\right) = \prod_{i=1}^{N}2\cosh(\beta h + x_i) \\ &= \exp\left(\sum_{i=1}^{N}\log\left(2\cosh(\beta h + x_i)\right)\right),\end{aligned} \tag{C.18}$$

so that in short

$$\begin{aligned}\mathcal{Z} &= \frac{\prod\limits_{i=1}^{N}\int\limits_{-\infty}^{\infty}\frac{\mathrm{d}x_i}{\sqrt{2\pi}}\exp\left(-\beta\mathcal{H}\right)}{\sqrt{\det(\tilde{\mathbf{J}})}}, \quad \text{with} \\ \mathcal{H} &= k_BT\,\frac{1}{2}\mathbf{x}^t\tilde{\mathbf{J}}^{-1}\mathbf{x} - k_BT\sum_{i=1}^{N}\log\left(2\cosh(\beta h + x_i)\right).\end{aligned} \tag{C.19}$$

Since only exact identities have been used, the partition function $\mathcal{Z}$ describing a continuous valued model is identical to the partition sum $Z$ of the Ising model with discrete values $s_i = \pm 1$. So far, the nature of the spin is not relevant to the thermodynamic behavior.

It is not necessary to determine $\det(\tilde{\mathbf{J}})$ in order to evaluate expectation values such as

$$\begin{aligned}\langle x_i\rangle &= \frac{\prod_{i=1}^{N}\int_{-\infty}^{\infty}\frac{\mathrm{d}x_i}{\sqrt{2\pi}}\,x_i\,\exp\left(-\beta\mathcal{H}\right)}{\sqrt{\det(\tilde{\mathbf{J}})}\,\mathcal{Z}}\\ &\overset{\text{Eq. (C.17)}}{=} \frac{\left(\frac{\partial}{\partial s_i}-\beta h\right)\mathcal{Z}}{\mathcal{Z}} \overset{\text{Eq. (C.14)}}{=} \frac{\sum_{\{s_i\}}(\tilde{\mathbf{J}}\mathbf{s})_i\,\exp\left(\frac{1}{2}\mathbf{s}^t\tilde{\mathbf{J}}\mathbf{s}+\tilde{\mathbf{h}}\mathbf{s}\right)}{\sum_{\{s_i\}}\exp\left(\frac{1}{2}\mathbf{s}^t\tilde{\mathbf{J}}\mathbf{s}+\tilde{\mathbf{h}}\mathbf{s}\right)}\\ &= \langle(\tilde{\mathbf{J}}\mathbf{s})_i\rangle = \Big\langle\sum_j\tilde{J}_{ij}s_j\Big\rangle = \sum_j\tilde{J}_{ij}\langle s_j\rangle = \sum_j\tilde{J}_{ij}m_j.\end{aligned} \tag{C.20}$$

Thus, the auxiliary vector $\mathbf{x}$ has a physical meaning as the components are closely related to the local magnetization $m_j$ of each site $j$. One can make us of that and define an OP $\phi = \tilde{\mathbf{J}}^{-1}\mathbf{x}$, so that $x_i = \sum_j\tilde{J}_{ij}\phi_j$ and $\langle\phi\rangle_i = m_i$. Substituting this into Eq. (C.19), one finds the Hamiltonian

$$\mathcal{H} = \frac{1}{2}\sum_{i,j}J_{ij}\phi_i\phi_j - k_BT\sum_{i=1}^{N}\log\left(2\cosh\left(\beta\Big(h+\sum_j J_{ij}\phi_j\Big)\right)\right). \tag{C.21}$$

We emphasize once more that the real-valued order parameter $\phi_i$ has the same expectation value $\langle\phi_i\rangle$ at each site $i$ as the local magnetization of spins in the Ising model. In the limit $N\to\infty$, the results in Eqs. (C.19) and (C.21) hold by identifying $\lim\limits_{N\to\infty}\prod_{i=1}^{N}\int_{-\infty}^{\infty}\frac{\mathrm{d}x_i}{\sqrt{2\pi}}$ with the functional integration $\int\mathcal{D}\phi$.

Exact transformations have served us well up to now, but eventually approximations need to be introduced in order to make progress. Around the critical point, with $h\to 0$, one expects $\phi_j$ to be also small. We expand the Hamiltonian up to fourth order $\phi_j^4$ and linear in $h$ using $\log(2\cosh(x)) \approx \log 2 + x^2/2 - x^4/12$:

$$\begin{aligned}\mathcal{H} =& \frac{1}{2}\sum_{i,j}J_{ij}\phi_i\phi_j - k_BT\sum_{i=1}^{N}\left[\log 2 + \frac{\beta^2}{2}\Big(\sum_j J_{ij}\phi_j\Big)^2 - \frac{\beta^4}{12}\Big(\sum_j J_{ij}\phi_j\Big)^4\right]\\ &- k_BT\sum_{i=1}^{N}\beta^2h\Big(\sum_j J_{ij}\phi_j\Big).\end{aligned} \tag{C.22}$$

From afar, one may start to recognize the quadratic and quartic structure of the Landau Hamiltonian. Still, the OP $\phi_i$ is defined only on lattice sites, whereas the aim is to arrive at a continuous field theory. A well-defined way of smearing out the lattice can be implemented in Fourier space. The necessary Fourier transforms into the reciprocal lattice with lattice vectors $\mathbf{k}$ are given by

$$\phi_i = \frac{1}{\sqrt{N}}\sum_{\mathbf{k}}e^{i\mathbf{k}\cdot\mathbf{r}_i}\,\phi_{\mathbf{k}}, \quad J_{ij} = \frac{1}{N}\sum_{\mathbf{k}}e^{i\mathbf{k}\cdot(\mathbf{r}_i-\mathbf{r}_j)}\,J_{\mathbf{k}}, \quad \delta_{\mathbf{k}-\mathbf{k}'} = \frac{1}{N}\sum_i e^{i(\mathbf{k}-\mathbf{k}')\cdot\mathbf{r}_i}, \tag{C.23}$$

which produce

$$\sum_j J_{ij}\phi_j = \frac{1}{\sqrt{N}}\sum_{\mathbf{k}} e^{i\mathbf{k}\cdot\mathbf{r}_i} J_{\mathbf{k}}\phi_{\mathbf{k}}, \tag{C.24}$$

$$\sum_i\sum_j J_{ij}\phi_j\phi_i = \sum_{\mathbf{k}} J_{\mathbf{k}}\phi_{\mathbf{k}}\phi_{-\mathbf{k}}, \tag{C.25}$$

$$\sum_i\Big(\sum_j J_{ij}\phi_j\Big)^2 = \sum_{\mathbf{k}} J_{\mathbf{k}}J_{-\mathbf{k}}\phi_{\mathbf{k}}\phi_{-\mathbf{k}}, \tag{C.26}$$

$$\sum_i\Big(\sum_j J_{ij}\phi_j\Big)^4 = \frac{1}{N}\sum_{\mathbf{k}_1,\mathbf{k}_2,\mathbf{k}_3,\mathbf{k}_4} \delta_{\mathbf{k}_1+\mathbf{k}_2+\mathbf{k}_3+\mathbf{k}_4} J_{\mathbf{k}_1}J_{\mathbf{k}_2}J_{\mathbf{k}_3}J_{\mathbf{k}_4}\,\phi_{\mathbf{k}_1}\phi_{\mathbf{k}_2}\phi_{\mathbf{k}_3}\phi_{\mathbf{k}_4}. \tag{C.27}$$

Since $\phi_i$ and $J_{ij}$ are real and $J(-\mathbf{r}) = J(\mathbf{r})$, the Fourier transformed Hamiltonian reduces to

$$\begin{aligned}\mathcal{H} =& - Nk_BT\log 2 - \beta\sqrt{N}hJ_{\mathbf{k}=0}\phi_{\mathbf{k}=0} + \frac{1}{2}\sum_{\mathbf{k}}(J_{\mathbf{k}} - \beta J_{\mathbf{k}}^2)\phi_{\mathbf{k}}\phi_{-\mathbf{k}} \\ &+ \frac{\beta^3}{12N}\sum_{\mathbf{k}_1,\mathbf{k}_2,\mathbf{k}_3,\mathbf{k}_4} \delta_{\mathbf{k}_1+\mathbf{k}_2+\mathbf{k}_3+\mathbf{k}_4} J_{\mathbf{k}_1}J_{\mathbf{k}_2}J_{\mathbf{k}_3}J_{\mathbf{k}_4}\,\phi_{\mathbf{k}_1}\phi_{\mathbf{k}_2}\phi_{\mathbf{k}_3}\phi_{\mathbf{k}_4}.\end{aligned} \tag{C.28}$$

For the nearest-neighbor interaction on $d$-dimensional lattice, $J_{\mathbf{k}}$ can be expanded in orders of $\mathbf{k} = \{k_1, \ldots, k_d\}$ as

$$\begin{aligned}J_{\mathbf{k}} &= \sum_i e^{i\mathbf{k}\cdot\mathbf{r}_i}J(\mathbf{r}_i) = \sum_{n=1}^{d}\left[Je^{ik_na} + Je^{-ik_na}\right] = \sum_{n=1}^{d} 2J\cosh(k_na) \\ &\approx \sum_{n=1}^{d} 2J\left(1 + \frac{(k_na)^2}{2}\right) = zJ\left(1 + \frac{\mathbf{k}^2a^2}{z}\right)\end{aligned} \tag{C.29}$$

Within Eq. (C.28), $J_{\mathbf{k}}$ occurs in the form of

$$\begin{aligned}J_{\mathbf{k}} - \beta J_{\mathbf{k}}^2 &\approx zJ(1-\beta zJ) - zJ(1-2\beta zJ)\frac{\mathbf{k}^2a^2}{z} \\ &\approx k_BT_c\left(\frac{T-T_c}{T}\right) + k_BT_c\frac{\mathbf{k}^2a^2}{z},\end{aligned} \tag{C.30}$$

which is expanded also in quadratic order and re-expressed using $T_c = Jz/k_B$ and $T \approx T_c$. It can be reasoned that this expansion is of general form for any short-ranged, molecular interaction. Finally, everything can be neatly substituted in order to yield the Hamiltonian in Fourier space

$$\begin{aligned}\beta\mathcal{H}[\{\phi_{\mathbf{k}}\}] \approx f_0 - \beta^2h_0\phi_{\mathbf{k}=0} &+ \frac{1}{2}\sum_{\mathbf{k}}\left(\tau + s\,\mathbf{k}^2\right)\phi_{\mathbf{k}}\phi_{-\mathbf{k}} \\ &+ \frac{u}{4!}\sum_{\mathbf{k}_1,\mathbf{k}_2,\mathbf{k}_3,\mathbf{k}_4} \delta_{\mathbf{k}_1+\mathbf{k}_2+\mathbf{k}_3+\mathbf{k}_4} J_{\mathbf{k}_1}J_{\mathbf{k}_2}J_{\mathbf{k}_3}J_{\mathbf{k}_4}\,\phi_{\mathbf{k}_1}\phi_{\mathbf{k}_2}\phi_{\mathbf{k}_3}\phi_{\mathbf{k}_4}.\end{aligned} \tag{C.31}$$

As a means to keep the notation concise, we have avoided to indicate specifically that the reciprocal lattice vector $\mathbf{k}$ is finite, limited in magnitude to the range $L^{-1} < |\mathbf{k}| < a^{-1}$, where $L$ is the system size and $a$ is the lattice spacing. However, one may introduce a intermediate, mesoscopic value and split the partitions function into contributions from wave numbers $\mathbf{k}_<$ smaller than, and wave numbers $\mathbf{k}_>$ larger than $\Lambda$, so that

$$\begin{aligned}\mathcal{Z} \sim \prod_{i=1}^{N} \int_{-\infty}^{\infty} \frac{\mathrm{d}\phi_i}{\sqrt{2\pi}} \exp\left(-\beta\mathcal{H}[\{\phi_i\}]\right) &= \prod_{L^{-1}<|\mathbf{k}|<a^{-1}} \int_{-\infty}^{\infty} \frac{\mathrm{d}\phi_{\mathbf{k}}}{\sqrt{2\pi}} \exp\left(-\beta\mathcal{H}[\{\phi_{\mathbf{k}}\}]\right) \\ &= \prod_{L^{-1}<|\mathbf{k}_<|<\Lambda} \int_{-\infty}^{\infty} \frac{\mathrm{d}\phi_{\mathbf{k}_<}}{\sqrt{2\pi}} \prod_{\Lambda<|\mathbf{k}_>|<a^{-1}} \int_{-\infty}^{\infty} \frac{\mathrm{d}\phi_{\mathbf{k}_>}}{\sqrt{2\pi}} \exp\left(-\beta\mathcal{H}[\{\phi_{\mathbf{k}_<}\},\{\phi_{\mathbf{k}_>}\}]\right). \qquad (C.32)\end{aligned}$$

When the Hamiltonian is expanded in orders of $\mathbf{k}$, one may choose to separate it into terms with small $\mathbf{k}_<$ and large $\mathbf{k}_>$. (Note this is strictly true for the $\phi_{\mathbf{k}}\phi_{-\mathbf{k}}$ term, but a wishful approximation for the $\phi_{\mathbf{k}_1}\phi_{\mathbf{k}_2}\phi_{\mathbf{k}_3}\phi_{\mathbf{k}_4}$ term. It is the power of the Renormalization Group theory to deal with the non-Gaussian term and to trace how it alters the critical behavior.) Around equilibrium, the most important contributions are expected to come from fluctuations with large wavelength, i.e., small wavenumber $\mathbf{k}$, whereas sharply varying fields with large wavenumbers $\mathbf{k}$ are supposedly suppressed. If so, and the lattice spacing $a$ is much smaller than the range of these fluctuations, one can place the cutoff $\Lambda$ such that the dominant contributions are contained within the first factor and the partition function reads

$$\mathcal{Z} \approx \prod_{L^{-1}<|\mathbf{k}_<|<\Lambda} \int_{-\infty}^{\infty} \frac{\mathrm{d}\phi_{\mathbf{k}_<}}{\sqrt{2\pi}} \exp\left(-\beta\mathcal{H}_<[\{\phi_{\mathbf{k}_<}\}]\right) := \int \mathcal{D}\phi \exp\left(-\beta\mathcal{H}_<[\{\phi\}]\right). \qquad (C.33)$$

The consequence of dropping the ultraviolet contributions with $|\mathbf{k}_>| > \Lambda$ is that the Fourier back transform results in a continuous, smoothed real-space OP $\phi(\mathbf{r}) = \frac{1}{V}\sum_{\mathbf{k}} e^{i\mathbf{k}\cdot\mathbf{r}_i}\phi_{\mathbf{k}}$, which effectively interpolates the OP over a mesoscopic region $\Lambda^{-d} > a^d$. Using $\phi_{\mathbf{k}} = \int \mathrm{d}^d\mathbf{r}\, e^{-i\mathbf{k}\cdot\mathbf{r}}\phi(\mathbf{r})$ and $\frac{1}{V}\sum_{\mathbf{k}} e^{i\mathbf{k}(\mathbf{r}-\mathbf{r}')} = \delta(\mathbf{r}-\mathbf{r}')$, one obtains the corresponding Landau-Ginzburg-Wilson Hamiltonian

$$\beta\mathcal{H}_< = \int \mathrm{d}^d\mathbf{r} \left[ f_0 + \frac{s}{2}(\nabla\phi(\mathbf{r}))^2 + \frac{\tau}{2}\phi(\mathbf{r})^2 + \frac{u}{4!}\,\phi(\mathbf{r})^4 - h_0\phi(\mathbf{r}) \right]. \qquad (C.34)$$

The name acknowledges the work of K. G. Wilson employing iterative momentum-cutoffs in the Renormalization Group theory [194]. Note that the upper cutoff is not a pure technicality. While it should raise doubts when a theory depends on the chosen cutoff value, it is meaningful here. One cannot expect any continuous theory to still hold on the atomic level. The cutoff is a reminder that this an effective macroscopic theory.

Despite this effort, the functional integration in Eq. (C.33), with the Ginzburg-Landau-Wilson Hamiltonian in Eq. (C.34) is far from being easily solvable. The form of Eq. (C.33) lends itself to apply the saddle-point approximation (method of steepest descent), so that the partition sum is approximated by the contribution with the largest statistical weight $\exp(-\beta\mathcal{H}[\phi])$. The dominant contribution comes from the minimum of the Hamiltonian $\partial\mathcal{H}[\phi]/\partial\phi|_{\phi=\langle\phi\rangle} = 0$. Note how the saddle-point approximation is equivalent to the self-consistency equation of the mean field Ising model. Thus, we are again on the level of a mean field theory, but for a continuous field. Conceptually, the dependence of the mean field theory on the magnetization is replaced by the order parameter $\phi(\mathbf{r})$, representing locally course-grained spins.

## C.3 Gaussian approximation

In order to go beyond the mean field approximation, one can include fluctuations around the equilibrium profile in quadratic order. We start from the Hamiltonian

$$\mathcal{H}[\phi(\mathbf{r})] = \int_V \mathrm{d}^d\mathbf{r}\ \frac{1}{2}\left(\nabla\phi(\mathbf{r})\right)^2 + \frac{\tau}{2}\,\phi(\mathbf{r})^2 + \frac{u}{4!}\,\phi(\mathbf{r})^4 - h(\mathbf{r})\phi(\mathbf{r}). \tag{C.35}$$

In contrast to Eq. (C.34), we have dropped the constant term $f_0$ as it cancels out in the calculation of any expectation value; specifically it does not alter $\langle\phi\rangle$. The external field $h_0 \to h(\mathbf{r})$ is now allowed to be spatially varying. For convenience, we further set $s = 1$ without loss of generality (the whole integrand can be normalized by $1/s$ in order to achieve this, which is then compensated by a rescaling of $\mathbf{r}$. As the partition function weights all possible OP profiles $\phi(\mathbf{r})$ in a functional integral, this does not affect the result). Consider a small perturbation $\delta\phi(\mathbf{r})$ of the OP in real space from the bulk value $\phi_0$, i.e., $\phi(\mathbf{r}) = \phi_0 + \delta\phi(\mathbf{r})$, inserted into Eq. (C.35). Then retaining only $\phi(\mathbf{r})^4 \approx \phi_0^4 + 4\,\phi_0^3\,\delta\phi(\mathbf{r}) + 6\,\phi_0^2\,(\delta\phi(\mathbf{r}))^2$ and applying a continuous Fourier transform $\phi(\mathbf{r}) = \frac{1}{\sqrt{2\pi}^d}\int \mathrm{d}^d\mathbf{q}\ \phi(\mathbf{q})\,e^{i\mathbf{q}\cdot\mathbf{r}}$ yields

$$\begin{aligned}\mathcal{H}[\phi(\mathbf{q})] = & V\left[\frac{\tau}{2}\phi_0^2 + \frac{u}{4!}\phi_0^4 - h(\mathbf{q}=0)\phi_0\right] + \left[\tau\phi_0 + \frac{u}{6}\phi_0^3\right]\delta\phi(\mathbf{q}=0) \\ & - \int \mathrm{d}^d\mathbf{q}\ h(\mathbf{q})\delta\phi(-\mathbf{q}) \\ & + \int \mathrm{d}^d\mathbf{q}\ \left[\frac{1}{2}|\mathbf{q}|^2 + \frac{\tau}{2} + \frac{u}{4}\phi_0^2\right]\delta\phi(\mathbf{q})\delta\phi(-\mathbf{q}).\end{aligned} \tag{C.36}$$

Note that, as before, there is an implicit ultraviolet cutoff $\Lambda$ and Eq. (C.36) represents an expansion to the highest order in which there is no coupling between different $\mathbf{q}$-contributions, so that the momentum-space cutoff can be applied straightforwardly.

The mean field bulk solution for $h(\mathbf{r}) = h(\mathbf{q}) = 0$ and $\delta\phi(\mathbf{r}) = \delta\phi(\mathbf{q}) = 0$ is obtained from the saddle-point approximation, i.e., $\partial\mathcal{H}/\partial\phi_0 = \tau\,\phi_0 + u/6\,\phi_0^3 = 0$, to be

$$\phi_0 = \begin{cases} 0 & \text{for } \tau > 0, \\ \sqrt{-6\tau/u} & \text{for } \tau < 0. \end{cases} \tag{C.37}$$

Plugging this back into Eq. (C.36) and substituting yields the form

$$\mathcal{H}[\phi(\mathbf{q})] = \mathcal{H}_0 + \int \mathrm{d}^d\mathbf{q}\,\frac{1}{2}\left[|\mathbf{q}|^2 + \xi^{-2}\right]\delta\phi(\mathbf{q})\delta\phi(-\mathbf{q}) - \int \mathrm{d}^d\mathbf{q}\;h(\mathbf{q})\delta\phi(-\mathbf{q}). \tag{C.38}$$

$$\text{with } \mathcal{H}_0 = \begin{cases} 0 & \text{for } \tau > 0, \\ -\frac{3}{2}\frac{\tau^2}{u} - h(\mathbf{q}=0)\sqrt{-\frac{6\tau}{u}} & \text{for } \tau < 0 \end{cases} \text{ and } \xi = \begin{cases} 1/\sqrt{\tau} & \text{for } \tau > 0, \\ 1/\sqrt{-2\tau} & \text{for } \tau < 0. \end{cases} \tag{C.39}$$

At fixed $\tau = T - T_c$, the additive constant $\mathcal{H}_0$ is not important for determining the fluctuations $\delta\phi(\mathbf{q})$. In the current context, $\xi$ is merely a mathematical substitution for $\tau$. The reader may anticipate its physical relevance, which will be addressed below. Eq. (C.38) is quadratic, so the partition function $\mathcal{Z} = \int \mathcal{D}\phi\,\exp(-\beta\mathcal{H})$ is of Gaussian form, which allows the use of helpful identities.

For the most simple Gaussian integral, the relation

$$I_1 := \int_{-\infty}^{\infty} \mathrm{d}x\; e^{-\frac{a}{2}x^2 + b\,x} = \sqrt{\frac{2\pi}{a}}\,e^{\frac{b^2}{2a}} \tag{C.40}$$

holds. This extends straightforwardly to multiple coordinates, using the vector $\mathbf{x} = \{x_i\}$ with $i \in \{1,\ldots,n\}$, giving the $n$-dimensional Gaussian integral

$$\begin{aligned} I_n &:= \int_{-\infty}^{\infty} \prod \mathrm{d}x_i\;\exp\left(-\frac{1}{2}\mathbf{x}^t\mathbf{G}^{-1}\mathbf{x} + \mathbf{b}^t\mathbf{x}\right) \\ &= \det(2\pi\mathbf{G})^{1/2}\,\exp\left(\frac{1}{2}\mathbf{b}^t\mathbf{G}\mathbf{b}\right) \end{aligned} \tag{C.41}$$

where $\mathbf{G}^{-1}$ is a diagonalizable real symmetric matrix.

The idea arises to replace the vector with a function $\phi$ in the continuous limit $n \to \infty$ in order to derive the corresponding Gaussian functional integral. We will skip the rigorous mathematical definition of functional integration. Instead, for a familiar access, let us borrow the Dirac notation from quantum mechanics, so that $\mathbf{x}^t \to \langle\phi|$ is a bra-vector and

$\mathbf{x} \to |\phi\rangle$ is a ket-vector, and

$$\begin{aligned} I_\infty &:= \int \mathcal{D}\phi \;\exp\left(-\frac{1}{2}\langle\phi|\mathbf{G}^{-1}|\phi\rangle + \langle b|\phi\rangle\right) \\ &= \det(2\pi\mathbf{G})^{1/2}\exp\left(\frac{1}{2}\langle b|\mathbf{G}|b\rangle\right). \end{aligned} \tag{C.42}$$

This mere change in notation carries with it the concept of generalizing the vector space of real numbers to the Hilbert space of square-integrable functions, without giving a rigorous treatment. (Note that the Hamiltonian in Eq. (C.35) can only be evaluated for square-integrable functions anyway.) The scalar products and operators involved are evaluated for functions as follows

$$\langle b|\phi\rangle = \int \mathrm{d}\mathbf{r}\;\langle b|\mathbf{r}\rangle\langle\mathbf{r}|\phi\rangle = \int \mathrm{d}\mathbf{r}\; b(\mathbf{r})^*\phi(\mathbf{r}), \tag{C.43}$$

$$\mathbf{G}|\phi\rangle = \int \mathrm{d}\mathbf{r}'\;\mathbf{G}|\mathbf{r}'\rangle\langle\mathbf{r}'|\phi\rangle = \int \mathrm{d}\mathbf{r}'\; G(\mathbf{r},\mathbf{r}')\,\phi(\mathbf{r}'), \text{ and} \tag{C.44}$$

$$\langle\phi|\mathbf{G}|\phi\rangle = \int \mathrm{d}\mathbf{r}\int \mathrm{d}\mathbf{r}'\;\langle\phi|\mathbf{r}\rangle\langle\mathbf{r}|\mathbf{G}|\mathbf{r}'\rangle\langle\mathbf{r}'|\phi\rangle = \int \mathrm{d}\mathbf{r}\int \mathrm{d}\mathbf{r}'\;\phi(\mathbf{r})^*\,G(\mathbf{r},\mathbf{r}')\,\phi(\mathbf{r}'). \tag{C.45}$$

The inverse of $\mathbf{G}$ is defined by the relation

$$\int \mathrm{d}\mathbf{r}'\;\mathbf{G}^{-1}(\mathbf{r},\mathbf{r}')\mathbf{G}(\mathbf{r}',\mathbf{r}'') = \delta(\mathbf{r}-\mathbf{r}''), \tag{C.46}$$

which is the extension of $\mathbf{G}^{-1}\mathbf{G} = \mathbf{1}$ where $\mathbf{1}$ is the unity matrix (or unity operator), itself defined by the property $\mathbf{1}|\phi\rangle = |\phi\rangle \Leftrightarrow \int \mathrm{d}\mathbf{r}'\;\delta(\mathbf{r}-\mathbf{r}')\phi(\mathbf{r}') = \phi(\mathbf{r})$.

The determinant $\det\mathbf{G}$ is a bit problematic to generalize to a functional determinant, as it scales proportionally to the rank $n$ of the matrix $\mathbf{G}$, i.e., the functional determinant tends to infinity. However, in the relevant quantities the functional determinant can be canceled out by proper normalization.

The quadratic contribution $\langle\phi|\mathbf{G}^{-1}|\phi\rangle$ to the Hamiltonian can be identified with $\int \mathrm{d}^d\mathbf{q}\;\frac{1}{2}\left[|\mathbf{q}|^2+\xi^{-2}\right]|\delta\phi(\mathbf{q})|^2$ or $\frac{1}{2}\int \mathrm{d}\mathbf{r}\left[(\nabla\phi(\mathbf{r}))^2+\xi^{-2}\phi(\mathbf{r})^2\right]$ in real space. Integrating by parts gives $\int \mathrm{d}\mathbf{r}\left[(\nabla\phi(\mathbf{r}))^2+\xi^{-2}\phi(\mathbf{r})^2\right] = \int \mathrm{d}\mathbf{r}\;\phi(\mathbf{r})\left(-\nabla^2+\xi^{-2}\right)\phi(\mathbf{r})$. Note that we assume the surface of integration space to be at infinity and that $\phi(\mathbf{r})$ decays sufficiently fast, so that $\nabla\phi(\mathbf{r}\to\infty) = 0$. Rewriting this as $\frac{1}{2}\int \mathrm{d}\mathbf{r}\int \mathrm{d}\mathbf{r}'\;\phi(\mathbf{r}')\delta(\mathbf{r}-\mathbf{r}')\left(-\nabla^2+\xi^{-2}\right)\phi(\mathbf{r})$, one finds

$$\mathbf{G}^{-1} = \delta(\mathbf{r}-\mathbf{r}')\left(-\nabla^2+\xi^{-2}\right). \tag{C.47}$$

Plugging this back in Eq. (C.46), one gets the relation for the proper operator $\mathbf{G}$

$$\left(-\nabla^2+\xi^{-2}\right)\mathbf{G}(\mathbf{r},\mathbf{r}'') = \delta(\mathbf{r}-\mathbf{r}''), \tag{C.48}$$

which produces the definition of the Green's function $\mathbf{G}$ to the differential operator

$(-\nabla^2+\xi^{-2})$. Note that $\mathbf{G}(\mathbf{r},\mathbf{r}'')=\mathbf{G}(\mathbf{r}-\mathbf{r}'')$ is translation invariant.

Correspondingly, one obtains in Fourier space

$$\begin{aligned}\mathcal{Z}&=\det(2\pi\mathbf{G})^{1/2}e^{-\beta\mathcal{H}_0}\\&\quad\times\int\mathcal{D}\phi\,\exp\left(-\frac{1}{2}\int\mathrm{d}^d\mathbf{q}\;\delta\phi(\mathbf{q})^*\left[|\mathbf{q}|^2+\xi^{-2}\right]\delta\phi(\mathbf{q})+\int\mathrm{d}^d\mathbf{q}\;h^*(\mathbf{q})\delta\phi(\mathbf{q}))\right)\\&=\det(2\pi\mathbf{G})^{1/2}e^{-\beta\mathcal{H}_0}\exp\left(\frac{1}{2}\int^d\mathrm{d}\mathbf{q}\;\frac{h^*(\mathbf{q})h(\mathbf{q})}{|\mathbf{q}|^2+\xi^{-2}}\right).\end{aligned}\tag{C.49}$$

Thus, within the Gaussian approximation the partition function is fully determined and the free energy follows to be

$$F=-k_BT\log\mathcal{Z}=\mathcal{H}_0-\frac{k_BT}{2}\log\left(\det(2\pi\mathbf{G})\right)-\frac{k_BT}{2}\int\mathrm{d}^d\mathbf{q}\;\frac{h^*(\mathbf{q})h(\mathbf{q})}{|\mathbf{q}|^2+\xi^{-2}}.\tag{C.50}$$

For the logarithm of the functional determinant, the following relation of the matrix determinant holds: $\log\left(\det(2\pi\mathbf{G})\right)=-\log\left(\det\left(\frac{\mathbf{G}^{-1}}{2\pi}\right)\right)=-\mathrm{tr}\log\left(\frac{\mathbf{G}^{-1}}{2\pi}\right)$, which leads to

$$F=\mathcal{H}_0+\frac{k_BT}{2}\int\frac{\mathrm{d}^d\mathbf{q}}{(2\pi)^d}\log(|\mathbf{q}|^2+\xi^{-2})-\frac{k_BT}{2}\int\mathrm{d}^d\mathbf{q}\;\frac{h^*(\mathbf{q})h(\mathbf{q})}{|\mathbf{q}|^2+\xi^{-2}}.\tag{C.51}$$

## C.4 Correlations

We are mainly interested in the excess of the two-point correlation function $\langle\phi(\mathbf{r})\phi(\mathbf{r}')\rangle$ of the OP beyond the trivial, uncorrelated estimate $\langle\phi(\mathbf{r})\rangle^2$, i.e.,

$$\langle\phi(\mathbf{r})\phi(\mathbf{r}')\rangle-\langle\phi(\mathbf{r})\rangle^2=\langle\delta\phi(\mathbf{r})\delta\phi(\mathbf{r}')\rangle.\tag{C.52}$$

In terms of Fourier transformed wavevectors, the excess correlation function is given by

$$\begin{aligned}\langle\delta\phi(\mathbf{r})\delta\phi(\mathbf{r}')\rangle&=\left\langle\int\frac{\mathrm{d}^d\mathbf{q}_1}{\sqrt{2\pi}^d}\,\delta\phi(\mathbf{q}_1)\,e^{i\mathbf{q}_1\cdot\mathbf{r}}\int\frac{\mathrm{d}^d\mathbf{q}_2}{\sqrt{2\pi}^d}\,\delta\phi(\mathbf{q}_2)\,e^{i\mathbf{q}_2\cdot\mathbf{r}'}\right\rangle\\&=\left\langle\int\frac{\mathrm{d}^d\mathbf{q}_1}{\sqrt{2\pi}^d}\int\frac{\mathrm{d}^d\mathbf{q}_2}{\sqrt{2\pi}^d}\,\delta\phi(\mathbf{q}_1)\delta\phi(\mathbf{q}_2)\,e^{i\mathbf{q}_1\cdot\mathbf{r}_{12}}e^{i(\mathbf{q}_1+\mathbf{q}_2)\cdot\mathbf{r}'}\right\rangle\end{aligned}\tag{C.53}$$

with $\mathbf{r}_{12}=\mathbf{r}-\mathbf{r}'$. Translation invariance requires that $\langle\delta\phi(\mathbf{r})\delta\phi(\mathbf{r}')\rangle=\langle\delta\phi(\mathbf{r}_{12})\delta\phi(0)\rangle\;\forall\mathbf{r}'$, from which it follows that

$$\begin{aligned}\langle\delta\phi(\mathbf{r})\delta\phi(\mathbf{r}')\rangle&=\int\frac{\mathrm{d}^d\mathbf{q}_1}{\sqrt{2\pi}^d}\int\frac{\mathrm{d}^d\mathbf{q}_2}{\sqrt{2\pi}^d}\,\langle\delta\phi(\mathbf{q}_1)\delta\phi(\mathbf{q}_2)\rangle\,e^{i\mathbf{q}_1\cdot\mathbf{r}_{12}}\delta(\mathbf{q}_1+\mathbf{q}_2)\\&=\int\frac{\mathrm{d}^d\mathbf{q}}{\sqrt{2\pi}^d}\,\langle\delta\phi(-\mathbf{q})\delta\phi(\mathbf{q})\rangle\,e^{i\mathbf{q}\cdot\mathbf{r}_{12}}.\end{aligned}\tag{C.54}$$

In the case of a constant external field $h$, one can easily calculate the expectation value of the OP from $\langle\phi\rangle = \frac{\partial}{\partial h}\log Z$. Similarly, for a spatially varying field, using functional derivation, this generalizes to $\langle\phi(\mathbf{q})\rangle = \frac{\delta}{\delta h(\mathbf{q})}\log\mathcal{Z} = \frac{h(\mathbf{q})}{|\mathbf{q}|^2+\xi^{-2}}$ and $\langle\phi(-\mathbf{q})\phi(\mathbf{q})\rangle = \frac{\delta^2\log\mathcal{Z}}{\delta h(\mathbf{q})\delta h(-\mathbf{q})} = \frac{1}{|\mathbf{q}|^2+\xi^{-2}}$. Thus, the excess correlation function of the OP is given by the Fourier transform

$$C(\mathbf{r}) = \langle\phi(\mathbf{r})\phi(0)\rangle - \langle\phi(\mathbf{r})\rangle^2 = \int\frac{\mathrm{d}^d\mathbf{q}}{(2\pi)^d}\,\frac{e^{i\mathbf{q}\cdot\mathbf{r}}}{|\mathbf{q}|^2+\xi^{-2}}. \tag{C.55}$$

The actual calculation Eq. (C.55) is complicated by the appropriate Jacobian for the $d$-dimensional integration. One can express the integration in general spherical coordinates for $n$ dimensions using $x_n = \cos(\theta_{n-1})$, $x_{n-1} = \sin(\theta_{n-1})\cos(\theta_{n-2})$, $\ldots$, $x_2 = \sin(\theta_{n-1})\sin(\theta_{n-2})\ldots\sin(\theta_2)\sin(\phi)$ and $x_1 = \sin(\theta_{n-1})\sin(\theta_{n-2})\ldots\sin(\theta_2)\cos(\phi)$, where the naming convention is broken on purpose for $\phi$ instead of $\theta_1$, in reminiscence of the spherical coordinates in $d = 3$. Thus,

$$C(\mathbf{r}) = \int\mathrm{d}q\,q^{d-1}\,\frac{1}{(2\pi)^d}\int_0^{2\pi}\mathrm{d}\phi\int_0^{\pi}\mathrm{d}\theta_2\sin(\theta_2)\cdots\int_0^{\pi}\mathrm{d}\theta_{n-1}\sin^{n-2}(\theta_{n-1})\frac{e^{iq|\mathbf{r}|\cos(\theta_{n-1})}}{q^2+\xi^{-2}}. \tag{C.56}$$

The integrations over $\phi,\theta_2,\ldots,\theta_{n-2}$ can be expressed as $K_d := S_d/\int_0^{\pi}\mathrm{d}\theta_{n-1}\sin^{n-2}(\theta_{n-1})$ where $S_d$ is the surface of the $d$-dimensional sphere (i.e., the integral over all coordinates except the radial coordinate $q$). Since

$$S_d = \frac{2\,\pi^{d/2}}{\Gamma\left(\frac{d}{2}\right)} \quad\text{and}\quad \int_0^{\pi}\mathrm{d}\theta_{n-1}\sin^{n-2}(\theta_{n-1}) = \frac{\sqrt{\pi}\,\Gamma\left(\frac{d-1}{2}\right)}{\Gamma\left(\frac{d}{2}\right)} \Rightarrow K_d = \frac{2\,\pi^{(d-1)/2}}{\Gamma\left(\frac{d-1}{2}\right)}. \tag{C.57}$$

Substitution $z = q|\mathbf{r}|$ yields

$$\begin{aligned} C(\mathbf{r}) &= \frac{K_d}{(2\pi)^d}\int\frac{\mathrm{d}z}{r}\,\frac{z^{d-1}}{r^{d-1}}\int_0^{\pi}\mathrm{d}\theta_{n-1}\sin^{n-2}(\theta_{n-1})\frac{e^{iz\cos(\theta_{n-1})}}{z^2/r^2+\xi^{-2}} \\ &= \frac{K_d}{(2\pi)^d}\,r^{-(d-2)}\int\mathrm{d}z\,z^{d-1}\int_0^{\pi}\mathrm{d}\theta_{n-1}\sin^{n-2}(\theta_{n-1})\frac{e^{iz\cos(\theta_{n-1})}}{z^2+\eta^2} \quad \text{with } \eta = r/\xi \\ &= \frac{K_d}{(2\pi)^d}\,r^{-(d-2)}\int\mathrm{d}z\,z^{d-1}\,\frac{\sqrt{\pi}J_{\frac{d-2}{2}}(z)\Gamma\left(\frac{d-1}{2}\right)}{\left(\frac{z}{2}\right)^{\frac{d}{2}-1}(z^2+\eta^2)}, \end{aligned} \tag{C.58}$$

with the Bessel function of the first kind $J$ and the Gamma function $\Gamma$,

$$\begin{aligned} C(\mathbf{r}) &= \frac{1}{(2\pi)^{d/2}}\,r^{-(d-2)}\int\mathrm{d}z\,z^{d/2}\,\frac{J_{\frac{d}{2}-1}(z)}{(z^2+\eta^2)} \\ &= \frac{1}{(2\pi)^{d/2}}\,r^{-(d-2)}\,\eta^{\frac{d}{2}-1}\,K_{\frac{d}{2}-1}(\eta) \\ &= \frac{1}{(2\pi)^{d/2}}\,\xi^{1-\frac{d}{2}}\,r^{1-\frac{d}{2}}\,K_{\frac{d}{2}-1}(\eta), \end{aligned} \tag{C.59}$$

where $K$ is the modified Bessel function of the second kind.

Naturally, $d = 3$ is an especially relevant case, for which one obtains simply

$$C(\mathbf{r}) = \frac{1}{4\pi} \frac{e^{-r/\xi}}{r}. \tag{C.60}$$

In general dimensions, it is insightful to consider two limits of the analytic Bessel functions: $\eta = r/\xi \ll 1$ (approaching the critical point) and $\eta = r/\xi \gg 1$ (far away from the critical point). In these two cases, one finds the limiting behaviors

$$C(\mathbf{r}) = \begin{cases} \dfrac{\Gamma\left(\frac{d}{2}-1\right)}{4\,\pi^{d/2}}\, r^{-(d-2)} & r/\xi \ll 1, \\ \dfrac{\xi^{2-d}}{2\,(2\pi)^{\frac{d-1}{2}}}\, \frac{e^{-r/\xi}}{(r/\xi)^{\frac{d-2}{2}}} & r/\xi \gg 1 \end{cases} \tag{C.61}$$

Evidently, the purely mathematical substitution of $\xi$ finally attains a physical relevance as the length on which the correlation between two points decays for large distances. Therefore, $\xi$ is called the correlation length. This role can be formally defined via

$$\xi := -\lim_{r\to\infty} \frac{r}{\log C(r)}. \tag{C.62}$$

Applied to either Eq. (C.59) or Eq. (C.61), the limit exists for all dimensions $d > 2$. For $d = 2$, one finds the peculiar result

$$C(\mathbf{r}) = \frac{1}{2\pi} K_0(r/\xi) \sim \log(r/\xi) \text{ for } \xi \to \infty. \tag{C.63}$$

Close to the critical point (i.e., for $\xi \to \infty$), $C(r)$ diverges for large $r$ with a leading order of $\log(r)$, in contrast to the algebraic decay $r^{-(d-2)}$ for $d > 2$. The divergence of the two-point correlation for large distances in $d \leq 2$ is understood to indicate that the fluctuation are not localized around an equilibrium value, but instead lead to non-localized waves traveling through the system. These so-called Goldstone modes occur in any system exhibiting spontaneous breakdown of continuous symmetries. Furthermore, the Mermin-Wagner theorem states that continuous symmetries cannot be spontaneously broken in systems with short-range interactions for dimensions $d \leq d_{\mathrm{lc}} = 2$ smaller than the lower critical dimension $d_{\mathrm{lc}}$, as the hypothetical ordered phase would be destroyed by such Goldstone modes. Note that the lattice Ising model has only discrete symmetry and thus still features a phase transition in $d = 2$, with the lower critical dimension being $d_{\mathrm{lc}} = 1$.

## C.5 Linear response and stress tensor

Let us consider a practical example of the saddle-point or mean field approximation $\partial\mathcal{H}[\phi]/\partial\phi|_{\phi=\langle\phi\rangle} = 0$ using Eq. (C.35) for $\mathcal{H}[\phi]$. The associated Euler-Lagrange equation (ELE) for the mean field profile $\phi_0$ in the case of vanishing bulk field $h(\mathbf{r}) = 0$ is found to be

$$\left.\frac{\delta\mathcal{H}[\phi(\mathbf{r})]}{\delta\phi(\mathbf{r})}\right|_{\phi=\phi_0} = \left(\tau\,\phi(\mathbf{r}) + \frac{u}{6}\,\phi(\mathbf{r})^3\right) - \nabla\cdot\nabla\phi(\mathbf{r}) = 0. \tag{C.64}$$

In the saddle-point approximation, the integral over all configuration in the partition function is approximated by

$$\mathcal{Z} = \int\mathcal{D}\phi\;\exp(-\beta\mathcal{H}[\phi(\mathbf{r})]) \approx \exp(\beta\mathcal{H}[\phi_0]). \tag{C.65}$$

For simplicity, we assume that the profile is inhomogeneous only in $z$ direction and invariant in the other directions, so that the ELE simplifies to

$$\phi_0''(z) = \tau\,\phi_0(z) + \frac{u}{6}\,\phi_0^3(z). \tag{C.66}$$

Evidently, the bulk solution with $\phi_0''(z) = 0$ is $\phi_b = \pm\sqrt{\frac{6}{u}\,(-\tau)}$ for $\tau < 0$. These solutions represent the two phases below the critical point. One may imagine a particular inhomogeneous solution that features two coexisting phases, such that $\phi_0(z \to -\infty) = -\sqrt{\frac{6}{u}\,(-\tau)}$ and $\phi_0(z \to \infty) = \sqrt{\frac{6}{u}\,(-\tau)}$, which translates into boundary conditions for the differential equation Eq. (C.66).

A well educated guess is given by the ansatz $\phi_0(z) = A\,\tanh\left(\frac{z}{2\,\xi}\right)$. Note that both $A$ and $\xi$ are, at this stage, undetermined coefficients. The differential equation is solved for $A = \sqrt{\frac{6}{u}\,(-\tau)}$ and $\xi = (-2\tau)^{-1/2}$.

This result requires some interpretation: $\phi_0(z) \sim \tanh(z/(2\,\xi))$ is an equilibrium profile obtained in saddle-point approximation, without accounting for fluctuation at all. Other than the choice of the symbol $\xi$, there is no immediate link to perturbations in any of the parameters. Still, we identify the same result as for the correlation length $\xi = (-2\tau)^{-1/2}$ found in Gaussian approximation (see Eqs. (C.39) and section C.4). One may come to the realization that it is impossible to have an equilibrium interface profile that varies on a smaller scale than the critical fluctuations; such a profile would be distorted immediately by the fluctuations. Any equilibrium profile must leave "room" for the fluctuation and can only vary on the scale of the correlation length $\xi$ of the fluctuations.

This is a fundamental consequence of the fluctuation-response theorem, which states that the equilibrium response to a small external force behaves like the dynamics of spontaneous fluctuations. Mean field theory does not capture fluctuation in the bulk. However, critical Casimir forces, as an instance of a fluctuation-induced force, occur only if the fluctuating fluid is confined between surfaces close together. At the same time, the surfaces represent boundary conditions leading to non-homogeneous equilibrium profiles, which can be obtained in MFT. The small fluctuations of the solvent adhere to the same boundary conditions as the equilibrium profile.

For a bounded system, the Hamiltonian Eq. (C.35) is amended by a surface term of the general form

$$\mathcal{H}_s = \int_{\partial V} \mathrm{d}^{(d-1)}\mathbf{s}\ \left[\frac{c}{2}(\phi(\mathbf{s}))^2 - h_s\phi(\mathbf{s})\right]. \tag{C.67}$$

Applying the saddle-point approximation, one obtains from this

$$\begin{aligned}\frac{\delta\mathcal{H}}{\delta\phi(\mathbf{r}')} &= \int_V \mathrm{d}^d\mathbf{r}\ (\nabla\phi(\mathbf{r}))\cdot\Bigg(\overbrace{\frac{\delta}{\delta\phi(\mathbf{r})}\nabla\phi(\mathbf{r})}^{=\nabla\frac{\delta\phi(\mathbf{r})}{\delta\phi(\mathbf{r}')}}\Bigg) \\ &+ \int_V \mathrm{d}^d\mathbf{r}\ \left[\tau\,\phi(\mathbf{r}) + \frac{u}{6}\,\phi(\mathbf{r})^3 - h(\mathbf{r})\right]\frac{\delta\phi(\mathbf{r})}{\delta\phi(\mathbf{r}')} + \int_{\partial V}\mathrm{d}^{(d-1)}\mathbf{s}\ [c\phi(\mathbf{s}) - h_s]\,\frac{\delta\phi(\mathbf{s})}{\delta\phi(\mathbf{r}')} \overset{!}{=} 0\end{aligned} \tag{C.68}$$

Gauss's theorem can be applied to the first term, yielding

$$\int_V \mathrm{d}^d\mathbf{r}\ (\nabla\phi(\mathbf{r}))\cdot\nabla\frac{\delta\phi(\mathbf{r})}{\delta\phi(\mathbf{r}')} = -\int_V \mathrm{d}^d\mathbf{r}\,(\nabla\cdot\nabla\phi(\mathbf{r}))\,\frac{\delta\phi(\mathbf{r})}{\delta\phi(\mathbf{r}')} + \int_{\partial V}\mathrm{d}^{(d-1)}\mathbf{s}\ (\nabla\phi(\mathbf{s})\cdot\mathbf{n})\,\frac{\delta\phi(\mathbf{s})}{\delta\phi(\mathbf{r}')}, \tag{C.69}$$

so that we need to solve

$$\begin{aligned}&\int_V \mathrm{d}^d\mathbf{r}\ \left[\tau\,\phi(\mathbf{r}) + \frac{u}{6}\,\phi(\mathbf{r})^3 - h(\mathbf{r}) - \nabla^2\phi(\mathbf{r})\right]\frac{\delta\phi(\mathbf{r})}{\delta\phi(\mathbf{r}')} \\ &+ \int_{\partial V}\mathrm{d}^{(d-1)}\mathbf{s}\ [(\nabla\phi(\mathbf{s})\cdot\mathbf{n}) + c\phi(\mathbf{s}) - h_s]\,\frac{\delta\phi(\mathbf{s})}{\delta\phi(\mathbf{r}')} \overset{!}{=} 0.\end{aligned} \tag{C.70}$$

Since $\frac{\delta\phi(\mathbf{r})}{\delta\phi(\mathbf{r}')} = \delta(\mathbf{r}-\mathbf{r}')$, and a point $\mathbf{r}$ is either within the Volume $V$ or on its surface $\partial V$, but not both, one ends with two equations that need to be solved simultaneously:

$$\tau\,\phi(\mathbf{r}) + \frac{u}{6}\,\phi(\mathbf{r})^3 - h(\mathbf{r}) - \nabla^2\phi(\mathbf{r}) = 0, \qquad \text{for } \mathbf{r}\in V, \tag{C.71}$$

$$\nabla\phi(\mathbf{s})\cdot\mathbf{n} + c\phi(\mathbf{s}) - h_s = 0, \qquad \text{for } \mathbf{s}\in\partial V. \tag{C.72}$$

The first equation is simply the Euler-Lagrange equation of the bulk case. The second equation is a Robin boundary condition to the differential equation. Notably, in the case of $c = 0$, it amounts to a von-Neumann boundary condition $\nabla\phi(\mathbf{s})\cdot\mathbf{n} = h_s$, whereas for $c\to\infty$, but with $\lim\limits_{c\to\infty} h_s/c \neq 0$, it represents a Dirichlet boundary condition $\phi(\mathbf{s}) = h_s/c$.

Within this thesis, we have obtained equilibrium OP profiles by solving this differential equation numerically using a finite-element method [101]. Another consequence of the confinement is the fact that, for a fixed configuration, the system is under stress, which is compensated by constraint forces. A virtual displacement $\mathbf{r}\to\mathbf{r}+\boldsymbol{\epsilon}(\mathbf{r})$ of the system (i.e., a coordinate transform) creates a virtual work $\delta\mathcal{H}$. Then, the stress tensor $T_{ij}$ is defined by the linear response relation

$$\delta\mathcal{H} = \int_V \mathrm{d}^d\mathbf{r}\,\frac{\partial\epsilon_i}{\partial x_j}\,T_{ij}, \tag{C.73}$$

where $\epsilon_i$ is the $i$-th component of $\epsilon_i$. The components of the stress tensor can be expressed in terms of the Lagrangian $\mathcal{L}$, which is the integrand of the Hamiltonian, i.e., $\mathcal{H}[\phi(\mathbf{r})] = \int_V \mathrm{d}^d\mathbf{r}\,\mathcal{L}(\phi(\mathbf{r}), \nabla\phi(\mathbf{r}))$, by performing explicitly the variation

$$\delta\mathcal{H} = \int_V \mathrm{d}^d\mathbf{r}\,\delta\mathcal{L}(\phi(\mathbf{r}), \partial_j\phi(\mathbf{r})) = \int_V \mathrm{d}^d\mathbf{r}\,\left(\frac{\partial\mathcal{L}}{\partial\phi}\delta\phi + \frac{\partial\mathcal{L}}{\partial(\partial_j\phi)}\delta\partial_j\phi\right), \tag{C.74}$$

where the OP $\phi$ and its derivative are treated as individual variables with the variations $\delta\phi(\mathbf{r}) = \epsilon_i\partial_i\phi(\mathbf{r})$ and $\delta\partial_j\phi(\mathbf{r}) = \epsilon_i\partial_j\partial_i\phi(\mathbf{r}) + (\partial_j\epsilon_i)\partial_i\phi(\mathbf{r})$. Substituting these into Eq. (C.74) and performing a partial integration yields Eq. (C.73) with the stress tensor being

$$T_{ij} = \frac{\partial\mathcal{L}}{\partial(\partial_j\phi)}\partial_i\phi - \delta_{ij}\mathcal{L}. \tag{C.75}$$

Suppose one chooses the particular coordinate transform with $\epsilon_z(\mathbf{r}) = \alpha$ for $\mathbf{r} \in V_s$ in a subvolume $V_s$, but $\epsilon_z(\mathbf{r}) = 0$ outside, and $\epsilon_i = 0$ for $i \neq z$. Then $\epsilon_z = \alpha\mathbf{1}_{V_s}$ is proportional to the the indicator $\mathbf{1}_{V_s}$ of the subvolume, and the derivative $\frac{\partial}{\partial x_i}\frac{\partial\epsilon_i}{\partial\alpha} = \frac{\partial\mathbf{1}_{V_s}}{\partial z}$ of the indicator represents a surface delta function, so that the force acting on that subvolume in z-direction is given by

$$F_z = -\frac{\partial\mathcal{H}}{\partial\alpha} = -\frac{\partial}{\partial\alpha}\int_V \mathrm{d}^d\mathbf{r}\,\frac{\partial\epsilon_i}{\partial x_j}\,T_{ij} = -\int_{\partial V_s} \mathrm{d}^{(d-1)}s\,T_{zj}n_j, \tag{C.76}$$

where $n_j$ is the $j$-th component of the outwards surface normal $\mathbf{n}$. With a view on continuum mechanics, the force acting on a volume of liquid is also acting on an enclosed particle. Thus, we can numerically calculate the critical Casimir force as the singular contribution to the force, after numerically minimizing the Hamiltonian using a finite element method, and evaluating the stress tensor on a conveniently chosen (virtual) surface enclosing a particle.

This way, we obtain numerically the equilibrium OP profile of a static, confined geometry, and concomitantly we can calculate the force corresponding to a small displacement of the walls within linear-response. The critical Casimir force is the singular and dominant contribution to the force at $T \to T_c$.

## C.6 Renormalization group theory

Renormalization group (RG) theory is a collective term for a number of powerful and complex methods for the calculation of critical exponents beyond MFT and Gaussian approximation [194, 195]. They may differ in details and their usage, but share a general idea. Conceptually, the basic steps of RG theory are

1. **Course-graining** or **Elimination:** This step can be done in various fashions that follow the same fundamental idea, but can lead to quite different mathematical procedures in practice. In principle, one reduces the number of degrees of freedom, for example, by grouping spins into blocks and averaging them to a single block-spin value, or by assigning to the block the majority value of its spin. Instead of working with the lattice in real-space, it is also possible to apply the renormalization group theory in momentum-space. In any case, one generates an iterative step that leads to an effective Hamiltonian $\mathcal{H}[\phi] \to \mathcal{H}'\left[\,\overline{\phi}\,\right]$ for the course-grained lattice, which possesses a larger lattice spacing and substituted coefficients.

2. **Rescaling:** The new lattice is then rescaled by a factor $b$ to match the lattice size of the original, so that the new coordinates are given by $\mathbf{r}' = \mathbf{r}/b$.

3. **Renormalizing**: The rescaling affects also the scale of the variations in the order parameter, i.e., the gradient term, which is remedied by normalizing the amplitude $\phi'_{\mathbf{r}'} = \overline{\phi}_{\mathbf{r}'}/\lambda$.

Since the partition function sums up all configurations for the order parameter $\phi$, and none of the above steps produces a new configuration $\phi'$ that was not possible before (even if it was an unlikely one), the partition function is preserved

$$\mathcal{Z} = \int \mathcal{D}\phi \;\exp(-\beta\mathcal{H}[\phi(\mathbf{r})]) = \int \mathcal{D}\phi' \;\exp(-\beta\mathcal{H}'[\phi'(\mathbf{r}')]). \tag{C.77}$$

It is assumed that the Hamiltonian $\mathcal{H}$ does not change its functional form after a RG step, although the values of the coefficients change. Of course, this is an excessive assumption and actually performing the RG iteration will generate additional, higher order terms. Thus, this is an approximation leading to effective coefficients.

However, we gain a new perspective on the problem. The coefficients of the Hamiltonian may be collected into a vector $\mathbf{H}$, and the RG iteration written as $\mathbf{H}_{n+1} = \mathbf{R}\,\mathbf{H}_n$, where $\mathbf{R}$ is an (non-linear) operator. Such an iteration may have fixed points (eigenvectors in the linear case), for which $\mathbf{H} = \mathbf{R}\,\mathbf{H}$. Now, for the Ising model and the Ginzburg-Landau Hamiltonian, three such fixed points exist, all with physical relevance: for the so-called high-temperature fixed point, the parameter associated with temperature $T$ behaves as if $T \to \infty$. For the Ising model, $J/k_BT \to 0$ and the spins become uncorrelated. Thus, at the high-temperature fixed point, the system is completely random so that scaling and renormalization will not make it any more or less random. At the low-temperature fixed-point, corresponding to $T \to 0$, the system attains an ordered ground state that does not change under RG. For example, if all Ising spins are aligned, course-graining or elimination of spins will not alter the overall orientation. The third fixed point is the subject of our scientific fetish.

One can conclude another property from this perspective on the RG. The vector **H** spans a parameter space of Hamiltonians. RG iterations result in trajectories through this parameter space. Thus, the fixed-points can in principle be of three types: attractive (all trajectories in the vicinity are moving into the fixed-point), repulsive (all trajectories in the vicinity move away) or mixed (some directions are attractive, others are repulsive). One observes that, starting a bit off the critical temperature and applying the RG, one moves either to the high-temperature or the low-temperature fixed point, which are therefore attractive. The critical point itself is a mixed fixed point.

In a similar spirit, let us analyze the dimensions of the coefficients in the Hamiltonian

$$\beta\mathcal{H} = \int_V \mathrm{d}^d\mathbf{r}\, \frac{s}{2}\,(\nabla\phi)^2 + \frac{\tau}{2}\,\phi^2 + \frac{u}{4!}\,\phi^4 \tag{C.78}$$

in units of a microscopic length $a$, e.g., the lattice spacing constant, or similarly a microscopic interaction range. Certainly, the result of the integration must be dimensionless and the integration itself corresponds to a factor $\sim a^d$. Suppose the order parameter $\phi$ has dimension $a^{-z}$, where $z \in \mathbb{Z}$, which will be determined in a moment. Analogously, let $\tau \sim a^{-y}$ and $u \sim a^{-x}$, with $x, y \in \mathbb{Z}$. From the three independent terms, we obtain three equations for the dimensional exponents. Thus, the fourth factor $s$ is undetermined and can be chosen freely. It is convenient to absorb it into $\phi$ and set $s = 1$. In order to obtain the correct physical dimensions, it is required that

1. $a^d \cdot (\nabla\phi)^2 \sim a^d \cdot (a^{-z-1})^2 \sim a^{d-2z-2} \overset{!}{=} 1 \Rightarrow z = \frac{d-2}{2}$,
2. $a^d \cdot \frac{\tau}{2}\,\phi^2 \sim a^{d-y-2z} \overset{!}{=} 1 \Rightarrow y = 2$,
3. $a^d \cdot \frac{u}{4!}\,\phi^4 \sim a^{d-x-4z} \overset{!}{=} 1 \Rightarrow x = 4 - d$.

In an RG step, the microscopic length $a$ is rescaled by a factor $b > 0$, giving the new length $a' = a/b$. Exactly at the critical point, the rescaling can be performed an arbitrary large number of times without changing the physics of the system, due to the self-similarity of the order parameter profile (scale-invariance). Thus, the corresponding length $a_n = a/b^n$ after step $n$ is expected to vanish with $n \to \infty$. Since $u \sim a^{-(4-d)}$, the parameter $u_n \sim a_n^{-(4-d)} \sim b^{n(4-d)}u$ reveals an interesting dependence on the spatial dimension $d$: For $d > 4$ and any value of $u$, after many RG steps, the parameter $u_n$ will become vanishingly small. On the other hand, for $d < 4$, no matter how small the initial value of $u$ was, $u_n$ increases without bounds. This has consequences for the Gaussian approximation, which relies on neglecting the quartic term and takes into account only the quadratic terms.

This is formally described by the Ginzburg criterion

$$\frac{\int_{V_\xi} \mathrm{d}^d\mathbf{r}\, \langle\phi(\mathbf{r})\phi(0)\rangle - \langle\phi(\mathbf{r})\rangle^2}{\int_{V_\xi} \mathrm{d}^d\mathbf{r}\, \langle\phi(\mathbf{r})\rangle^2} \ll 1 \tag{C.79}$$

which represents the relative strength of the fluctuations compared to the mean value of the order parameter. For this comparison, one integrates the fluctuations over at least a cube of size $V_\xi = \xi^d$ over which the fluctuations are correlated. Since we evaluate the fluctuations using the Gaussian approximation, whereas the mean value is aptly obtained from mean field theory, the Ginzburg criterion also indicates whether the Gaussian approximation is a small correction to the mean field result. In that sense, it announces the breakdown of the Gaussian approximation if that assumption is no longer valid.

The Ginzburg criterion evaluates to

$$\frac{\int_{V_\xi} \mathrm{d}^d\mathbf{r}\, \langle\phi(\mathbf{r})\phi(0)\rangle - \langle\phi(\mathbf{r})\rangle^2}{\int_{V_\xi} \mathrm{d}^d\mathbf{r}\, \langle\phi(\mathbf{r})\rangle^2} = \frac{\int_{V_\xi} \mathrm{d}^d\mathbf{r}\, C(\mathbf{r})}{\xi^d \cdot \sqrt{\frac{6}{u}(-\tau)}^{\,2}} \tag{C.80}$$

using $\xi = 1/\sqrt{-2\tau}$ and Eq. (C.59), we arrive at

$$\frac{\int_{V_\xi} \mathrm{d}^d\mathbf{r}\, \langle\phi(\mathbf{r})\phi(0)\rangle - \langle\phi(\mathbf{r})\rangle^2}{\int_{V_\xi} \mathrm{d}^d\mathbf{r}\, \langle\phi(\mathbf{r})\rangle^2} = c(d)\,\frac{u}{3}\,\xi^{4-d}, \tag{C.81}$$

where $c(d)$ is a positive, numeric factor depending on the number of spatial dimensions $d$. For $d > 4$, the relative strength of the fluctuations becomes arbitrary small close to $T_c$ as $\xi \to \infty$ and thus the quadratic approximation is valid. For $d < 4$, fluctuations are only negligible not too close criticality, when $\xi \ll 1$; otherwise the $\phi^4$ term becomes the dominant contribution.

In conclusion, for the bulk situation mean field theory is valid above the upper critical dimension $d_{uc}$, whereas in lower dimensions, e.g., $d = 3$, fluctuations start to become important. Below the lower critical dimension $d_{\mathrm{lc}}$, phase transitions are completely destroyed.

# Bibliography

[1] E. W. Lemmon, M. O. McLinden, and D. G. Friend, "Thermophysical Properties of Fluid Systems" in *NIST Chemistry WebBook, NIST Standard Reference Database Number 69*, edited by P. J. Linstrom and W. G. Mallard (National Institute of Standards and Technology, Gaithersburg, MD) (retrieved Nov. 2017 at http://webbook.nist.gov/chemistry/fluid).

[2] T. Andrews, Phil. Trans. Roy. Soc. London **159**, 575 (1869).

[3] M. v. Smoluchowski, Ann. Phys. **330**, 205 (1908).

[4] A. Einstein, Ann. Phys. **338**, 1275 (1910).

[5] L. Landau, Zh. Eksp. Teor. Fiz **7**, 19 (1937), reprinted and translated into English in Ukr. J. Phys. **53**, Special Issue, 25 (2008).

[6] T. Graham, Phil. Trans. Roy. Soc. London **151**, 183 (1861).

[7] International Union of Pure and Applied Chemistry, *Manual of Symbols and Terminology for Physicochemical Quantities and Units, Appendix II: Definitions, Terminology and Symbols in Colloid and Surface Chemistry*, published in Pure Appl. Chem. **31**, 577 (1972).

[8] H. N. W. Lekkerkerker and R. Tuinier, *Colloids and the Depletion Interaction*, *Lecture Notes in Physics*, vol. 833 (Springer, Heidelberg, 2011).

[9] W. B. Russel, D. A. Saville, and W. R. Schowalter, *Colloidal Dispersions* (Cambridge University Press, Cambridge, 1989).

[10] R. J. Hunter, *Foundations of Colloid Science* (Clarendon Press, Oxford, 1989).

[11] J. Israelachvili, *Intermolecular and Surface Forces, 2nd ed.*, (Academic, New York, 1992).

[12] S. Asakura and F. Oosawa, J. Chem. Phys. **22**, 1255 (1954).

[13] H. G. B. Casimir, Proc. K. Ned. Akad. Wet. **51**, 793 (1948).

[14] S. K. Lamoreaux, Phys. Rev. Lett. **78**, 5 (1997); ibid. **81**, 5475 (1998).

[15] M. E. Fisher and P. G. de Gennes, C. R. Acad. Sci., Paris, Ser. B **287**, 207 (1978).

[16] M. Fukuto, Y. F. Yano, and P. S. Pershan, Phys. Rev. Lett. **94**, 135702 (2005).

[17] S. Rafai, D. Bonn, and J. Meunier, Physica A **386**, 31 (2007).

[18] R. Garcia and M. H. W. Chan, Phys. Rev. Lett. **88**, 086101 (2002).

[19] T. Ueno, S. Balibar, T. Mizusaki, F. Caupin, and E. Rolley, Phys. Rev. Lett. **90**, 116102 (2003).

[20] R. Garcia and M. H. W. Chan, Phys. Rev. Lett. **83**, 1187 (1999).

[21] A. Ganshin, S. Scheidemantel, R. Garcia, and M. H. W. Chan, Phys. Rev. Lett. **97**, 075301 (2006).

[22] A. Hucht, Phys. Rev. Lett. **99**, 185301 (2007).

[23] O. Vasilyev, A. Gambassi, A. Maciołek, and S. Dietrich, EPL **80**, 60009 (2007).

[24] O. Vasilyev, A. Gambassi, A. Maciołek, and S. Dietrich, Phys. Rev. E **79**, 041142 (2009); ibid. **80**, 039902(E) (2009).

[25] M. Hasenbusch, J. Stat. Mech. **2009**, P07031 (2009).

[26] M. Hasenbusch, Phys. Rev. B **82**, 174434 (2010).

[27] M. Hasenbusch, Phys. Rev. B **82**, 104425 (2010).

[28] C. Hertlein, L. Helden, A. Gambassi, S. Dietrich, and C. Bechinger, Nature **451**, 172 (2008).

[29] A. Gambassi, A. Maciołek, C. Hertlein, U. Nellen, L. Helden, C. Bechinger, and S. Dietrich, Phys. Rev. E **80**, 061143 (2009).

[30] F. Pousaneh, A. Ciach, and A. Maciołek, Soft Matter **8**, 7567 (2012).

[31] B. Derjaguin, Kolloid Z. **69**, 155 (1934).

[32] M. Hasenbusch, Phys. Rev. E **87**, 022130 (2013).

[33] T. W. Burkhardt and E. Eisenriegler, Phys. Rev. Lett. **74**, 3189 (1995); ibid. **78**, 2867 (1997).

[34] E. Eisenriegler and U. Ritschel, Phys. Rev. B **51**, 13717 (1995).

[35] A. Hanke, F. Schlesener, E. Eisenriegler, and S. Dietrich, Phys. Rev. Lett. **81**, 1885 (1998).

[36] F. Schlesener, A. Hanke, and S. Dietrich, J. Stat. Phys. **110**, 981 (2003).

[37] E. Eisenriegler, J. Chem. Phys. **121**, 3299 (2004).

[38] P. A. Kralchevsky and N. D. Denkov, Curr. Opin. Colloid Interface Sci. **6**, 383 (2001).

[39] R. Evans, U. M. B. Marconi, and P. Tarazona, J. Chem. Soc., Faraday Transactions 2: Mol. and Chem. Phys. **82**, 1763 (1986).

[40] H. K. Christenson, J. Colloid and Interf. Sci. **104**, 234 (1985).

[41] R. Okamoto and A. Onuki, Phys. Rev. E **88**, 022309 (2013).

[42] S. Yabunaka, R. Okamoto, and A. Onuki, Soft Matter **11**, 5738 (2015).

[43] C. Bauer, T. Bieker, and S. Dietrich, Phys. Rev. E **62**, 5324 (2000).

[44] A. Malijevský, Mol. Phys. **113**, 1170 (2015).

[45] A. Malijevský and A. O. Parry, Phys. Rev. E **92**, 022407 (2015).

[46] O. A. Vasilyev, Phys. Rev. E **90**, 012138 (2014).

[47] O. Vasilyev, S. Kondrat, and S. Dietrich, "Nonadditive Interactions and Phase Transitions in Strongly Confined Colloidal Systems", unpublished (2017).

[48] B. Chacko, R. Evans, and A. J. Archer, J. Chem. Phys. **146**, 124703 (2017).

[49] D. Beysens and D. Estève, Phys. Rev. Lett. **54**, 2123 (1985).

[50] P. D. Gallagher and J. V. Maher, Phys. Rev. A **46**, 2012 (1992); P. D. Gallagher, M. L. Kurnaz, and J. V. Maher, Phys. Rev. A **46**, 7750 (1992).

[51] T. Narayanan, A. Kumar, E. S. R. Gopal, D. Beysens, P. Guenoun, and G. Zalczer, Phys. Rev. E **48**, 1989 (1993).

[52] B. M. Law, J.-M. Petit, and D. Beysens, Phys. Rev. E **57**, 5782 (1998).

[53] D. Beysens, J.-M. Petit, T. Narayanan, A. Kumar, and M. L. Broide, Ber. Bunsenges. Phys. Chem. **98**, 382 (1994).

[54] D. Beysens and T. Narayanan, J. Stat. Phys. **95**, 997 (1999).

[55] P. G. de Gennes, Rev. Mod. Phys. **64**, 645 (1992).

[56] Q. Chen, S. C. Bae, and S. Granick, Nature **469**, 381 (2011).

[57] F. Romano and F. Sciortino, Soft Matter **7**, 5799 (2011).

[58] S. N. Fejer and D. J. Wales, Soft Matter **11**, 6663 (2015).

[59] A. B. Pawar and I. Kretzschmar, Macromol. Rapid Commun. **31**, 150 (2010).

[60] E. Bianchi, R. Blaak, and C. N. Likos, Phys. Chem. Chem. Phys. **13**, 6397 (2011).

[61] N. Prasad, J. Perumal, C.-H. Choi, C.-S. Lee, and D.-P. Kim, Adv. Funct. Mater. **19**, 1656 (2009).

[62] A. Walther, M. Drechsler, S. Rosenfeldt, L. Harnau, M. Ballauff, V. Abetz, and A. H. E. Müller, J. Am. Chem. Soc. **131**, 4720 (2009).

[63] G.-R. Yi, D. J. Pine, and S. Sacanna, J. Phys.: Condens. Matter **25**, 193101 (2013).

[64] J. Zhang, E. Luijten, and S. Granick, Ann. Rev. of Phys. Chem. **66**, 581 (2015).

[65] C. Yu, J. Zhang, and S. Granick, Angew. Chem. Int. Ed. **53**, 4364 (2014).

[66] L. Hong, A. Cacciuto, E. Luijten, and S. Granick, Nano Lett. **6**, 2510 (2006).

[67] E. Bianchi, G. Kahl, and C. N. Likos, Soft Matter **7**, 8313 (2011).

[68] F. Soyka, O. Zvyagolskaya, C. Hertlein, L. Helden, and C. Bechinger, Phys. Rev. Lett. **101**, 208301 (2008).

[69] M. Tröndle, O. Zvyagolskaya, A. Gambassi, D. Vogt, L. Harnau, C. Bechinger, and S. Dietrich, Mol. Phys. **109**, 1169 (2011).

[70] M. Tröndle, S. Kondrat, A. Gambassi, L. Harnau, and S. Dietrich, EPL **88**, 40004 (2009).

[71] Y. Iwashita and Y. Kimura, Soft Matter **9**, 10694 (2013).

[72] Y. Iwashita and Y. Kimura, Soft Matter **10**, 7170 (2014).

[73] T. F. Mohry, A. Maciołek, and S. Dietrich, Phys. Rev. E **81**, 061117 (2010).

[74] M. Labbé-Laurent, M. Tröndle, L. Harnau, and S. Dietrich, Soft Matter **10**, 2270 (2014).

[75] M. Labbé-Laurent and S. Dietrich, Soft Matter **12**, 6621 (2016).

[76] S. G. Stuij, M. Labbé-Laurent, T. E. Kodger, A. Maciołek, and P. Schall, Soft Matter **13**, 5233 (2017).

[77] M. Labbé-Laurent, A. D. Law, and S. Dietrich, J. Chem. Phys **147**, 104701 (2017).

[78] J.-P. Hansen and I. R. McDonald, *Theory of Simple Liquids* (Academic, London, 1986).

[79] J. J. Binney, N. J. Dowrick, A. J. Fisher, and M. E. J. Newman, *The Theory of Critical Phenomena: An introduction to the renormalization group* (Clarendon Press, Oxford, 1992).

[80] B. Widom, J. Chem. Phys. **43**, 3898 (1965).

[81] M. Krech, *The Casimir Effect in Critical Systems* (World Scientific, Singapore, 1994).

[82] A. Pelissetto and E. Vicari, Phys. Rep. **368**, 549 (2002).

[83] M. Kardar, *Statistical Theory of the Fields* (Cambridge University Press, Cambridge, 2007).

[84] D. Bonn, J. Otwinowski, S. Sacanna, H. Guo, G. Wegdam, and P. Schall, Phys. Rev. Lett. **103**, 156101 (2009); A. Gambassi and S. Dietrich, Phys. Rev. Lett. **105**, 059601 (2010).

[85] H. B. Tarko and M. E. Fisher, Phys. Rev. Lett. **31**, 926 (1973); Phys. Rev. B **11**, 1217 (1975).

[86] K. Binder, in *Phase Transitions and Critical Phenomena*, vol. 8, edited by C. Domb and J. L. Lebowitz (Academic, London, 1983), p. 1.

[87] H. W. Diehl, in *Phase Transitions and Critical Phenomena*, vol. 10, edited by C. Domb and J. L. Lebowitz (Academic, London, 1986), p. 75.

[88] J. M. Brankov, D. M. Danchev, and N. S. Tonchev, *Theory of critical phenomena in finite-size systems* (World Scientific, Singapore, 2000).

[89] A. Gambassi, J. Phys. Conf. Ser. **161**, 012037 (2009).

[90] M. Krech and S. Dietrich, Phys. Rev. Lett. **66**, 345 (1991); Phys. Rev. A **46**, 1886 (1992); ibid. **66**, 1922 (1992).

[91] M. Krech, Phys. Rev. E **56**, 1642 (1997).

[92] T. F. Mohry, A. Maciołek, and S. Dietrich, J. Chem. Phys. **136**, 224902 (2012); ibid. **136**, 224903 (2012).

[93] T. F. Mohry, S. Kondrat, A. Maciołek, and S. Dietrich, Soft Matter **10**, 5510 (2014).

[94] M. Hasenbusch, Phys. Rev. B **85**, 174421 (2012).

[95] O. Vasilyev and S. Dietrich, EPL **104**, 60002 (2014).

[96] O. Vasilyev, Phys. Rev. B **90**, 012138 (2014).

[97] Z. Borjan and P. J. Upton, Phys. Rev. Lett. **101**, 125702 (2008).

[98] R. Okamoto and A. Onuki, J. Chem. Phys. **136**, 114704 (2012).

[99] A. Hanke and S. Dietrich, Phys. Rev. E **59**, 5081 (1999).

[100] S. Kondrat, L. Harnau, and S. Dietrich, J. Chem. Phys. **126**, 174902 (2007).

[101] S. Kondrat, *F3DM - a numerical library for the 3d finite element method* (available online at http://sourceforge.net/projects/f3dm/).

[102] S. Kondrat, L. Harnau, and S. Dietrich, J. Chem. Phys. **131**, 204902 (2009).

[103] M. Tröndle, S. Kondrat, A. Gambassi, L. Harnau, and S. Dietrich, J. Chem. Phys. **133**, 074702 (2010).

[104] D. Dantchev and M. Krech, Phys. Rev. E **69**, 046119 (2004).

[105] C. M. Sorensen and G. A. Larsen, J. Chem. Phys **83**, 1835 (1985).

[106] J. K. Bhattacharjee, R. A. Ferrell, R. S. Basu, and J. V. Sengers, Phys. Rev. A **24**, 1469 (1981).

[107] S. K. Das, J. V. Sengers, and M. E. Fisher, J. Chem. Phys. **127**, 144506 (2007).

[108] H. C. Burstyn, J. V. Sengers, J. K. Bhattacharjee, and R. A. Ferrell, Phys. Rev. A **28**, 1567 (1983).

[109] H. C. Burstyn and J. V. Sengers, Phys. Rev. A **25**, 448 (1982).

[110] K. Kawasaki, in *Phase Transitions and Critical Phenomena*, vol. 5a, edited by C. Domb and M. S. Green (Academic, London, 1976), p. 165.

[111] A. Oleinikova, L. Bulavin, and V. Pipich, Int. J. Thermophys. **20**, 889 (1999).

[112] D. B. Abraham and A. Maciołek, Phys. Rev. Lett. **105**, 055701 (2010).

[113] O. Vasilyev, A. Maciołek, and S. Dietrich, Phys. Rev. E **84**, 041605 (2011).

[114] M. Hasenbusch, Phys. Rev. B **83**, 134425 (2011).

[115] V. D. Nguyen, S. Faber, Z. Hu, G. H. Wegdam, and P. Schall, Nature Commun. **4**, 1584 (2013).

[116] J.-P. Hansen and H. Löwen, Annu. Rev. Phys. Chem. **51**, 209 (2000).

[117] J.-L. Barrat and J.-P. Hansen, *Basic concepts for simple and complex liquids* (Cambridge University Press, Cambridge, 2003).

[118] V. A. Parsegian, *Van der Waals forces* (Cambridge University Press, New York, 2006).

[119] Y. Levin, Rep. Prog. Phys. **65**, 1577 (2002).

[120] G. A. Vliegenthart and H. N. W. Lekkerkerker, J. Chem. Phys. **112**, 5364 (2000).

[121] M. G. Noro and D. Frenkel, J. Chem. Phys. **113**, 2941 (2000).

[122] J. D. Weeks, D. Chandler, and H. C. Andersen, J. Chem. Phys. **54**, 5237 (1971).

[123] R. J. Baxter, J. Chem. Phys. **49**, 2770 (1968).

[124] M. A. Miller and D. Frenkel, Phys. Rev. Lett. **90**, 135702 (2003); M. A. Miller and D. Frenkel, J. Chem. Phys. **121**, 535 (2004).

[125] D. Dantchev and G. Valchev, J. Colloid Interface Sci. **372**, 148 (2012).

[126] M. Sprenger, F. Schlesener, and S. Dietrich, J. Chem. Phys. **124**, 134703 (2006).

[127] M. Labbé-Laurent, Bachelor thesis, Universität Stuttgart (2010).

[128] J. P. Straley, Phys. Rev. A **4**, 675 (1971).

[129] D. Frenkel and R. Eppenga, Phys. Rev. A **31**, 1776 (1985).

[130] F. Parisen Toldin, M. Tröndle, and S. Dietrich, Phys. Rev. E **88**, 052110 (2013).

[131] M. Labbé-Laurent, Master thesis, Universität Stuttgart (2012).

[132] F. Parisen Toldin and S. Dietrich, J. Stat. Mech. **2010**, P11003 (2010).

[133] N. Kern and D. Frenkel, J. Chem. Phys. **118**, 9882 (2003).

[134] F. Sciortino, A. Giacometti, and G. Pastore, Phys. Rev. Lett. **103**, 237801 (2009).

[135] F. Sciortino, A. Giacometti, and G. Pastore, Phys. Chem. Chem. Phys. **12**, 11869 (2010).

[136] A. Giacometti, C. Gögelein, F. Lado, F. Sciortino, S. Ferrari, and G. Pastore, J. Chem. Phys. **140**, 094104 (2014).

[137] H. Shin and K. S. Schweizer, Soft Matter **10**, 262 (2014).

[138] B. D. Marshall, Soft Matter **13**, 6506 (2017).

[139] G. Foffi and F. Sciortino, J. Phys. Chem. B **111**, 9702 (2007).

[140] P. Frodl and S. Dietrich, Phys. Rev. A **45**, 7330 (1992).

[141] B. Groh and S. Dietrich, Phys. Rev. E **50**, 3814 (1994).

[142] B. Groh and S. Dietrich, Phys. Rev. E **55**, 2892 (1997).

[143] A. D. Law, L. Harnau, M. Tröndle, and S. Dietrich, J. Chem. Phys. **141**, 134704 (2014).

[144] M. Krech and S. Dietrich, Phys. Rev. A **46**, 1886 (1992).

[145] V. Privman, P. C. Hohenberg, and A. Aharony, in *Phase Transitions and Critical Phenomena*, vol. 14, edited by C. Domb and J. Lebowitz (Academic, London, 1991), p. 1.

[146] T. Bieker and S. Dietrich, Physica A **252**, 85 (1998).

[147] G. Mason and W. Clark, Chem. Eng. Sci. **20**, 859 (1965).

[148] N. Hijnen and P. S. Clegg, Langmuir **30**, 5763 (2014).

[149] M. Hampton and A. Nguyen, Adv. Colloid Interf. Sci. **154**, 30 (2010).

[150] O. Pitois, P. Moucheront, and X. Chateau, J. Colloid and Interf. Sci. **231**, 26 (2000).

[151] D. N. Mazzone, G. I. Tardos, and R. Pfeffer, J. Colloid and Interf. Sci. **113**, 544 (1986).

[152] C. D. Willett, M. J. Adams, S. A. Johnson, and J. P. Seville, Langmuir **16**, 9396 (2000).

[153] R. A. Fisher, J. Agric. Sci. **16**, 492 (1926).

[154] G. Lian, C. Thornton, and M. J. Adams, J. Colloid and Interf. Sci. **161**, 138 (1993).

[155] P. F. Noble, O. J. Cayre, R. G. Alargova, O. D. Velev, and V. N. Paunov, J. Am. Chem. Soc. **126**, 8092 (2004).

[156] E. P. Lewandowski, P. C. Searson, and K. J. Stebe, J. Phys. Chem. B **110**, 4283 (2006).

[157] E. P. Lewandowski, M. Cavallaro, L. Botto, J. C. Bernate, V. Garbin, and K. J. Stebe, Langmuir **26**, 15142 (2010).

[158] C. W. Shields IV, S. Zhu, Y. Yang, B. Bharti, J. Liu, B. B. Yellen, O. D. Velev, and G. P. Lopez, Soft Matter **9**, 9219 (2013).

[159] D. Jasnow, Rep. Prog. Phys. **47**, 1059 (1983).

[160] K. Binder, Annu. Rev. Mater. Res. **38**, 123 (2008).

[161] V. Privman and M. E. Fisher, J. Stat. Phys. **33**, 385 (1983).

[162] M. P. Gelfand and R. Lipowsky, Phys. Rev. B **36**, 8725 (1987).

[163] D. Wilms, A. Winkler, P. Virnau, and K. Binder, Phys. Rev. Lett. **105**, 045701 (2010); A. Winkler, D. Wilms, P. Virnau, and K. Binder, J. Chem. Phys. **133**, 164702 (2010).

[164] P. J. Upton, J. O. Indekeu, and J. M. Yeomans, Phys. Rev. B **40**, 666 (1989).

[165] K. Rejmer, S. Dietrich, and M. Napiórkowski, Phys. Rev. E **60**, 4027 (1999).

[166] C. Rascón and A. O. Parry, Nature **407**, 986 (2000).

[167] A. Hanke, M. Krech, F. Schlesener, and S. Dietrich, Phys. Rev. E **60**, 5163 (1999).

[168] G. Palágyi and S. Dietrich, Phys. Rev. E **70**, 046114 (2004).

[169] M. E. Fisher and S.-Y. Zinn, J. Phys. A **31**, L629 (1998).

[170] M. E. Fisher, J. Phys. Soc. Japan. Suppl. **26**, 87 (1969).

[171] A. Drzewiński, A. Maciołek, A. Barasiński, and S. Dietrich, Phys. Rev. E **79**, 041145 (2009).

[172] H. Guo, T. Narayanan, M. Sztuchi, P. Schall, and G. H. Wegdam, Phys. Rev. Lett. **100**, 188303 (2008).

[173] C. Gögelein, M. Brinkmann, M. Schröter, and S. Herminghaus, Langmuir **26**, 17184 (2010).

[174] M. T. Dang, A. V. Verde, V. D. Nguyen, P. G. Bolhuis, and P. Schall, J. Chem. Phys. **139**, 094903 (2013).

[175] B. V. Prafulla, T. Narayanan, and A. Kumar, Phys. Rev. A **45**, 1266 (1992).

[176] P. K. M. Unni, The Journal of Chemical Physics **124**, 054505 (2006).

[177] J. C. Crocker and D. G. Grier, J. Colloid Interface Sci. **179**, 298 (1996).

[178] D. Allan, T. Caswell, N. Keim, and C. van der Wel, *Trackpy v0.3.1.*, Zenodo, 55143 (2016).

[179] P. S. Mohanty, D. Paloli, J. J. Crassous, E. Zaccarelli, and P. Schurtenberger, J. Chem. Phys. **140**, 094901 (2014).

[180] J. D. Cox, J. Chem. Soc. **1952**, 4606 (1952).

[181] A. Oleinikova, L. Bulavin, and V. Pipich, Chem. Phys. Lett. **278**, 121 (1997).

[182] M. Wagner, O. Stanga, and W. Schröer, Phys. Chem. Chem. Phys **4**, 5300 (2002).

[183] M. L. Kurnaz and J. V. Maher, Phys. Rev. E **51**, 5916 (1995); M. L. Kurnaz and J. V. Maher, Phys. Rev. E **55**, 572 (1997).

[184] I. S. Gradshteyn and I. M. Ryzhik (Editors), *Table of Integrals, Series, and Products* (Academic, London, 2000); for the correct asymptotic limit of $K(x \gg 1)$, $\arctan x$ must be expanded up to $1/x^3$, see Eq. 1.644.2.

[185] T. G. Mattos, L. Harnau, and S. Dietrich, J. Chem. Phys **138**, 074704 (2013).

[186] T. G. Mattos, L. Harnau, and S. Dietrich, Phys. Rev. E **91**, 042304 (2015).

[187] S. Paladugu, A. Callegari, Y. Tuna, L. Barth, S. Dietrich, A. Gambassi, and G. Volpe, Nature Commun. **7**, 11403 (2016).

[188] U. Nellen, J. Dietrich, L. Helden, S. Chodankar, K. Nygård, J. F. van der Veen, and C. Bechinger, Soft Matter **7**, 5360 (2011).

[189] M. Bier, A. Gambassi, M. Oettel, and S. Dietrich, EPL **95**, 60001 (2011).

[190] D. J. Kraft, J. Hilhorst, M. A. P. Heinen, M. J. Hoogenraad, B. Luigjes, and W. K. Kegel, J. Phys. Chem **115**, 7175 (2011).

[191] J. R. Wolters, G. Avvisati, F. Hagemans, T. Vissers, D. J. Kraft, M. Dijkstra, and W. K. Kegel, Soft Matter **11**, 1067 (2015); also Disney, Walt, *Steamboat Willie*, short film (1928).

[192] T. A. Nguyen, A. Newton, S. J. Veen, D. J. Kraft, P. G. Bolhuis, and P. Schall, Adv. Mater. **29**, 1700819 (2017).

[193] L. Onsager, Phys. Rev. **65**, 117 (1944).

[194] K. G. Wilson, Phys. Rev. B **4**, 3174 (1971); ibid. **4**, 3184 (1971).

[195] L. P. Kadanoff, W. Götze, D. Hamblen, R. Hecht, E. A. S. Lewis, V. V. Palciauskas, M. Rayl, J. Swift, D. Aspnes, and J. Kane, Rev. Mod. Phys. **39**, 395 (1967).

# Danksagung

Den größten Dank möchte ich Ihnen, Prof. Siegfried Dietrich, dafür aussprechen, dass ich diese Doktorarbeit in ihrer Abteilung verfolgen durfte. Ihre konstruktiv eingebrachte Sachkenntnis war stets enorm und lehrreich. Erst ihr Feinschliff an den Projekten verlieh ihnen den nötigen Glanz. Auch die persönliche Sorge um ihre Mitarbeiter war stets wohltuend.

Ihnen, Prof. Udo Seifert und Prof. Jörg Wrachtrup, danke ich für die bereitwillige Übernahme des Mitberichts bzw. des Vorsitzes des Prüfungsausschusses.

Weiteren Dank schulde ich meinen früheren “Lehrmeistern” Ludger Harnau und Matthias Tröndle, die mich in die wissenschaftliche Arbeit einführten. Zu schade, dass eure Lebenswege euch zwischenzeitlich von hier wegführten. Alles Gute für die Zukunft.

Danke Dir, Ania Maciołek, für die Zusammenarbeit, hilfreiche Diskussionen und den Kontakt zu der Arbeitsgruppe von Prof. Peter Schall. Selbigem, sowie Simon Stuij, danke ich ebenso für die konstruktive Zusammenarbeit.

Unschätzbare praktische Hilfe verdanke ich Anke Geigle, der Chef-Organisatorin aller Formalitäten verwaltungstechnischer Art, besonders bei Dienstreisen. Danke auch für die vielen Reisegeschichten, mit denen du mich unterhalten hast.

Andreas, treuer Zimmergenosse, Konferenz-Reisebegleiter und gemeinsamer Kaffeemaschinen-Verschmutzer und -Bereiniger, ich muss dir wohl kaum erklären, dass ich die Zeit genossen habe.

Allen weiteren Mitarbeitern danke ich für die gute Stimmung und die schöne Zeit, insbesondere Nima Farahmand Bafi für die musikalische Untermalung.

Letztlich verdanke ich meinen Eltern alles, selbst in den für euch schwierigen Zeiten.
Bleibt gesund.